

Bangor University

DOCTOR OF PHILOSOPHY

Wave generated flow over sand ripples and the resulting entrainment and suspension of sediment.

Block, Martin Edward

Award date:
1994

Awarding institution:
Bangor University

[Link to publication](#)

General rights

Copyright and moral rights for the publications made accessible in the public portal are retained by the authors and/or other copyright owners and it is a condition of accessing publications that users recognise and abide by the legal requirements associated with these rights.

- Users may download and print one copy of any publication from the public portal for the purpose of private study or research.
- You may not further distribute the material or use it for any profit-making activity or commercial gain
- You may freely distribute the URL identifying the publication in the public portal ?

Take down policy

If you believe that this document breaches copyright please contact us providing details, and we will remove access to the work immediately and investigate your claim.

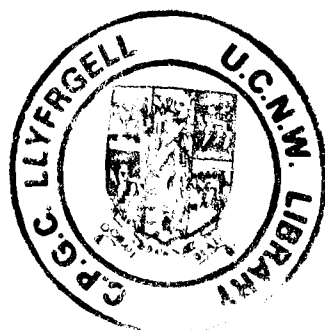
WAVE GENERATED FLOW OVER SAND RIPPLES AND THE RESULTING ENTRAINMENT AND SUSPENSION OF SEDIMENT

**A thesis submitted in accordance with the requirements of the University of Wales for
the degree of Doctor of Philosophy.**

Martin Edward Block

**University College of North Wales,
School of Ocean Sciences,
Menai Bridge,
Anglesey. LL59 5EY.
U.K.
February 1994.**

This thesis is dedicated to my parents, Harry and Edyth Block



ABSTRACT

A theoretical simulation of the wave generated flow and associated suspension of sediment over steep, round crested, two dimensional ripples has been developed. The two main aims of this simulation are (i) to increase understanding of the vortex shedding regime over ripples, and (ii) to provide details of sediment concentrations over rippled beds.

For these purposes, a time-stepping 'discrete vortex' hydrodynamical model has been developed to recreate the flow over ripples. In turn, this hydrodynamical model drives a separate, but co-existent boundary layer model. Sediment is entrained at the crest at a rate dictated by the boundary layer model. Once in suspension, it is moved in a purely convective, Lagrangian fashion, with a fall component.

Results from the hydrodynamical model provide details of the motion of vortices for various values of the ratio of orbital excursion to ripple wavelength (d/λ).

Results from the suspended sediment simulation include both instantaneous and time-averaged concentration profiles, as well as snap-shot plots of sediment motion.

The first aim of the simulation was successful, with the hydrodynamical model providing much useful information on the flow structure over ripples.

The second aim has met with mixed success. A wealth of data comparisons suggest that the present simulation performs well in replicating key features of the suspended sediment regime over ripples. However, it tends to underestimate sediment concentrations.

Two other allied studies were undertaken. The first concerned the force acting on the bed 'per ripple', illustrated by the behaviour of the friction factor f_w and the energy dissipation factor f_o . The second concerned the usage of the simulation to predict ripple stability, which involved the calculation of sediment transport rates over the entire ripple profile.

ACKNOWLEDGEMENTS

I am indebted to my supervisor, Dr Alan G. Davies, for his help and support throughout this thesis. He has always found time to see me amidst his obviously very busy schedule. Alan's unerring enthusiasm for the project has been a real benefit to me, and has made this PhD an enjoyable experience. Special thanks, Alan.

I also got 'very good value' from my supervisory committee team, comprising Prof. J. H. Simpson, Dr A. Elliott and Dr C.F. Jago. Their input went far beyond the committee brief, and it is my pleasure to thank them. Thankyou John, Alan and Colin.

My friends in Craig Mair Phd room have helped out in two ways. Firstly, they kept me in a state of mind acceptably close to sanity. Secondly, they gave me loads of advice with my work, specifically Graeme Allan, Tim O'Hare, Reginaldo Durazzo, Alex Souza, Tom Rippeth, Jonathan Sharples, Pat Hyder, Andy Peet and Janice Chapman. Cheers everyone - you know who you are.

A special thankyou to some of the team (past and present) at the UCNW computing centre in Bangor: to Terry Williams for loads of Fortran help in the early days, to Dafydd Roberts for help with graphics and to Paul Wood and Simone Barberosi for teaching me Wordperfect.

Many thanks to Catherine Villaret (at LNH, Paris) who provided us with the sediment concentration data that forms the backbone of Chapter 5. Also, I would like to acknowledge the work of Bruce Macpherson, whose 1984 thesis provided such a lot of guidance in the early parts of this study.

A special thankyou to Margy Newens, who gave up a lot of her time to proof-read the manuscript. Fortunately, she resisted the temptation to translate it into Russian.

Finally, I would like to thank my family for enthusing over my wayward plans. They didn't blanch too much when I told them I was chucking a good job in to do this. Special thanks Mum and Dad, to whom this thesis is dedicated.

This project was funded by the Science and Engineering Research Council, who stepped in with a grant at the 11th hour.

CONTENTS

1.	INTRODUCTION	1
1.1	Coastal sedimentation	2
1.2	The role of the present study	3
1.3	The structure of the present study	3
2.	RIPPLES AND VORTICES : AN INTRODUCTION	5
2.1	Introduction	6
2.2	The formation of ripples	7
2.3	Experimental studies of ripples	8
2.3.1	Laboratory studies	8
2.3.2	Field studies	8
2.4	Some parameters that have a bearing on ripples	9
2.4.1	Ripple steepness	9
2.4.2	Orbital diameter of the oscillatory motion	9
2.4.3	Wave Reynold's number and Mobility number	9
2.4.4	Ratio of orbital amplitude and median grain size	10
2.5	The vortices formed over ripples	11
2.5.1	Vortex formation and shedding	11
2.5.2	Experimental studies	11
2.6	Complex potential representation of vortices	12
2.6.1	Rectilinear vortex filaments	12
2.6.2	Velocity field associated with vortices	13
2.6.3	Radius of the vortex core	14
2.6.4	The 'log sine' potential	14
3.	THE HYDRODYNAMICAL MODEL	15
3.1	Introduction	16
3.1.1	Discrete vortex method (d.v.m)	16
3.1.2	Application of d.v.m to osc. flow over ripples	19

3.1.3	Standing vortex models	21
3.1.4	Direct solution of the Navier Stokes equation	21
3.2	The hydrodynamical model	23
3.2.1	Development of the hydrodynamical model	23
3.2.2	Description of the hydrodynamical model	28
3.2.3	Parameter choices and their justification	30
3.2.4	Computational aspects of the model	32
3.3	Results	34
3.3.1	Computational aspects of the hydrodynamical model	34
3.3.2	Effects of ripples steepness	35
3.3.3	Model results for the central run ($d_0/\lambda=1.62$, $h/\lambda=0.17$)	36
3.3.4	Sensitivity tests based on the central run settings	39
3.3.5	Two further runs; $d_0/\lambda=1.1$ and 2.5 .	
3.4	Discussion	43
3.4.1	Comparisons with experimental data	43
3.4.2	Comparisons with theoretical results	44
3.4.3	Implications of these comparisons	45
3.5	Conclusions	46
4.	THE BOUNDARY LAYER MODEL	47
4.1	Introduction	48
4.1.1	Classification of the boundary layer flow regime	48
4.1.2	Structure of the boundary layer	49
4.1.3	Theoretical descriptions of the boundary layer	50
4.1.4	Boundary layer over ripples	52
4.2	Formulation of the boundary layer model	52
4.2.1	Adaptations to the original Fredsoe (1984) model	52
4.2.2	The development of the present boundary layer model	53
4.3	Implementation of the boundary layer model	55
4.3.1	Outer velocity for the boundary layer model	55
4.3.2	Flow reversals in the time series of $R_b(t)$	56

4.3.3	Boundary layer model at the ripple crest	56
4.3.4	Boundary layer model over entire ripple profile	57
4.4	Results	58
4.4.1	Replicating the results of Fredsoe (1984)	58
4.4.2	Boundary layer model at the ripple crest	58
4.4.3	Boundary layer model over entire ripple profile	59
4.5	Discussion	60
4.6	Conclusions	62
5.	THE ENTRAINMENT AND SUSPENSION OF SEDIMENT	63
5.1	Introduction	64
5.1.1	Laboratory studies of suspended sediment over ripples	64
5.1.2	Field studies of suspended sediment over ripples	67
5.1.3	Theoretical studies of suspended sediment over ripples	69
5.2	The experimental data of C. Villaret (1992, 1993)	72
5.3	The suspended sediment simulation	73
5.3.1	Introduction	73
5.3.2	Simulating the entrainment of sediment	73
5.3.3	Simulating the suspension of sediment	74
5.3.4	Obtaining instantaneous concentrations	74
5.3.5	Obtaining vertical concentration profiles ($C(Y)$)	75
5.4	Results	75
5.4.1	The choice of the value of τ_c	75
5.4.2	Results for Test 1 ($d_s/\lambda = 1.62$, $h/\lambda = 0.16$)	75
5.4.3	Results for Test 2 ($d_s/\lambda = 2.63$, $h/\lambda = 0.11$)	78
5.4.4	Sensitivity tests	81
5.4.5	Comparisons with the data of Villaret (1992, 1993)	82
5.4.6	Comparisons with other data	84

5.5	Discussion	85
5.5.1	Prediction of the quantity of suspended sediment	85
5.5.2	Simulation of the movement of suspended sediment	88
5.5.3	Measuring box	88
5.6	Conclusions	89
6.	RIPPLE STABILITY : BEDLOAD TRANSPORT OVER THE RIPPLE	90
6.1	Introduction	91
6.2	Computational methodology	91
6.3	Results	93
6.3.1	Results with no threshold of motion ($\tau_c = 0$)	93
6.3.2	Inclusion of a threshold of motion	95
6.4	Discussion	96
6.5	Conclusions	97
7.	THE FORCE ON THE BED "PER RIPPLE"	98
7.1	Introduction	99
7.1.1	Time averaged quantities:- energy dissipation factor	99
7.1.2	Instantaneous quantities	101
7.2	Computational algorithms for calculating $\overline{C_D}$ and f_w	102
7.2.1	Algorithm for obtaining $\overline{C_D}$	103
7.2.2	Algorithm for obtaining f_w	104
7.3	Results	105
7.3.1	Results for $\overline{C_D}$	105
7.3.2	Results for τ_o and f_w	106
7.4	Discussion	106
7.5	Conclusions	108
8.	CONCLUSION	110
8.1	Introduction	111
8.2	A brief resume of each of the chapters	111

8.2.1	Hydrodynamical model (Chapter 3)	111
8.2.2	Boundary layer model (Chapter 4)	112
8.2.3	The suspended sediment simulation (Chapter 5)	112
8.2.4	Ripple stability (Chapter 6)	113
8.2.5	Force on the bed ' per ripple' (Chapter 7)	113
8.3	General conclusions concerning the present study	113
8.4	Improvements to the present study	114
8.5	The scope for further work	114

REFERENCES	i
APPENDIX 1	ix
APPENDIX 2	xv

LIST OF SYMBOLS

a	radius of a vortex core
a_o	orbital excursion amplitude
b	ripple amplitude
B, C, D, E	coefficients used in boundary layer model solution
C	sediment concentration
$\overline{C}(Y)$	cycle-averaged vertical concentration profile
C_o	Nielsen's reference concentration
C_D, \overline{C}_D	instantaneous and cycle averaged drag coefficients
$C, C_1..C_4$	The contours used in the derivation in appendix 2
d	water depth
d_o	orbital excursion
D_{50}	median grain diameter of sediment
E	energy dissipation rate
F	the (total) drag force acting on the bed 'per ripple'
$F_{osc, vort}$	the oscillatory and vortex contributions to F
f_o	energy dissipation factor
f_w	Jonsson's friction factor
$F(Z)$	Nielsen's distribution function for C
g	acceleration due to gravity
G	the lift force acting on the bed 'per ripple'
h	ripple height
H	wave height
j	parameter used in boundary layer model solution
J_1 (etc)	symbolism used in the derivation of the force on the bed per ripple
k	wavenumber of surface waves
k_s	equivalent roughness lengthscale
l	wavenumber of ripples
l_r	lengthscale for the decay of $C(Y)$ with height
M	mobility number

P	fluid pressure
$p(t)$	Nielsen's time-varying pick-up function
Q	flux of sediment
Q_b	volumetric sediment transport rate per unit width of flow
r	radial distance from a vortex centre
R_b	magnitude of resultant velocity at top of boundary layer
RE	wave Reynolds number
s	Relative density of sediment
t	time
t_{age}	age of vortices
T	timeperiod of oscillatory water motion
U, V	Generalised horizontal and vertical velocity components
U_z, V_z	velocity components in the z plane
U_ζ, V_ζ	velocity components in the ζ plane
U_b	horizontal velocity at edge of boundary layer
U_{bl}	horizontal velocity within boundary layer
U_*	friction velocity
U_o	velocity amplitude of oscillatory motion
V_θ	tangential velocity induced by the rotating vortex
w_s	fall velocity of sediment
Y	vertical co-ordinate measured from the bed level
Y_o	roughness lengthscale
$z=x+iy$	point in the z plane
Z	vertical co-ordinate measured from the bed level (used in Ch. 5)
α_1, α_2	coefficients used in the derivation of velocity components due to vortices
β	($= \sqrt{(\sigma/2\nu)}$) flow parameter often used by Sleath and allied researchers
γ	($= s-1$), factor associated with relative density of sediment
γ_o	the resuspension coefficient
Γ	circulation of a vortex
δ	boundary layer thickness
δ_1	Jonsson's definition of boundary layer thickness

δ_w	Smith's definition of boundary layer thickness
δt	model timestep
ΔK_s	($=K_{s,u} - K_{s,l}$) notation employed to simplify the expression for F_{vort}
ε	eddy viscosity
ε_s	sediment diffusivity
$\zeta=\xi+i\chi$	point in the ζ plane
θ, θ_c	Shields parameter with associated critical value
θ_r	Shields parameter for flow over ripples
κ	Von Karman's constant
K	strength of a vortex
λ	ripple wavelength
Λ	vorticity
ν	kinematic viscosity
ρ, ρ_s	density of water and sediment respectively
σ	frequency of oscillatory motion
τ	shear stress
τ_o	shear stress acting on ripple (form drag)
τ_b, τ_c	bed shear stress (skin friction) and associated critical value
ϕ	angle of static repose of sediment
ϕ_b	non-dimensional volumetric sediment transport rate per unit width
ψ	streamfunction
ω	angular velocity of the vortex core
Ω	complex potential

When considering an individual vortex, the notation for its centre is z_o or ζ_o . For numerous vortices, though, the notation is z_s or ζ_s . The suffixes "osc" and "vort" refer to the oscillatory and vortex components of a parameter (eg τ_{osc}).

CHAPTER 1

INTRODUCTION

This thesis is concerned with the interaction of surface waves with two-dimensional ripples on the seabed and the resulting entrainment and suspension of sediment into the water column. The motivation to study these relatively small scale processes lies in the desire to increase our knowledge about large scale sediment transport in the nearshore region.

1.1 Coastal sedimentation

The coastline of Britain is surrounded by vast quantities of deposited sediment. In the active nearshore region, large scale movement and subsequent deposition of this sediment may occur as a result of waves and currents.

Before the Second World War, this (large scale) relocation of sediment was viewed as a nuisance, causing the denudation of beaches, silting up of harbour approaches and so on. The wisdom of the day was to take local action (groynes, dredging etc) to interrupt the course of nature. No great effort was made to understand the sediment movement itself.

In recent years, technological and environmental demands have forced the need for a more thorough understanding of nearshore marine processes, including the role of sediment. We now know that the movement and deposition of sediment forms an integral part of the nearshore marine regime. Far from being a nuisance, deposited beds of sediment help form a natural buffer against wave attack.

In the future, it seems likely that our increased knowledge of large scale sediment movement will be put further to the test. Two scenarios can be envisaged :-

- (i) The strategic dumping of sediment offshore to form large, stable bedforms which could help spare the coastline from excessive erosion.
- (ii) The (possible) construction of offshore power generating apparatus which would require an assessment of the impact on the local sediment regime and vice-versa.

1.2 The role of the present study

Our knowledge of these large scale movements of sediment will remain incomplete without an understanding of the much smaller scale processes in operation at the bed itself. Specifically, we have spoken of sediment movement without addressing the question of how this sediment has entered the water column from the bed.

It is here that this (theoretically based) study fits in. The interaction of surface waves with sand ripples on the sea bed is a very potent mechanism for entraining sediment from the bed into the water column. The two main goals of this thesis are (i) to provide more understanding of the vortex shedding regime that is associated with this interaction, and (ii) to provide, via a simulation of the resulting entrainment and suspension of sediment, details of sediment concentration over rippled beds for use by coastal engineers.

1.3 The structure of the present study

To this end, a *hydrodynamical model* has been developed (using an approach called the 'discrete vortex method') in order to provide a description of the flow over two dimensional ripples. This, coupled with a separate but co-existent *boundary layer model* (which provides the basis for sediment entrainment) allows the theoretical prediction of the suspended sediment regime. The hydrodynamical model and boundary layer model provide useful information in their own right, which complements the suspended sediment studies.

The structure of the thesis has been strongly influenced by the modular nature of the research undertaken. The three main modules (the hydrodynamical model, the boundary layer model and the suspension studies) were developed separately, each being self contained. It seemed inappropriate to have the relevant literature for these three modules in one (large) literature chapter, so each has its own literature review.

Chapter 2 provides essential background information on ripples. Chapters 3 and 4 go through the development of the hydrodynamical and boundary layer models. These models are then combined in Chapter 5, where the sediment suspension regime over

ripples is simulated. Chapters 6 and 7 represent interesting extensions to the main thrust of the thesis: in Chapter 6, the suite of models is used to predict changes in ripple morphology (and hence ripple stability); Chapter 7 discusses how the hydrodynamical model can be used to obtain both instantaneous and cycle-averaged drag coefficients associated with the force exerted on the ripple profile by the flow. Finally, in Chapter 8, the overall findings of the thesis are reviewed.

Throughout the thesis, every effort has been made to compare our model results with established experimental and theoretical data. For this purpose, we have made use of sand concentration data obtained experimentally by C. Villaret (1992, 1993) at LNH - Chatou, France. To distinguish between so-called experimental and model data, we use the terms 'data' and 'measurement' when referring to experimental data, and 'results' for data obtained from theoretical modelling.

CHAPTER 2

RIPPLES AND VORTICES : AN INTRODUCTION

2.1 Introduction

Ripples are formed on the seabed as a consequence of wave-induced water motions. Linear wave theory predicts that these motions are elliptical near the water surface, becoming increasingly attenuated with depth. Near the bed, the wave-induced water motion is oscillatory in nature. Parameters associated with this *oscillatory motion* can be obtained from the wave regime itself. The time period of a complete oscillation, T , is given by

$$T = \frac{2\pi}{\sigma} \quad 2.1$$

and the velocity amplitude by

$$U_o = \frac{H\sigma}{2\sinh(kd)} \quad 2.2$$

where k is the wavenumber of the waves, H the wave height and d the water depth. The orbital diameter of the near-bed motion (d_o) is

$$d_o = \frac{2U_o}{\sigma} \quad 2.3$$

Figure (2.1) is a schematic diagram illustrating these quantities.

This oscillatory motion can be recreated in the laboratory using a flume (where the waves themselves produce the near-bed motions) or by artificially creating the oscillations using either an oscillatory flow water tunnel or an oscillating tray. When using this equipment to produce stable ripples, certain features make a strong visual impact. Firstly, the ripples are regularly spaced with an identifiable wavelength and geometry. If the flow parameters are altered, then the ripples alter in sympathy until they settle into a new stable configuration. Secondly, for ripples of sufficient steepness, vortices are formed in the lee of each ripple in every half time period (referred to as a half cycle). These vortices are subsequently ejected as the flow changes direction, Meanwhile a new vortex forms on the other side of the ripple. As with the ripple spacing, the formation and ejection of vortices seems a very ordered process. Finally,

the vortices themselves have a marked effect on the suspension of sediment over the bed, perceived as a layer of suspended sediment oscillating with the flow.

2.2 The formation of ripples

How does a flat, unrippled sand bed develop in this way and which of the flow parameters control the regularity of their spacing? Bagnold (1946) addressed these questions by observing the development of ripples on an oscillating tray. The following is a descriptive resume of what was observed by both Bagnold and subsequent researchers.

A pre-requisite for the development of ripples from an initially flat bed is that the oscillatory motion is energetic enough to actually move the sediment - the so-called threshold of sediment movement. At around this threshold point, sediment grains are noted to roll back and forth across the bed. Despite the apparent randomness of this process, these grains have a tendency to collect in well defined, low relief ridges at right angles to the flow. Sleath (1984) demonstrated that slight waviness in the bed produces circulation cells in the flow that tend to collect sediment in the ridges. Bagnold called these ridges 'rolling grain ripples'. Their morphology is governed by the constituent grains and they exhibit low steepnesses. Manohar (1955) and Sleath (1976b) have made experimental studies of rolling grain ripples, whilst Blondeaux and Vittori (1991) have modelled their development theoretically. As the flow speed is increased, the rolling grain ripples become steep enough to allow flow separation to occur at their crests, and vortex formation ensues. These bedforms steepen and mutate until they form the stable ripples described earlier, called 'vortex ripples'. Figure (2.1) is a schematic diagram showing (vortex) ripples with the associated vortex shedding. *From here on, we shall refer to vortex ripples simply as ripples.* In reality, this idealised process of ripple development can be short-circuited by obstacles on the bed. Such obstacles produce vigorous flow separation in their wake, creating a 'domino effect' of ripple formation that advances from the obstacle.

2.3 Experimental studies of ripples

2.3.1 Laboratory studies

Historically, most laboratory studies of ripples have been directed towards ripple formation and morphology, as well as the analysis of which parameters are fundamental to ripples. In some cases (e.g. Bagnold (1946), Carstens *et al* (1969)), derived data, such as drag coefficients have been obtained. We group a selection of these studies according to the equipment used: *flume* (Kennedy and Falcon (1965), Mogridge and Kamphuis (1972)), *oscillatory water tunnel* (Carstens and Nielsen (1967), Carstens *et al* (1969), Lofquist (1978)) and *oscillating tray* (Bagnold (1946), Mogridge and Kamphuis (1972)). [Miller and Komar (1980a) assess the effect of these different pieces of equipment on ripple generation.]

In recent years, the tendency has been for researchers to study the flow structure and sediment entrainment regime over the ripples, as opposed to the ripples themselves. Two pioneering studies of this genre are Tunstell and Inman (1975) and DuToit and Sleath (1981).

2.3.2 Field studies

There have been numerous studies of ripples in the field, including Inman (1957), Miller & Komar (1980b), Davies (1984a,b) and Boyd *et al* (1988). These researchers found that ripples in the field have longer wavelengths than their laboratory counterparts. Boyd *et al* (1988) observed ripples on an ocean shoreface, 1 km offshore and in 10 m of water. They found that the ripples always had a wavelength greater than 0.06 m, and suggested that this 'long wavelength' tendency of offshore ripples could help in defining paleo-oceanic environments. Boyd *et al* also found that ripples responded rapidly to changes in the wave regime. This finding concurs with the fact that ripples in the field show much more three-dimensionality than those in the laboratory.

2.4 Some parameters that have a bearing on ripples

2.4.1 Ripple steepness

The combined effects of the oscillatory motion (acting up the stoss face) and the rotation of the lee vortex force sediment up to the crest of the ripple. However, the tendency for sediment to migrate towards the crest is counteracted by gravity. Ultimately, the developing ripple achieves an equilibrium steepness where these agencies are in balance. Various researchers have put the steepness of equilibrium ripples in the range $0.10 < h/\lambda < 0.25$, where h is the ripple height and λ the ripple wavelength. Nielsen (1981) quotes the maximum steepness of ripples to be

$$\left(\frac{h}{\lambda}\right)_{\max} = 0.32 \tan \phi \quad 2.4$$

where ϕ is the angle of repose of the sediment ($= 33^\circ$).

2.4.2 The orbital diameter of the near-bed flow

The generally accepted criterion for the compliance of the ripple wavelength to changes in the flow parameters is that it adjusts itself to a fixed proportion of the orbital excursion d_o . The reason for this is not fully clear, but the 'accepted wisdom' is that the distance of travel of the ejected vortices (which depends on d_o) can either aid or hinder ripple development. The often quoted ratio for which ripples seem to be stable lies in the range $1.3 < d_o/\lambda < 1.5$, although in fact, stable ripples form well outside this range.

2.4.3 The wave Reynolds number and the mobility number

Two other parameters that have a bearing on the geometry and occurrence of ripples are the *wave Reynolds number* (RE) and the *mobility number* (M):

$$RE = \frac{U_o a_o}{\nu} \quad M = \frac{U_o^2}{(s-1) g D_{50}} \quad 2.5 (a, b)$$

where a_o is the excursion amplitude ($=d_o/2$), ν is the kinematic viscosity ($= 10^{-6} \text{ m}^2/\text{s}$), S is the relative density of sand ($= 2.65$), g is the acceleration due to gravity and D_{50} is the median diameter of the sediment. Both RE and M are non-dimensional measures of the 'activity' of the flow, relative to the inertial properties of the fluid (for RE) and the substrate (for M). High values of both parameters suggest an active, energetic flow regime. Figure (2.2) (from Jonsson (1966)) shows a variety of flow regimes which are dependent on RE and the ratio a_o/k_s (called the 'relative roughness') where k_s is Nikuradse's equivalent roughness. This is Jonsson's 'delineation of regimes'. Ripples are generally found to occur in the rough turbulent regime for relatively small values of a_o/k_s . Figure (2.3a,b) (from Nielsen (1979)), shows two graphs (λ/a_o versus M and h/a_o versus M), with various researchers' data plotted on it. The datapoints lie clustered along fairly regular curves, which gives a further basis for predicting the occurrence of ripples.

2.4.4 The ratio of the orbital amplitude to the median grain size (a_o/D_{50})

Carstens *et al* (1969), Mogridge and Kamphuis (1972) and Lofquist (1978) have all used the ratio a_o/D_{50} to define when ripples cease to scale on the orbital diameter d_o (the so-called 'cut-off point'). Carstens *et al* (1969) provide the condition

$$\frac{a_o}{D_{50}} > 750 \quad 2.6$$

for the 'cut-off' point. Practically, this cut-off point is where ripples cease to be organised, two-dimensional features, and start to show significant three dimensionality. For still higher values of a_o/D_{50} , sheet flow conditions prevail; the (three dimensional) ripples are washed out, to be replaced by (two-dimensional) rolling grain ripples.

2.5 The vortices formed over ripples

2.5.1 Vortex formation and shedding

The formation of vortices and their motion is governed by the wave generated oscillatory motion. In the idealised situation of symmetric surface waves, this motion can be represented by a sine curve with phase determined by the timeperiod, T , of the surface wave. In each half cycle, the velocity increases from zero to a maximum at $T/4$, then wanes to flow reversal at $T/2$. The second half cycle mirrors the first. The interaction of this oscillatory flow with the ripple profile generates vorticity. This vorticity rolls up to form an identifiable growing vortex over the lee slope. On flow reversal, this growing vortex ceases to develop, but is ejected up the lee slope and over the crest. Meanwhile, another growing vortex is forming on the opposite side of the ripple, and so on. Tunstell and Inman (1975) put the 'effective lifetime' of an ejected vortex as about half a time period i.e. although a coherent vortex may be identified for longer than this, it ceases to influence the flow regime.

2.5.2 Experimental studies of vortex formation and shedding over ripples

Studies of the vortices that are such a feature of ripples under wave action include Tunstell and Inman (1975), Sawamoto (1980) and, more recently, Marin (1992) and Ranasoma (1992). Sleath (1982a) made observations of vortex formation and ejection in connection with sediment entrainment at the ripple crest.

In making experimental studies of vortex shedding, most researchers have used either a combination of natural and artificial ripples (e.g. Tunstell and Inman (1975)) or purely artificial ripples (Sawamoto (1980), Ranasoma (1992)). A commonly employed technique is to generate natural ripples on an erodible bed, then solidify their profiles with chemical sealant. Tunstell and Inman (1975) used hydrogen bubbles to aid flow visualisation, then performed calculations from cine film of their motion. More recent studies (e.g. Ranasoma (1992)) have used remote sensing techniques, such as a laser doppler anemometer.

Tunstell and Inman (1975) directed their study towards finding out the amount of energy bound up in vortex growth (and hence lost from the waves), establishing that

up to 7% of the total rate of energy loss from the waves was absorbed in this fashion. Their calculations also provided useful information concerning the formation and shedding of vortices. Marin (1992) and Ranasoma (1992) use time-sequenced vorticity contour plots to illustrate the formation and shedding of vortices over ripples. This method of presenting information on the developing vorticity field is very popular in contemporary research.

Recently, Japanese researchers (Sato *et al* (1987), Ikeda *et al* (1991)) have made experimental studies of the flow regime over artificial ripples. They used a laser doppler velocimeter to produce vector plots of velocity and turbulent fluctuations over the ripples. In general, though, their work has been directed towards turbulent structure within the flow.

2.6 Complex potential representation of vortices

In anticipation of the mathematical methods in this thesis, it will be useful to review the complex potential theory as it relates to vortices. The following arguments are due to Milne-Thomson (1968).

2.6.1. Rectilinear vortex filaments

The complex potential of a 'rectilinear vortex filament' of strength K at $z = z_0$ is given by

$$\Omega = i K \log (z - z_0) \quad 2.7$$

The theory of complex potentials relies on the fact that the flow is irrotational - this is not the case for a rectilinear vortex filament. For this reason, a circular, rotational region is defined, called the *vortex core*. Figure (2.4) illustrates this vortex core. The tangential velocity (V_θ) increases linearly from zero at the vortex centre, to a maximum ($V_{\theta(\max)}$) at the core edge (where the core radius $r = a$). We have, therefore,

$$V_{\theta(\max)} = a \omega = \frac{1}{2} a \Lambda \quad 2.8$$

where Kelvin's vortex theorem has been used to replace the angular velocity (ω) with the vorticity (Λ). The circulation at $r = a$ is given by

$$\Gamma = \int_0^{2\pi} V_{\theta(\max)} \cdot a d\theta = \int_0^{2\pi} \frac{1}{2} a \Lambda \cdot a d\theta = \pi a^2 \Lambda \quad 2.9$$

The strength of a rectilinear vortex filament (K) is defined such that

$$\Gamma = 2\pi K \quad 2.10$$

thus

$$2\pi K = \pi a^2 \Lambda \quad 2.11$$

or

$$K = \frac{1}{2} a^2 \Lambda$$

This expression may be written as

$$K = \frac{\Lambda}{2\pi} \cdot \pi a^2 \quad 2.13$$

where πa^2 is the cross sectional area of the core.

If we let $a \rightarrow 0$ and $\Lambda \rightarrow \infty$ in such a way that K remains constant, we obtain a rectilinear vortex filament. The complex potential is as in equation (2.7), with $K > 0$ for anti-clockwise rotation.

2.6.2 The velocity field associated with vortices

Two important parameters can be obtained from the complex potential: the streamfunction ψ from the imaginary part of Ω , and the velocity field from its first derivative with respect to z . The velocity field associated with a rectilinear vortex filament and its core is shown in figure (2.5). It should be noted that the induced velocity at the vortex centre is zero, prompting the statement that vortices induce no movement in themselves, but move under the action of the other flow agencies present.

In reality, viscosity decays the strength of vortices as they age, until they eventually become indistinguishable from the host flow. With time, this *vortex decay* manifests itself in a growth of the vortex core. Figure (2.5) illustrates this point: as 'a'

increases, $V_{\theta(\max)}$ decreases, which, in turn, decreases Γ and K . Lamb (1932) has included the dissipative effects of viscosity in an expression for V_{θ} :

$$V_{\theta} = \frac{K}{r} \left[1 - \exp \left(\frac{-r^2}{4\nu t_{age}} \right) \right] \quad 2.14$$

where ν is the coefficient of kinematic viscosity, ' t_{age} ' is the vortex age and the other notation is as before. Figure (2.6) shows how this expression predicts both a smoother transition of velocity at the core edge, and a decrease in $V_{\theta(\max)}$ with age.

2.6.3 The radius of the vortex core

Equation (2.14) can be used as a basis for predicting the radius of the vortex core in time (the core radius ' a ' is the value of ' r ' for which V_{θ} is maximal). Tunstell and Inman (1975) have done this, assuming that the core radius grows linearly in time, and their result for the core radius as a function of vortex age is

$$a = 2.24 \sqrt{\nu t_{age}} \quad 2.15$$

2.6.4 The 'log sine' potential

Milne-Thomson (1968) and Davies (1984a) describe the development of a complex potential that describes an infinite row of vortices of strength K , centred at z_0 :

$$\Omega = iK \log \sin \frac{\pi}{\lambda} (z - z_0)$$

where λ is the spacing of the vortices within the row. Figure (2.7) shows one of these vortex rows. This complex potential can then be used to simulate vortices over an infinite bed of ripples.

A sequence of figures from literature reviewed concerning ripples and vortices, coupled with some explanatory diagrams.

Figure 2.1 A schematic diagram illustrating the oscillatory flow over vortex ripples, with the associated notation.

Figure 2.2 Jonsson's 'delineation of regimes' diagram, copied and adapted from Jonsson (1966).

Figure 2.3 (a,b) Two 'ripple occurrence' diagrams, relating (non-dimensional) ripple wavelengths and heights to the mobility number 'M'. Copied and adapted from Nielsen (1979).

Figure 2.4 A schematic diagram that illustrates the disk-like nature of the vortex core. The radius of the core is 'a'.

Figure 2.5 The induced velocity due to a vortex, from its centre to distances outside the vortex core. The three lines show that as the core expands, 'a' increases through 'a₁' to 'a₃'. This, in turn, brings about dissipation of the vortex's strength by reducing $V_{\theta(max)}$.

Figure 2.6 The induced velocity due to a vortex with viscosity incorporated (based on Lamb (1932)). The expansion of the vortex core in time ($t_4 > t_1$), dissipates the vortex's strength by reducing $V_{\theta(max)}$.

Figure 2.7 The 'log sine' complex potential arises from an infinite row of vortices, centred at $z = z_0$.

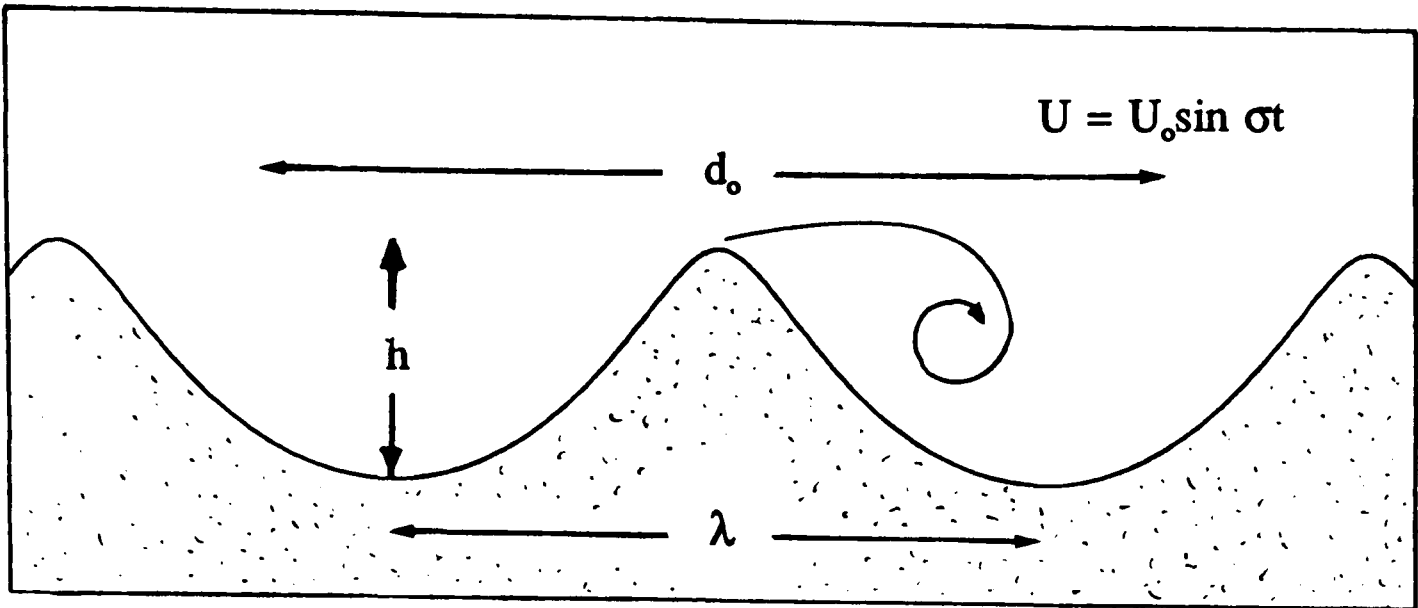
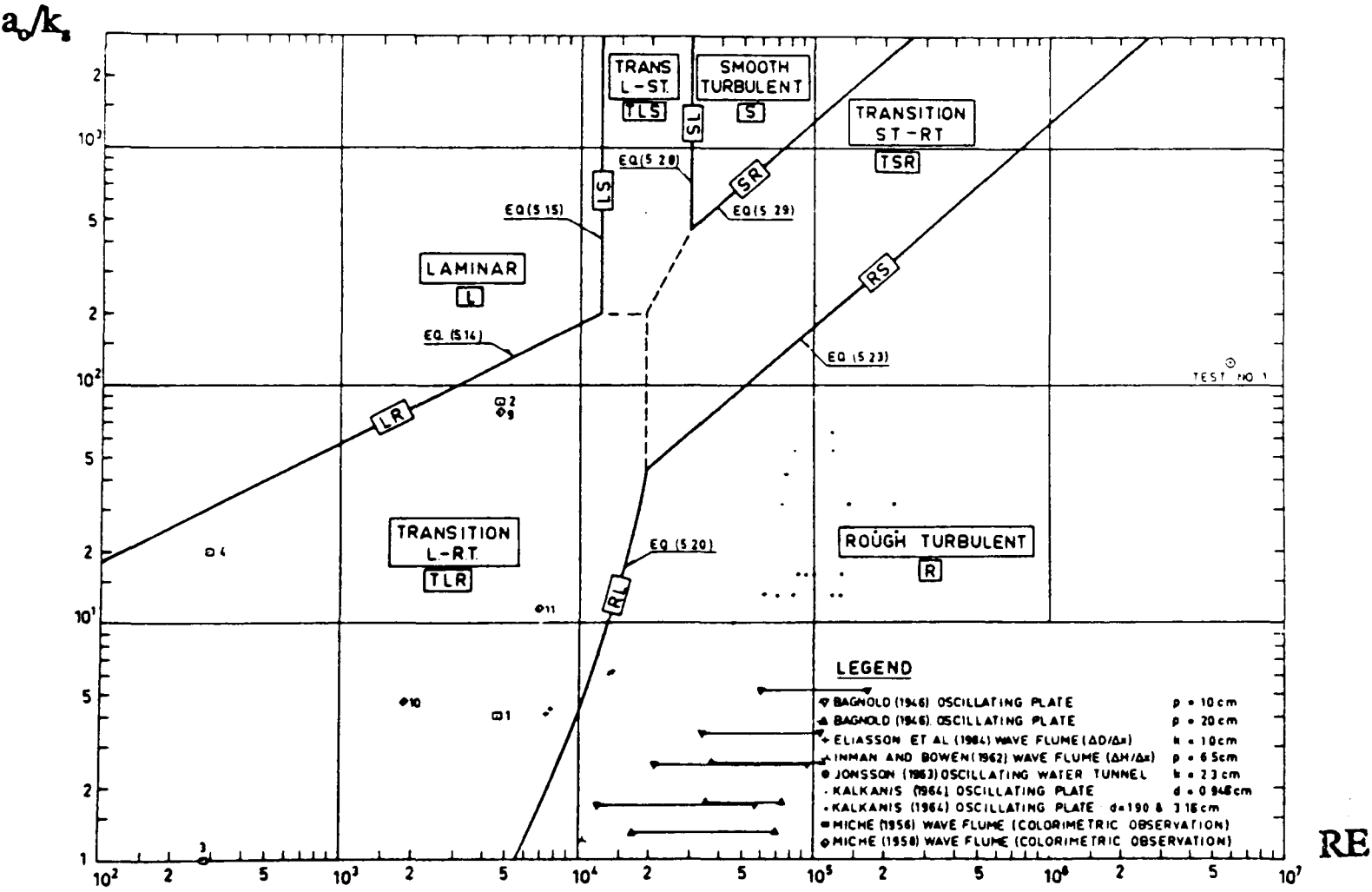


Figure 2.1

Figure 2.2



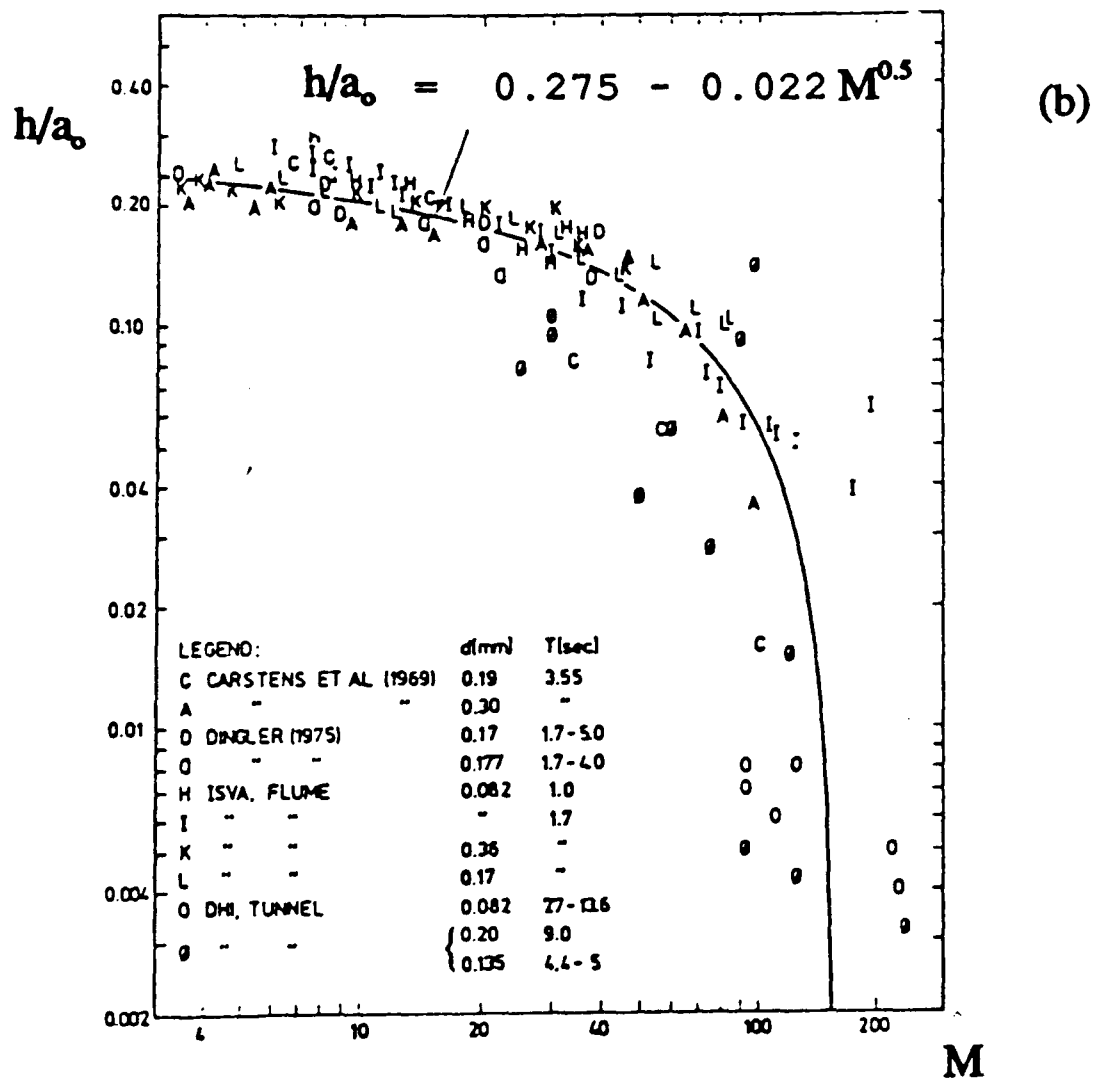
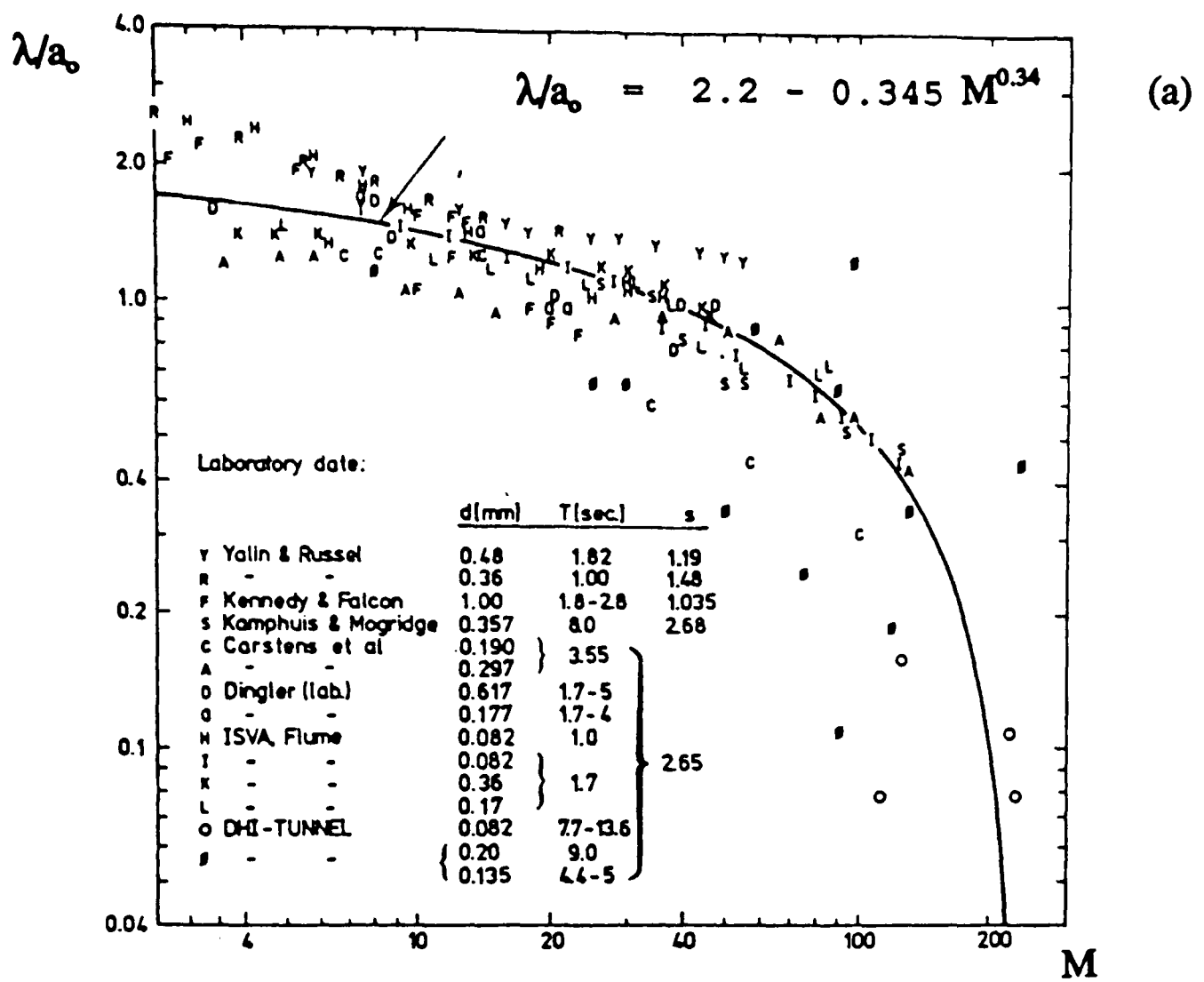


Figure 2.3 (a,b)

Figure 2.4

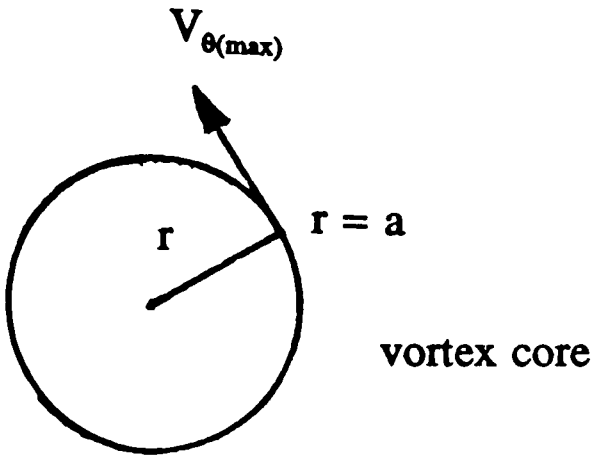


Figure 2.5

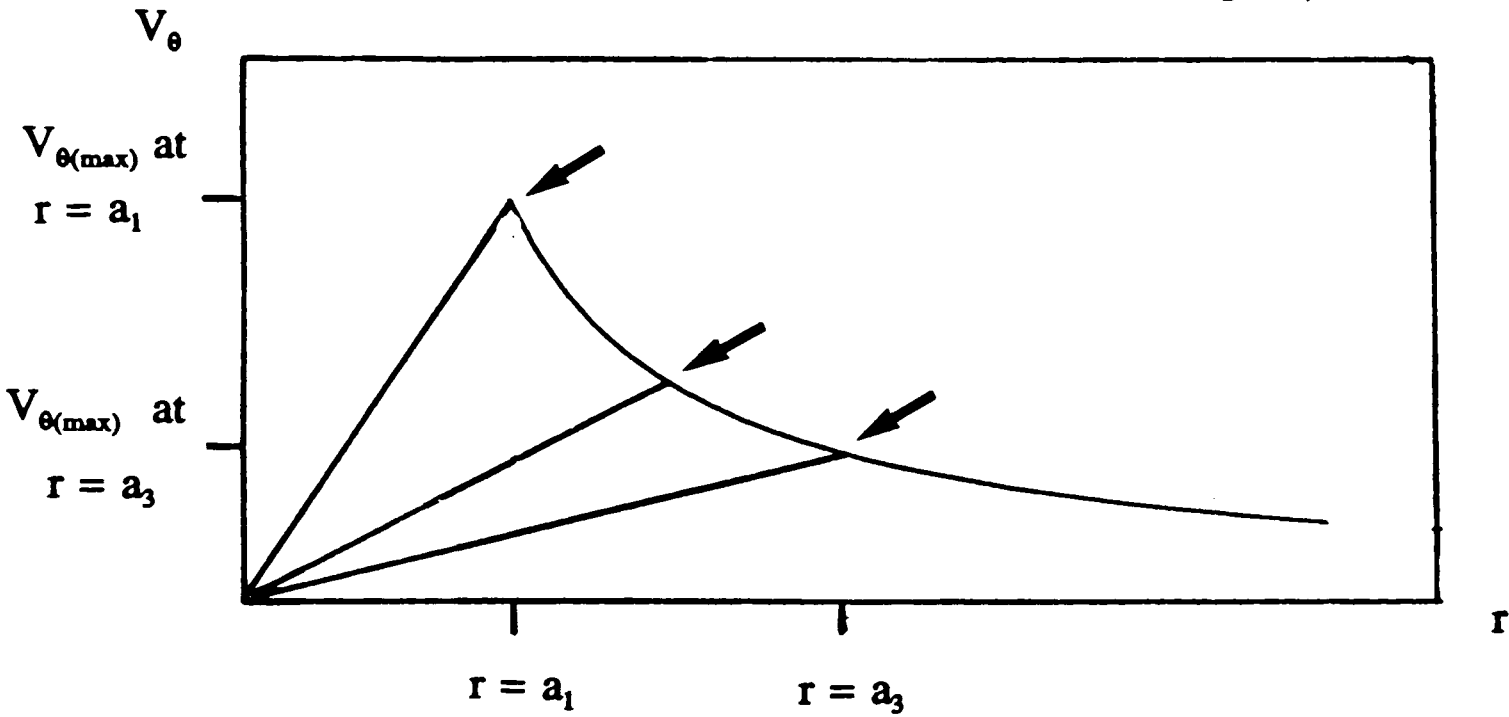
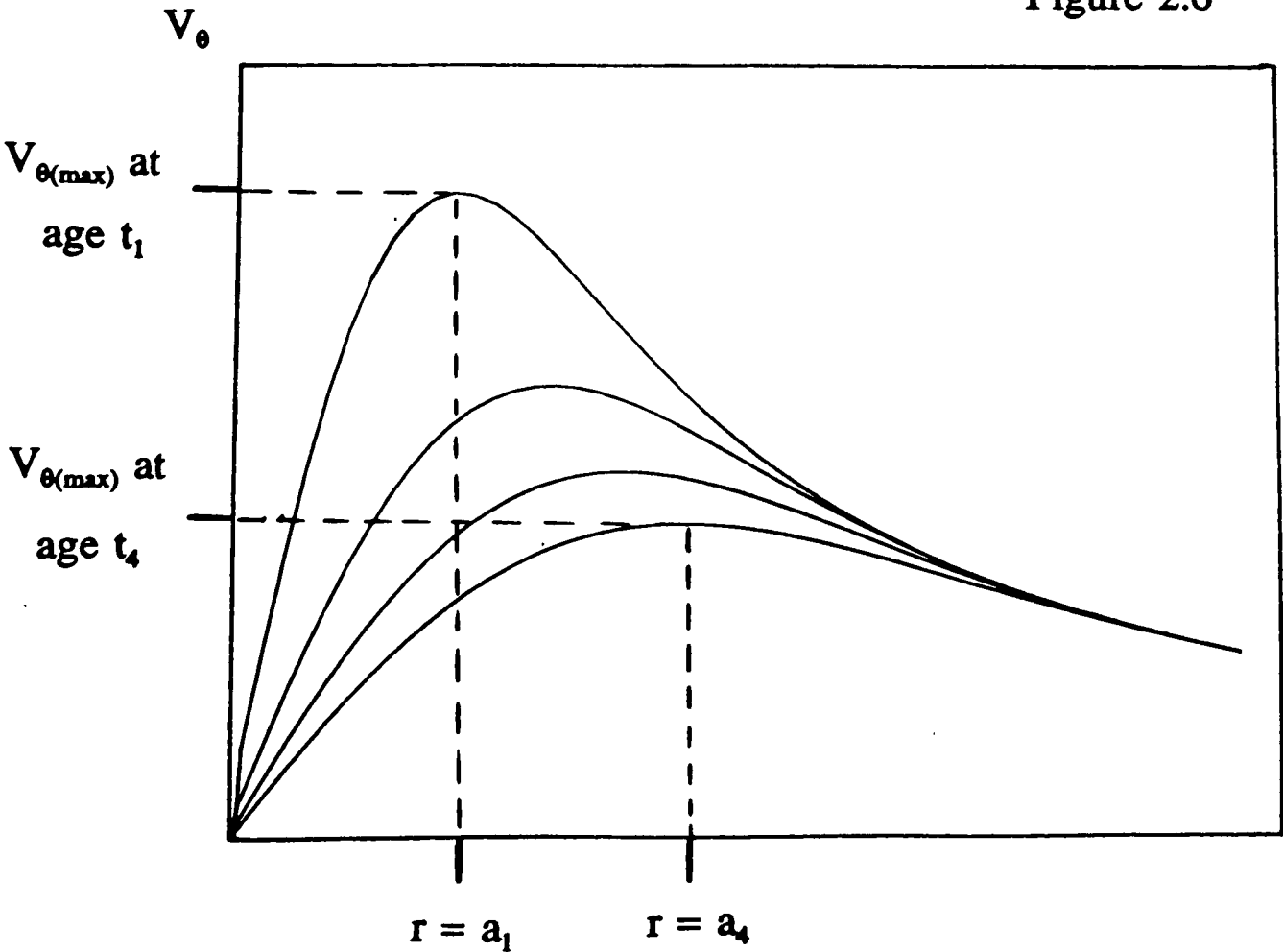


Figure 2.6



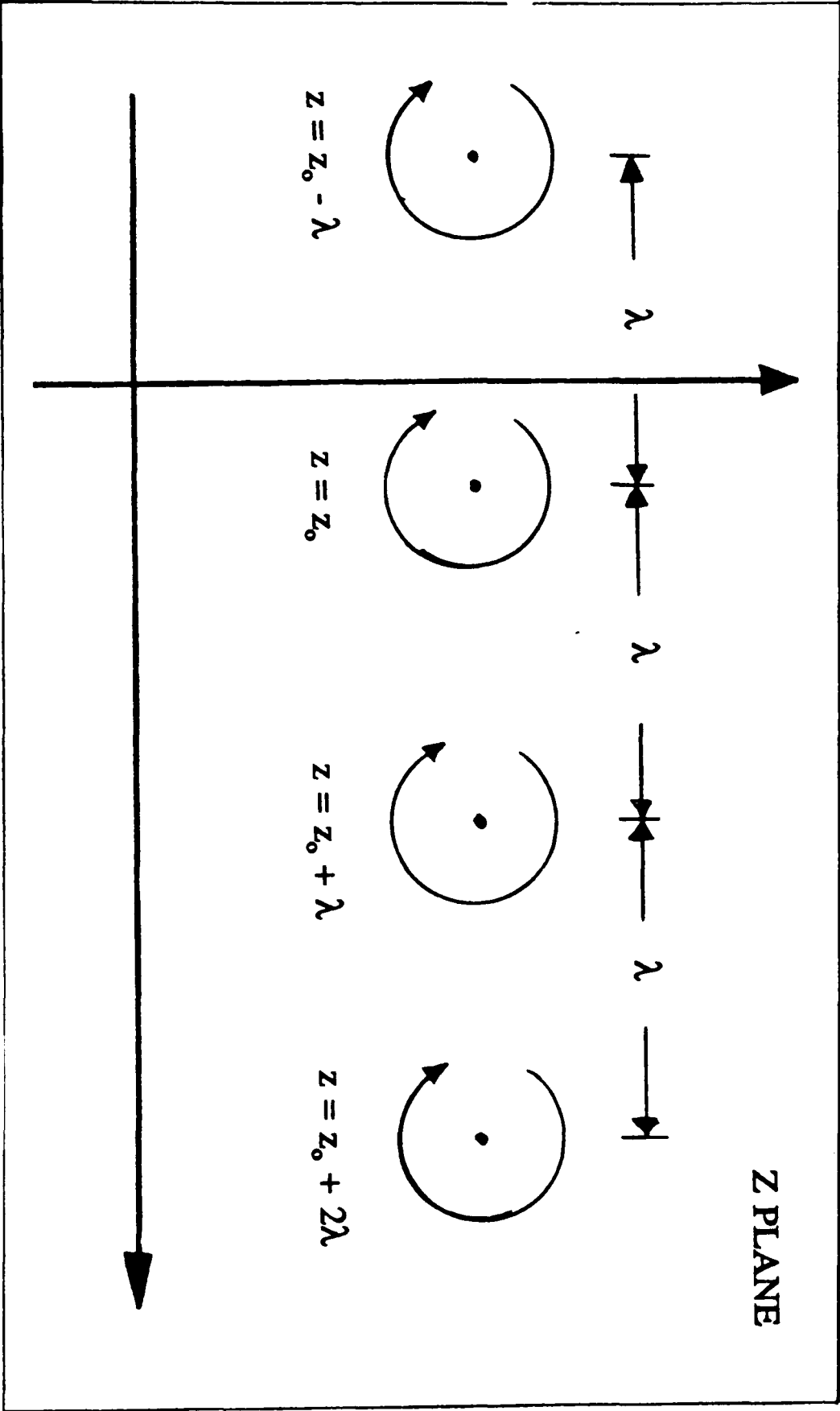


Figure 2.7

CHAPTER 3

THE HYDRODYNAMICAL MODEL

3.1 Introduction

A realistic description of the flow field over ripples is an essential prerequisite for sediment transport studies, because it provides the criteria for both the entrainment and movement of sediment. Most researchers have opted for one of two flow descriptions. The first is a direct solution of the Navier Stokes equation with viscosity incorporated. The second description uses the discrete vortex method, an inviscid approximation to the Navier Stokes equation that makes use of potential flow theory.

This chapter outlines the background to, and details of, a 'discrete vortex' model of the flow field over ripples. The resulting hydrodynamical model aims to accurately describe the process of vortex shedding and ejection, via which information on the velocity field may be obtained.

3.1.1 The discrete vortex method

Historically, the discrete vortex method has its origins in a study by Rosenhead (1931). Rosenhead demonstrated that the motion of individual, strategically placed vortices could give a rudimentary picture of flow development between two contraflowing fluids of equal density.

The principle of using numerous discrete vortices to represent more diffuse areas of vorticity (so-called vortex sheets), is called the *discrete vortex method*. It finds its main application in studies of wake development behind bluff bodies. Simply stated, a stream of discrete vortices that are shed from the bluff body serve to represent the (actually diffuse) wake development. Examples of its use include studies of flow past a cylinder (Gerrard (1967), Stansby (1977), Sarpkaya and Schoaff (1979)), flow past bluff bodies (Clements (1973), Evans and Bloor (1977)) and flow past an inclined plate (Sarpkaya (1975), Kiya and Arie (1977 a,b)). Of particular relevance to the present study is the use of the method to simulate vortex shedding over (steep) ripples (e.g. Longuet-Higgins (1981)).

A key review paper in this field (including some historical background) is by Clements and Maull (1975). Papers by Leonard (1980) and Sarpkaya (1988) provide similar material but are much more technical in nature. Sarpkaya's review paper aims to bring together the technological advances in the method, its content demonstrating just how sophisticated the discrete vortex method has become.

Applications of the discrete vortex method have certain features in common:

- (a) a mapping to simplify the body boundary profile,
- (b) an algorithm to calculate the amount of vorticity introduced into the flow,
- (c) a discussion as to where this introduction/calculation should take place,
- (d) rules for both the destruction and consolidation of vortices,
- (e) damping of the vortex field in some models.

These features will be considered in turn.

(a) *Mapping to simplify the body profile*

The discrete vortex method operates on the basis of potential flow theory in which a common practice for ensuring no flow across boundaries is the method of images. However, the complicated profiles considered do not lend themselves directly to this procedure because of difficulties in locating the image positions. For this reason, discrete vortex applications often take place in artificial mapping planes, where the image positions are easy to locate. Information obtained in the mapping plane is then mapped back to the actual physical situation (the physical plane) using a conformal mapping. The mapping process preserves complex potentials and vortex strengths, whilst account can be taken for its affect on streamlines and velocities. Unfortunately, sharp corners in the original profile appear as singularities in the mapping plane.

(b) *The amount of vorticity entering the flow*

A fundamental feature of any discrete vortex model is the manner in which vorticity is generated and then allowed into the flow. Evans and Bloor (1977) noted this as a major source of error. In reality, vorticity is generated in a thin boundary layer

adjacent to the body, then released into the main flow in the region of the flow separation point. Prandtl (1934) proposed a law for calculating the flux of vorticity across this layer - Prandtl's rule

$$\frac{d\Gamma}{dt} = \frac{1}{2} U_\delta^2 \quad 3.1$$

where U_δ is the horizontal velocity at the upper edge of the boundary layer. Figure (3.1) explains how Prandtl's rule is derived. One method, therefore, of calculating vorticity input is to give each nascent vortex an amount of vorticity (based on Prandtl's rule) as it enters the flow. The sign of this vorticity is dictated by the local flow direction at the instant of generation. Sarpkaya (1975) and Sawamoto (1980) suggested that Prandtl's rule overestimates the amount of vorticity that actually ends up in a vortex wake by up to 40%. A computational problem noted by researchers (e.g. Sarpkaya (1975), Sarpkaya and Schoaff (1979)) is the feedback effect of recently shed vortices on vorticity production, which can create numerical instability. One method of counteracting this problem is to regularly allow purely advective time steps, giving newly shed vortices a chance to escape (see Clements (1973)).

(c) *The point of introduction of vorticity*

Newly generated vorticity, in the form of discrete nascent vortices, is shed at the point of flow separation. For sharp cornered bodies, separation occurs at the corners themselves. Unfortunately, these corners are singularities in the mapping plane so vortices must be introduced at an artificially chosen point nearby. Rounded profiles do not suffer from this problem, but are prone to the (well documented) difficulties in the definition of the separation point in oscillatory flow (see Despard and Miller (1971), Williams (1977)). Experimental data on flow separation over rounded profiles provides a reasonable way to resolve this problem (Gerrard(1967), Stansby(1977)).

Prandtl's rule requires the evaluation of velocity at the edge of the boundary layer. This value physically represents the boundary layer thickness and is invariably a free parameter in discrete vortex applications. Yet another free parameter is the release point of nascent vorticity. Evans and Bloor (1977) linked the release and

calculation points by specifying the calculation point (and hence the boundary layer thickness), then setting the release point as half this value. This so-called 'release at half height' is quite plausible since discrete vortices can be considered to emanate from the centre of the boundary layer with diameter equal to the boundary layer thickness.

(d) *Destruction and consolidation of vortices*

The vortex core (see §2.6) is some measure of the spatial size of the vortex. The core radius may be used to define the criteria for deleting and consolidating vortices; for example, vortices whose cores touch the flow boundary may be deleted, whilst vortices of the same sense of rotation, whose cores touch, may be coalesced. Milne-Thomson (1968) discusses vortex amalgamation, stating that an amalgamated vortex has strength equal to the sum of the constituent strengths, and centre at the combined centre of vorticity.

(e) *Damping of the vortex field*

The absence of viscosity in the discrete vortex method allows vortices to retain their strength indefinitely. This causes computational problems, especially in oscillatory flows where older vortices that are swept towards the source body can disrupt the shedding regime. Core expansion (eg Longuet-Higgins (1981)) is one form of damping. However, it does not seem to be vigorous enough for models involving large, amalgamated vortices (Macpherson (1984)). In this case, further damping is required. Chorin (1973) introduced a random walk component into the time stepping movement of vortices, the aim of which was to 'diffuse' vortices further apart and hence reduce their mutual interaction.

3.1.2 Applications of the discrete vortex method to oscillatory flow over ripples

The discrete vortex method lends itself to the modelling of vortex shedding in the oscillatory flow above steep ripples. Account needs to be taken of the generation of new vorticity in the ripple crest region, of the vortex structure as it rolls up over the

lee slope and of the observed fate of decaying vortices as they are ejected from the lee slope on flow reversal.

In a pioneering study, Longuet-Higgins (1981) applied the discrete vortex method to vortex shedding off steep, sharp crested ripples. He mapped a specified number of adjacent ripples (5 or 6 usually) onto a polygon, the corners of which represented the crests of the ripples. A further Schwartz-Christoffel transformation mapped the polygon onto a circle with the fluid occupying the interior. The crests themselves mapped to singularities. Discrete vortices were released from a fixed point vertically above the crest, their strengths being derived from Prandtl's rule. The direction of vortex shedding was governed strictly by the sense of velocity at the point of vorticity calculation (and not by the direction of the wave induced oscillatory flow). Vortex damping was achieved solely by core expansion whilst coalescence and destruction followed the procedures outlined in §3.1.1(e). As the model solution progressed, identifiable clusters of vorticity rose a couple of ripple heights above the crest level. Longuet-Higgins demonstrated that these clusters could be amalgamated into larger vortex pairs.

For computational reasons, Longuet-Higgins' model was only run for a few wave cycles; thus it never had the chance to demonstrate that it settled to a final, converged state. Macpherson (1984) adapted the model to allow it to run for many cycles, presenting results only when it had been shown to settle down. In this adapted model, nascent vortices were released some way above the crest, although the strengths were calculated at a point half way between this release point and the crest level. The rules of vortex coalescence were applied to add newly generated vorticity to a single growing vortex as it moved away from the crest. This innovative procedure meant that only a handful of vortices were present in the flow at any one time, with a vast saving in computational effort. Macpherson fixed core size on the basis of the experimental data of Tunstell and Inman (1975). Two amalgamated vortices were shed in every half cycle, forming a vortex pair in the same manner as the original Longuet-Higgins model. Justification for this vortex shedding regime was provided by the streakline photographs of Taneda (1977) and Longuet-Higgins' model results. Vortex decay in time was prescribed by applying exponential decay of strength to the ejected vortices.

Figures (3.2), (3.3) show results for both Longuet Higgins' model and the adapted model of Macpherson. Ejected vortices are seen to travel towards the neighbouring ripple, then rise a significant height from the bed (due to the extra impetus caused by vortex pairing).

3.1.3 Standing vortex models

A simpler family of papers assumes that the growing lee vortex is already in existence and fixed in position over the lee slope. These are referred to as *Standing Vortex models*. They utilise complex potential techniques, but are not discrete vortex models (Tunstall and Inman (1975), Sawamoto and Yamaguchi (1979), Shibayama and Horikawa (1980) and Davies (1984a,b)). Tunstell and Inman used their laboratory information on core size, strength and vortex position over the lee slope, to calculate the wave energy dissipation rate (see Chapter 2). Davies extended their work to the case of an infinite bed of ripples.

3.1.4 Direct solution of the Navier Stokes equation

Complex potential simulations of the flow over ripples are inviscid, irrotational approximations to the solution of the full Navier Stokes equation of motion. However, it is also possible to solve the equation of motion directly. Three differing methods of direct solution are reviewed.

Analytical solutions have recently been sought by, amongst others, Hara and Mei (1991) and, in the context of ripple formation, Blondeaux (1990). The analysis of Hara and Mei (1991) requires the ripple steepnesses to be small, which allows the linearisation of the equation of motion. Blondeaux assesses the fate of a flat bed subjected to a small perturbation. These studies give useful information on the formation of and flow structure over *rolling grain ripples* (where flow separation over the ripples does not occur), but are not suitable for fully fledged vortex ripples.

Numerical studies of flow over (steep) vortex ripples include Sleath (1973, 1976a), Blondeaux and Vittori (1991) and Asp Hansen *et al* (1991). Blondeaux and Vittori solved simultaneously the equation of vorticity and a form of Poisson's

equation, the former using finite differences and the latter using a 'spectral method'. The spectral method involved Fourier analysis of the variables in Poisson's equation, which was solved by (computationally rapid) fast Fourier transform techniques. This saving in computational time allowed the usage of a fine computational grid. Figure (3.4) is an example of their results for the vorticity field over a ripple. It shows a far more detailed vorticity structure than Longuet-Higgins (1981). Vortices nearing the bed can themselves produce new vortex structures over the bed itself. Blondeaux and Vittori are quite critical of discrete vortex simulations for two main reasons. Firstly, the omission of viscosity is an excessive simplification. Secondly, vortex generation is only allowed to occur in the region of the ripple crests, so vortex production over the slopes of ripples is not accounted for. There are, however, many similarities between Blondeaux and Vittori's results and the flow features inherent in Longuet-Higgins (1981). One of the main conclusions of Blondeaux and Vittori is the phenomena of vorticity being generated in a thin strip underneath the (contra-rotating) growing vortex. This strip of vorticity is pushed over the crest at flow reversal, forming the basis for the new growing vortex on the far side of the ripple. The existence of this strip has been observed experimentally by Marin (1992).

In an ongoing program, a new numerical approach has been adopted by Asp Hansen *et al* (1991) to simulate flow over ripples. Their methodology introduces some of the more recent developments in this field, including the 'cloud in cell' technique (Stansby and Dixon (1983), Stansby and Isaacson (1987)) and the splitting of the vorticity transport equation. Firstly, Poisson's equation is solved on a curvilinear grid over the ripple profile, to give the flow field. This calculation requires the contributions of the numerous vortices within the flow. To do this, the vorticity within each grid cell is summed, then distributed to the four nodes of the grid cell. (This is the 'cloud in cell' method, which helps reduce computational time.) New vortices are introduced over the ripple profile, where a boundary layer model is in operation. The strengths of these vortices are given by the local flow circulation. Vortices within the flow are moved using a split form of the vorticity transport equation: the first (convective) part moves vortices with the local flow, while the second (diffusive) part mimics diffusion by

adding a random walk component to the vortices' motion. Vortex cores are allowed to expand with time and the usual rules are applied when cores touch. No other form of damping is used. The results of Asp Hansen *et al* (1991) are difficult to interpret in terms of the motion of (larger) growing and ejected vortices. An important feature of their results is the prediction that vorticity generated at the bed can rise some considerable height above the ripples. Figure (5.4), in Chapter 5, shows some of their results.

3.2 The hydrodynamical model

The hydrodynamical model developed here aims to simulate the (observed) flow field over *two dimensional, round crested ripples* when under the action of surface waves. It is of fundamental significance in this simulation that the flow field can be treated as potential flow, allowing the use of the discrete vortex method to model the production, ejection and decay of vortices.

The present (discrete vortex) hydrodynamical model requires the same basic considerations as the applications reviewed in §3.1, namely the suitability of the mapping plane, the method and location of vorticity generation and release and so on. In §3.2.1, a detailed discussion of the mapping procedures used in the present model is given. Then, in §3.2.2, a typical cycle of the model is described, including details of the manner in which growth, ejection and decay of the vortices is accounted for. The parameter choices thus introduced are discussed in §3.2.3.

3.2.1 The development of the hydrodynamical model

3.2.1 (a) *The mapping function*

It will be useful to establish certain theoretical results concerning the mapping procedures. These derivations rely heavily on the material reviewed in §2.6.

With a few exceptions, all flow field calculations are made in a mapping or transform plane (called the ζ plane). The flow occupies the upper half of this plane with the bed as the real axis. Information obtained in the ζ plane is then mapped to the

physical (z) plane (where ripples are present) using the conformal transformation

$$z = \zeta + i \frac{h}{2} e^{il\zeta} \quad 3.2$$

where $z = x + iy$, $\zeta = \xi + i\chi$ are points in their respective planes, h is the ripple height and $l (= 2\pi/\lambda)$ is the wavenumber of the ripple spacing. This mapping has been commonly used in studies of round crested ripples (e.g. Sleath (1976a), Blondeaux and Vittori (1991)) because the 'pinched' sinusoidal profile is a good representation of the naturally occurring ripple shape (see figure (3.5)). Equating real and imaginary parts gives

$$x = \xi - \frac{h}{2} e^{-l\chi} \sin l\xi, \quad y = \chi + \frac{h}{2} e^{-l\chi} \cos l\xi \quad 3.3 \text{ (a,b)}$$

and specifically for the bed profile itself (where $\chi = 0$),

$$x_B = \xi - \frac{h}{2} \sin l\xi, \quad y_B = \frac{h}{2} \cos l\xi \quad 3.4 \text{ (a,b)}$$

Figure (3.6) illustrates how this mapping perturbs streamlines of the flow. The mapping also simulates flow enhancement in the crest region. As an example, for a ripple of steepness 0.15, the mapping enhances horizontal velocities by a factor of 1.9 at the crest.

3.2.1(b) Complex potential representation of the flow in the ζ plane

The hydrodynamical model makes use of the complex potential

$$\Omega = -i(U_0 \sin \sigma t) \zeta + \sum iK_s \log \sin \frac{\pi}{\lambda} (\zeta - \zeta_s) - \sum iK_s \log \sin \frac{\pi}{\lambda} (\zeta - \bar{\zeta}_s) \quad 3.5$$

where K_s are the strengths of the s vortex rows in the upper half ζ plane, λ is the spacing of constituent vortices within these rows, and ζ_s and $\bar{\zeta}_s$ are the centres of these rows in the upper and lower half plane respectively. In turn, the three terms represent (i) the oscillatory flow, (ii) the vortices actually in the flow and (iii) the image vortices

in the lower half plane. It is these image vortices that provide the kinematic bottom boundary condition: no flow through the bed. Equation (3.5) provides a complex potential representation of a repeatable flow pattern over an infinite number of adjacent ripples. In this thesis, we invariably refer to isolated vortices as opposed to vortex rows; it is to be understood that our 'vortices' are, in fact, the central members of infinite vortex rows.

3.2.1(c) *The velocity components in the ζ plane*

The mathematical linearity of the potential flow regime allows the (u_ζ, v_ζ) velocity components at a point ζ to be found by adding the individual contributions from the available vortices and the oscillatory flow. These contributions are found by using the convention

$$\frac{d\Omega}{d\zeta} = -U_\zeta + iV_\zeta \quad 3.6$$

By applying equation (3.6) and equating real and imaginary parts, the velocity components are found to be

(a) for the oscillatory flow;

$$U_{\zeta,osc} = U_0 \sin \sigma t, \quad V_{\zeta,osc} = 0 \quad 3.7 \text{ (a,b)}$$

and (b) for the vortices;

$$U_{\zeta,vort} = \frac{\pi K}{\lambda} \frac{\tanh \alpha_2 (1 + \tan^2 \alpha_1)}{\tan^2 \alpha_1 + \tanh^2 \alpha_2} \quad 3.8 \text{ (a)}$$

$$V_{\zeta,vort} = \frac{\pi K}{\lambda} \frac{\tan \alpha_1 (1 - \tanh^2 \alpha_2)}{\tan^2 \alpha_1 + \tanh^2 \alpha_2} \quad 3.8 \text{ (b)}$$

where

$$\alpha_1 = \frac{\pi}{\lambda}(\xi - \xi_0) , \quad \alpha_2 = \frac{\pi}{\lambda}(\chi - \chi_0) \quad 3.9 (a,b)$$

3.2.1(d) *The velocity components in the (physical) z plane*

In general, velocities are transformed from the ζ to the z plane using

$$\frac{d\Omega}{dz} = \frac{d\Omega}{d\zeta} \frac{d\zeta}{dz} \quad \text{i.e.} \quad -U_z + iV_z = \frac{d\zeta}{dz} (-U_\zeta + iV_\zeta) \quad 3.10$$

Equation (3.10) works perfectly well for all velocity transformations with one crucial exception:- the velocity at vortex centres. Routh discovered that vortex centre velocities did not faithfully map from plane to plane and that a correction needed to be applied - Routh's correction. The following derivation of Routh's correction is due to Clements (1973), though with a different sign convention. We are at liberty to consider a single vortex (as opposed to an infinite row) for simplicity, since we are assessing an effect at an isolated vortex centre.

For a conformal transformation, the (total) complex potential remains the same in each plane, so

$$\Omega_z + iK \log(z - z_0) = \Omega_\zeta + iK \log(\zeta - \zeta_0) \quad 3.11$$

where Ω_z and Ω_ζ are potentials due to all causes except the vortex of interest at z_0 and ζ_0 . This gives

$$\Omega_z = \Omega_\zeta + iK \log \frac{\zeta - \zeta_0}{z - z_0} \quad 3.12$$

If we express ζ as a power series in z about z_0 , noting that $\zeta = f(z)$ is the mapping function under consideration, then

$$\Omega_z = \Omega_\zeta + iK \log [f'(z_0) + \frac{1}{2}(z-z_0)f''(z_0) + ..] \quad 3.13$$

The velocity components in the z plane are found by differentiating this result with respect to z . The (Routh corrected) velocity at the vortex centre z_0 is found by letting z tend to z_0 .

$$\left. \frac{d\Omega_z}{dz} \right|_{z_0} = \frac{d\Omega_\zeta}{d\zeta} \frac{d\zeta}{dz} + iK \frac{f''(z_0)}{2f'(z_0)} \quad 3.14$$

Equation (3.14) is similar to the (more normal) equation (3.10), the second term being Routh's correction. This result gives a basis for correcting velocities in the z plane. However, in keeping with other velocity calculations in the model, it would be preferable to perform Routh's correction in the ζ plane. We therefore take Clements' analysis one stage further. Factorising equation (3.14), we obtain

$$\frac{d\Omega_z}{dz} = \frac{d\zeta}{dz} \left[\frac{d\Omega_\zeta}{d\zeta} + iK \frac{f''(z_0)}{2f'^2(z_0)} \right] \quad 3.15$$

Equation (3.15) is an alternative statement of equation (3.10) that is suitable for application in the ζ plane. The term in square brackets represents a Routh-corrected form of $d\Omega_\zeta/d\zeta$. Vortex centre velocities in the ζ plane are corrected by an amount

$$iK \frac{f''(z_0)}{2f'^2(z_0)} \quad 3.16$$

Equation (3.16) agrees with Longuet-Higgins' result for the Routh correction.

3.2.1(e) The streamfunction ψ

The streamfunction ψ comes from the imaginary part of the complex potential 'Ω'. For the oscillatory component (Ω_{osc}), the streamfunction is and for the vortices,

$$\psi_{osc} = (-U_o \sin \sigma t) \chi \quad 3.17 (a)$$

$$\psi_{vort} = \frac{K}{2} \log[\sin^2 \alpha_1 + \sinh^2 \alpha_2] \quad 3.17 (b)$$

where the notation is as before.

3.2.2 A description of the hydrodynamical model

The hydrodynamical model is driven by the oscillatory flow ($U = U_o \sin \sigma t$) over the ripples, whose time period (T) is resolved into 500 time steps.

3.2.2(a) *The growing and ejected vortices*

In the hydrodynamical model, a growing vortex is conceived at the time of local flow reversal, at a point z_T that is 12.5% of a ripple height above the crest level. The position of z_T is illustrated in figure (3.7a). At each time step thereafter, a nascent vortex is released at z_T and then amalgamated with the (forming) growing vortex over the lee slope. The strength of each of these nascent vortices is given by Prandtl's rule

$$\frac{dK}{dt} = \frac{1}{4\pi} U_T^2 \quad 3.18$$

where U_T is the horizontal velocity in the z plane, calculated at z_T . It is necessary to calculate this velocity in the z plane in order to account for flow enhancement in the crest region. The point z_T is where vorticity input is both calculated and released. Physically, it represents the 'hydrodynamical model' choice of the average boundary layer thickness. Amalgamation of these nascent vortices with the growing vortex follows the method of Macpherson (1984), namely that the newly fed growing vortex has strength equal to the sum of the constituent vortices and lies at their centre of vorticity. Figure (3.7b) illustrates the operation of this process. The amalgamation rule may well become more suspect as the distance between the constituent vortices increases. The process of vortex feeding continues until the next local flow reversal at z_T , at which time vortex feeding is transferred to the other side of the ripple.

The growing vortex is now classed as an ejected vortex, which is free to move at the local velocity.

3.2.2(c) *Movement of vortices*

Vortices in the upper half ζ plane are moved using a simple, linear advancement scheme

$$\zeta_{new} = \zeta_{old} + (U_{\zeta}, V_{\zeta}).\delta t \quad 3.19$$

where the timestep δt is $T/500$. The velocity components (U_{ζ}, V_{ζ}) are computed from all vortices present using equations (3.7)-(3.9) along with the Routh correction (equation (3.16)). Once the position of the upper half plane vortices are established, the positions of the respective image vortices are imposed. Figure (3.8) illustrates the motion of vortices within the ζ plane, and how the positions of image vortices are imposed. The position of vortices can then be mapped to the z -plane as required.

3.2.2(c) *Decay of vortex strength*

Exponential decay of vortex strength is applied to both the growing and ejected vortices at each time step. Two decay regimes are applied. For the growing vortex, a linearly phased-in decay regime is applied, from no decay at its inception to 0.9% decay at the end of the growing phase. Ejected vortices are subject to a constant decay rate of 0.9% strength loss at each time step. Figure (3.9) illustrates these points.

3.2.2(d) *Core expansion*

Vortices are subject to core expansion from their inception, at a rate given by

$$radius\ of\ core = 2.24 \sqrt{\nu t_{age}} \quad 3.20$$

(see §2.6). Velocities calculated within the core are damped using the following result from Longuet-Higgins (1981):

The core radius also provides one of the two conditions for amalgamation of vortices. If two vortices of the same rotation touch, they are amalgamated using the same rules

$$\text{damping factor} = \frac{(\zeta - \zeta_o)^2}{(\text{radius of core})^2} \quad 3.21$$

as for the growing vortex.

3.2.2(e) *Destruction of vortices*

Vortices are destroyed (and hence deleted from the model) on the basis of one of three criteria: (i) their cores touch the bed, (ii) their strength is less than 1% of its maximum; and (iii) the vortices are older than 1.5 time periods.

It is this continual process of production, ejection and subsequent decay of vortices that forms the framework of the hydrodynamical model. The model is run until it settles into a steady state (where cycle by cycle changes are small) at which stage model results are obtained. Figure (3.12) is a flow diagram showing the sequencing of the stages in the hydrodynamical model.

3.2.3 Parameter choices and their justification

The parameter choices for the hydrodynamical model were selected with an eye to both established experimental observation and previous theoretical studies in this field. For this purpose, the work of Tunstell and Inman (1975), DuToit and Sleath (1981), Longuet-Higgins(1981), Macpherson(1984) and Sleath (1982b, 1984) provided useful information on vortex movement, the effective lifetime of vortices, the phase shift between vortex ejection and oscillatory flow reversal, and cycle averaged drag coefficients.

The model should be able to simulate some of the main features of vortex shedding over ripples highlighted by these and other researchers. Firstly, the growing vortex should form about half way down the lee slope. Secondly, this growing vortex should eject prior to the oscillatory flow reversal. Thirdly, the ejected vortex should at least reach the neighbouring ripple before it is swept back again. Finally, the ejected vortex should be well dissipated one cycle after inception.

The parameter choices are discussed in turn, although in reality, they were considered simultaneously. An effort was made to keep to a minimum the height at which the calculation and release of vorticity was made, not least to preserve the assumptions of Prandtl's rule (namely, that the boundary layer is thin enough for vertical velocity components to be neglected). Irrespective of the vortex decay regime adopted, it was found that the smallest height settings that maintained computational robustness were calculating and releasing vorticity at 12.5% of a ripple height. Releasing vorticity at half height (the most preferable situation) only worked if the calculation point was 25% of a ripple height above the bed. This was thought to be too high.

Here, we must anticipate the results from the next chapter.....

The hydrodynamic model was completed a year prior to the boundary layer model. From the outset, it was hoped that the boundary layer model would give further credence to our (purely computational) choice of boundary layer thickness. As it transpired, the Fredsoe (1984) boundary layer model that we adopted gave rather large boundary layer thicknesses - too large for the realistic application of Prandtl's rule. To demonstrate that our choice of a representative boundary layer thickness is not unreasonable, we proceed as follows:-

Figure (2.3) suggests that the majority of ripples form in a regime where $0.15 < h/a_0 < 0.25$.

Jonsson (1980) states that, typically, the boundary layer thickness (δ) is 2-4% of a_0 . i.e. $0.02 < \delta/a_0 < 0.04$.

Choosing the central (3%) value for δ/a_0 , we combine these results to obtain $0.12 < \delta/h < 0.20$.

The present choice of δ as 12.5% of a ripple height is, therefore, consistent with this (albeit rough) argument. Comparisons between the 12.5% rule and other 'average' boundary layer thickness definitions are discussed in Chapter 4.

Three possible exponential decay regimes were examined: decay at a constant rate from the vortices' inception; decay at a constant rate from the time of ejection (Macpherson's chosen regime); and a compromise whereby decay was phased in during the growing phase to a constant (maximum) value at the time of ejection. The first two regimes were found to be too strong and too weak respectively, while the compromise regime gave the best response. This may seem surprising in view of the similarities between the present model and that of Macpherson. One reason is that the vortex cores were much larger in the Macpherson model, thereby providing significant damping during the growing phase. DuToit and Sleath's crest graph (figure (3.11a)) was used to tune the constant (maximum) decay rate to a 0.9% loss of strength at each time step.

It was important to simulate the observed phase lead between velocities in the crest region (where the vortices' presence gives rise to early flow reversal) and the outer, oscillatory motion. DuToit and Sleath's (1981) graph of horizontal velocity in the region of the crest (figure (3.11a)) was used as a good example of data in order to get the correct phase shift, aiding in the choice of both the decay regime and decay rate.

Chapter 7 introduces and provides details of the cycle averaged drag coefficient $\overline{C_D}$. Its calculated value was used as a further indicator of suitable parameter settings, specifically the decay regime and decay rate.

3.2.4 Computational aspects of the model

The hydrodynamical model has been non-dimensionalised with respect to the ripple wavenumber ' l ' and the wave frequency ' σ '. These choices were motivated by the fact that most experimentalists quote ripple wavelengths and waveperiods in their accounts, making re-dimensionalisation easy. Primed symbols represent non-dimensional (model) quantities, whilst unprimed symbols are dimensional (natural) quantities (eg $z' = lz$, $t' = \sigma t$). Specifically, both the model ripple wavelength λ' ($= l\lambda$) and the model timeperiod T' ($= \sigma T$) equal 2π .

The mapping now becomes

$$z' = \zeta' + ib'e^{i\zeta'} \quad 3.22$$

where b' is the ripple amplitude.

The two primary inputs to the model are the velocity amplitude of the oscillatory flow, U_o , (through which d_o/λ is varied), and the ripple steepness, h/λ , which accounts for the bed profile. For a particular case study, these two parameters are extracted from the experimental or theoretical description and input as follows:

$$\frac{d_o}{\lambda} = \frac{2U_o}{\sigma} \cdot \frac{1}{\lambda} = \frac{2}{\sigma} \cdot \frac{\sigma U_o'}{l} \cdot \frac{l}{\lambda'} = \frac{U_o'}{\pi} \quad \rightarrow \quad U_o' = \pi \frac{d_o}{\lambda} \quad 3.23$$

and

$$b' = \frac{h'}{2} \frac{2\pi}{\lambda'} = \pi \frac{h'}{\lambda'} \quad \rightarrow \quad b' = \pi \frac{h}{\lambda} \quad 3.24$$

The sense of rotation of each vortex is given by the sign of K (see §2.6). In general, there are six vortices present: a growing vortex, an ejected vortex, a relic vortex and the three associated image vortices. The use of the complex potential for an infinite row of vortices allows the model to make use of the repeated flow pattern over adjacent ripples. The calculations in the hydrodynamical model are made over a central, parent ripple. Figure (3.10) illustrates the computational domain of the model over this ripple. A vortex that strays out of this domain is simply replaced by the neighbouring member of the vortex row. Two time scales operate within the hydrodynamical model - one based on flow reversals in the oscillatory flow and the other based on local flow reversals at z_T . The hydrodynamical model runs on the latter, while results are referenced with respect to the former. The model solution does not settle into a rigid steady state, but tends to fluctuate about a mean state. These fluctuations are small, as indicated in figure (3.13), which shows cycle by cycle variation of the cycle averaged drag coefficient $\overline{C_D}$. The results in this chapter were obtained in the 11th and 12th cycle.

3.3 Results

The results from the hydrodynamical model are based on the experimental run parameters of DuToit and Sleath (1981), hereafter referred to as the *central run*. The central run parameters are $d/\lambda = 1.42$, $h/\lambda = 0.17$ and $\nu' = 0.00125$. This value for the non-dimensional kinematic viscosity has been obtained from DuToit and Sleath's parameter ' β/l ' as follows:

$$\frac{\beta}{l} = 20 \rightarrow \frac{1}{l} \sqrt{\frac{\sigma}{2\nu}} = 20 \quad 3.25$$

which gives, after non-dimensionalisation, $\nu' = 0.00125$.

The results from §3.3.1 are concerned with the purely computational features of the model. §3.3.2 shows results connected with the effects of ripple steepness on the output from the hydrodynamical model. In §3.3.3, model results from the central run are presented, while §3.3.4 assesses the sensitivity of these results to the free parameters. Finally, in §3.3.5, the central run output is compared with two other outlying runs ($d/\lambda = 1.1, 2.5$).

3.3.1 Computational aspects of the hydrodynamical model

Figure (3.13) is a cycle by cycle plot of the cycle averaged drag coefficient ($\overline{C_D}$). The values of $\overline{C_D}$ settle into an essentially steady state after 4 cycles. However, a rigid steady state is never reached. Other modellers (e.g. Blondeaux and Vittori (1991)) also found cycle by cycle variability in their results which cannot be attributable to numerical instability. *From here on, unless otherwise stated, the results presented were obtained in the twelfth cycle.*

Figure (3.14) shows two crest velocity traces (one for each half cycle). The fact that the traces are almost identical indicates the symmetry of the solution in the two half cycles.

Experience with the hydrodynmaical model suggested that it became computationally unreliable at around $d/\lambda = 3.0$, although this varied according to ripple steepness etc. The hydrodynamical model invariably 'crashed' because the time series

of velocity at z_T contained two flow reversals at successive time steps, thus placing two nascent vortices on top of each other.

3.3.2 The effects of ripple steepness

Figures (3.15), (3.16) illustrate how varying the ripple steepness (but otherwise retaining the central settings) affects crest velocities and vortex strengths. Both figures show that increased steepness leads to enhanced crest velocities, which is consistent with the physical situation.

Figures (3.17)-(3.20) are a suite of diagrams relating to the growth and subsequent ejection of vortices. Figures (3.17) and (3.18) show how the time of vortex ejection (i.e when the vortex has stopped being fed vorticity) and the time of passage of the ejected vortex over the crest, vary with d/λ for four ripple steepnesses. The vertical (time) axes are in degrees of phase relative to flow reversal of the oscillatory flow. Figure (3.19) shows how far (horizontally) the centre of the growing vortex is from its parent crest at the time of ejection. Figure (3.17) shows that, for $d/\lambda < 2.1$, ejection times are not unduly affected by ripple steepness, lying between -10° and -15° . At $d/\lambda = 2.1$ however, the time of ejection suddenly occurs earlier, and, for subsequent values of d/λ , the ejection times are earlier for the steeper ripples. In figure (3.18), below $d/\lambda = 2.1$, the passage time is dependent on ripple steepness, with later passage being linked to the steeper ripples. A hiatus in the traces for $h/\lambda = 0.17, 0.19$ is followed by a more confused pattern. Most of the above findings can be explained through figure (3.19). Specifically, for $d/\lambda < 2.1$, the steeper ripples encourage growing vortices to travel further from their parent crest, which in turn explains why their passage times are later.

One thing that is not explained by these three figures is why there is a hiatus at $d/\lambda = 2.1$, especially for the steeper ripples. This hiatus is quite disconcerting because it could represent an upper bound for the applicability of the model. What happens to the hydrodynamical model at $d/\lambda = 2.1$ that evidently does not occur at $d/\lambda = 2.0$? Figure (3.20) shows the trail of the growing vortex at $d/\lambda = 2.0, 2.2$ for a ripple of steepness 0.19. The fundamental difference in the trails is that, for $d/\lambda = 2.2$, the

growing vortex has already started to travel towards the parent crest under the action of the image vortex. This in turn encourages earlier flow reversal in the crest region and so on.

The behaviour of the growing vortex for $d/\lambda = 2.1$ is quite reasonable in a mathematical/computational sense, but is it physically realistic? To answer this, we refer to the results presented in Chapter 7, concerning the force exerted by the fluid on the ripple profile. There exists established experimental data for derived quantities of this force, specifically the cycle averaged drag coefficient. The model results for this quantity (figure (7.6)) show misbehaviour beyond $d/\lambda = 2.0$, suggesting that the model prediction of the motion of the growing vortex is physically unrealistic beyond $d/\lambda = 2.1$. Despite this, model results for a run with $d/\lambda = 2.5$ will be presented in this chapter in order to provide a worthwhile triplet of contrasting hydrodynamical cases studies. In Chapter 5, one of the test cases (Test 2) is for $d/\lambda = 2.63$. Here, the ripples are very shallow ($h/\lambda = 0.11$) and the problems referred to are far less pronounced. For $d/\lambda < 2.1$, the hydrodynamical model appears to function well in all respects.

3.3.3 Model results for the central run ($d/\lambda = 1.42$, $h/\lambda = 0.17$)

Figure (3.21) shows the position of the vortices over four ripples at various instants in the first half cycle, during which time the oscillatory flow is from left to right. The timescale is such that $t/T = 0.0$ corresponds to flow reversal of the oscillatory flow. At $t/T = 0.05$, a *growing vortex* (G) has already started to form over the lee slope whilst the recently grown vortex, the *ejected vortex* (E), is travelling out of the trough. Both this ejected vortex and the *relic vortex* (R) from the previous cycle (which follows behind the ejected vortex) are losing strength as a result of the exponential decay rule. The ejected vortex passes over its *parent crest* just after $t/T = 0.10$. At $t/T = 0.15$, the ejected vortex has passed over the growing vortex, whilst the relic vortex is in the vicinity of the parent crest. The core radius of this relic vortex is approximately one fifth of a ripple height, and analysis of the raw data reveals that this vortex just misses the crest. During $t/T = 0.20, 0.25, 0.30$, the oscillatory flow is near to its maximum velocity and the growing vortex increases in strength. The ejected vortex has passed

over the growing vortex and, by $t/T = 0.30$, has moved towards the neighbouring ripple. Meanwhile, as the relic vortex follows, it is forced down too close to the bed by the combined rotations of the growing and ejected vortices. This causes its deletion from the model (at $t/T = 0.23$). By $t/T = 0.35$, the ejected vortex has reached the neighbouring crest and the growing vortex has reached its maximum strength. The ejected vortex then passes over this neighbouring ripple crest and, at $t/T = 0.40$, is interacting with this ripple's growing vortex. The oscillatory flow is now waning. Consequently, the (dissipative) exponential decay of the growing vortex is larger than the input vorticity, so it suffers net decay of strength. The phase instant $t/T = 0.45$ is just before flow reversal at the crest (this occurs at $t/T = 0.462$). Therefore, by $t/T = 0.50$, another vortex has started to form over the ripple crest.

The growing vortex has ended up about halfway down the lee slope and slightly above the crest level, while the ejected vortex has ended up in the right hand trough of the neighbouring ripple, having travelled about 1.75λ from its generation point. This whole process then repeats itself in the second half cycle, with the oscillatory flow in the opposite direction.

Figure (3.22a) shows the variation in both the (pure) oscillatory flow and the horizontal velocity (including vortex effects) at the crest. Two obvious features stand out: firstly, the phase lead of the velocity at the crest over the oscillatory flow; secondly, the difference in magnitudes between the two traces at times of maximum oscillatory flow. Treating these in turn, the presence of the vortices gives rise to early flow reversal at the crest (as discussed in Chapter 2) and hence to the observed phase lead. This lead is generally about $20^\circ \pm 5^\circ$. The difference in magnitude between the two traces is accounted for primarily by the growing vortex. At times of maximum oscillatory flow, it is relatively strong and opposes the direction of the oscillatory flow at the crest. The passage of ejected and relic vortices causes the local maxima and minima at $t/T = 0.10, 0.60$ and $t/T = 0.15, 0.65$ respectively. The much smaller maxima at $t/T = 0.35, 0.85$ are associated with the passage of a (weakened) ejected vortex from a neighbouring ripple.

Figure (3.22b) shows the strength ‘signature’ of a vortex in this regime, from its conception at $t/T = -0.038$ to its deletion from the model at $t/T = 1.23$. The vortex strength is increasing until $t/T = 0.344$, at which time the linearly phased-in decay is sufficient to exceed the new vorticity being added to the growing vortex. Thereafter, the vortex suffers net decay of strength. After $t/T = 0.462$, no new vorticity is added in and its strength is approximately 70% of the maximum. Now, the vortex is classed as an ejected vortex and is subject to constant decay at a rate of 0.9% strength loss every time step. After one complete cycle of existence ($t/T = 0.962$), the vortex possesses only 7% of its maximum strength. Finally, when the vortex is deleted out of the model (because its core touches the bed), its age is about 1.25 cycles and its strength is 2% of maximum.

The linearly phased-in decay regime applied in the model, has two noteworthy effects. Firstly, in the growing phase, maximum strength is achieved prior to the cessation of vorticity accumulation. Secondly, the phasing in of decay produces a realistically smooth strength signature.

Figure (3.22c) shows the trail of a vortex during its lifetime. It clearly shows the motion of the growing vortex as it develops over the lee slope. The oscillatory flow then reverses, and the ejected vortex travels over to the neighbouring ripple crest. As the oscillatory reverses yet again, the vortex starts to travel ‘backwards’ under the influence of both the oscillatory flow and the recently ejected vortex. Ultimately, the vortex is caught up in the rotation of a (relatively strong) growing vortex and is swept to the bed.

Figure (3.23a-j) is a series of streamline diagrams corresponding to the time instants of figure (3.21). Its value was calculated (using equation (3.17a,b)) on a fine mesh of nodal points in the ζ plane. These points were then mapped to the physical z plane along with their (unchanged) streamfunction values, where they were contoured using the UNIMAP contouring package.

In figure (3.23a) ($t/T = 0.05$), the ejected vortex is leaving the trough region and advancing up the lee slope towards the crest. However, the growing vortex is still too weak to form a separation region. From $t/T = 0.10$ to 0.20, the (weakening) ejected

vortex becomes increasingly insignificant in influencing the streamlines, whereas the growing vortex forms a developing separation region over the lee slope in which reverse flow occurs near the bed. By $t/T = 0.25$, the oscillatory flow is maximum and the streamlines are closely packed. The separation region occupies about half the lee slope and constricts the streamlines over its top. At $t/T = 0.30$ and 0.35 , the ejected vortex from a neighbouring ripple impinges slightly on the streamlines over the crest, while the separation region continues to enlarge. The waning oscillatory flow causes the streamlines to spread apart. The separation region occupies most of the lee slope by $t/T = 0.40$ and extends nearly one ripple height above the crest. At $t/T = 0.45$, the separation region occupies the whole of the lee slope. However, the rest of the flow domain is quiescent with a large area of almost stationary fluid over the stoss face. The streamline diagrams highlight the growth of the separation region, with the parting of the stagnation points as it develops. By $t/T = 0.45$, the forward stagnation point has almost reached the crest position itself. Finally, at $t/T = 0.50$, the local flow at z_T has already reversed and the growing vortex is being ejected.

3.3.4 Sensitivity tests based on the central run settings

The model operates using three free parameters: the height at which the input vorticity is calculated and released, the decay rate of vortex strength with time, and the decay regime. Sensitivity tests are presented showing the effects of variation in these parameters for the central run. The standard values for these free parameters are:

- release/evaluation of new vorticity at 12.5% of a ripple height above the crest;
- decay of 0.9% of vortex strength per time step;
- linearly phased in decay of vortex strength until ejection (constant thereafter).

The effect of variations in the kinematic viscosity (ν) is also considered. This is not a free parameter, but does play a key role in the model as it determines the rate of growth of vortex cores and hence the propensity of vortices to hit the bed.

The model outputs chosen to assess these effects are the horizontal velocities at the crest (c.f. figure (3.22a)), the strength signature (c.f. figure 3.22b)) and the vortex trail (c.f. figure (3.22c)).

Figures (3.24)-(3.27) show the effect of varying these four parameters. This particular case study ($d/\lambda = 1.42$) is quite exacting because of the closeness with which the relic vortex approaches the bed as it crosses the ripple crest (see §3.4.1). With all of the four parameters considered, one of the settings causes this relic vortex to hit the bed early. The effect of this is common to all the plots; the vortex trail stops short, the strength signature cuts off early, and the velocity plot loses the local minima at $t/T = 0.15, 0.65$.

Variation in the release/evaluation height (figures (3.24a-c)) principally affects the strength signature. Small differences in strength ($\pm 3\%$ at its peak) cause the growing vortex to travel to different positions over the lee slope. These two factors in turn affect the impact of the growing vortex on the velocity at the crest, exemplified by a variation in the velocity magnitudes of about $\pm 10\%$ during peak oscillatory flow. Importantly, the velocity phases remain unchanged, as do the times of peak strength. The differences outlined above are significant only for certain parts of the cycle.

The kinematic viscosity (figures (3.25a-c)) seems to be a very insensitive parameter, the relevant output showing little variation for the three settings. However, the larger core for the setting $\nu' = 5 \times 10^{-3}$ causes early deletion of the relic vortex.

Changes in the results associated with both the decay rate and the regime (figures (3.26a-c), (3.27a-c)) are much more marked, suggesting that the model is sensitive to these two parameters. Varying either parameter to strengthen or weaken the vortices significantly alters the strength signatures and the vortex trails. Varying the decay rate by $\pm 0.1\%$ causes a corresponding 25% difference in peak strengths. The decay rate does not unduly affect the velocity traces. However, the 'strong' decay regime increases the influence of the vortices so much that the velocity phase lead is essentially doubled. Comparing different decay regimes at the same decay rate may well be a spurious exercise, but it serves to illustrate its profound impact on the model.

In summary, the hydrodynamical model is sensitive to the rate and manner in which vortex decay is represented, less sensitive to the release/evaluation height and rather insensitive to the choice of kinematic viscosity.

3.3.5 Two further runs; $d_0/\lambda = 1.1$ and $d_0/\lambda = 2.5$

The results from two further runs are presented, with $d_0/\lambda = 1.1$ and $d_0/\lambda = 2.5$. Otherwise, all the input parameters are the same as in the ' $d_0/\lambda = 1.42$ ' case. The motivation for these two runs is to give the opportunity for comparison between three differing flow regimes.

$d_0/\lambda = 1.1$

In this case, the horizontal excursion of the oscillatory motion barely exceeds the ripple wavelength. Figure (3.28) is the familiar format of instantaneous vortex positions. It shows that the growing vortex is behaving in the same manner as in the central run case. The ejected vortex again passes over the parent crest at $t/T = 0.10$, but then proceeds very slowly over the trough and only just reaches the neighbouring crest by flow reversal. By this stage, it is very weak and so does not influence this ripple's growing vortex. Rather, the growing vortex forces the ejected vortex backwards and upwards. The (even older) relic vortex simply drifts over the trough at a higher level.

Figures (3.29a-c) compare velocity output, strength and vortex trails in a similar manner to §3.3.3. The velocity plot (figure (3.29a)) lacks any conspicuous local maxima and minima associated with vortex passage over the crest. At $t/T = 0.10, 0.60$, the passage of the ejected vortex over the parent crest causes a slight kink in the curve. Despite the weakness of the flow regime, there are certain similarities between this case and the $d_0/\lambda = 1.42$ case; the magnitude of the curves are equivalent (the proportionate affect of the growing vortex being similar), and the phase lead of the crest velocity in advance of the (pure) oscillatory flow is not markedly different. Compared with the $d_0/\lambda = 1.42$ case, the strength signature (figure (3.29b)) shows a 25° phase lead in the occurrence of peak vortex strength. The vortex trail for the $d_0/\lambda = 1.1$ case (figure (3.29c)) shows the growing vortex forcing the ejected vortex back from the crest.

$$d/\lambda = 2.5$$

Material from this run setting is presented, fully in the knowledge that the hydrodynamical model may well be giving unphysical results for the motion of the growing vortex.

The instantaneous vortex positions for this case (figure (3.30)) show that flow reversal in the crest region occurs much earlier than for the other two cases. This is evident at $t/T = 0.05$ where the growing vortex is already well formed. An earlier start to formation and high strength are the two primary features of the growing vortex. The ejected vortex passes the parent crest somewhat before $t/T = 0.10$. It reaches the neighbouring crest at $t/T = 0.20$, then moves on towards the next ripple. As it passes over this third crest, it is forced to the bed by this ripple's growing vortex and is deleted from the model. For this reason, there is no relic vortex in the flow. The ejected vortex has thus travelled over three crests to end up two ripples downstream.

The crest velocity plot (figure (3.31a)) shows three maxima associated with the passage of the ejected vortex over successive crests ($t/T = 0.05, 0.20, 0.35$ and $0.55, 0.70, 0.85$). The intermediate minima at $t/T = 0.15, 0.25$ and $0.65, 0.75$ are due to the position of the ejected vortex on the right of the ripple, which allows it to reduce the magnitude of the velocity at the crest. The 'mean' magnitude of the velocity plots remains about the same as for the other cases, but the phase lead of the crest velocity over the oscillatory flow is much larger, in accordance with the earlier flow reversal.

The strength signature (figure (3.31b)) exhibits peak strength at the same time as in the $d/\lambda = 1.42$ case; both cases also have the same cut-off time when the vortex is killed. However, between $t/T = 0.20$ and 0.35 , the signature shows increased variability.

The vortex trail (figure (3.31c)) shows a confused pattern as the vortex grows over the lee slope. This conforms with some of the doubtful aspects of the setting, as outlined in §3.3.2. Its subsequent ejection and passage over the neighbouring ripples is more ordered, as is its ultimate descent to the bed.

3.4 Discussion

3.4.1 Comparisons with experimental data

The hydrodynamical model predicts that the growing vortex forms about half way down the lee slope with its centre slightly above the crest level, findings that are in agreement with the observations of Tunstell and Inman (1975). Ranasoma (1992) has produced vorticity contour plots over solidified, natural ripples with steepness 0.18. Of his experimental runs, test 5A is the most suitable for present purposes ($d/\lambda = 1.6$, $RE = 6680$). For this case, the growing vortex extends over the whole of the lee slope and upto 2 ripple heights above the crest. Similar features can be observed in figure (3.23), though for a slightly lower value of d/λ .

Ranasoma also suggests that peak vortex strength may occur prior to ejection, which is consistent with the vortex decay regime adopted here. Unfortunately, there is very little experimental data on vortex strengths with which to justify the model assumptions in detail. An empirical formula for the peak strength of vortices is given by Tunstell (1973):

$$\kappa_{\max} = 0.39 U_o h \quad 3.26$$

If equation (3.26) is applied to the three runs in this chapter, it gives the non-dimensional peak strength as 1.43, 1.86 and 3.28, compared with the peak strengths from the model of 1.95, 3.26 and 10.34. These values are substantially larger, especially for the $d/\lambda = 2.5$ case, for reasons which remain unclear.

Tunstell and Inman (1975) provide an empirical criteria to estimate the dimensions of the vortex core, namely that its radius is $0.4h$ at ejection. This is very large compared with the equivalent model cores, whose radii are approximately $0.1h$ at the time of ejection for all three runs. One possible reason for this discrepancy is that Tunstell and Inman used particle motion to determine core diameters. Measuring core diameters on the basis of particle motion may well overestimate the actual core size because particles outside the core may still be observed circling the vortex.

If the present model is run for Ranasoma's test 5A settings, the ejected vortex passes over the parent crest at $t/T = 0.11$ and the neighbouring crest at $t/T = 0.31$.

These phases are in close agreement with the approximate passage times obtained from Ranasoma's contour plots ($t/T = 0.083, 0.31$), though the model's ejected vortex passes the parent crest rather later. As in the present model, Ranasoma finds that vortex ejection occurs earlier with increased d/λ .

Sleath (1982a) commented on the interaction between the ejected vortex and the growing vortex of the neighbouring ripple, saying that it gave an added impetus to the growing vortex. For the central run, the ejected vortex does pass over the top of a neighbouring growing vortex, giving the opportunity for the two vortices to interact as described by Sleath. However, the strength signature (figure (3.22b)) does not show the sudden increase in vortex strength noted by Sleath. One possible explanation is that the present vortex decay regime is too excessive, damping out these relatively late increases in vortex strength.

Figures (3.32a,b) show a comparison between the hydrodynamical model and the experimental results of DuToit and Sleath (1981), taken over the crest and the trough of solidified, natural ripples. The phase information in figure (3.32a) was used to tune the model, so comparison of the phases in this instance is not strictly fair. However, the model does replicate the two peaks at $t/T = 0.15, 0.65$. The magnitude of the model velocity is consistently lower than DuToit and Sleath's. This is also the case in the trough, as shown in Figure (3.32b). Here, the timings of the peaks at $t/T = 0.20, 0.70$ show good agreement. In both figures, the experimental data shows some asymmetry between the two half cycles.

3.4.2 Comparisons with theoretical results

A comparison of results from the central run ($d/\lambda = 1.42, h/\lambda = 0.17$) with those of Longuet-Higgins (1981) and Macpherson (1984) ($d/\lambda = 1.5, h/\lambda = 0.17$) shows differences in the heights reached by the vortices. The present model predicts that the vortices travel fairly close to the bed, while both of the other models have vortices rising steadily after ejection until they are 2-3 ripple heights above the crests (Longuet-Higgins) or higher (Macpherson). As stated in §3.1.2, the mechanism that accounts for this rise is vortex pairing, where two vortices mutually drive each other, allowing the

pair to escape from the bed. Both Longuet-Higgins and Macpherson have vortex pairing in their models (see §3.1.2 and figures (3.2), (3.3)). The present model does not predict vortex pairing. Approximate passage times of vortices ($t/T = 0.07, 0.28$ (Longuet Higgins) and $t/T = 0.15, 0.30$ (Macpherson)) are earlier and later than the hydrodynamical model for the same settings ($t/T = 0.106, 0.324$).

The finite difference solution of Blondeaux and Vittori (1991) shows more complicated vortex structures over the ripple profile. The structure associated with the growing vortex shows many of the features from the experimental data of Ranasoma (1992), namely vorticity production under the growing vortex and, for more vigorous flows, more than one growing vortex. Figure (3.4) is taken from Blondeaux and Vittori (1991) showing vorticity contours for a run with $d/\lambda = 1.5$, steepness = 0.15. These results suggest vortex passage over the parent crest between $t/T = 0.50$ and 0.625 , with passage over the neighbouring crest between $t/T = 0.75$ and 0.875 . These passage times are consistent with the present hydrodynamical model and Ranasoma's findings. Moreover, Blondeaux and Vittori's vortices form over the lee slope and travel up to about one ripple height above the bed. A comparison between the present hydrodynamical model and the results of Asp Hansen *et al* (1991) is given in Chapter 5.

3.4.3 Implications of these comparisons

One of the more notable features of the present model is its prediction that vortices remain fairly close to the bed. Casual inspection of the vortex shedding process through the side walls of a flume suggests that ejected vortices do stay fairly close to the bed until flow reversal, at which time they appear to leave the bed and move backwards and upwards into the flow. By this stage, however, the vortex has become almost indistinguishable from the water mass. The inference from such observations is that the hydrodynamical model works well in recreating the motion of the growing and ejected vortices, but may not cope properly with the older, relic vortices. These tend to be propelled towards the bed by other, stronger vortices. Longuet Higgins and Macpherson do get vortices high in the flow, but relatively early in their 'life'. The *true*

picture appears to be somewhere between the present model and those of Longuet-Higgins and Macpherson. The vorticity contours of Blondeaux and Vittori (1991) and Ranasoma (1992) have vortices travelling close to the bed in the first half cycle after ejection, but do not record a particular vortex's fate for longer than this.

In the context of sediment movement, the good phase agreement between the hydrodynamical model and the data of DuToit and Sleath (1981) and Ranasoma (1992) is encouraging. Time varying sediment concentrations are linked to the motion of the vortices. However, it may well be that sediment does not get high enough into the flow because of the low travel heights of the vortices.

3.5 Conclusions

The hydrodynamical model cannot hope to produce as detailed a picture of the vortex field as the finite difference solutions of, say, Blondeaux and Vittori (1991). However, by introducing the essential physics in a modular, 'building block' fashion, a physically realistic model of vortex shedding over ripples has been achieved. Output from the model can be readily linked to the actual flow situation and generally agrees with available data.

Computationally, the hydrodynamical model is swift, robust and adaptable. It can be run up to $d/\lambda \approx 3.0$, although beyond $d/\lambda = 2.1$, the motion of the (evolving) growing vortex becomes unphysical. This behaviour seems to not adversely affect the subsequent fate of the vortex. For $d/\lambda < 2.1$, the hydrodynamical model gives a consistently good account of itself.

The hydrodynamical model would benefit from more substantial information regarding both the fate and decay rates of vortices. This will hopefully answer the two key question marks that surround the model in its present form: the choice of decay regime and the height to which vortices rise over the bed. Encouraging agreement in the timing of key 'vortex events' suggests that the present assumptions regarding the manner and rate of vortex decay are not unreasonable.

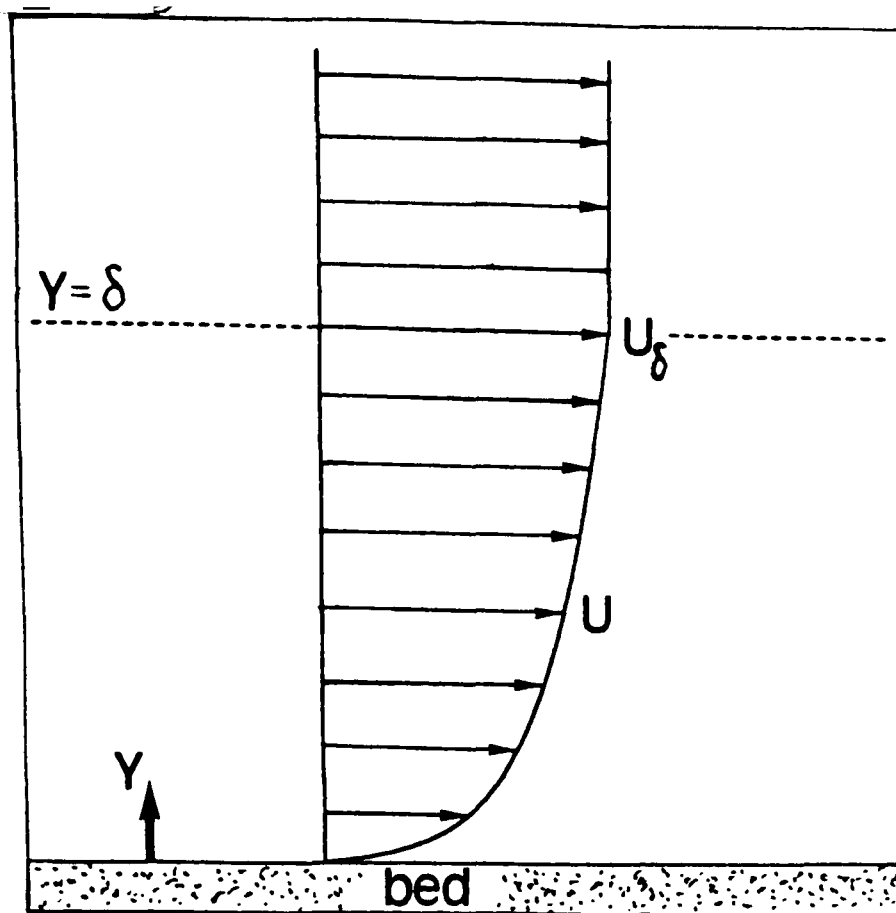
A sequence of figures relating to literature on modelling the flow over ripples.

Figure 3.1 An explanation of Prandtl's rule.

Figure 3.2 Some of the results from the discrete vortex model of Longuet-Higgins (1981). At $\sigma t = 2.70$, the oscillatory flow is from left to right, with $\sigma t = 3.15$ approximating to flow reversal. The next flow reversal would be at $\sigma t = 6.28$. Diagram copied and adapted from Longuet-Higgins (1981). ($d/\lambda = 1.5$, $h/\lambda = 0.17$).

Figure 3.3 Some of the results from the discrete vortex model of Macpherson (1984). Here, the oscillatory flow is from right to left in all the pictures, with flow reversal at $t/T = 1.0$. The arcs surrounding the vortices represent their sense of rotation (by the inclination of the arc) and their strength (by the arc area). Copied and adapted from Macpherson (1984). ($d/\lambda = 1.5$, $h/\lambda = 0.17$).

Figure 3.4 Some of the results from the finite difference model of Blondeaux and Vittori (1991). The oscillatory flow is initially from left to right, then reverses at $t/T = 0.50$.



Consider the generation of vorticity within the boundary layer adjacent to the bed, which is thin enough for vertical velocities to be ignored:

The vorticity generated at height Y within boundary layer is therefore

$$\frac{\partial U}{\partial Y}$$

The flux of this generated vorticity within the boundary layer is given by

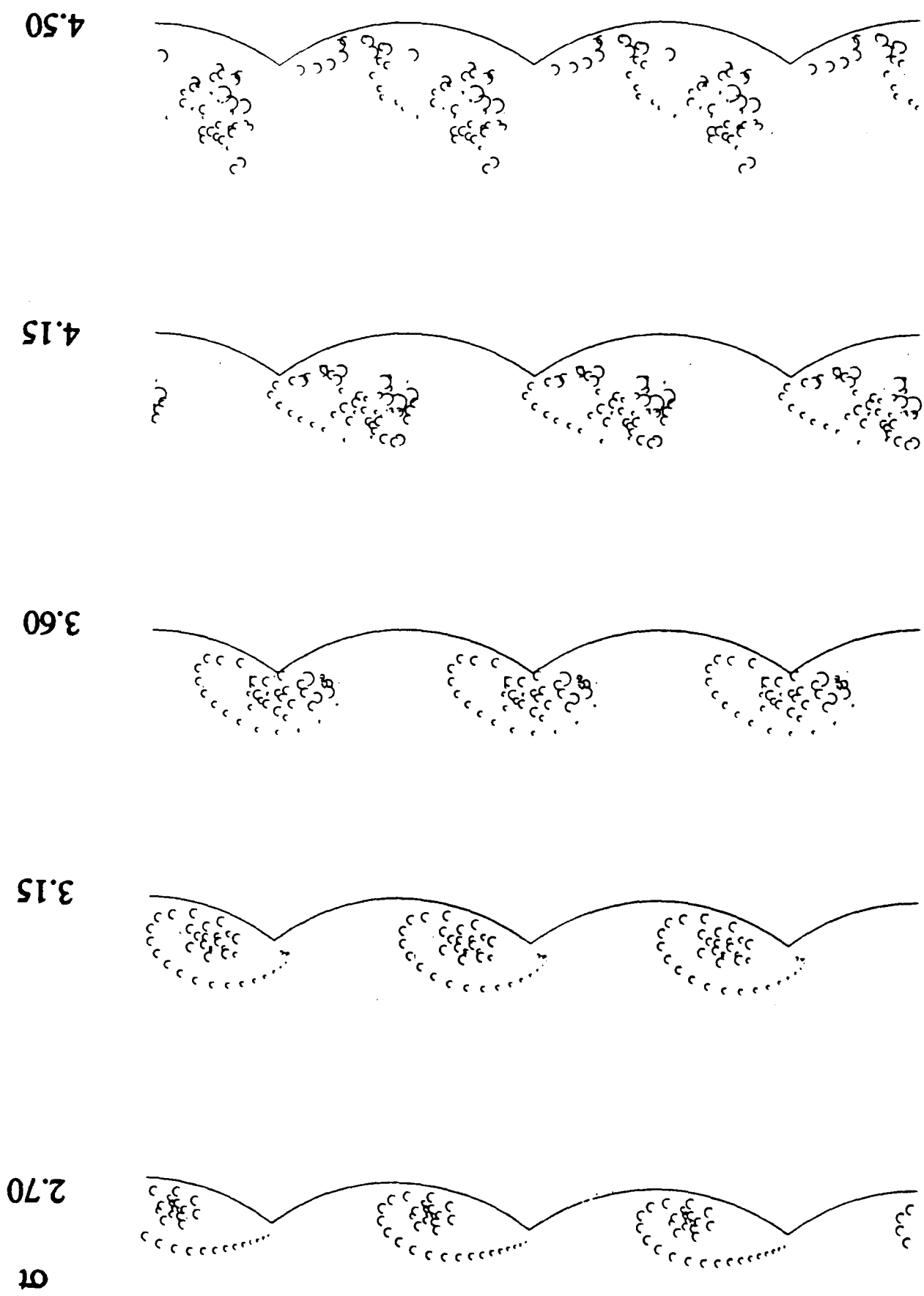
$$\int_0^{\delta} U \frac{\partial U}{\partial Y} dY = \frac{1}{2} U_{\delta}^2$$

where U_{δ} is the horizontal velocity at the upper edge of the boundary layer. This quantity (essentially the input of generated vorticity into the flow) is equal to the rate of change of circulation within the boundary layer. Therefore

$$\frac{d\Gamma}{dt} = \frac{1}{2} U_{\delta}^2$$

Figure 3.1

Figure 3.2



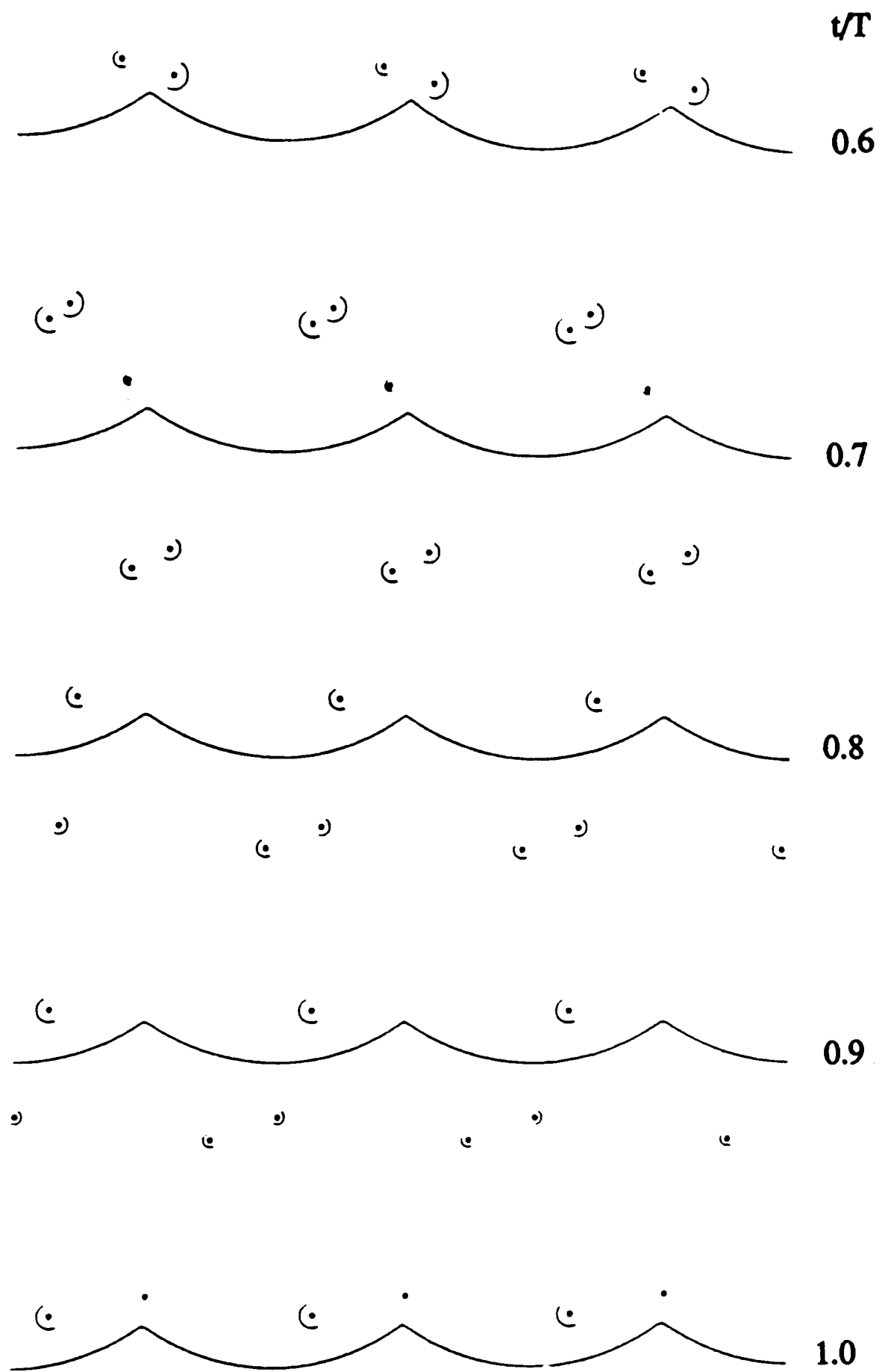
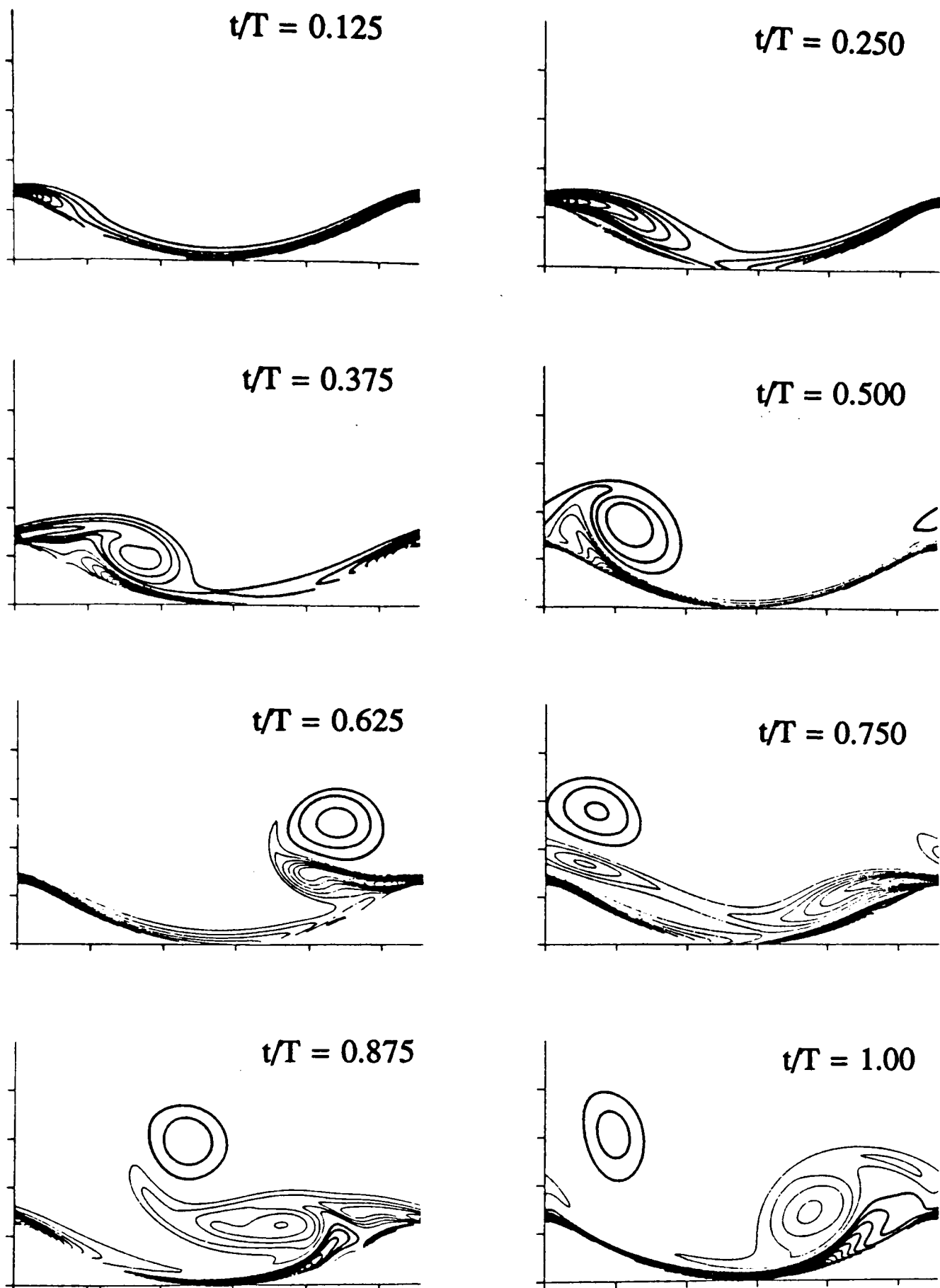


Figure 3.3



thick lines represent clockwise vorticity
thin lines represent anticlockwise vorticity

Figure 3.4

A set of figures concerned with the development and operation of the hydrodynamical model

Figure 3.5 A comparison of the profile of some naturally formed ripples against the mapping used in the hydrodynamical model. From Sleath (1984)

Figure 3.6 A streamline diagram, illustrating the effect of the mapping.

Figure 3.7a The position of ' z_T ', where vorticity input is calculated and released.

Figure 3.7b An illustration of the vortex amalgamation procedure used to simulate the input of new vorticity into the (existing) growing vortex.

Figure 3.8(a,b) Two schematic diagrams illustrating how the hydro. model moves vortices in the ζ plane, which then have their positions mapped into the z plane.

Figure 3.9 An illustration of the different decay regimes applied a vortex's life.

Figure 3.10 An illustration of the repeatable pattern of vortices over adjacent ripples, also showing the 'computational domain' in which calculations were performed.

Figure 3.11 (a,b) Two velocity time series, measured by DuToit and Sleath (1981) over the crest and the trough of a ripple.

Figure 3.12 A flow diagram of the procedures followed by the hydrodynamical model.

Figure 3.13 Convergence of the hydrodynamical model; variation of the cycle-averaged drag coefficient over 20 cycles. (Central settings.)

Figure 3.14 Symmetry of the results in the two half cycles: (normalised) velocities at the crest for each half cycle, grafted on top of each other. (Central settings.)

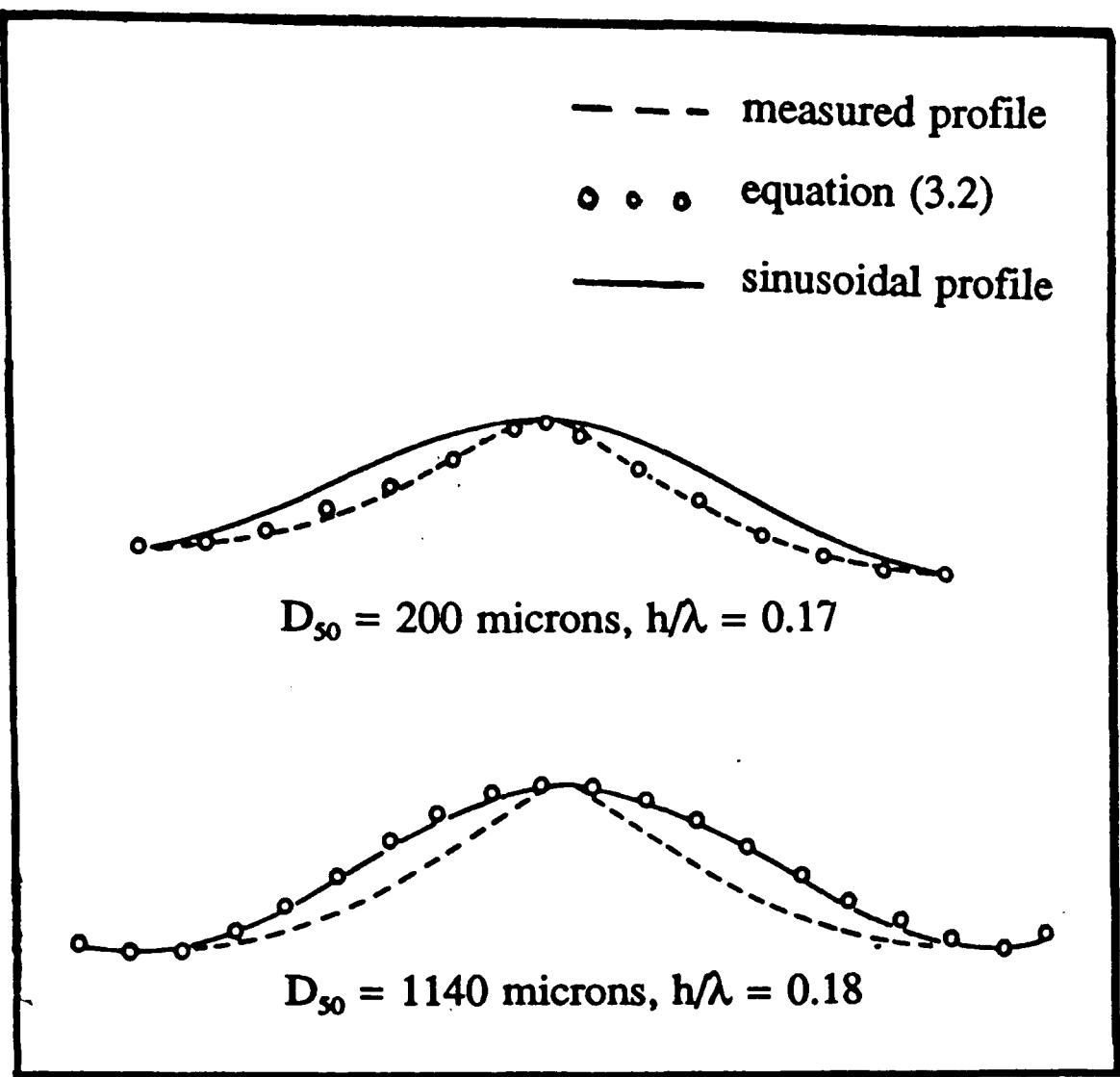


Figure 3.5

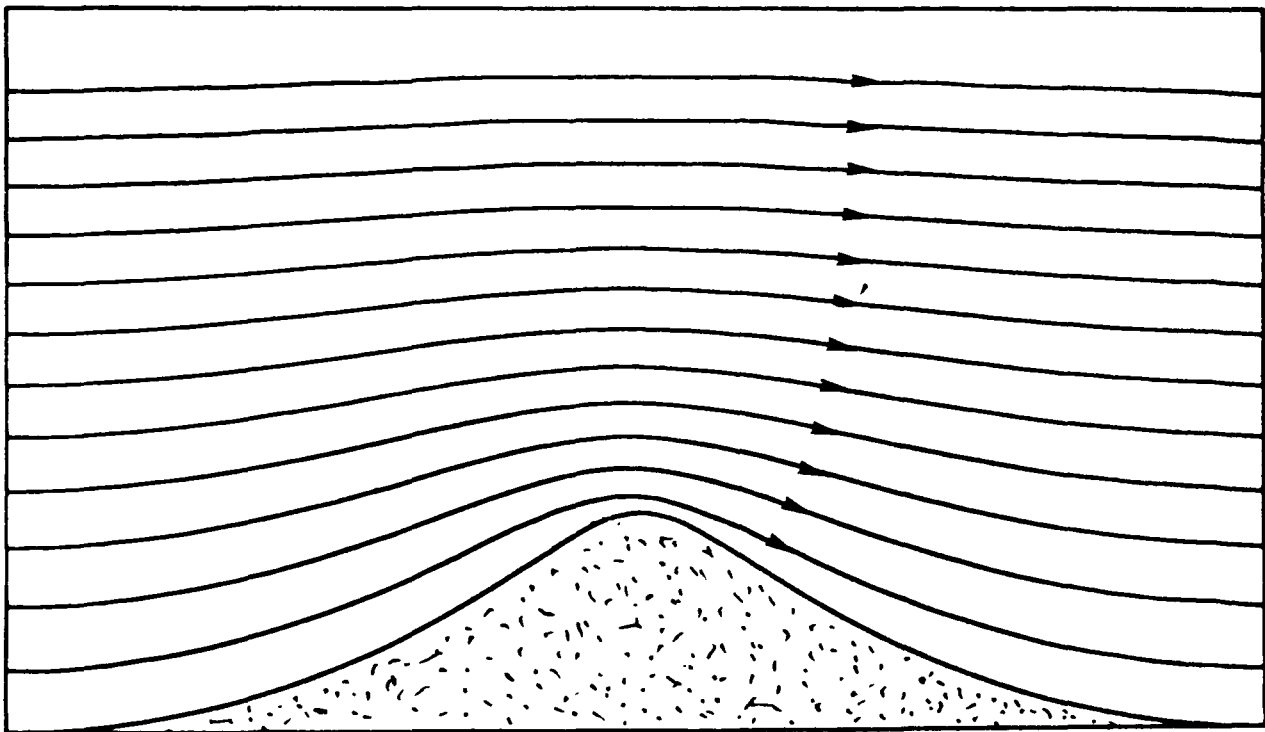
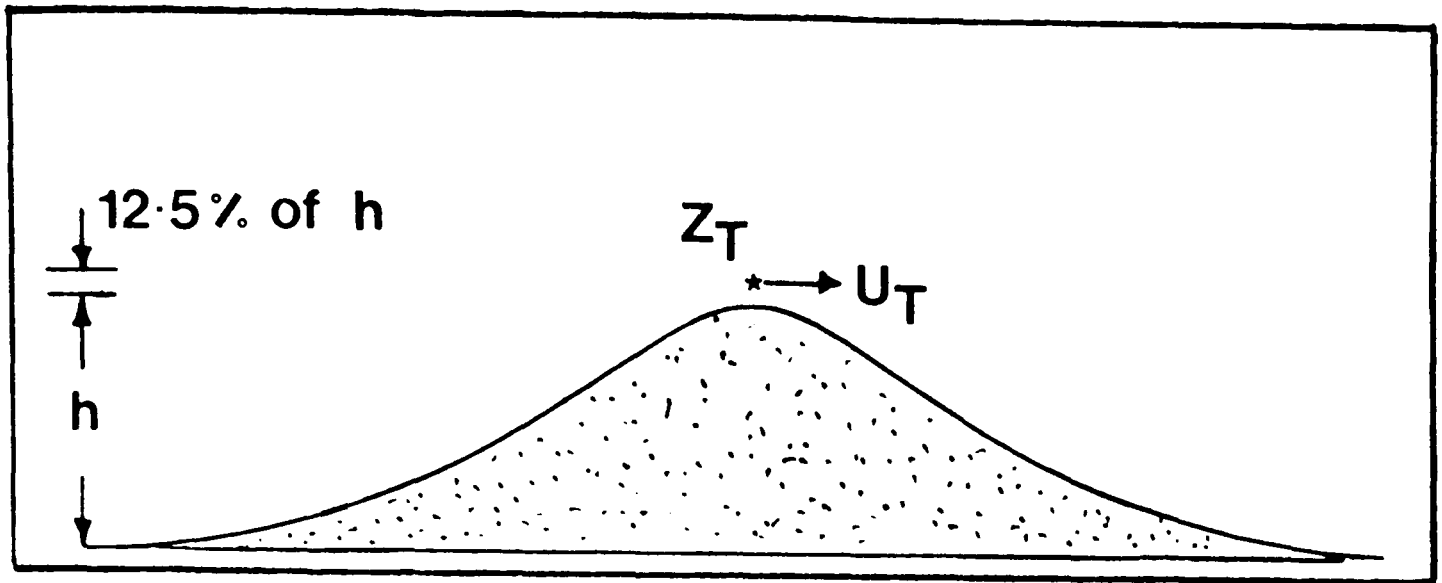


Figure 3.6

(a)



(b)

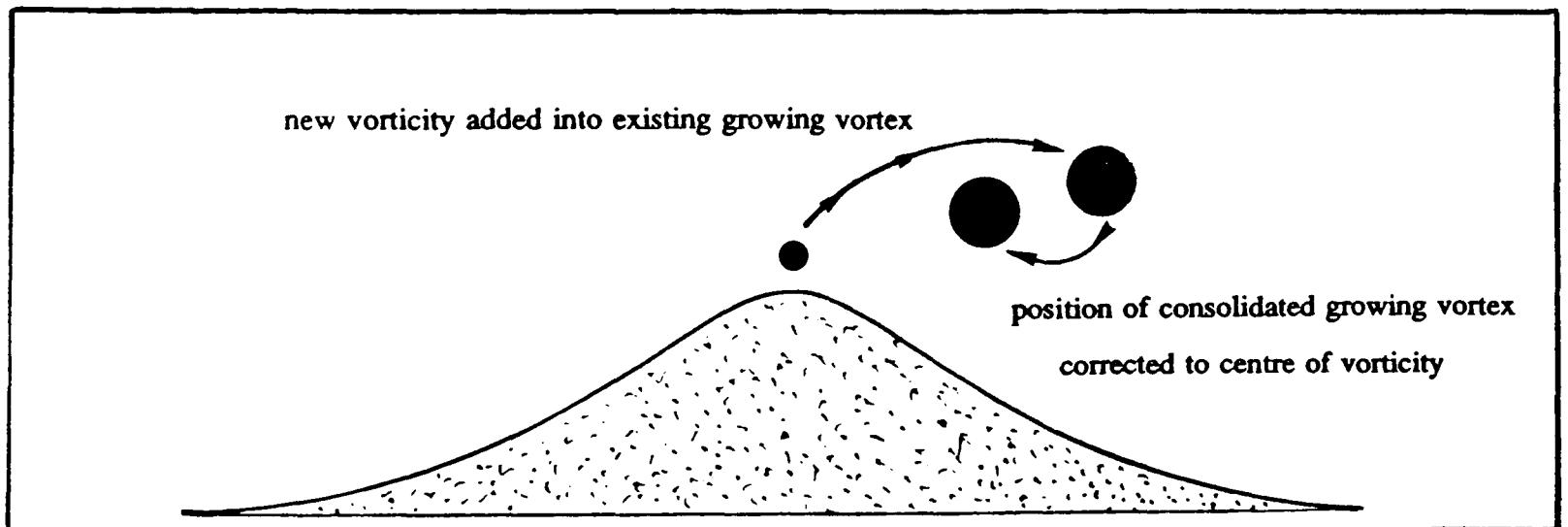
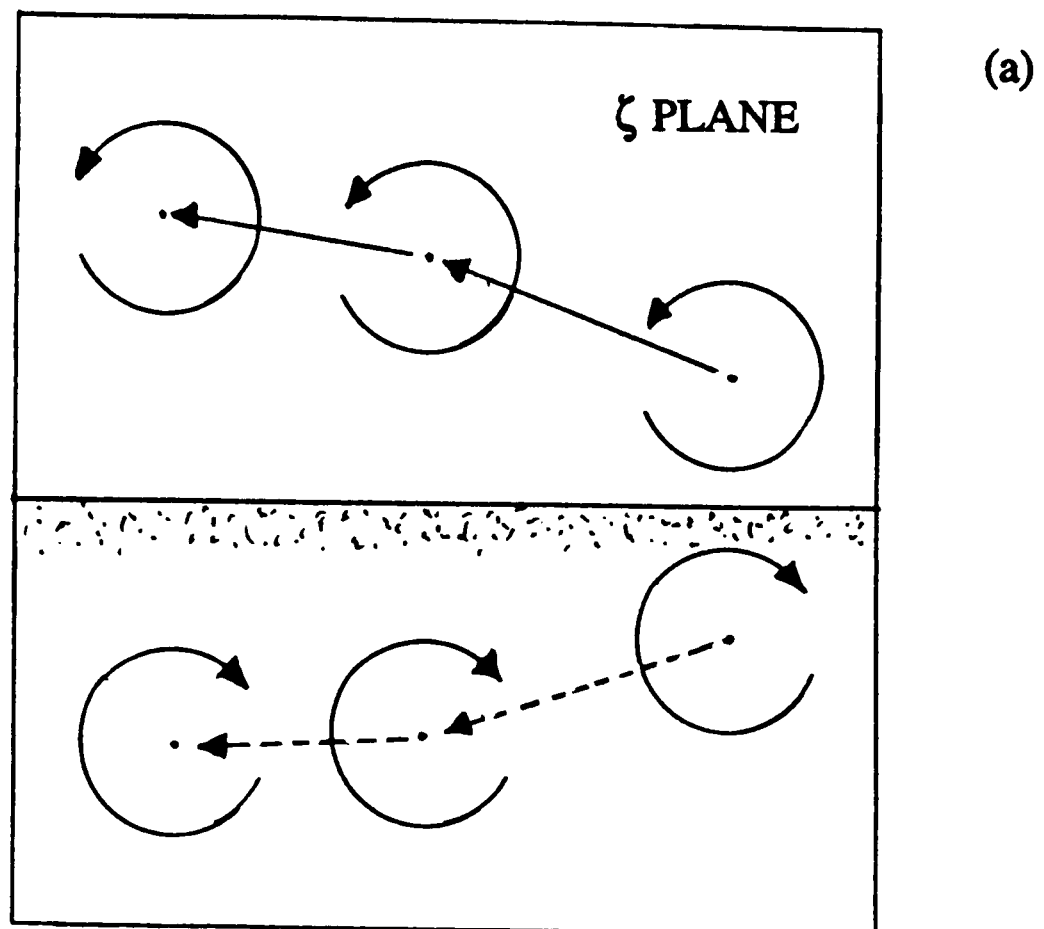


Figure 3.7 (a,b)



Vortices are moved in the ζ plane, with the image vortices simply having their positions imposed (figure (3.8a)). If required (graphics etc), vortex positions can then mapped to the z plane (figure (3.8b)).

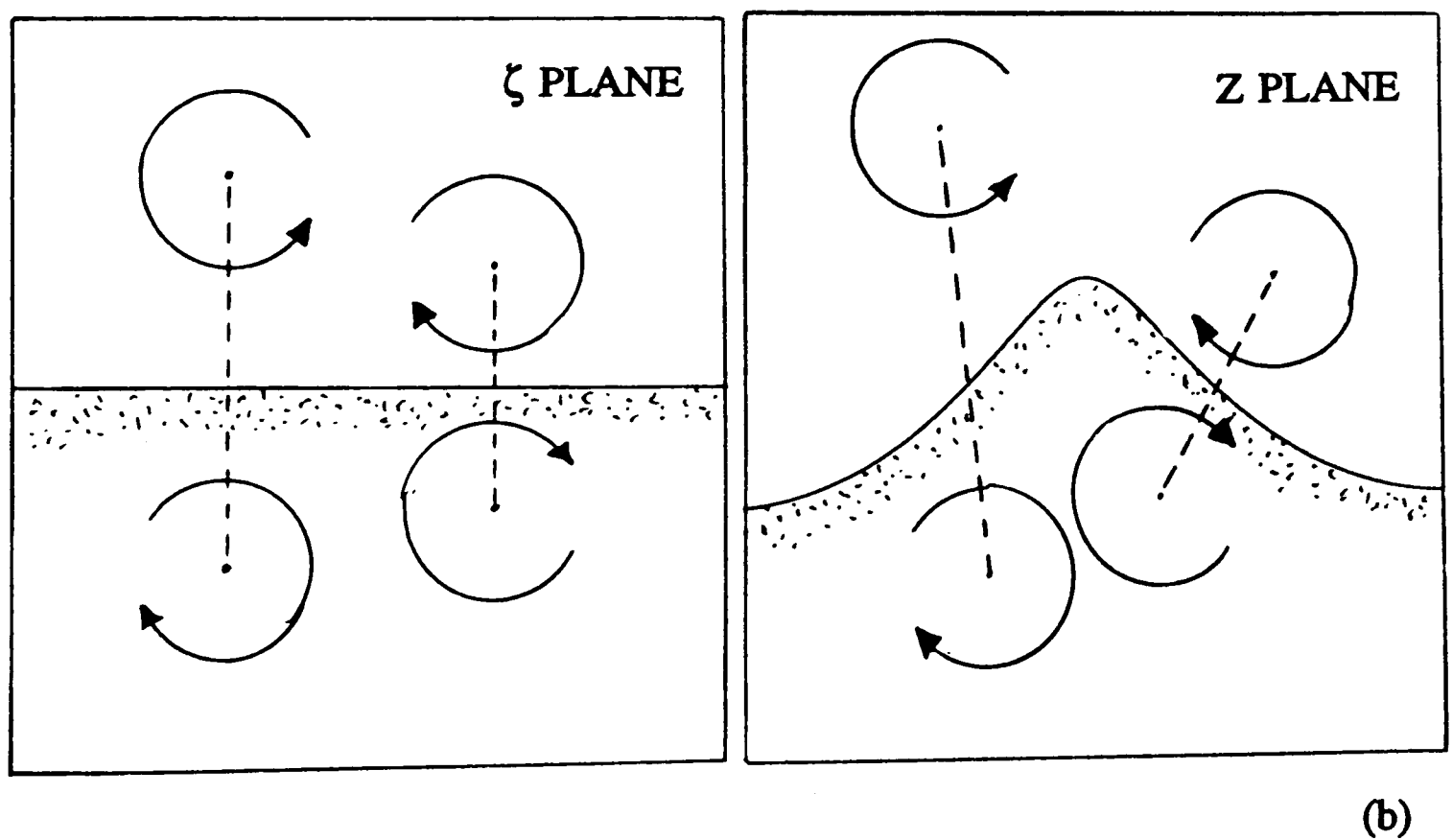


Figure 3.8 (a,b)

Figure 3.9

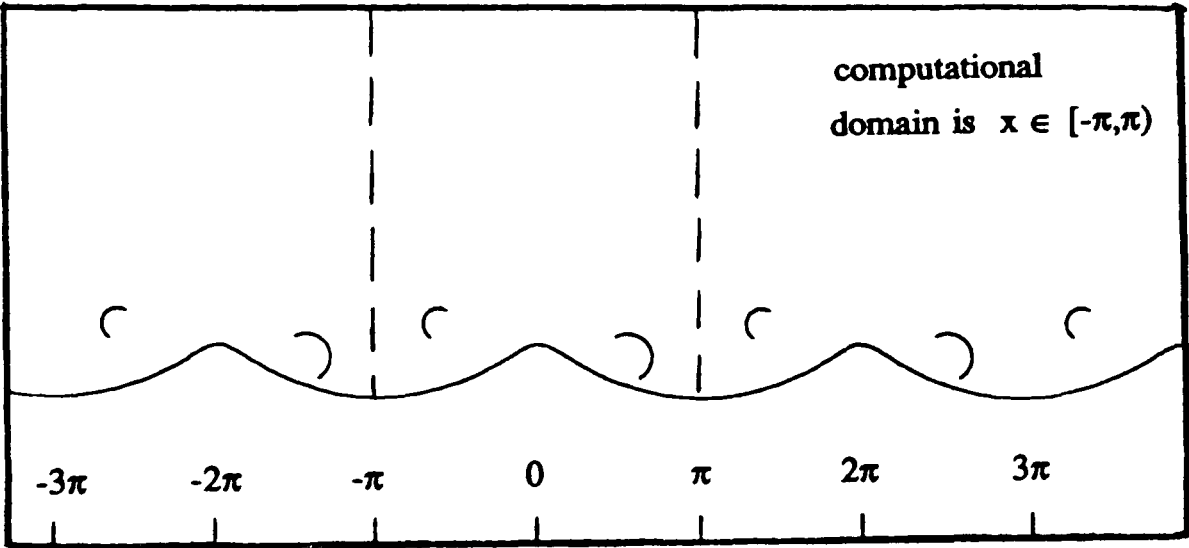
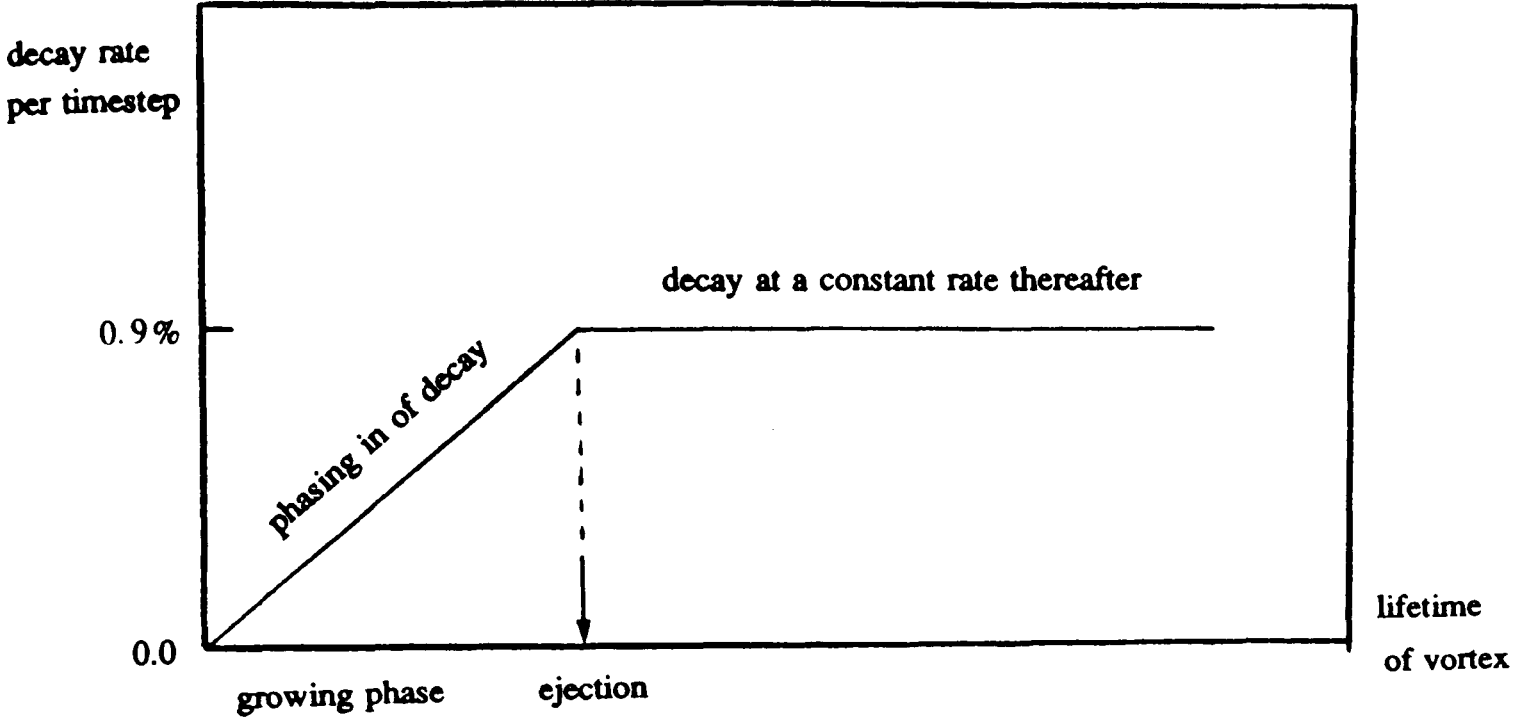


Figure 3.10

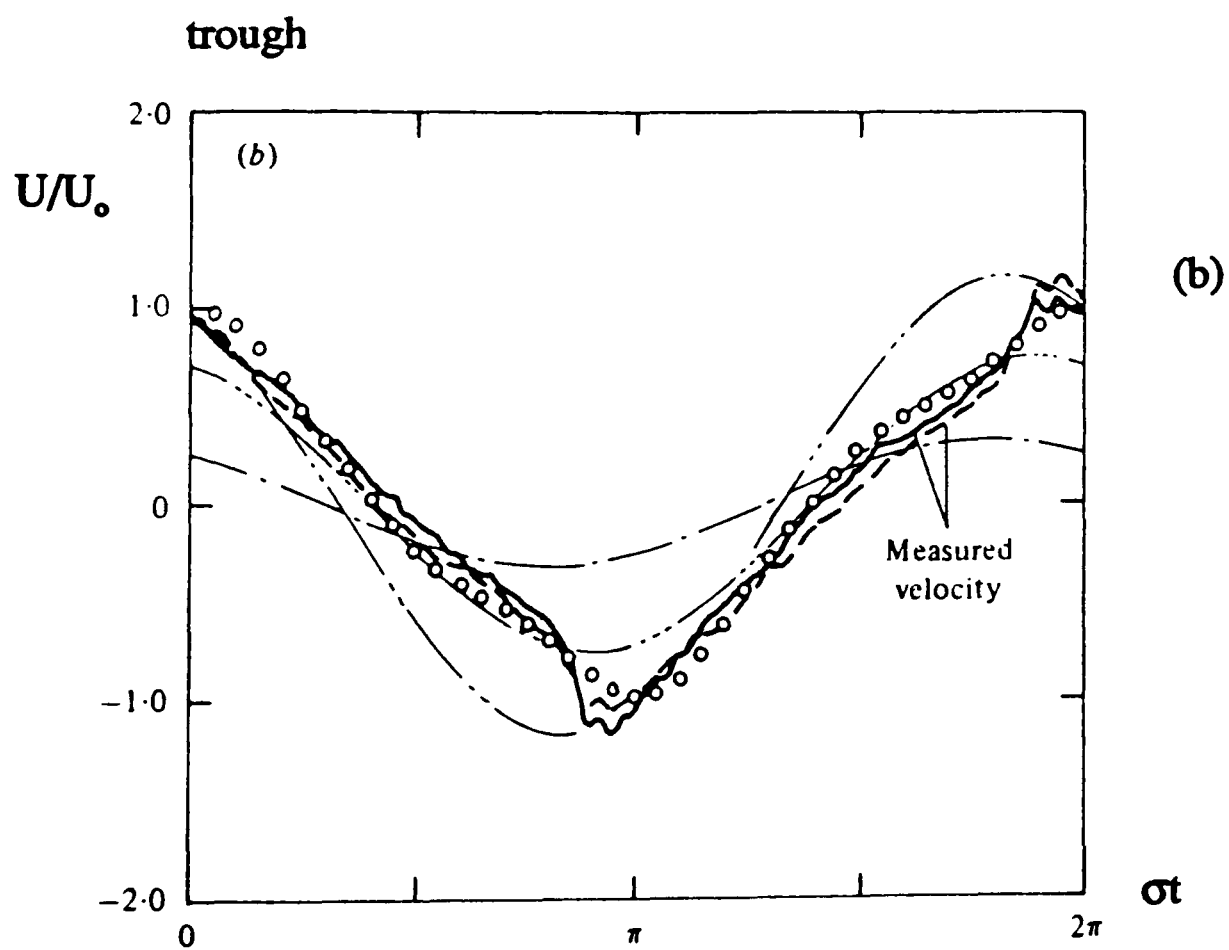
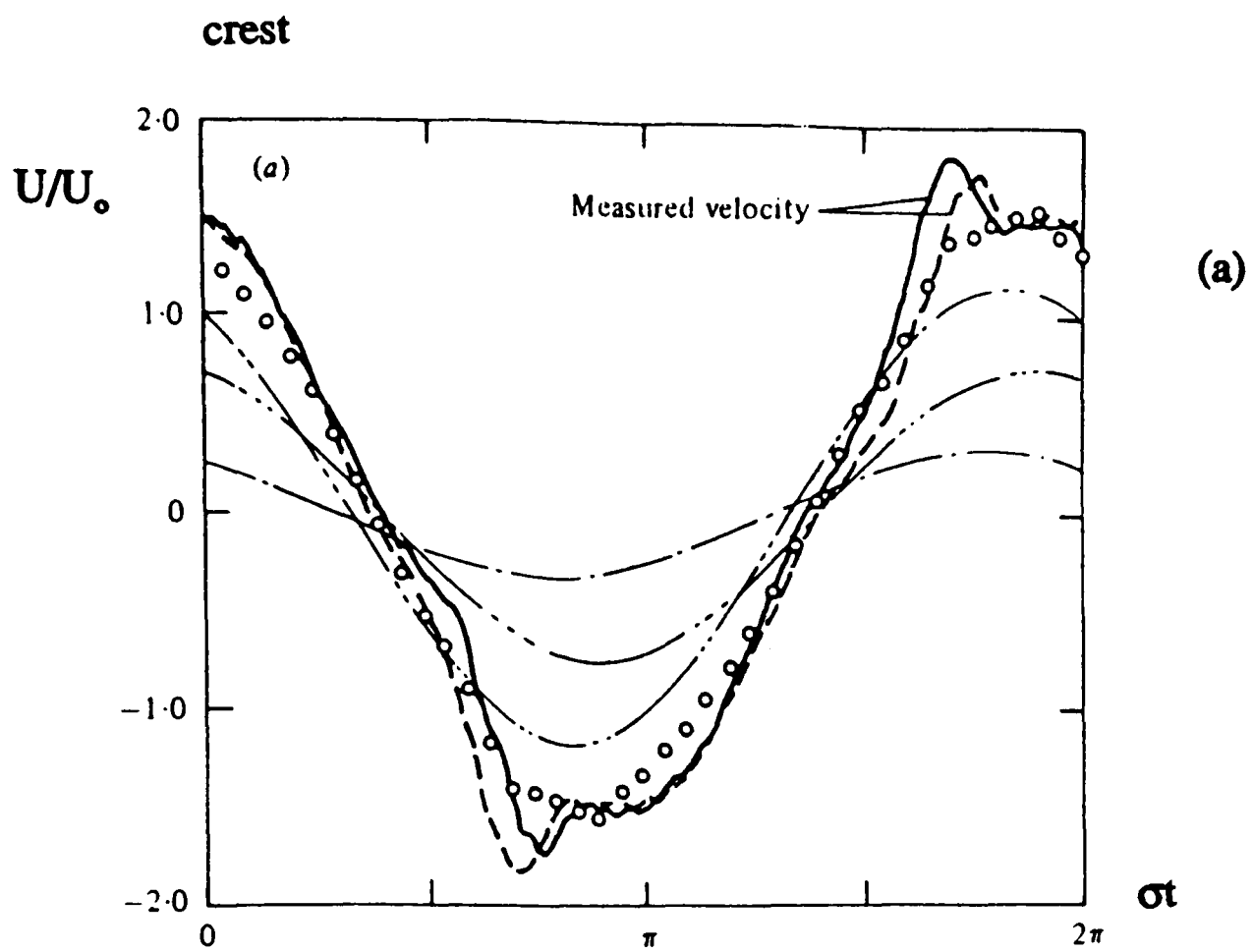


Figure 3.11 (a,b)

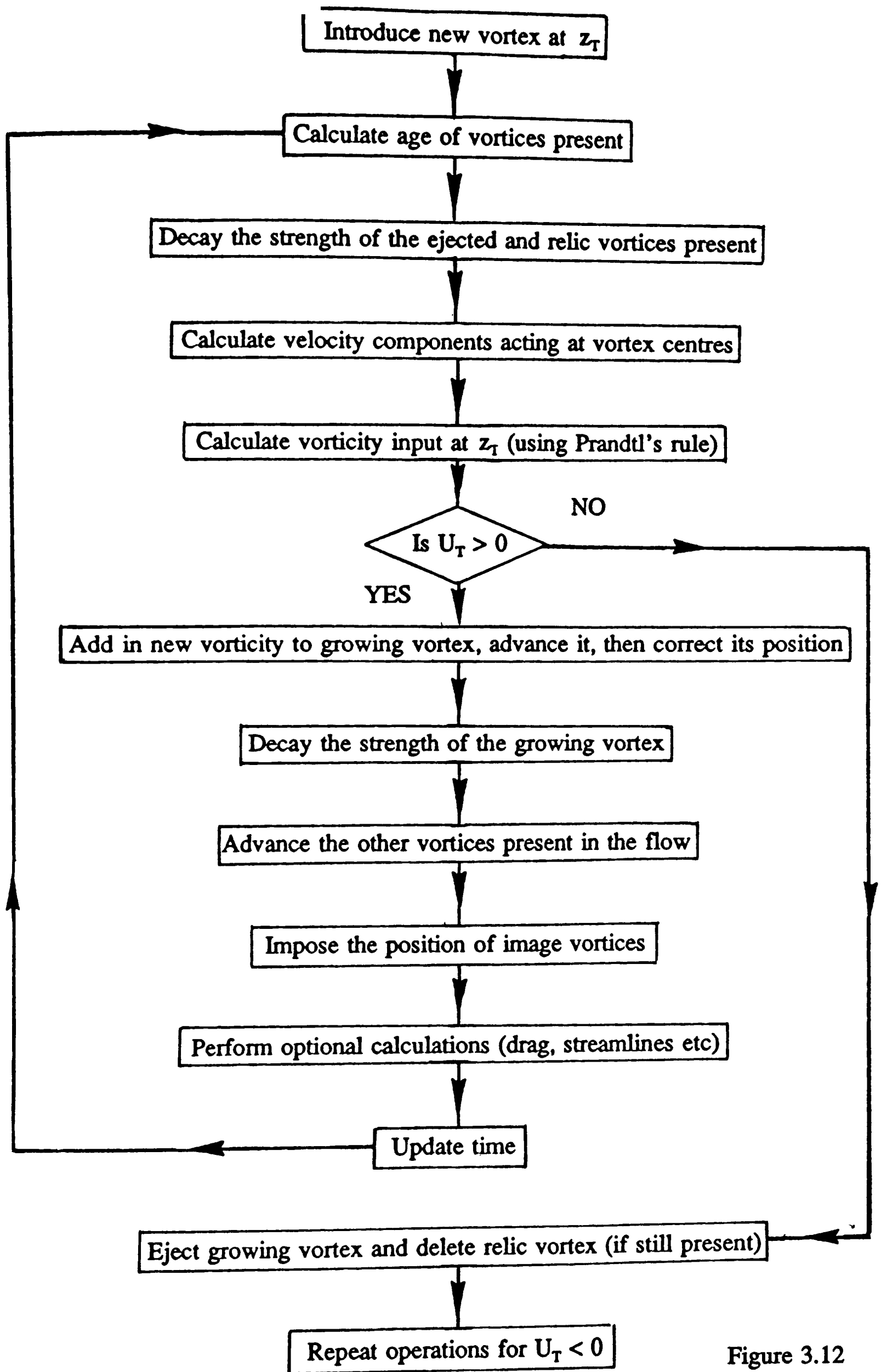


Figure 3.12

Figure 3.13

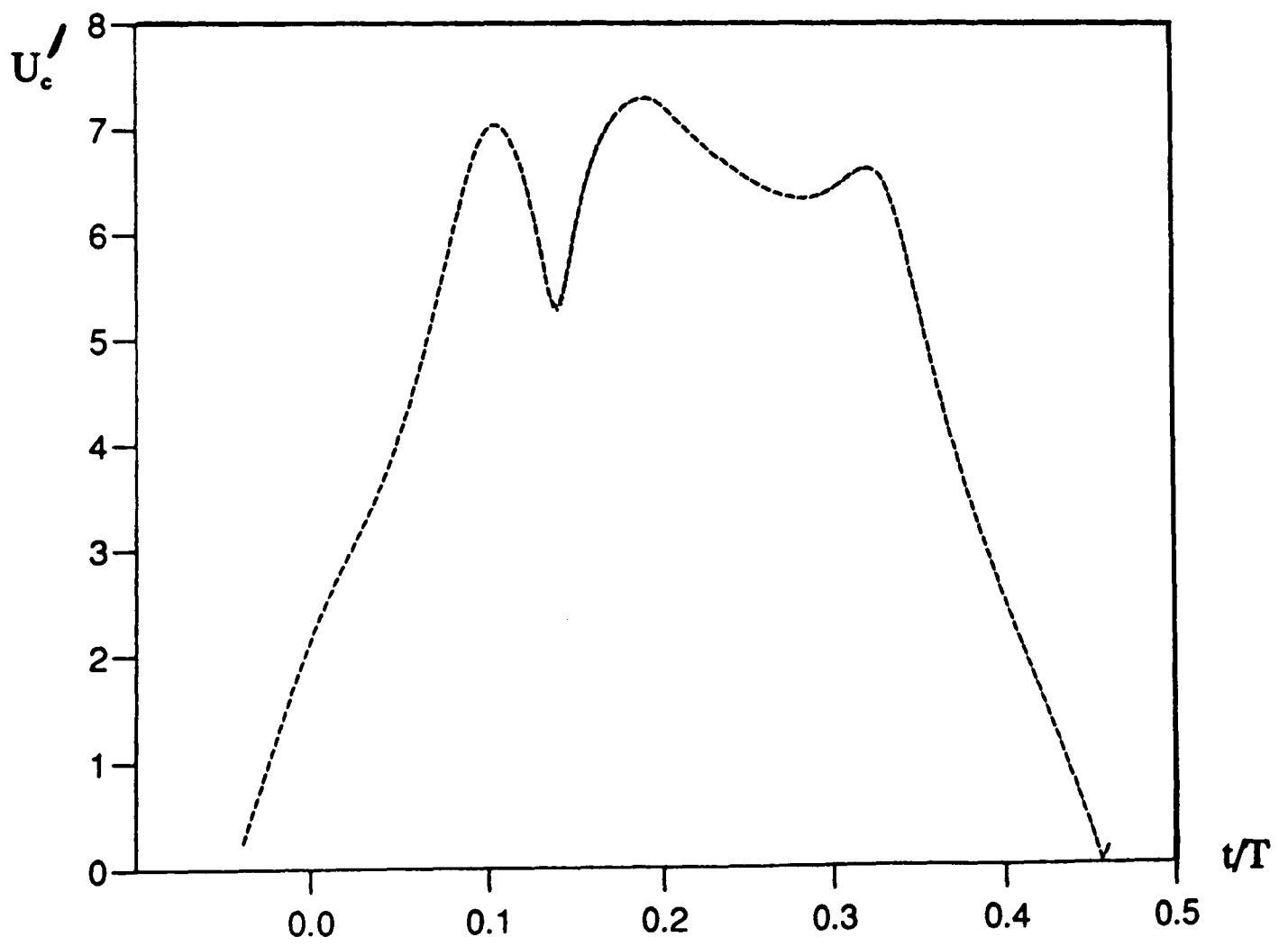
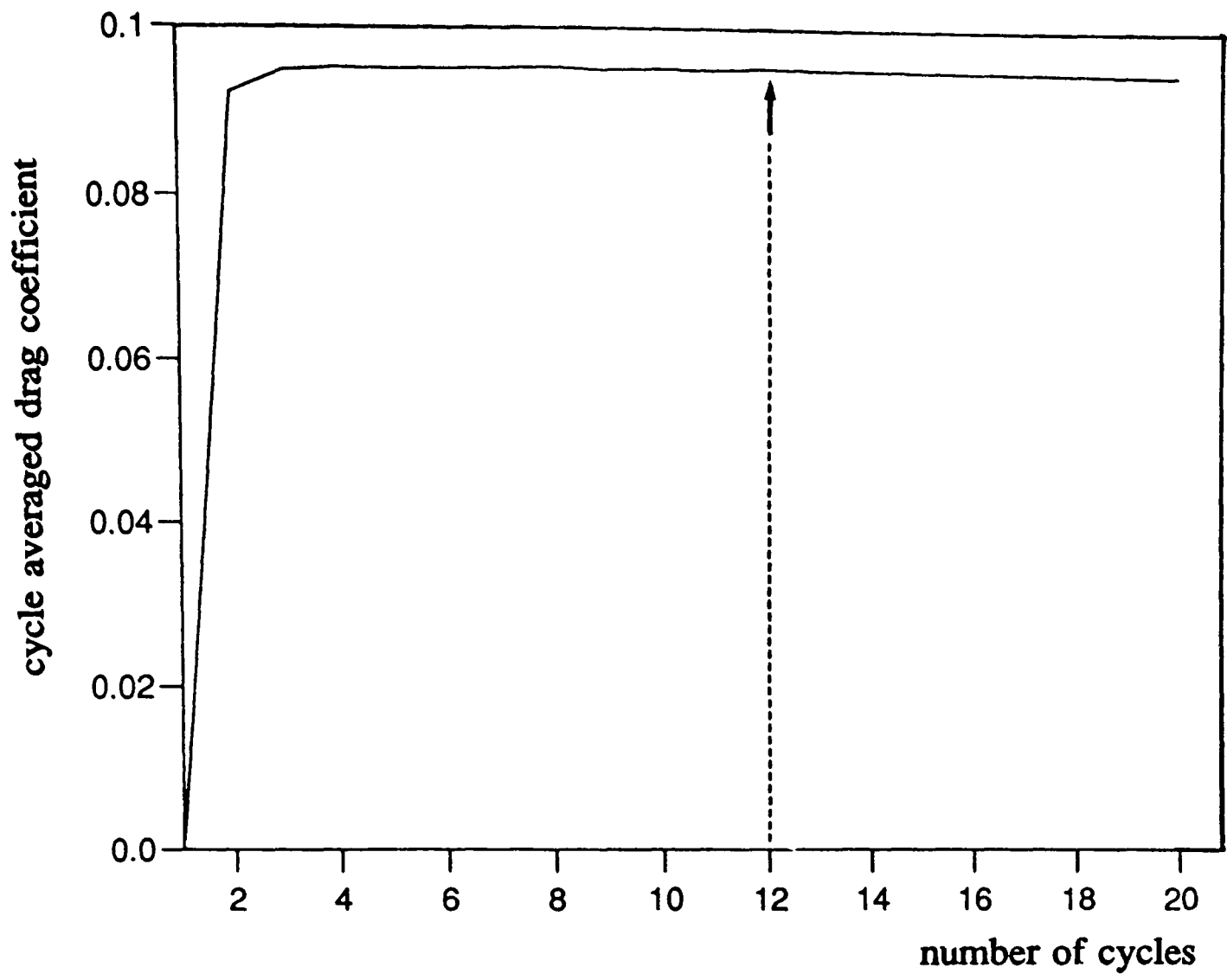


Figure 3.14

Some results concerning (a) the effect of ripple steepness on output from the hydrodynamical model, and (b) the effect of both ripple steepness and d/λ on the motion of the growing vortex.

Figure 3.15 Variation in (normalised) velocity at the crest through a complete cycle for $h/\lambda = 0.13, 0.15$ and 0.17 . ($d/\lambda = 1.42$).

Figure 3.16 Variation in (non-dimensional) vortex strength during the lifespan of a vortex, for $h/\lambda = 0.13, 0.15$ and 0.17 . ($d/\lambda = 1.42$).

Figure 3.17 Variation (in degrees of phase) of the time of ejection of the growing vortex with d/λ for four steepnesses: $h/\lambda = 0.13, 0.15, 0.17$ and 0.19 .

Figure 3.18 Variation (in degrees of phase) of the passage time of the ejected vortex over the parent crest with d/λ , for four steepness: $h/\lambda = 0.13, 0.15, 0.17$ and 0.19 .

Figure 3.19 Variation of the position of the growing vortex's centre on ejection with d/λ , for four ripple steepnesses: $h/\lambda = 0.13, 0.15, 0.17$ and 0.19 .

Figure 3.20 The motion of the growing vortex's centre from conception to ejection for $d/\lambda = 2.0, 2.2$ and $h/\lambda = 0.19$.

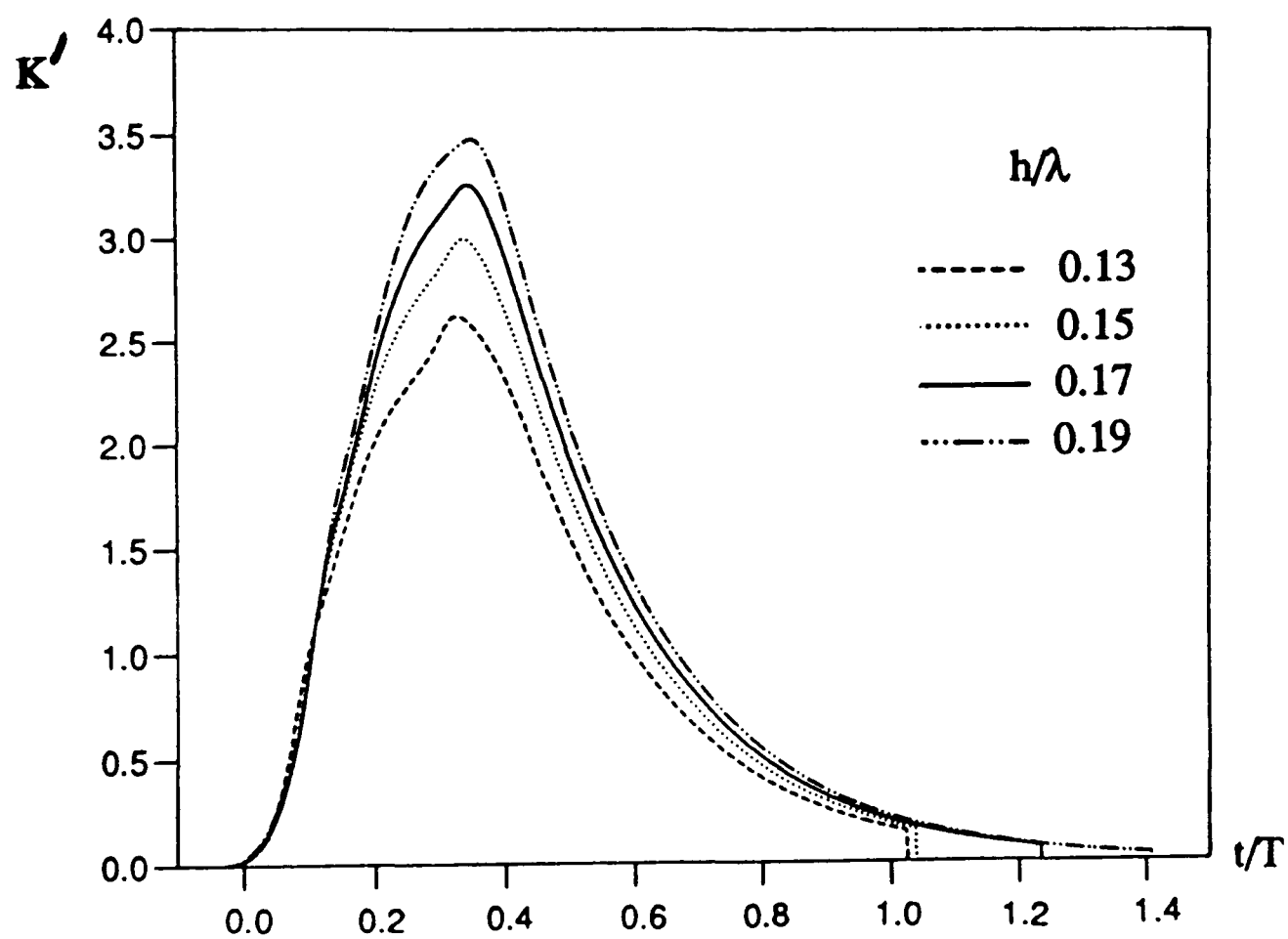
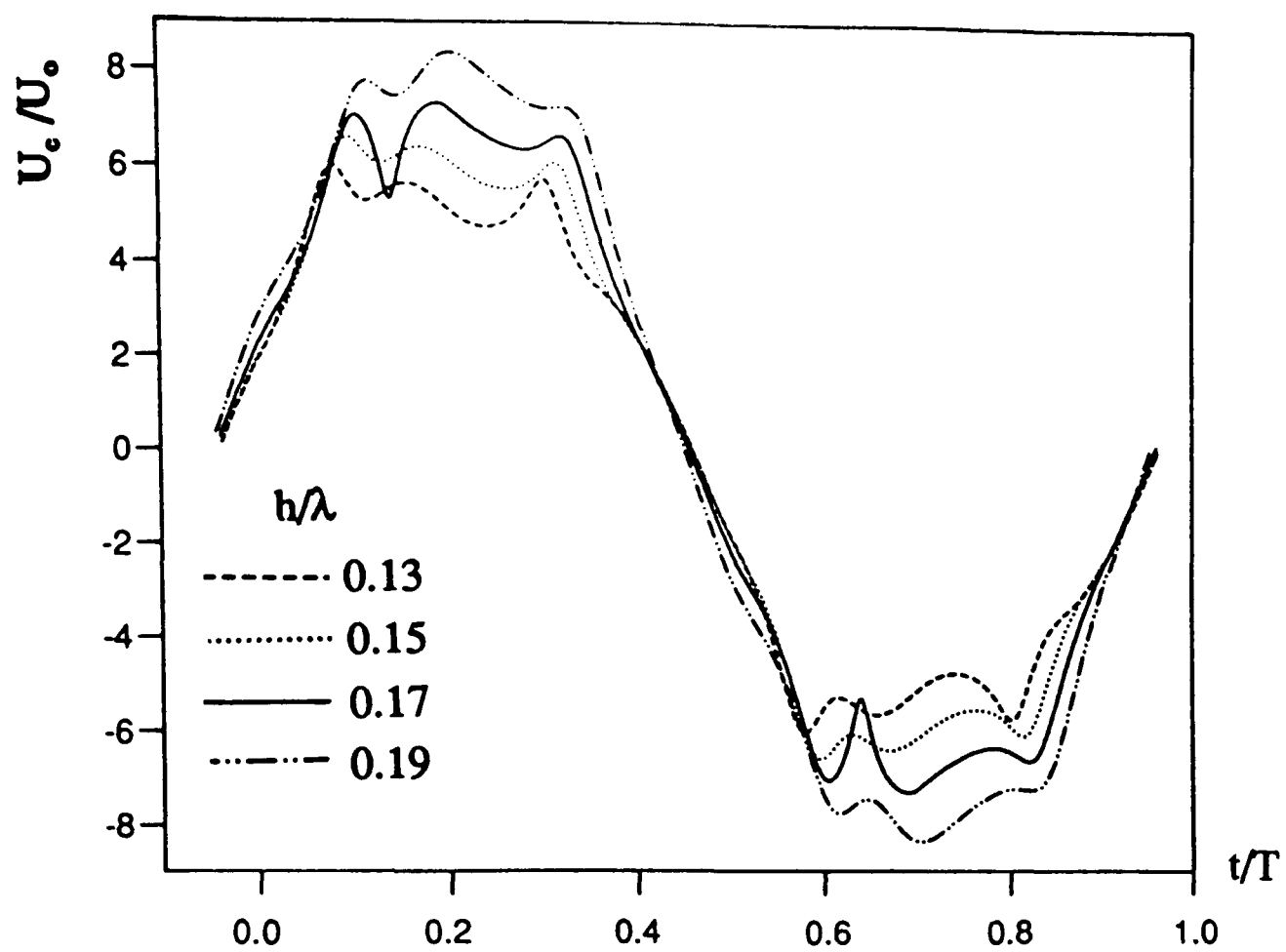


Figure 3.16

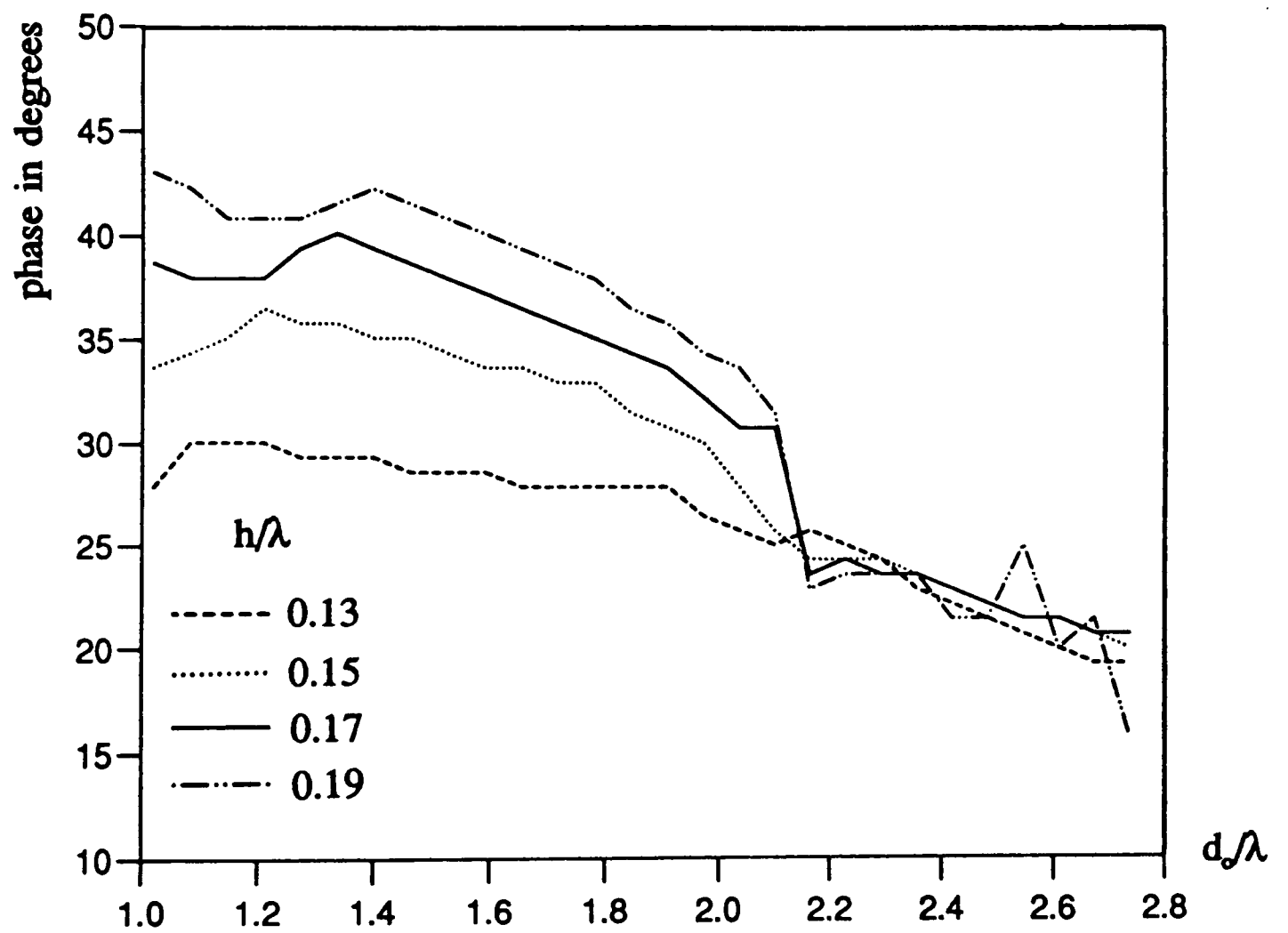
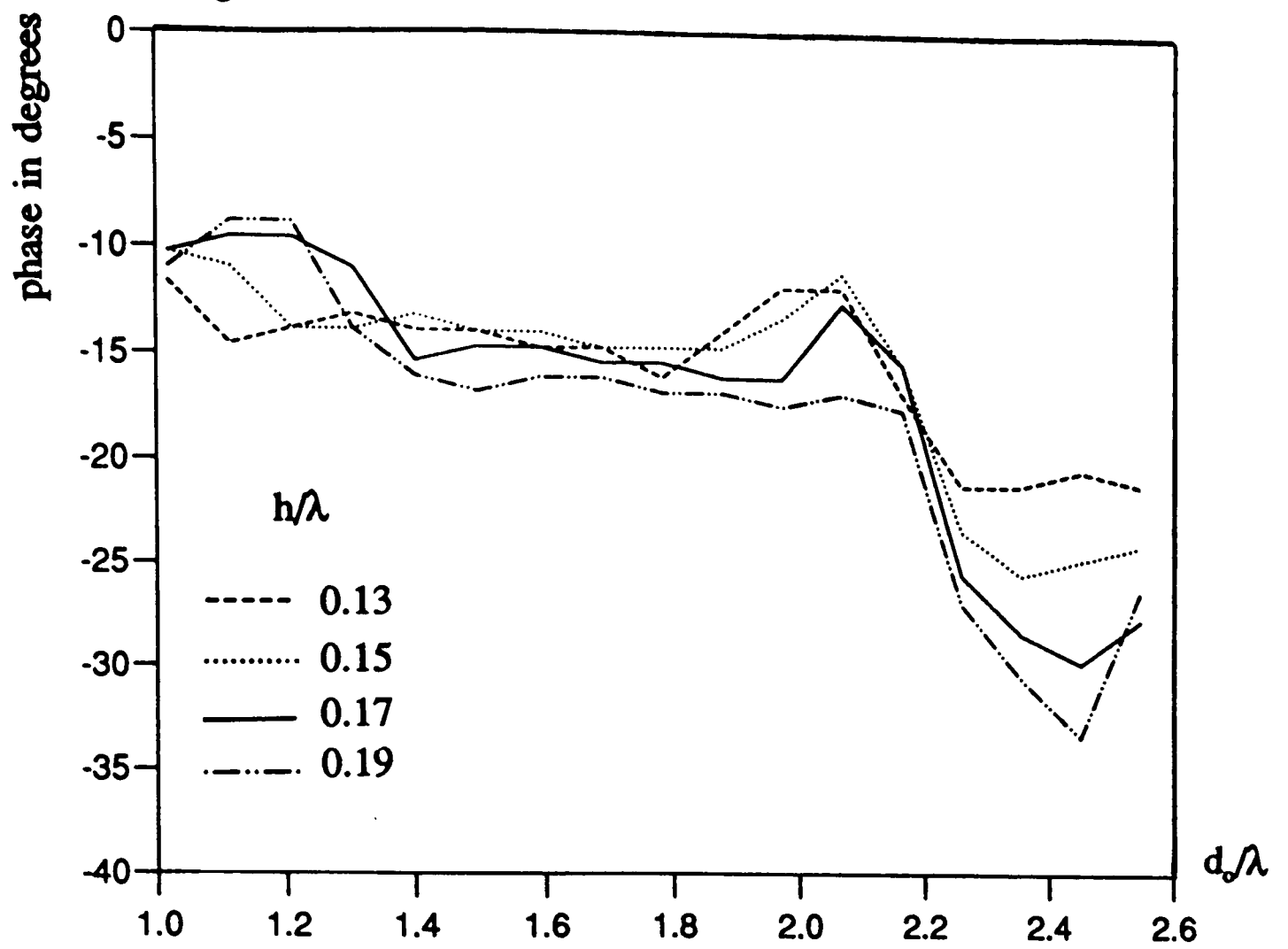


Figure 3.18

Figure 3.19

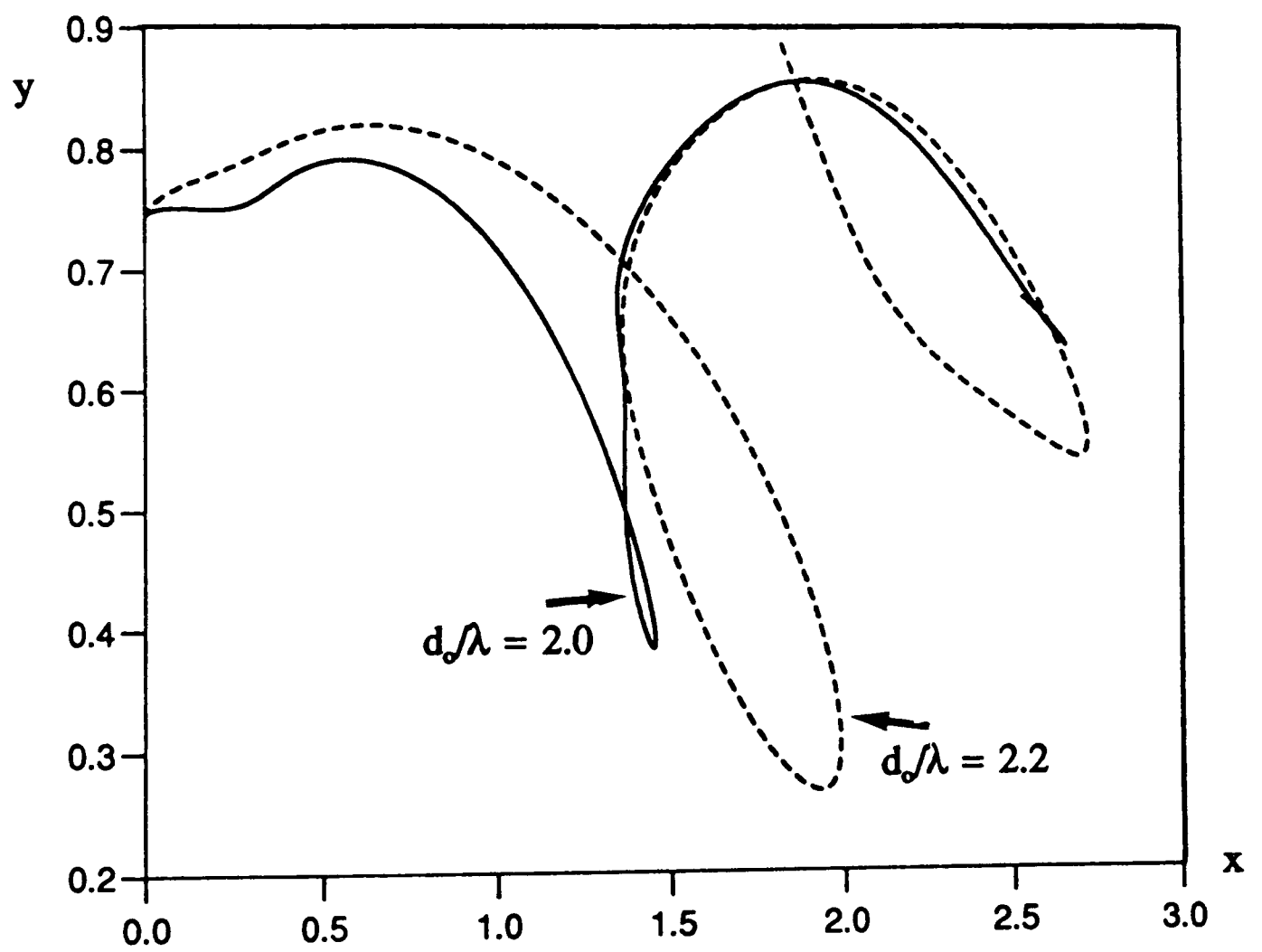
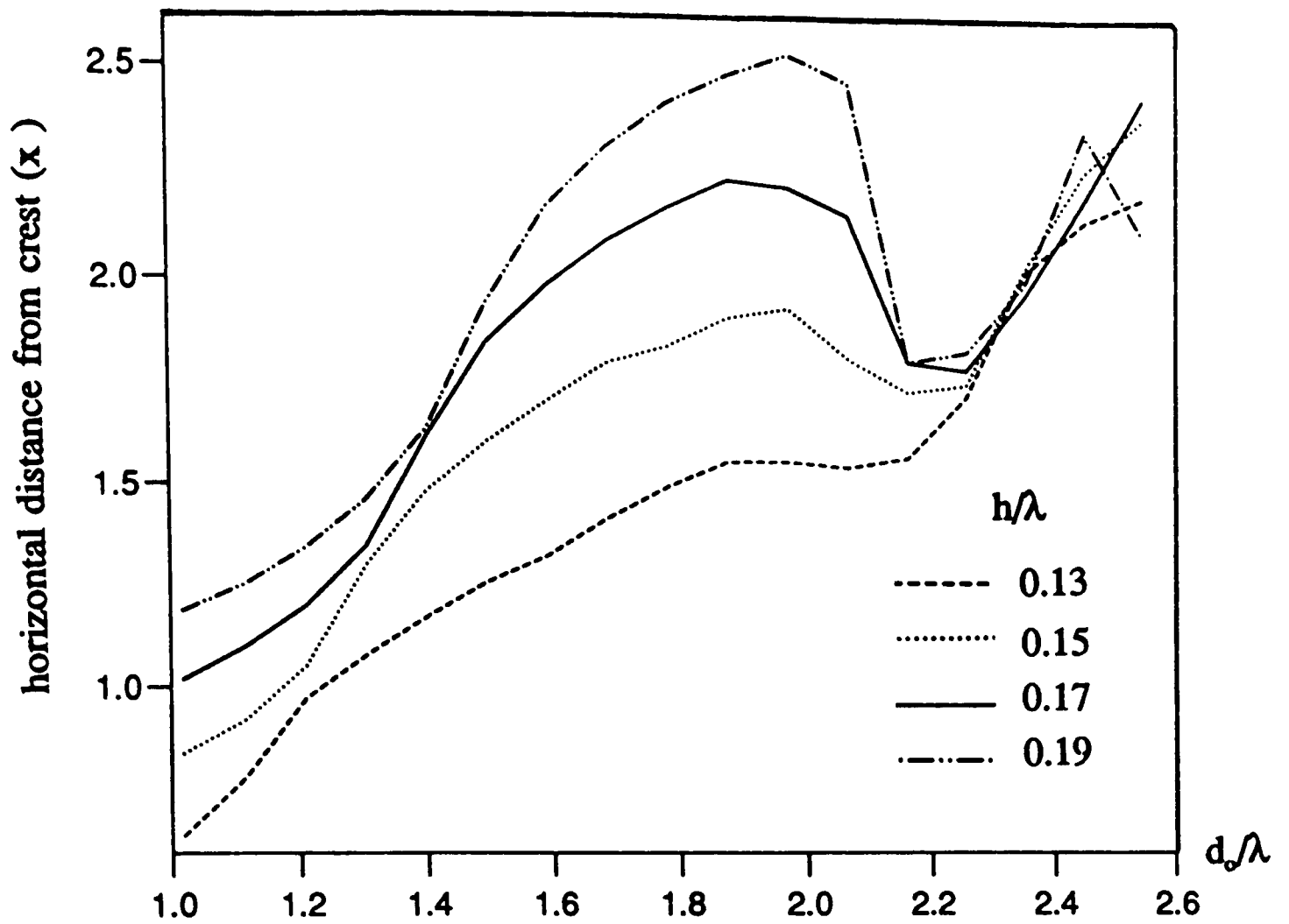


Figure 3.20

Results for the so-called 'central settings' of $d_0/\lambda = 1.42$, $h/\lambda = 0.17$.

Figure 3.21 Vortex positions in the first half cycle. (Central settings.) (G = growing vortex, E = ejected vortex, R = relic vortex.)

Figure 3.22(a) Variation of the (normalised) crest velocity for a complete cycle. (Central settings.)

Figure 3.22(b) Variation of the (non-dimensional) vortex strength for a vortex's lifespan. (Central settings.)

Figure 3.22(c) The trail of a vortex, from conception to destruction. (Central settings.)

Figure 3.23 (a)-(j) Streamline diagrams for the first half cycle. (Central settings.)

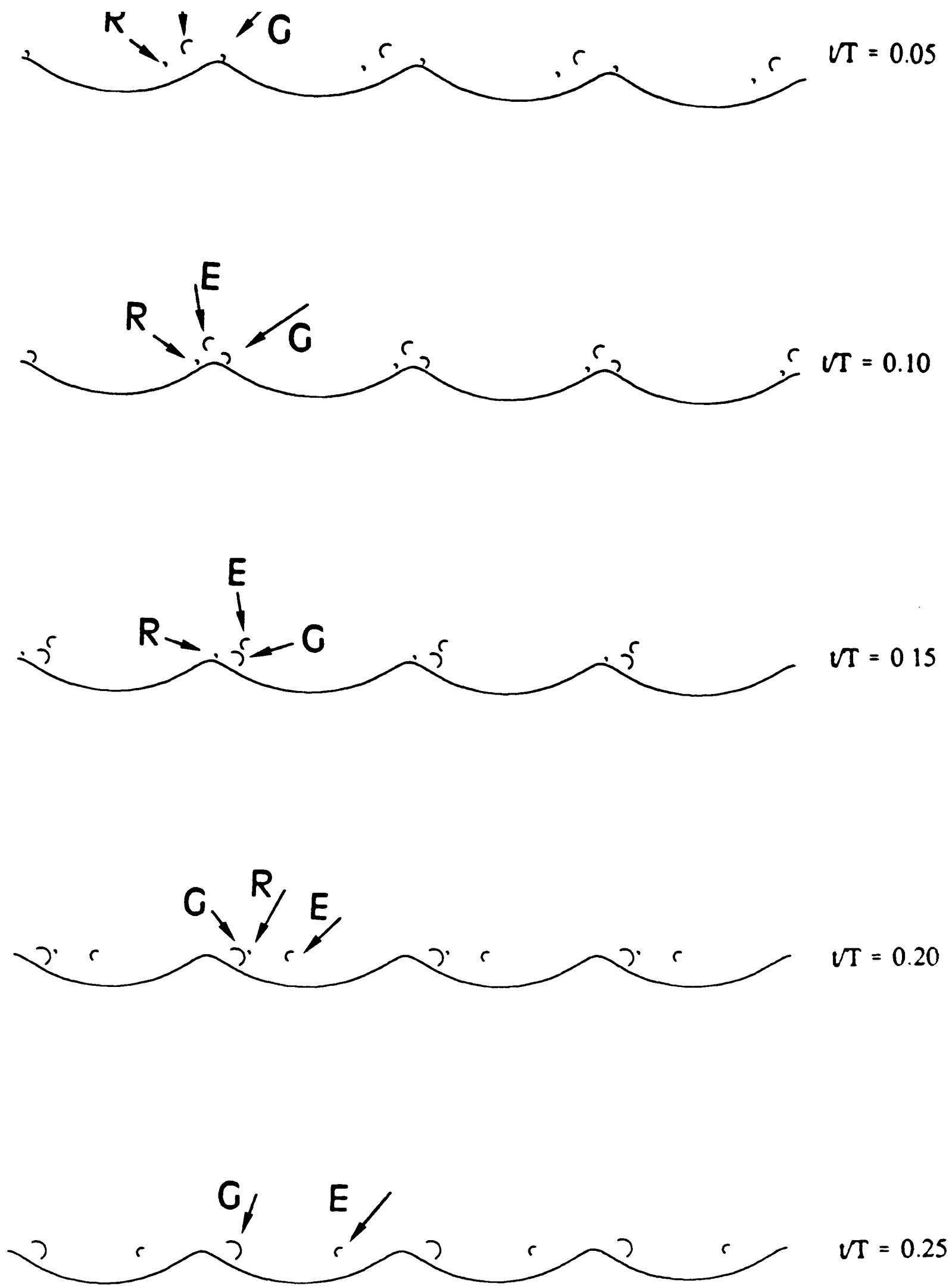


Figure 3.21

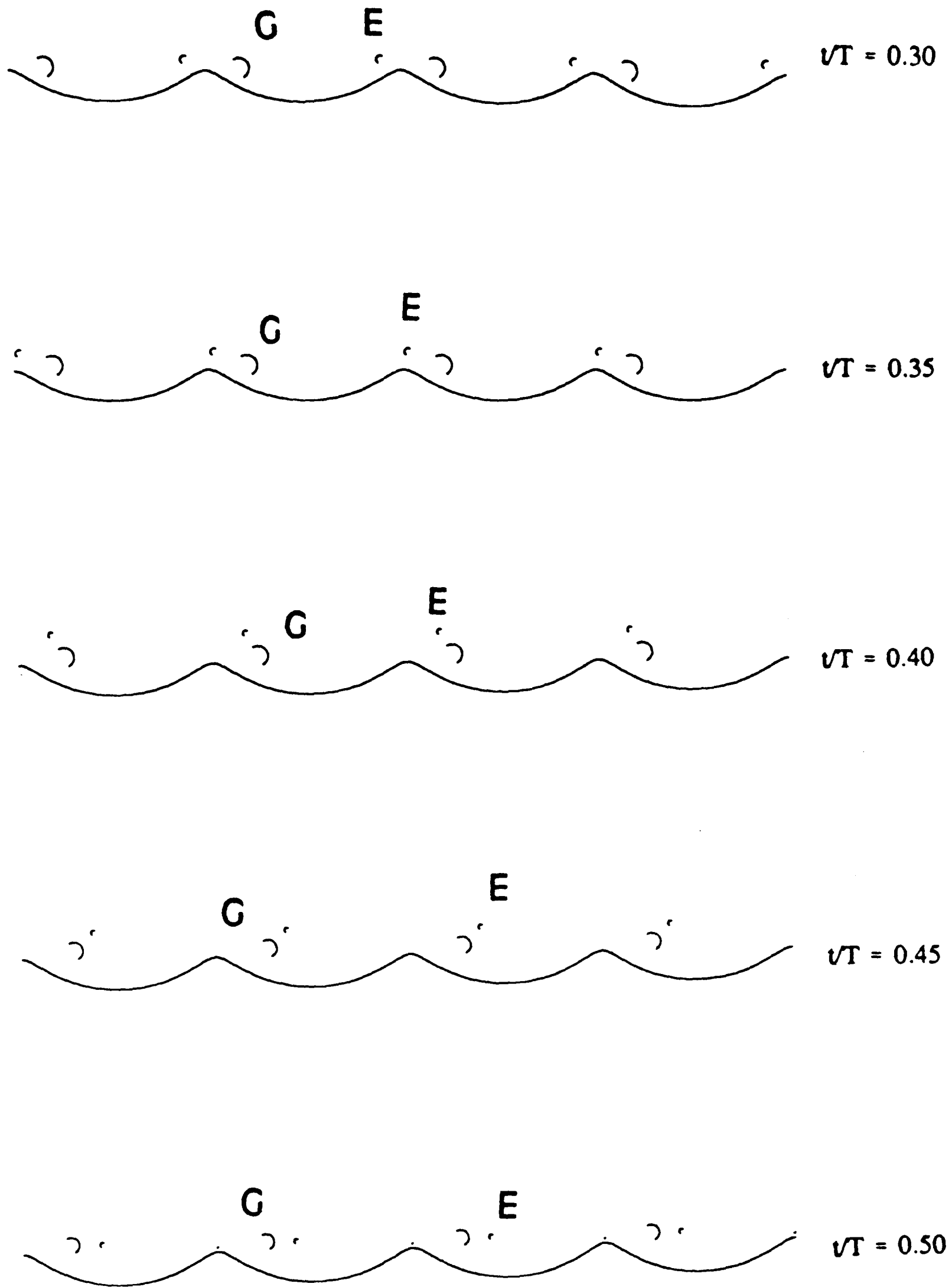


Figure 3.21

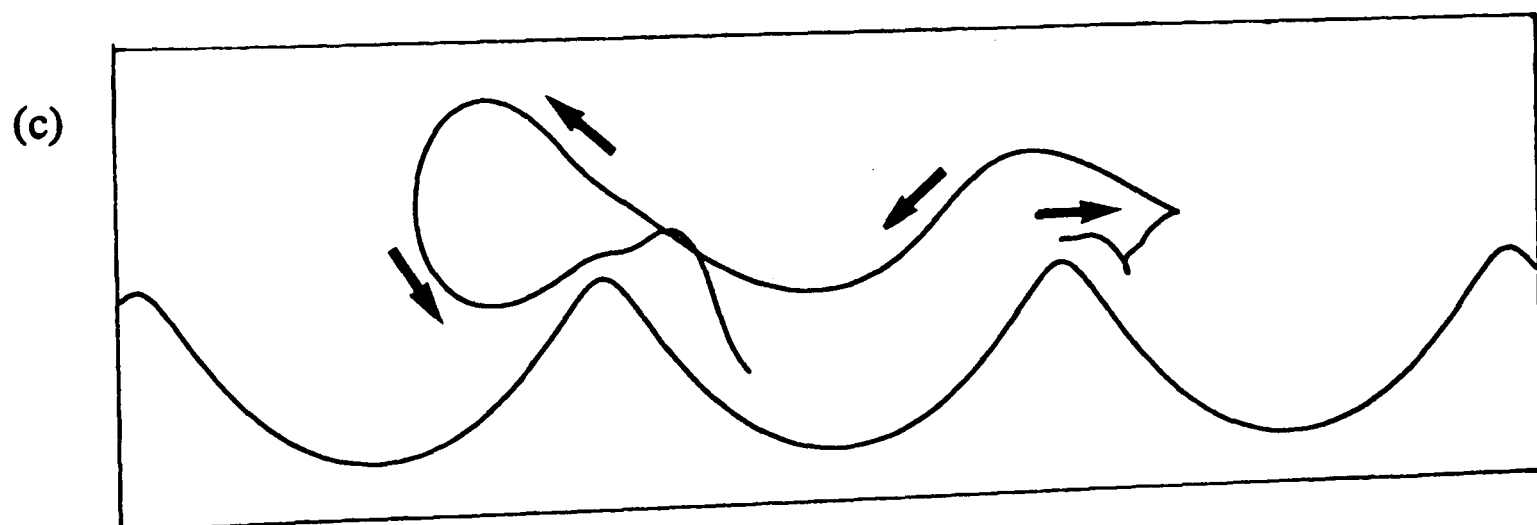
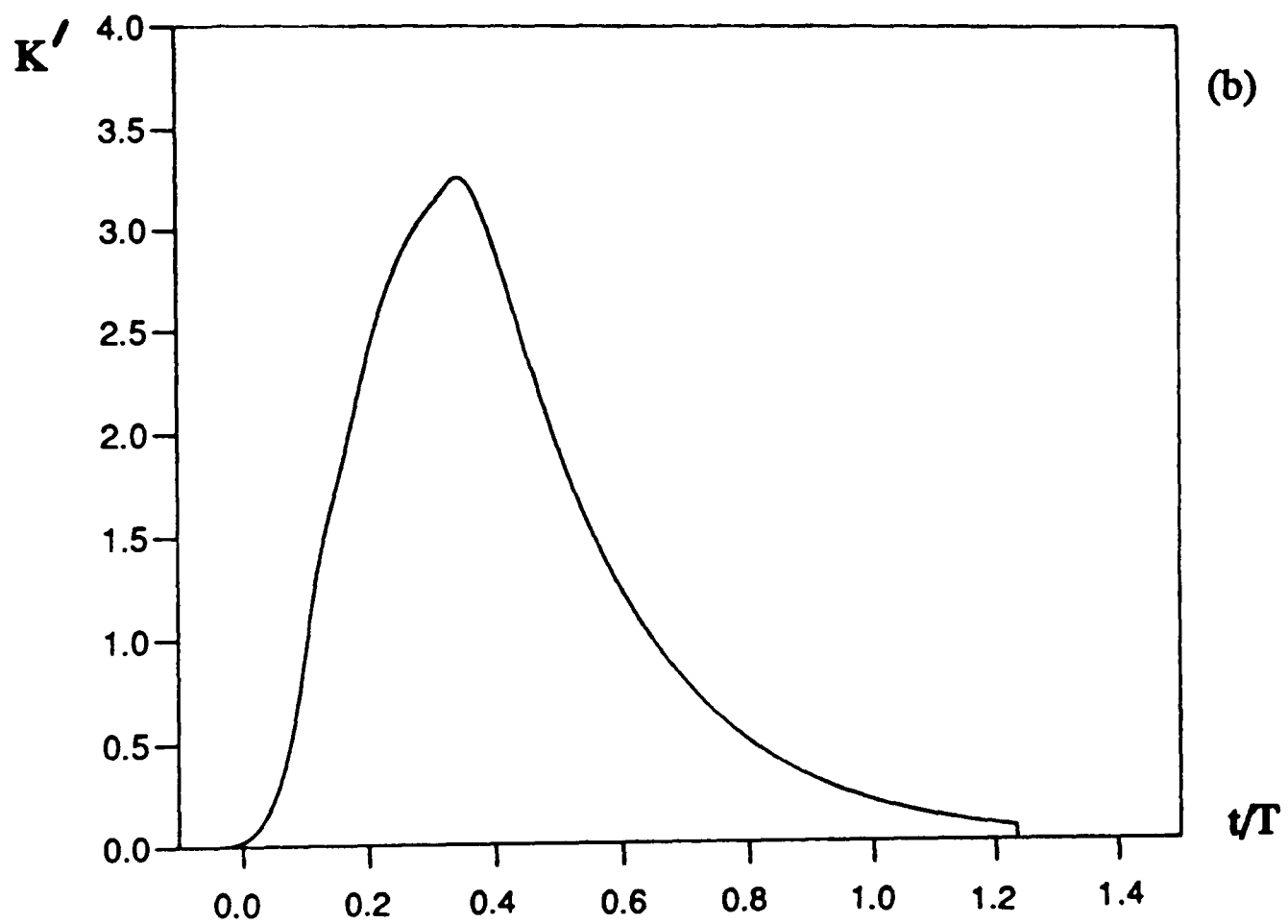
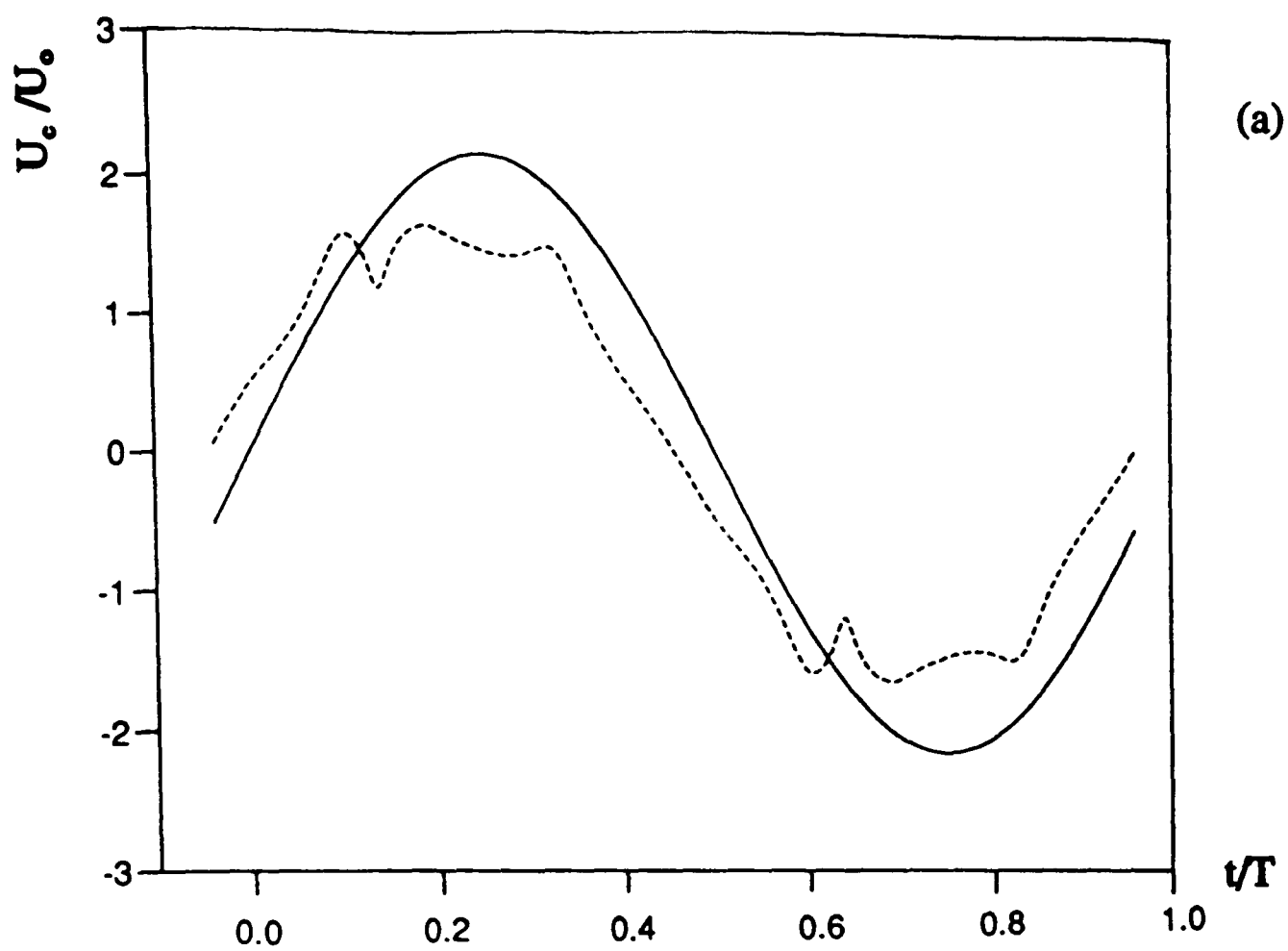


Figure 3.22
(a)-(c)

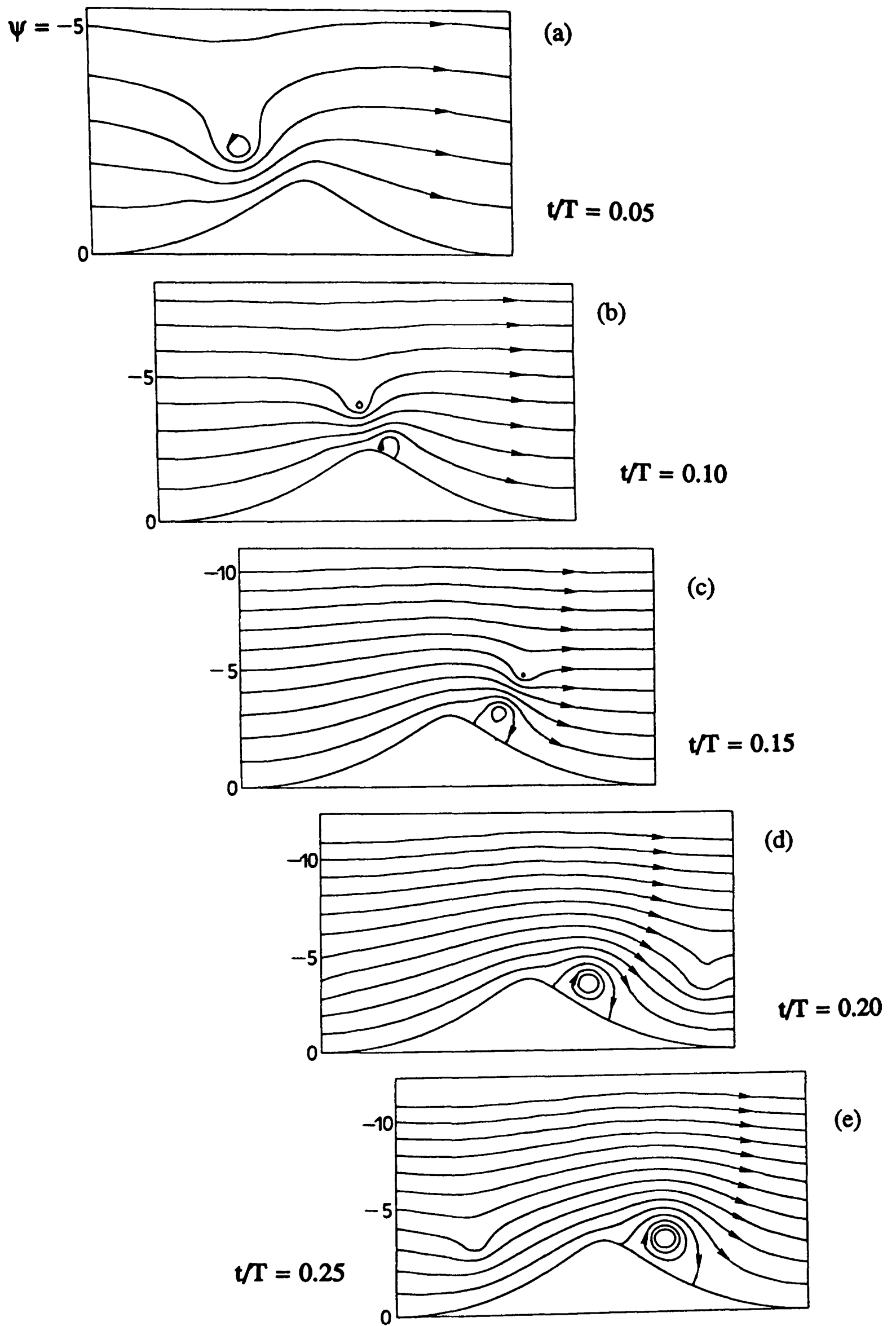


Figure 3.23 (a)-(e)

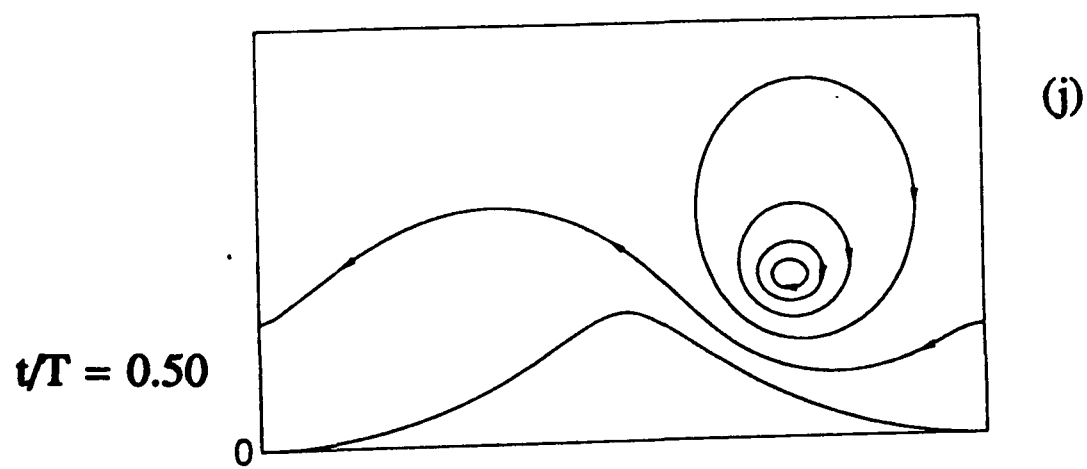
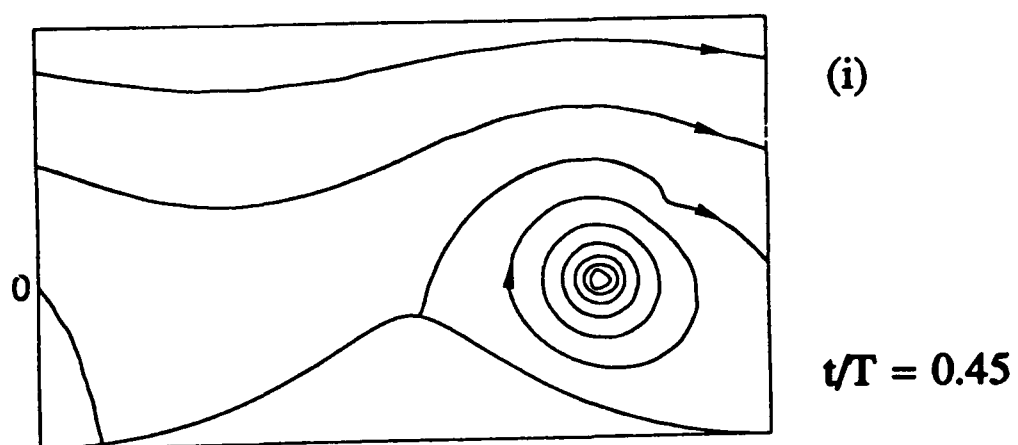
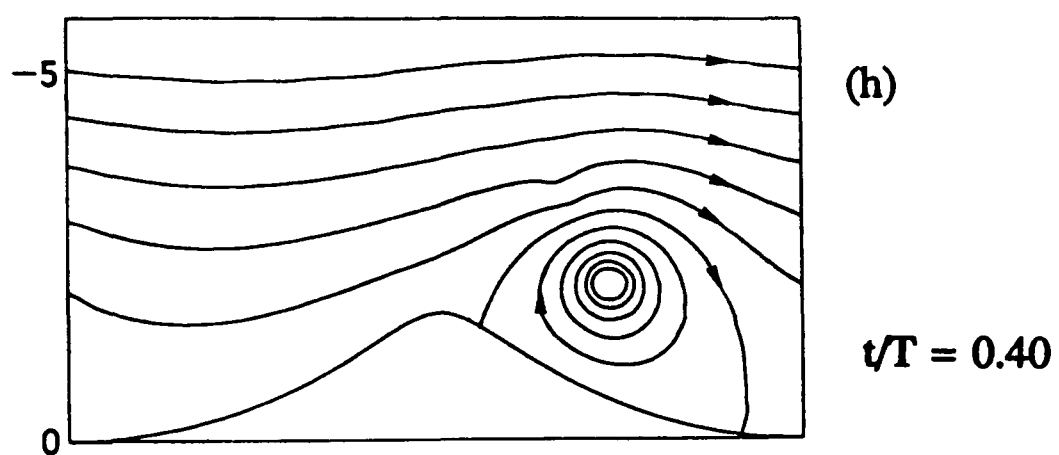
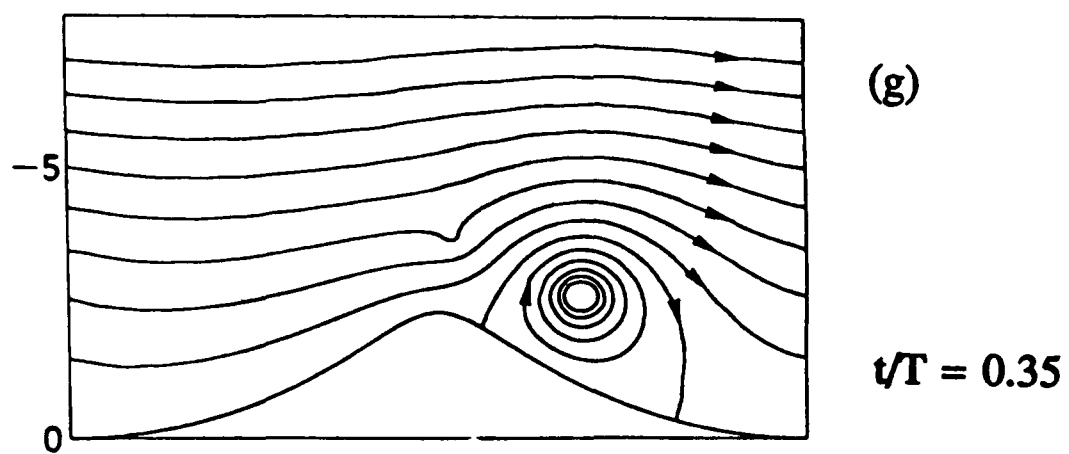
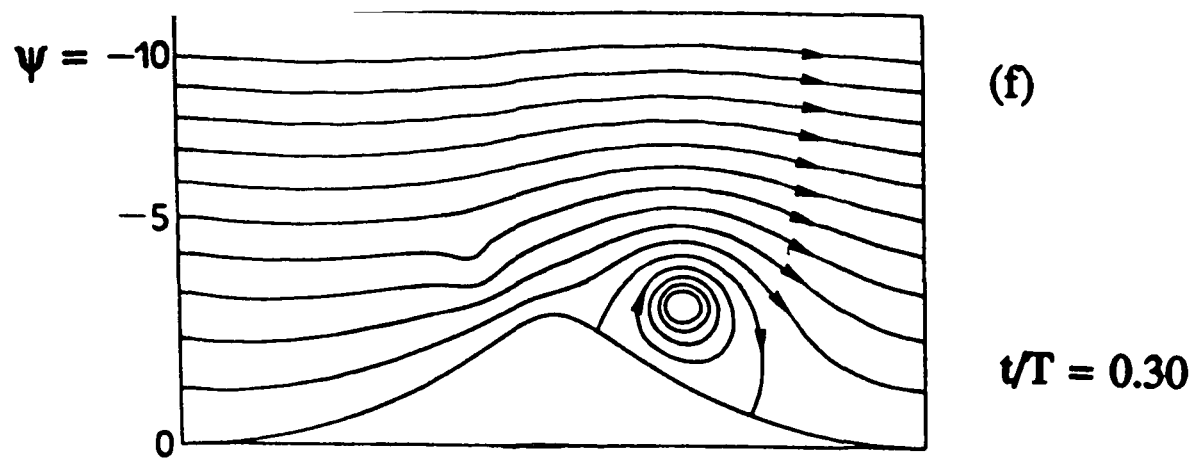


Figure 3.23 (f)-(j)

The results of sensitivity tests carried out on four of the parameters from the model: the position of ζ_T , the value chosen for the kinematic viscosity ν , the rate at which vortex strength is decayed and the manner in which it is decayed.

Figure 3.24 (a)-(c) A series of sensitivity tests, assessing the effect of varying the value of ζ_T (the point at which vorticity input is calculated and introduced) on (a) the (normalised) crest velocity for a complete cycle, (b) the (non-dimensional) vortex strength during the vortex's lifespan and (c) the trail of a vortex from conception to destruction.

Figure 3.25 (a)-(c) Equivalent sensitivity tests concerning the kinematic viscosity ν .

Figure 3.26 (a)-(c) Equivalent sensitivity tests concerning the rate at which vortex strength is decayed per timestep.

Figure 3.27 (a)-(c) Equivalent sensitivity test concerning the manner in which vortex strength is decayed. 'Strong' means no decay until ejection of growing vortex; 'linear' means linear phasing in of decay during the growing phase; 'weak' means constant decay from the vortex's conception.

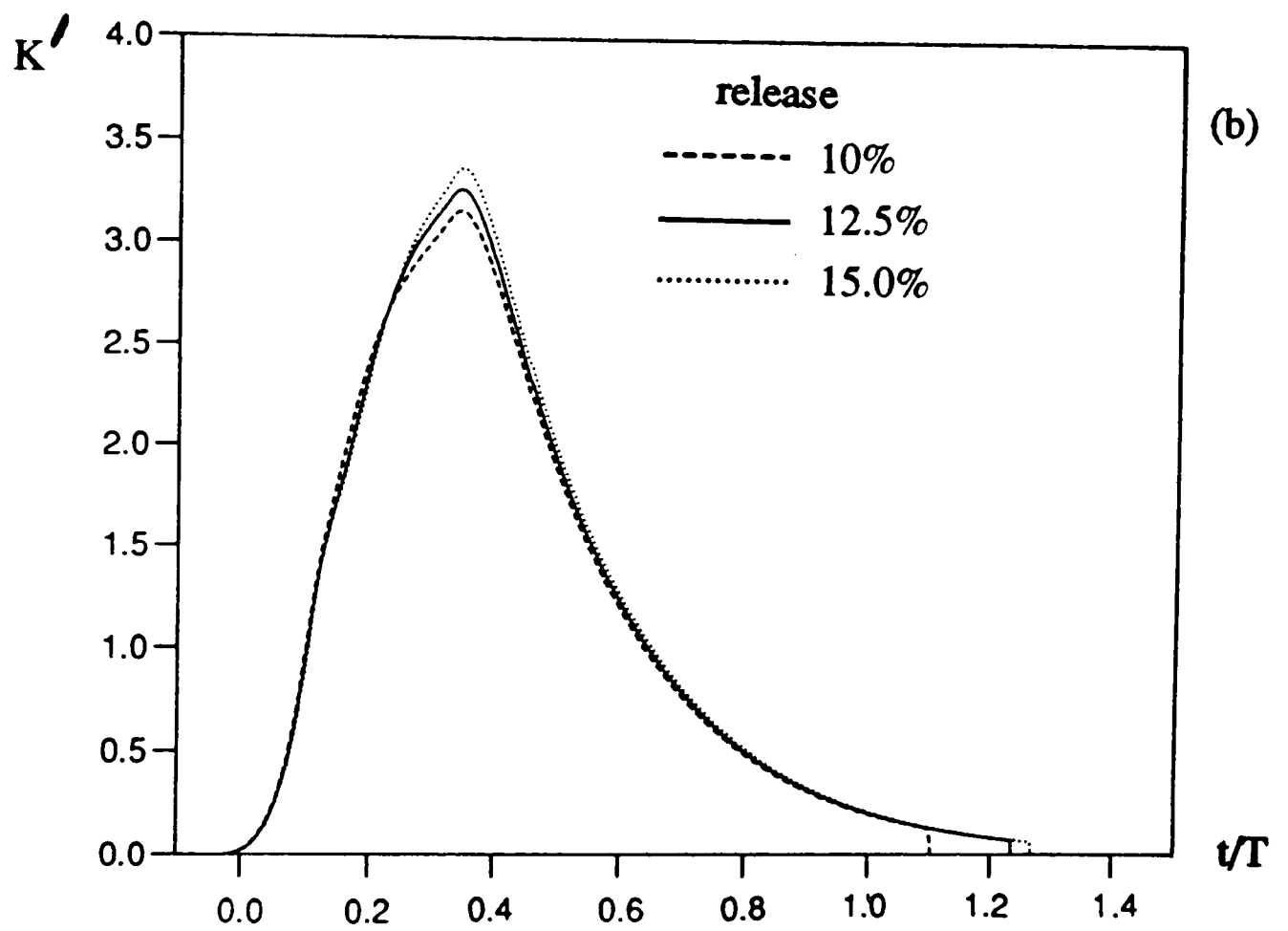
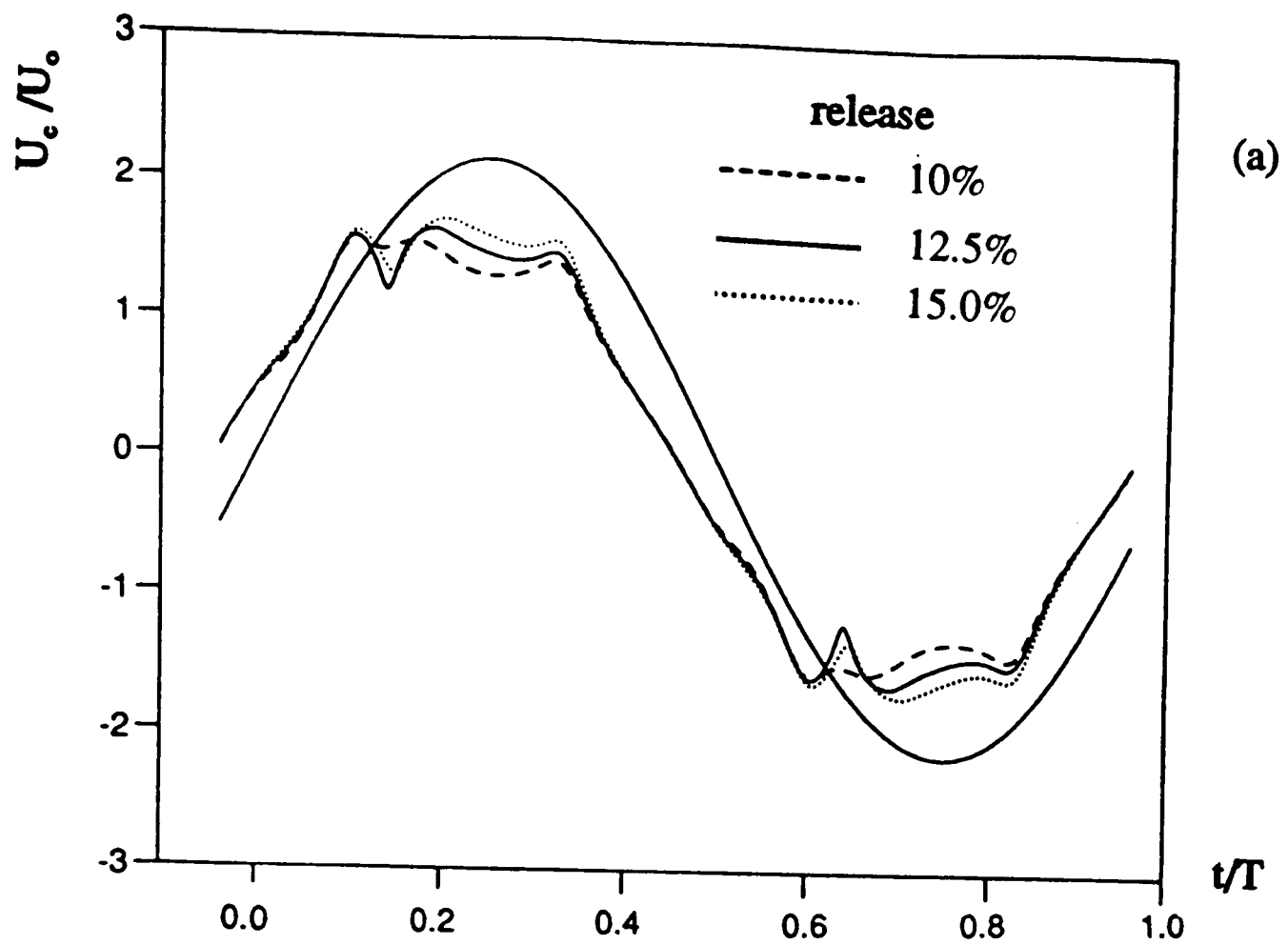
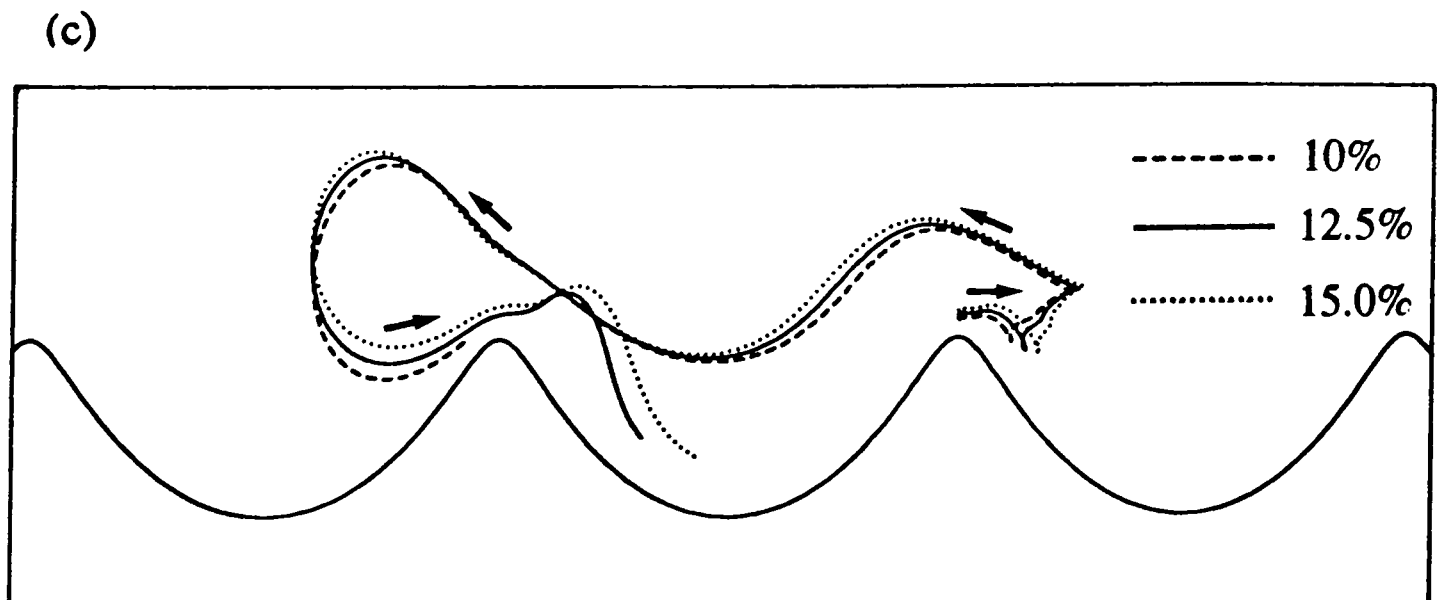


Figure 3.24
(a)-(c)



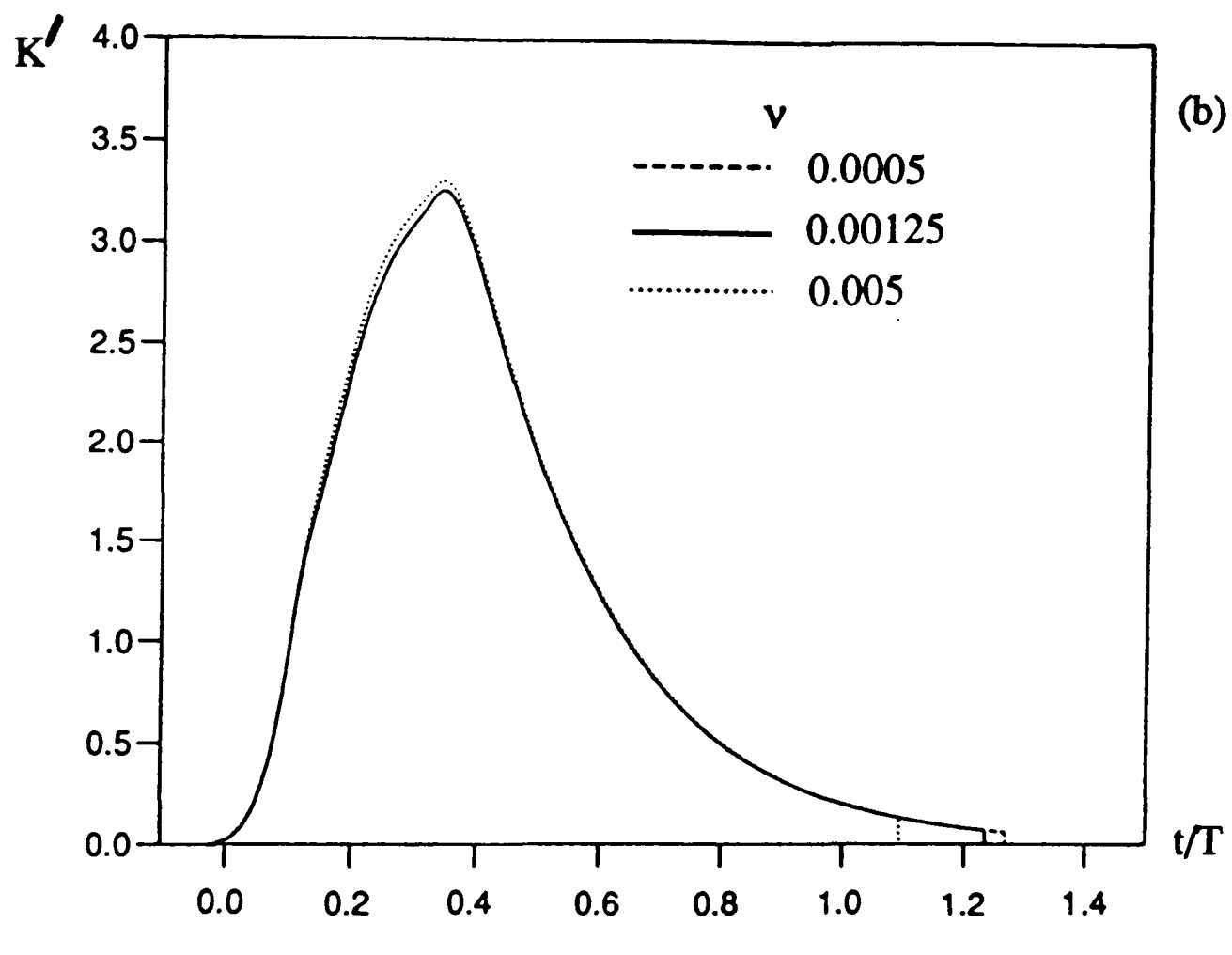
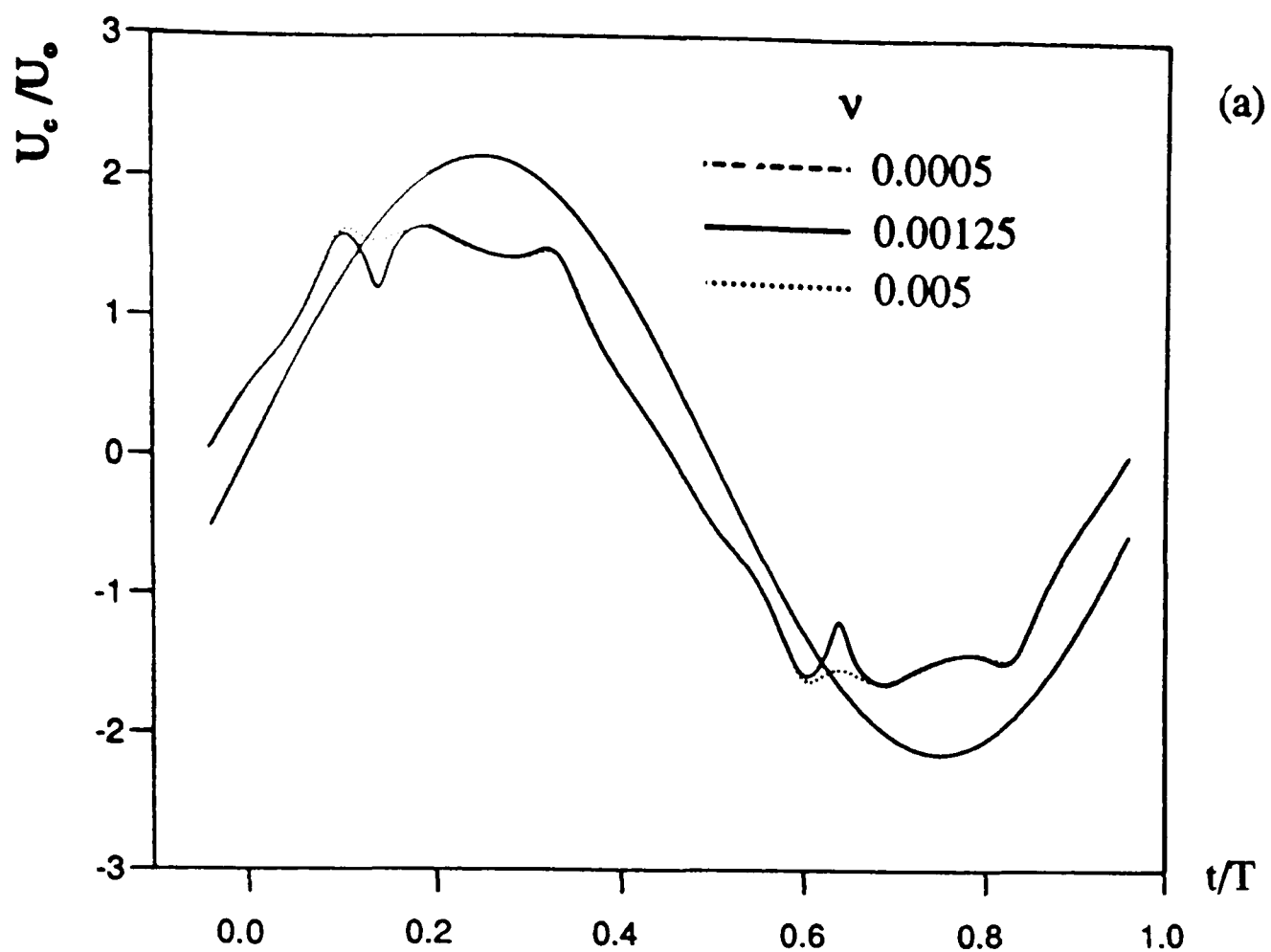
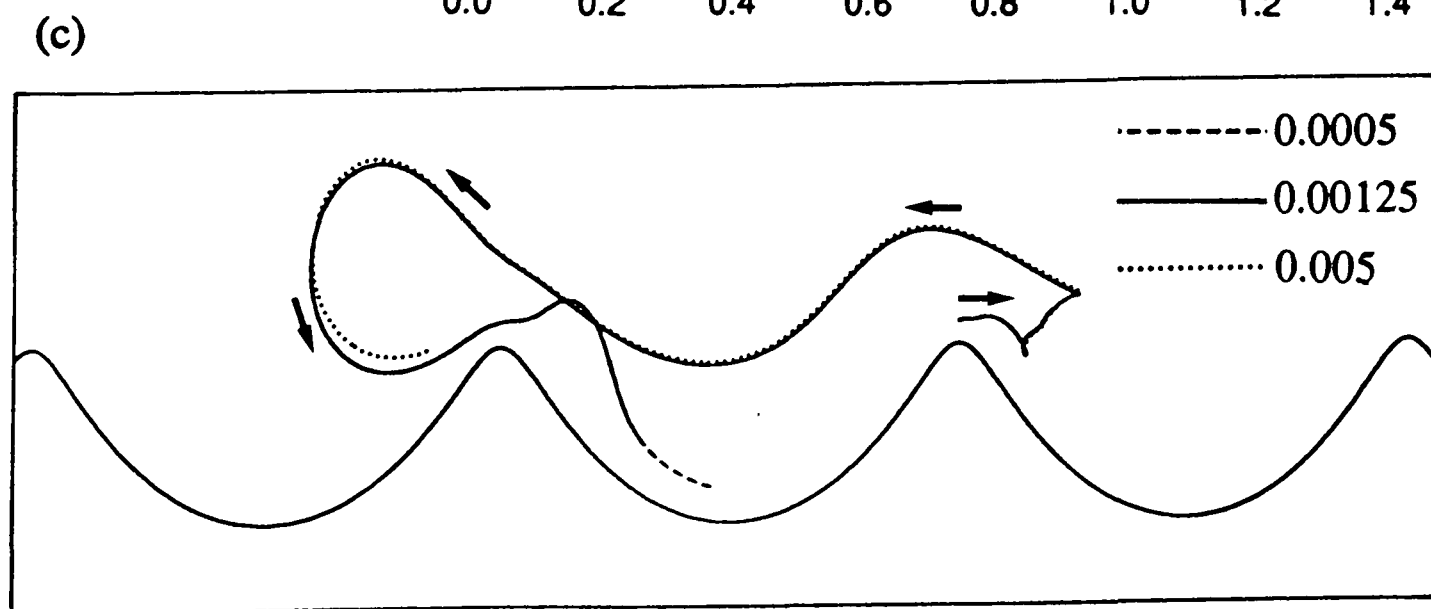
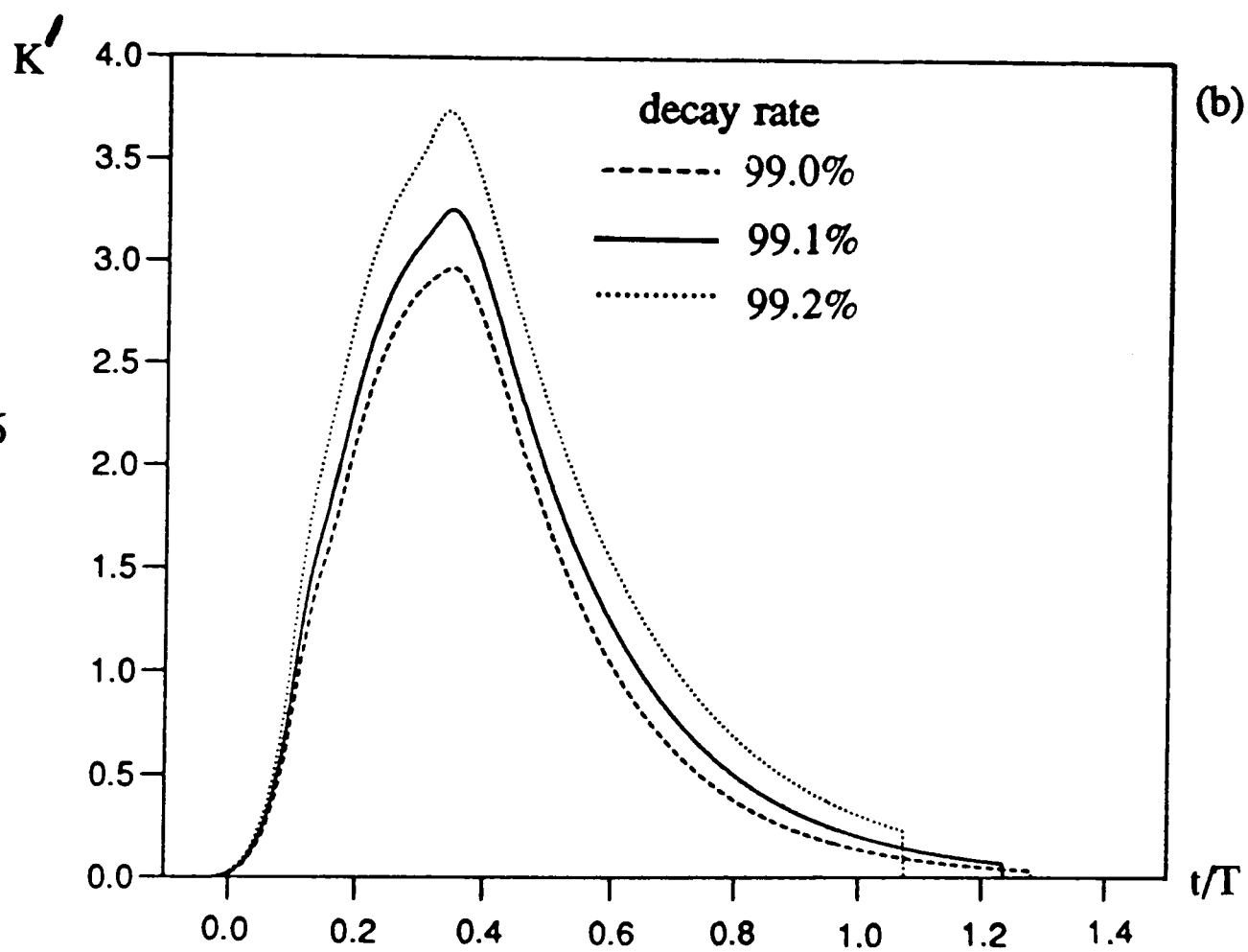
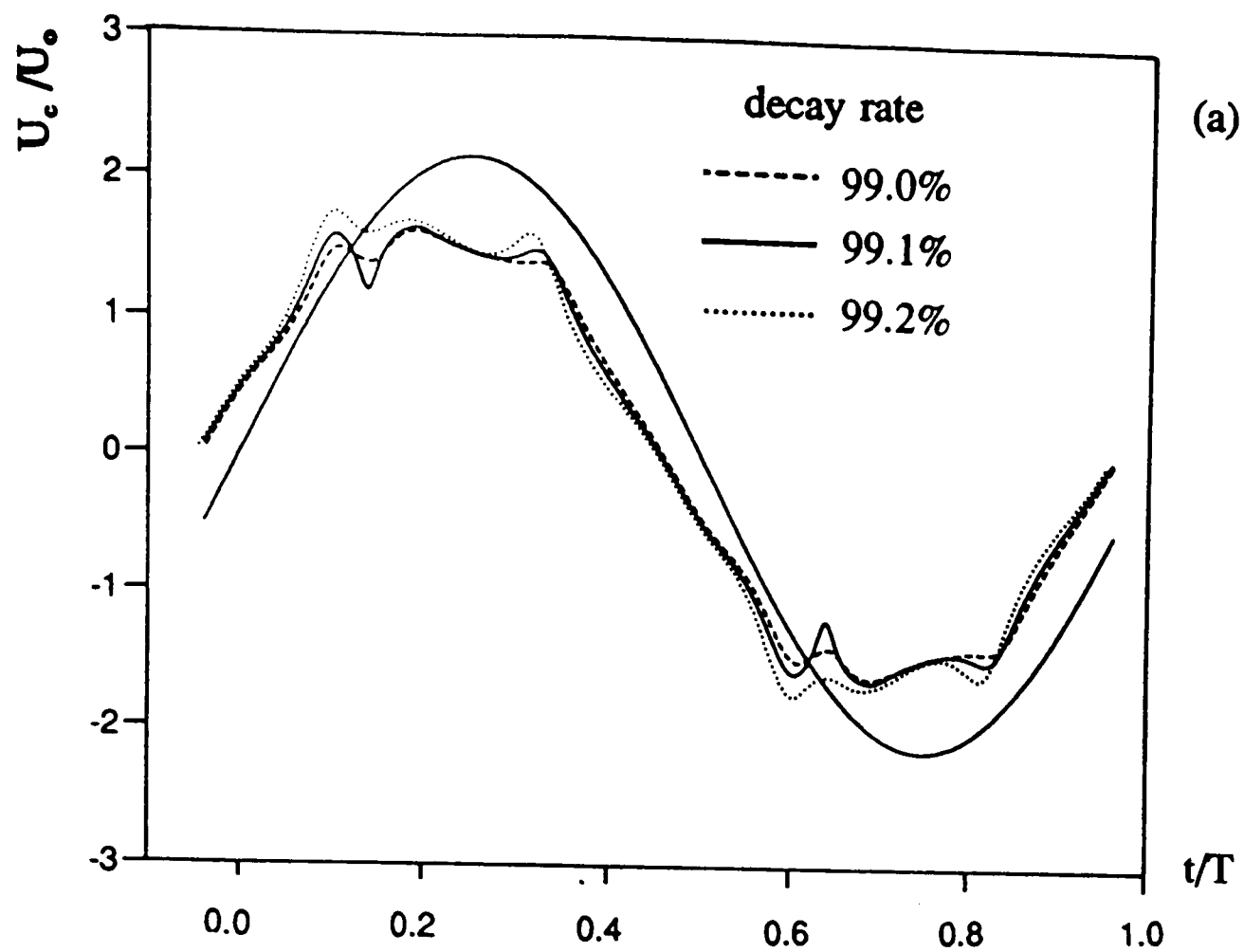


Figure 3.25
(a)-(c)





(c)

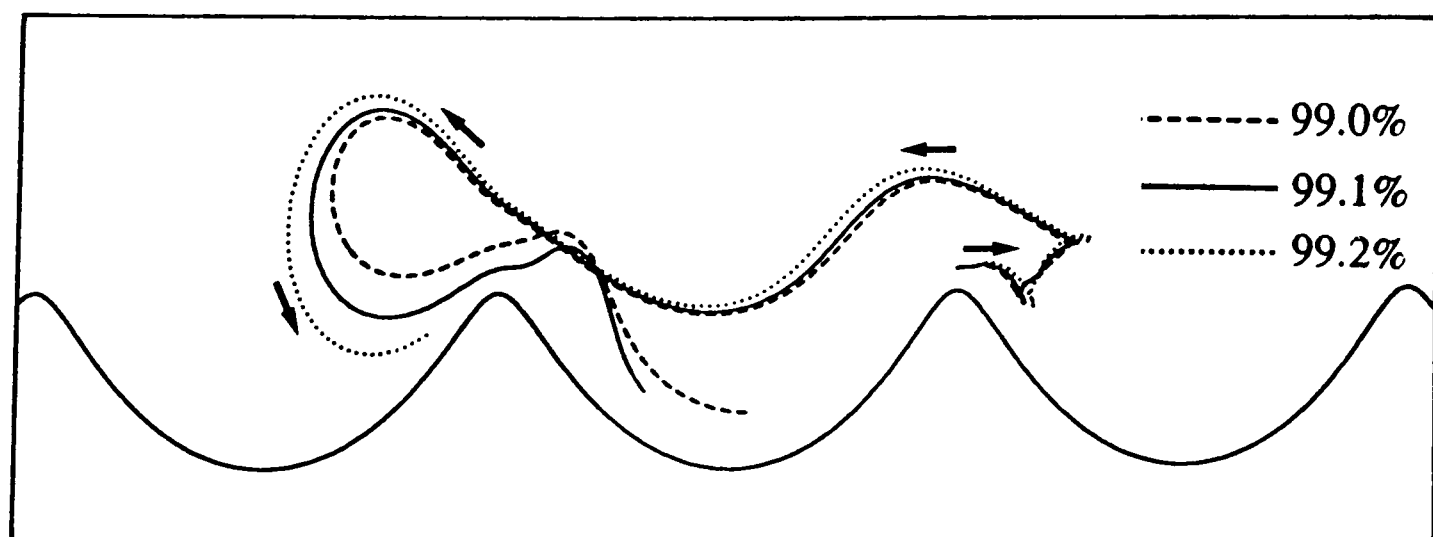


Figure 3.26
(a)-(c)

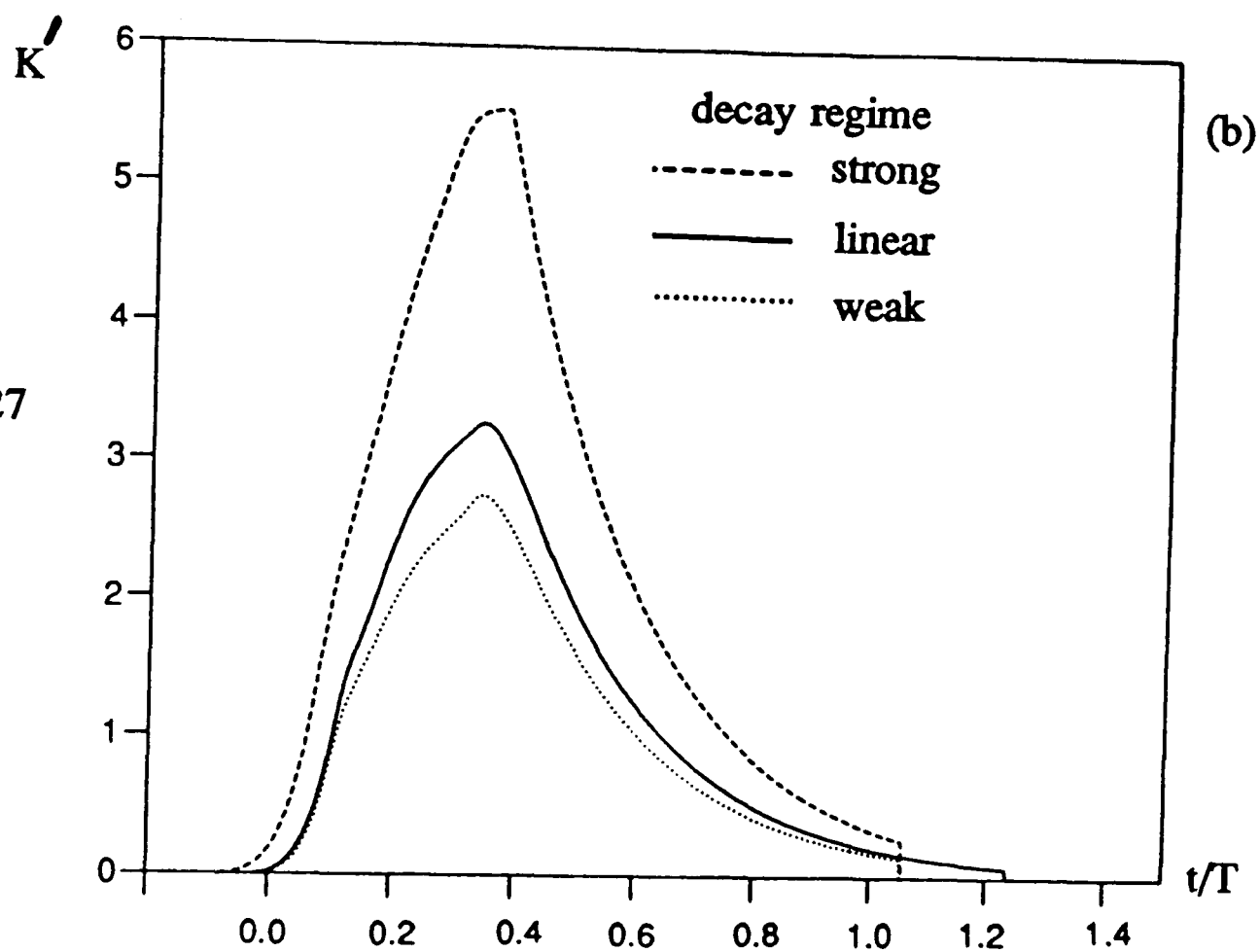
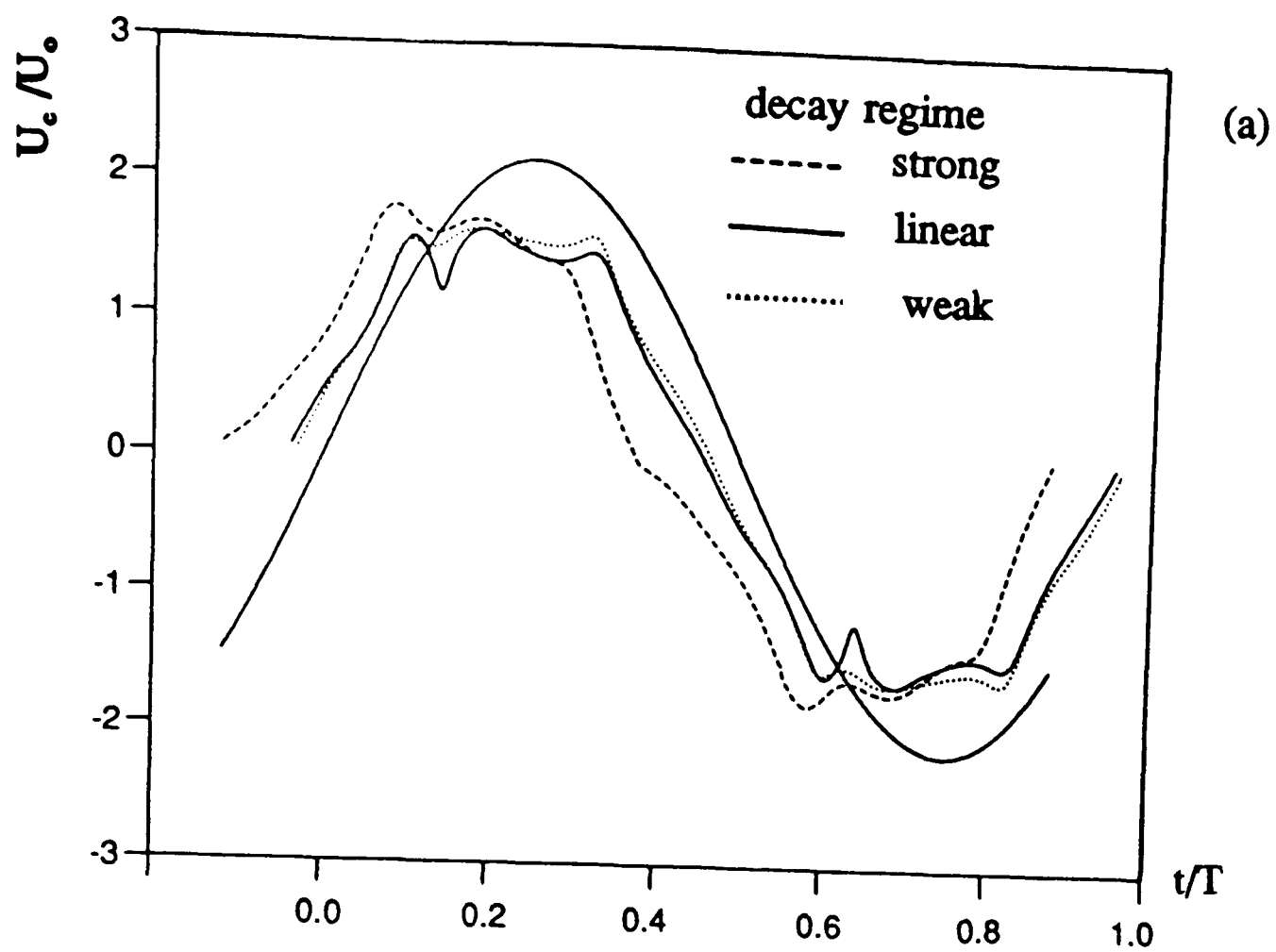
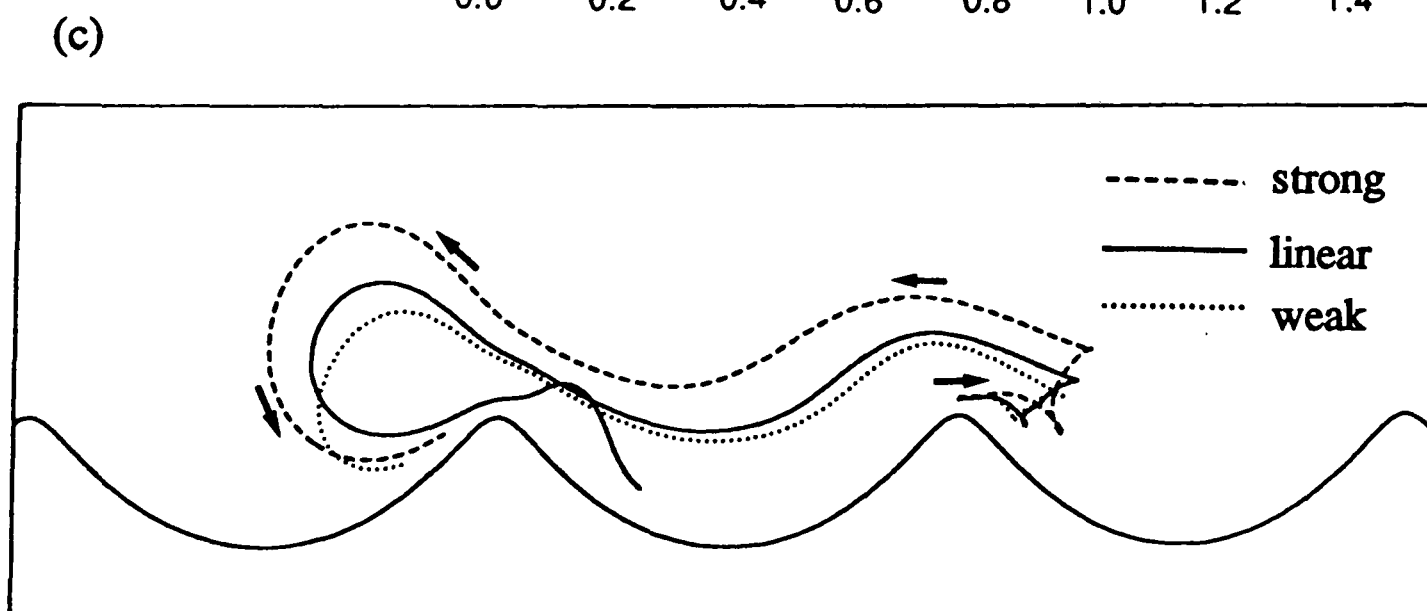


Figure 3.27
(a)-(c)



Results for $d_0/\lambda = 1.1$, $h/\lambda = 0.17$.

Figure 3.28 Vortex positions in the first half cycle. ($d_0/\lambda = 1.1$, $h/\lambda = 0.17$.) (G = growing vortex, E = ejected vortex, R = relic vortex.)

Figure 3.29 (a) Variation of the (normalised) crest velocity for a complete cycle. ($d_0/\lambda = 1.1$, $h/\lambda = 0.17$.)

Figure 3.29 (b) Variation in (non-dimensional) vortex strength during a vortex's lifespan. ($d_0/\lambda = 1.1$, $h/\lambda = 0.17$.)

Figure 3.29 (c) The trail of a vortex from conception to destruction. ($d_0/\lambda = 1.1$, $h/\lambda = 0.17$.)

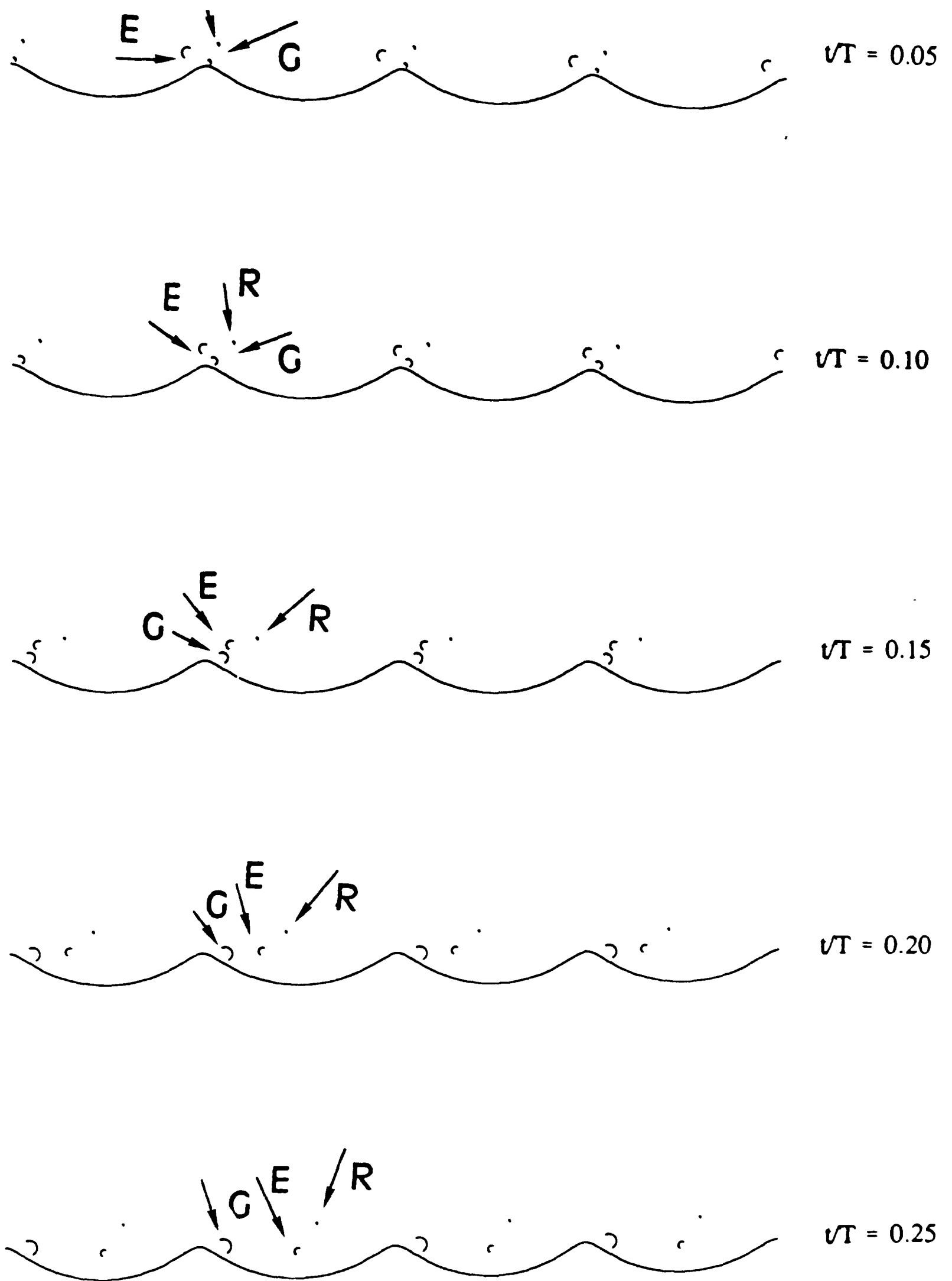


Figure 3.28

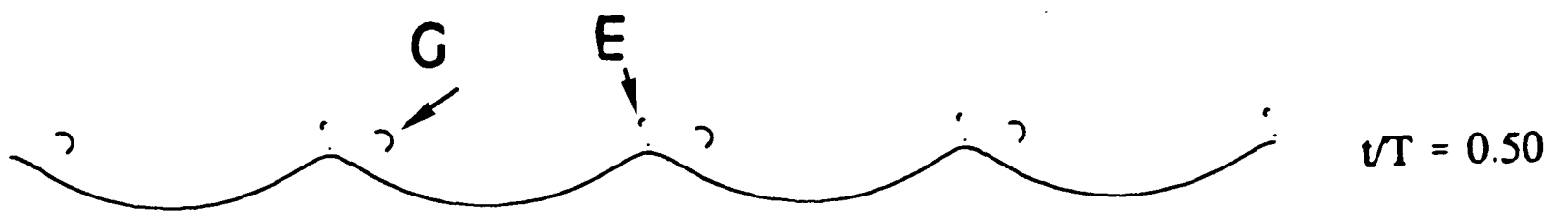
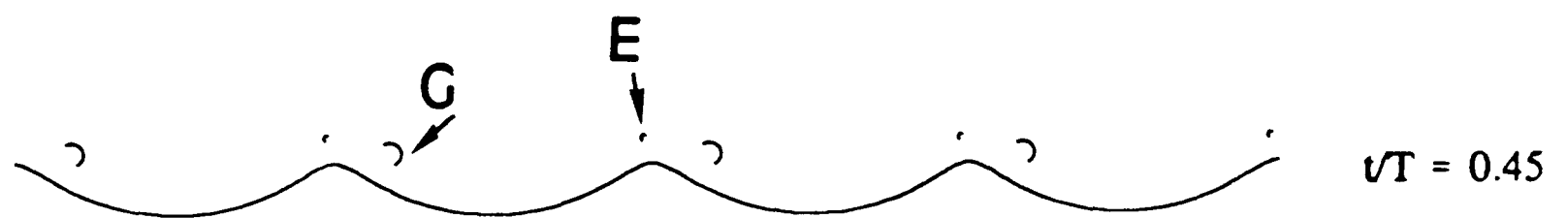
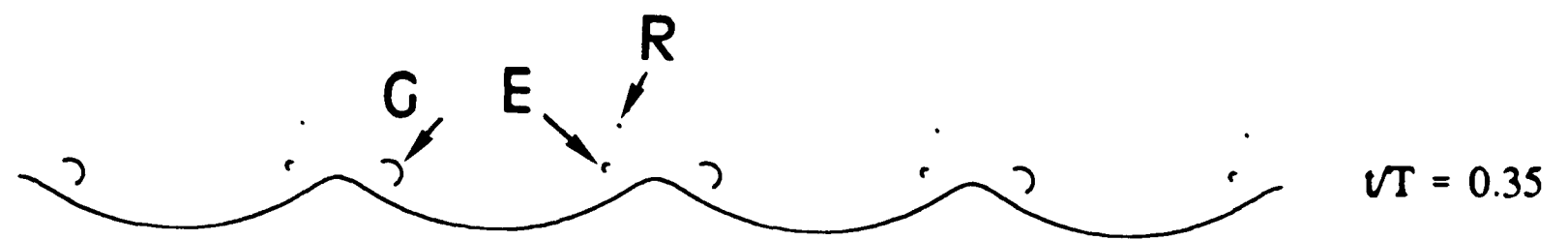
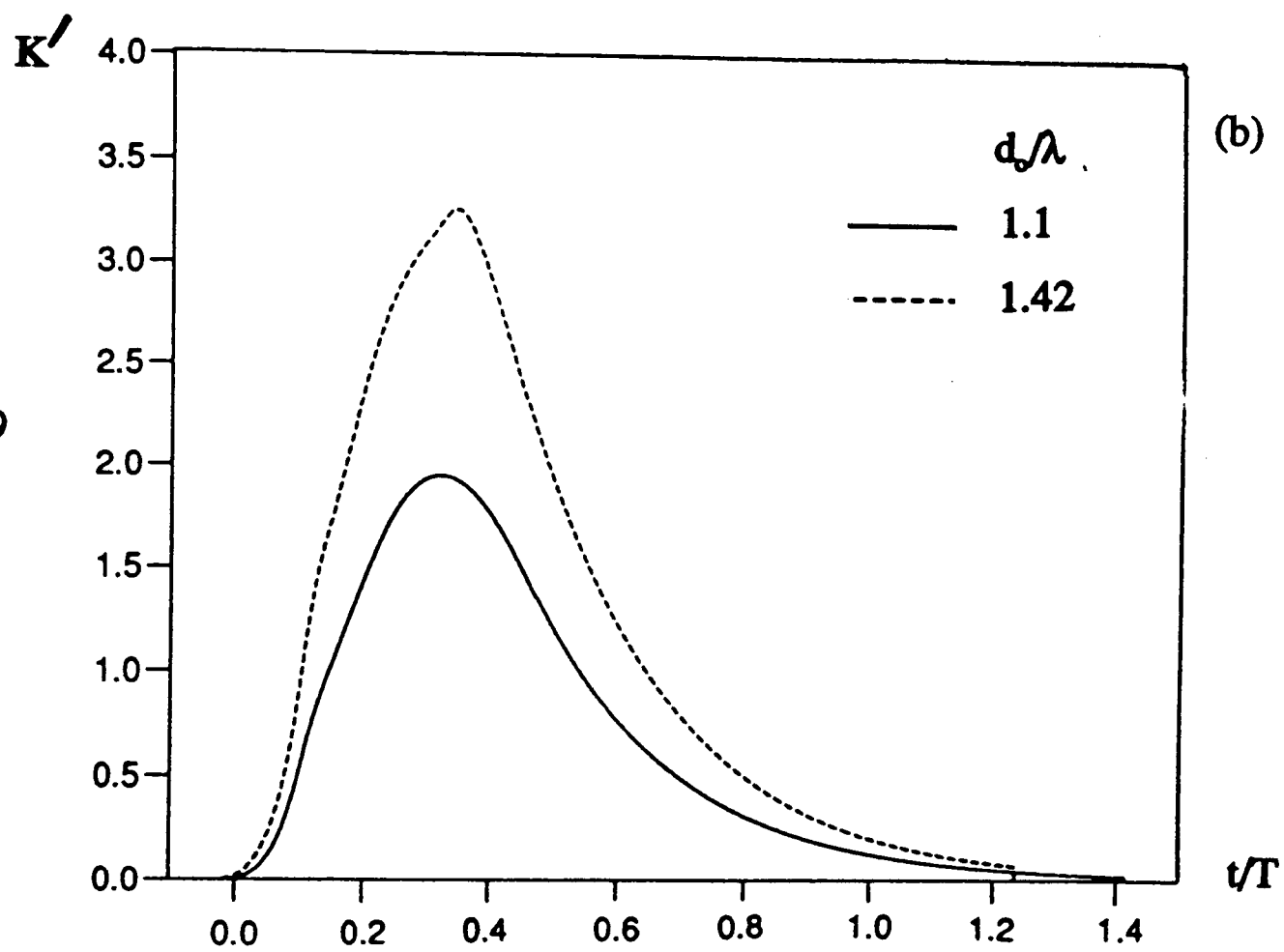
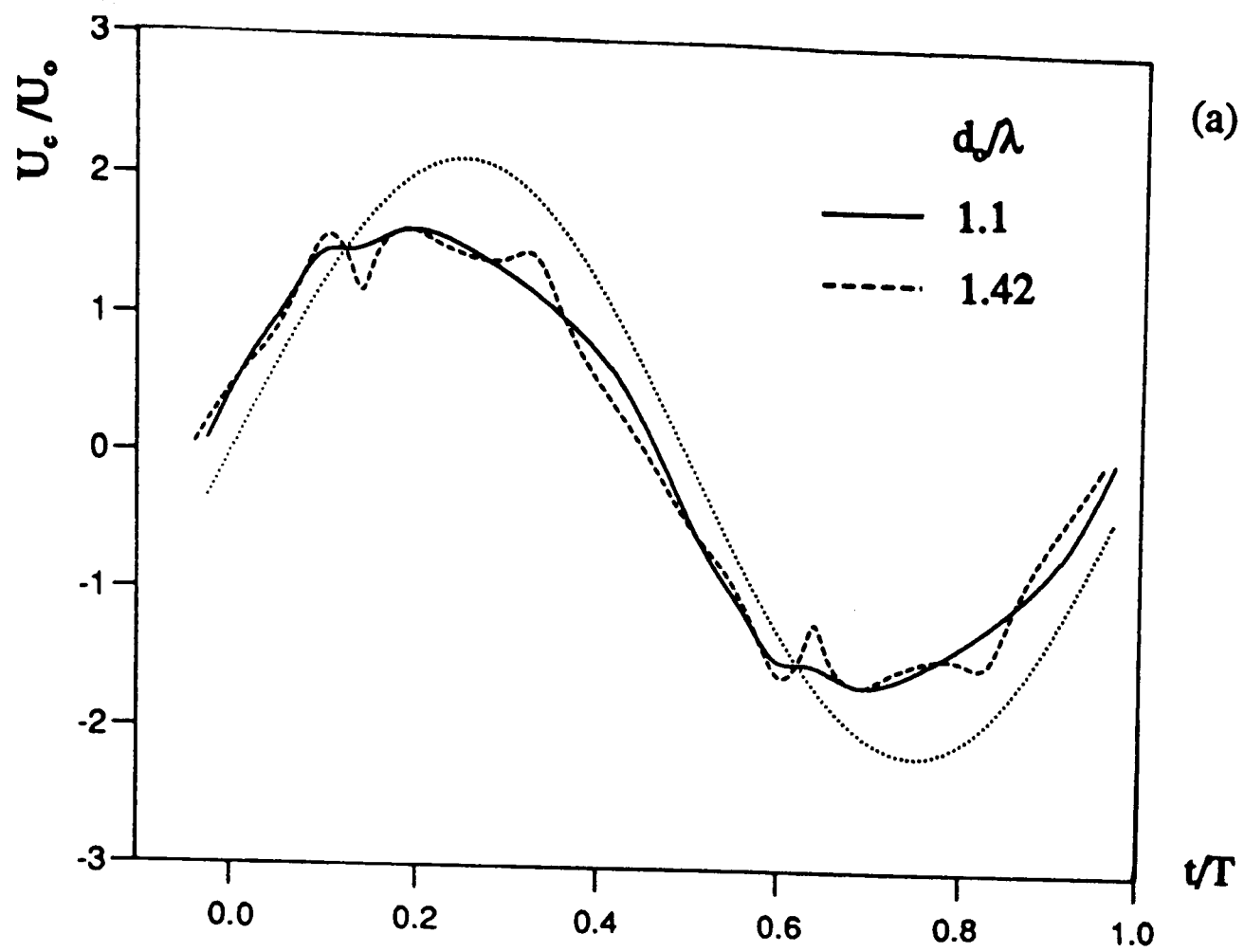


Figure 3.28



(c)

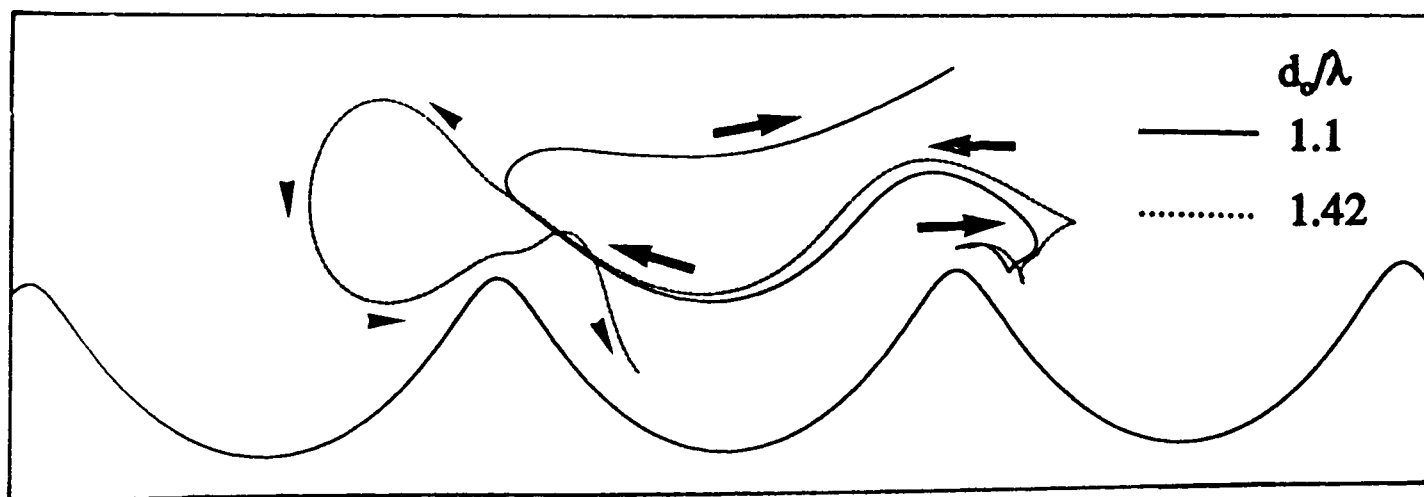


Figure 3.29
(a)-(c)

Results for $d_0/\lambda = 2.5$, $h/\lambda = 0.17$.

Figure 3.30 Vortex positions in the first half cycle. ($d_0/\lambda = 2.5$, $h/\lambda = 2.5$.) (G = growing vortex, E = ejected vortex, R = relic vortex.)

Figure 3.31 (a) Variation of the (normalised) crest velocity for a complete cycle. ($d_0/\lambda = 2.5$, $h/\lambda = 0.17$.)

Figure 3.31 (b) Variation of the (non-dimensional) vortex strength during a vortex's lifespan. ($d_0/\lambda = 2.5$, $h/\lambda = 0.17$.)

Figure 3.31 (c) The trail of a vortex from conception to destruction. ($d_0/\lambda = 2.5$, $h/\lambda = 0.17$.)

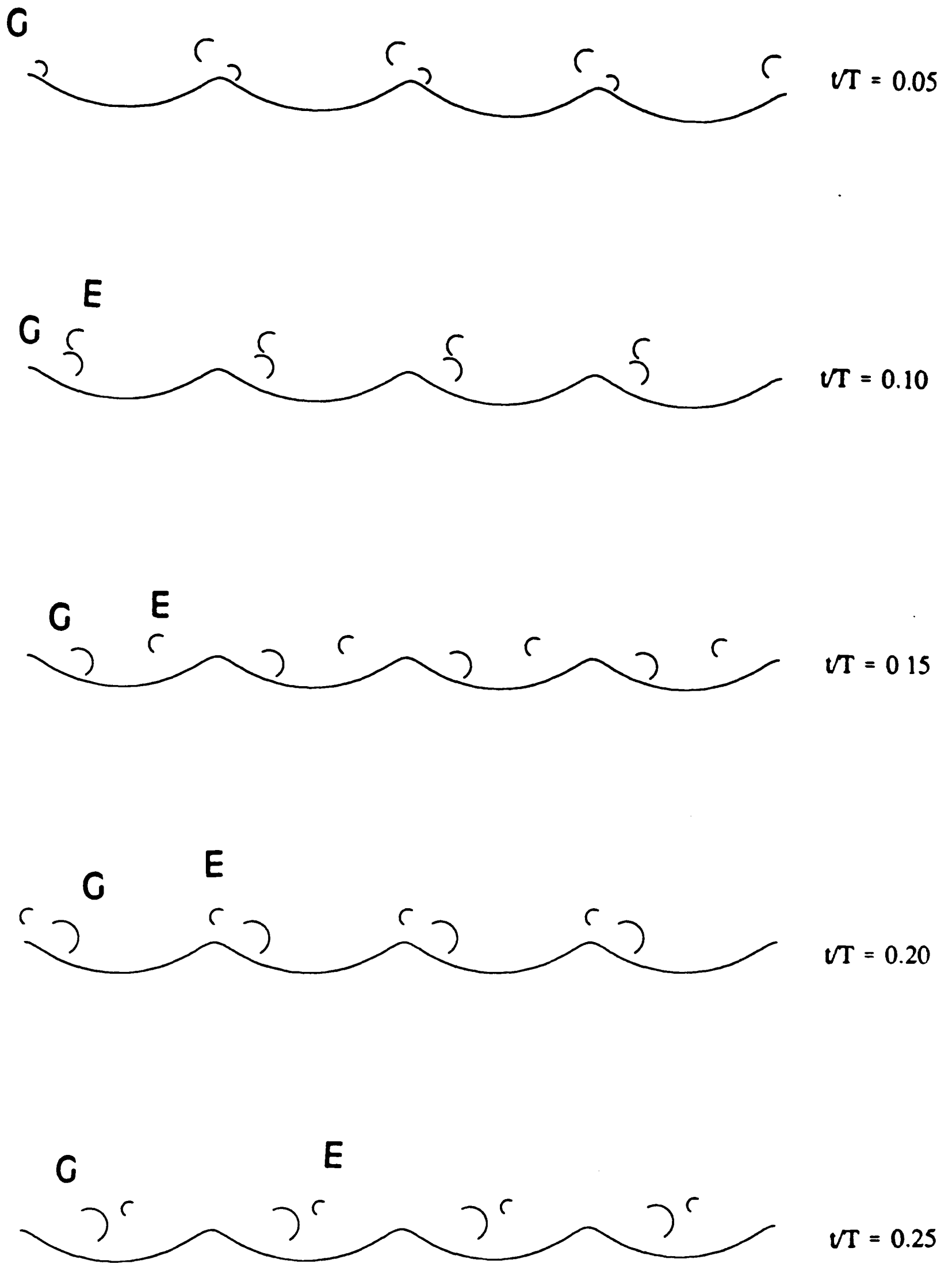
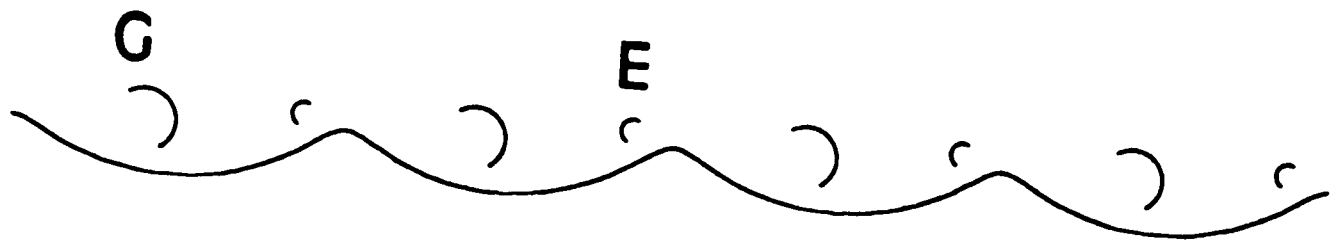
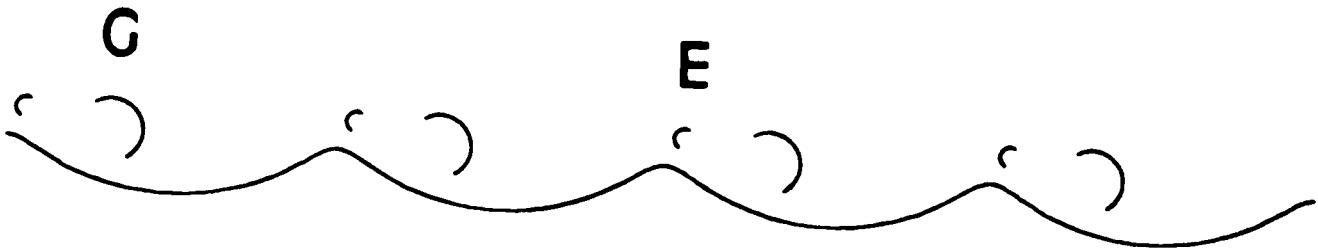


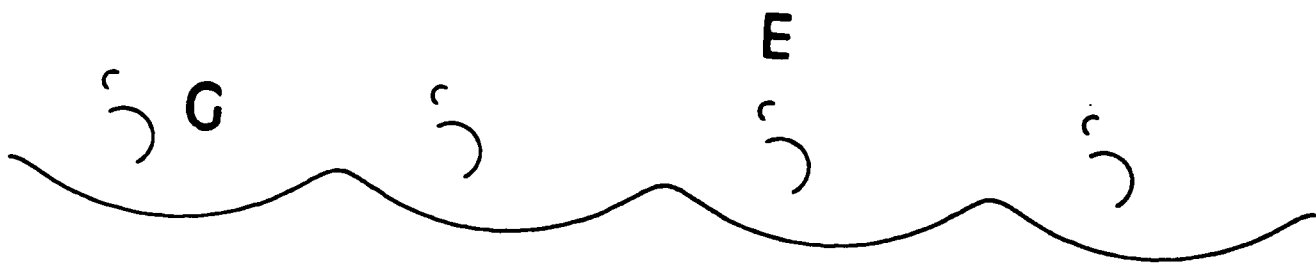
Figure 3.30



$\nu T = 0.30$



$\nu T = 0.35$



$\nu T = 0.40$



$\nu T = 0.45$



$\nu T = 0.50$

Figure 3.30

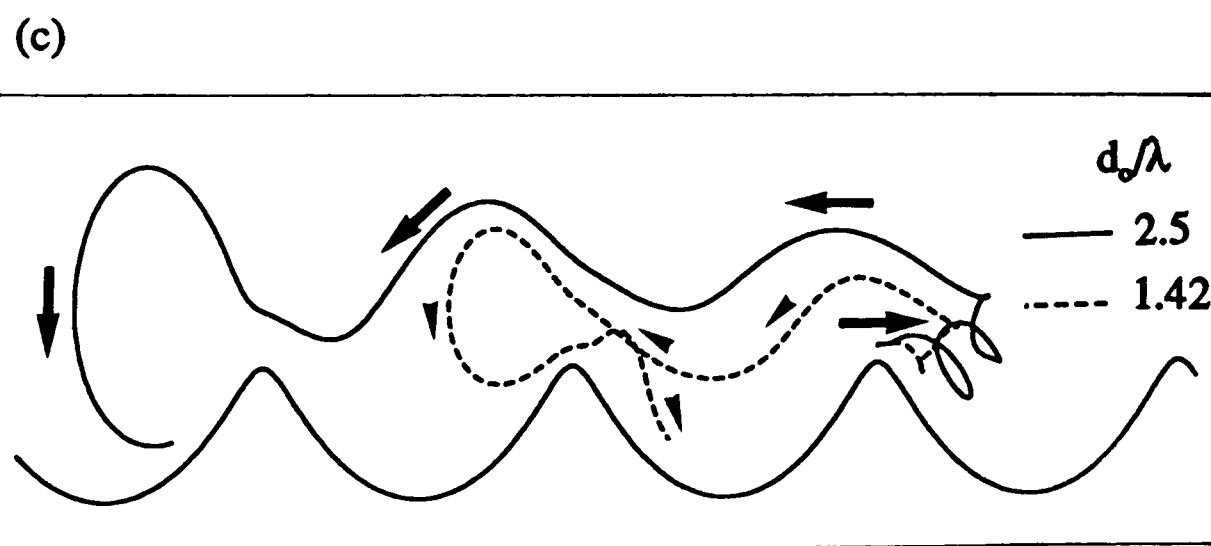
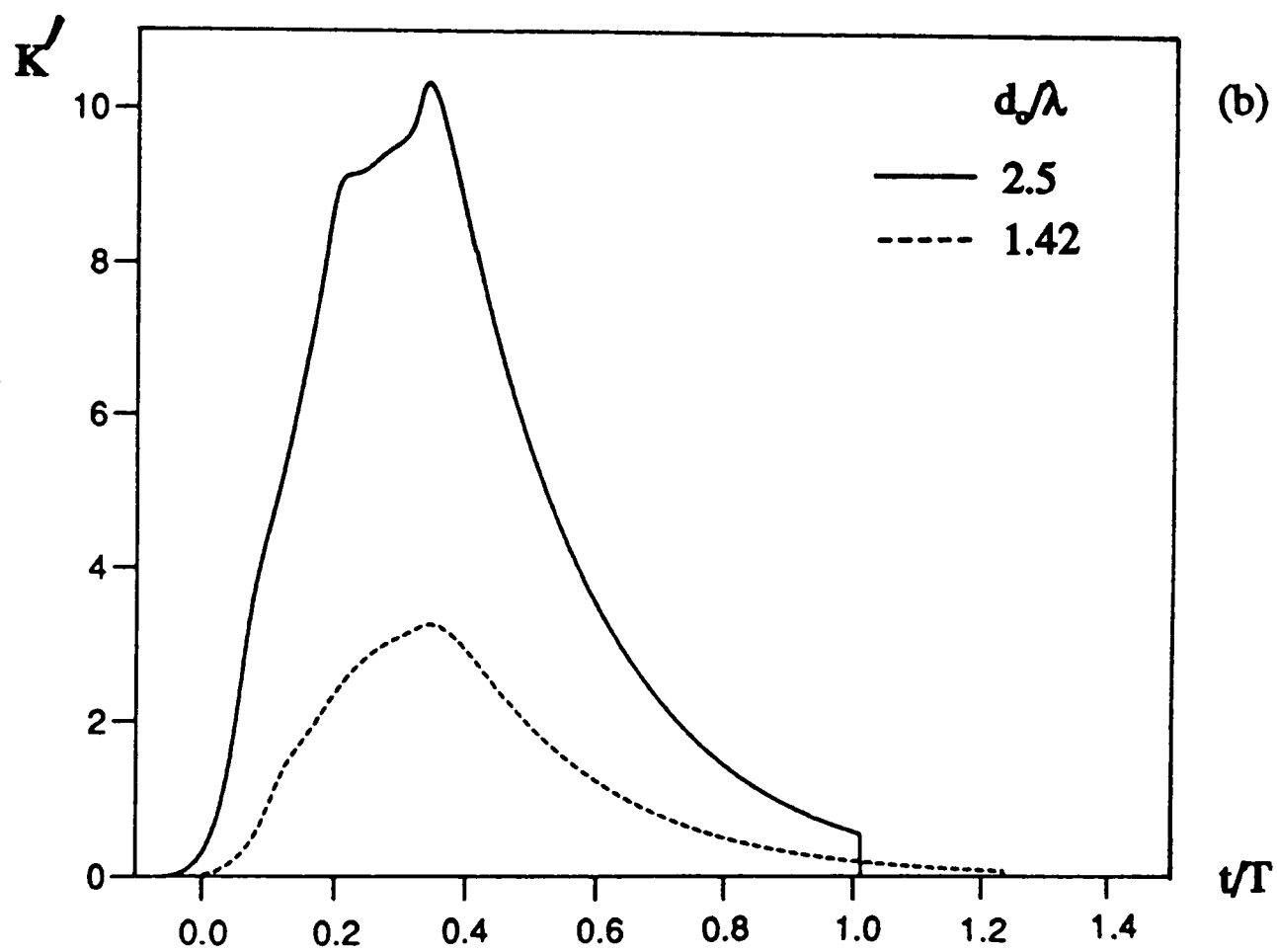
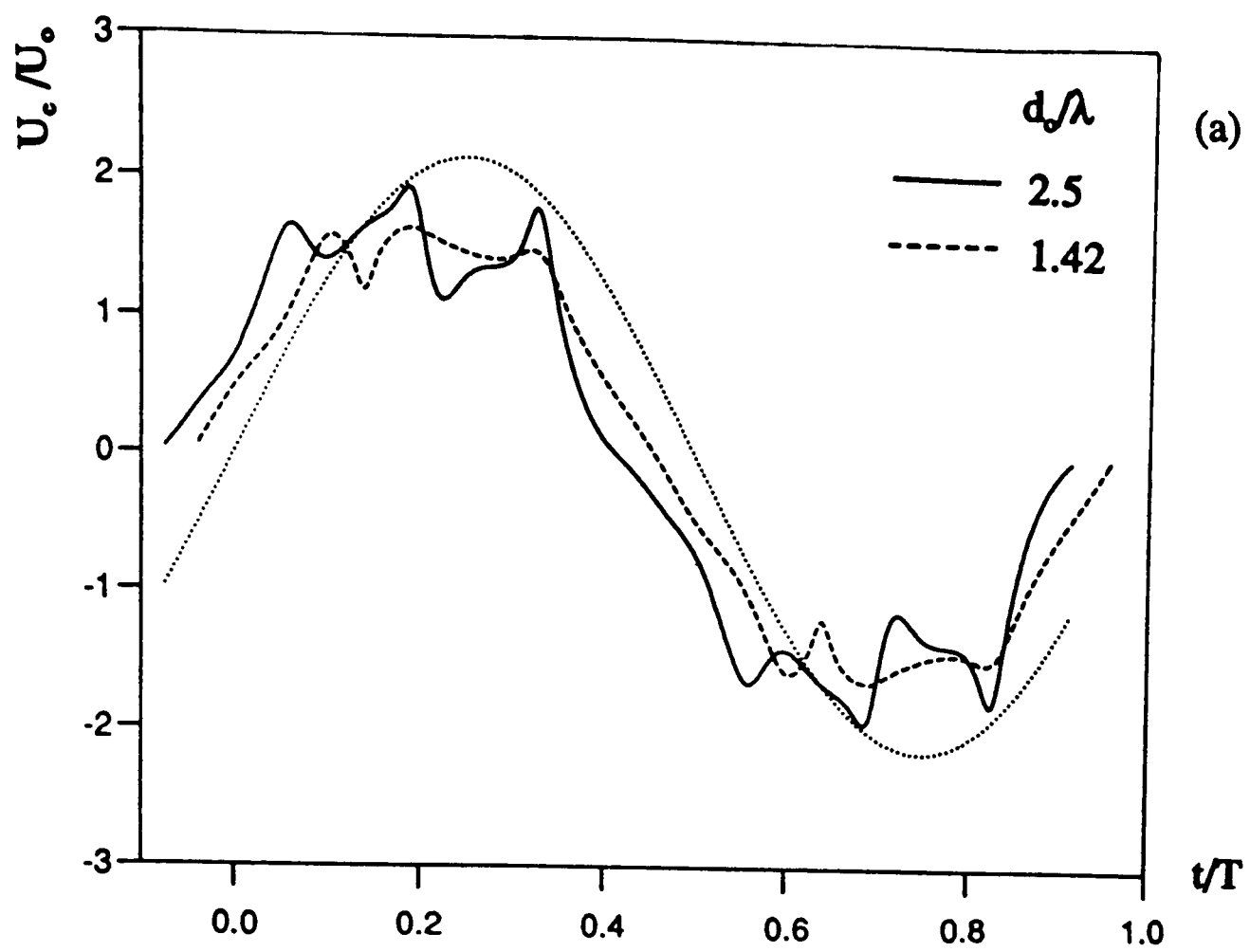


Figure 3.31
(a)-(c)

Some model comparisons with the data of DuToit and Sleath (1981).

Figure 3.32 (a,b) Comparison between the model predictions of (normalised) horizontal velocity and the data of DuToit and Sleath (1981) over (a) the crest, and (b) the trough.

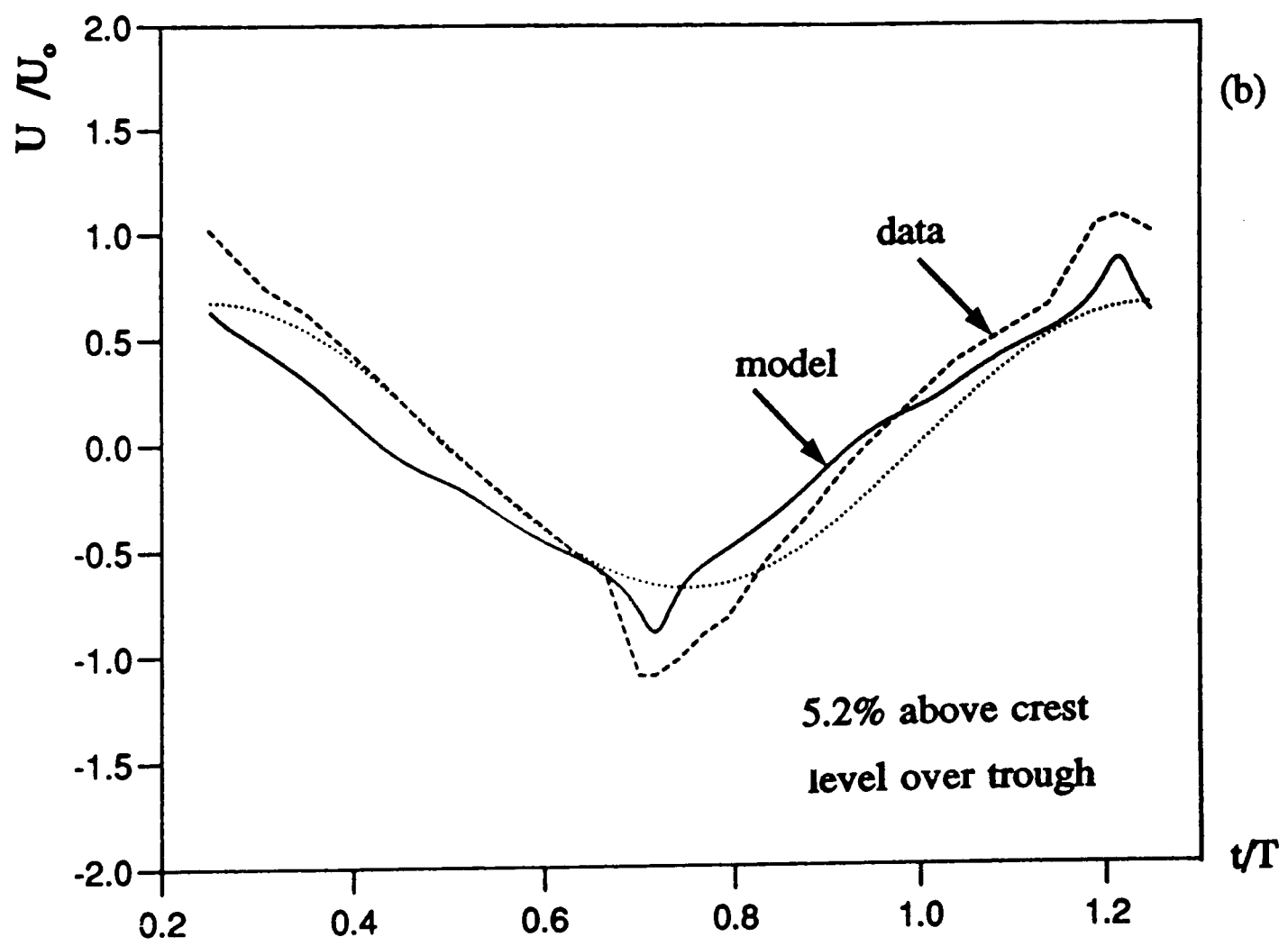
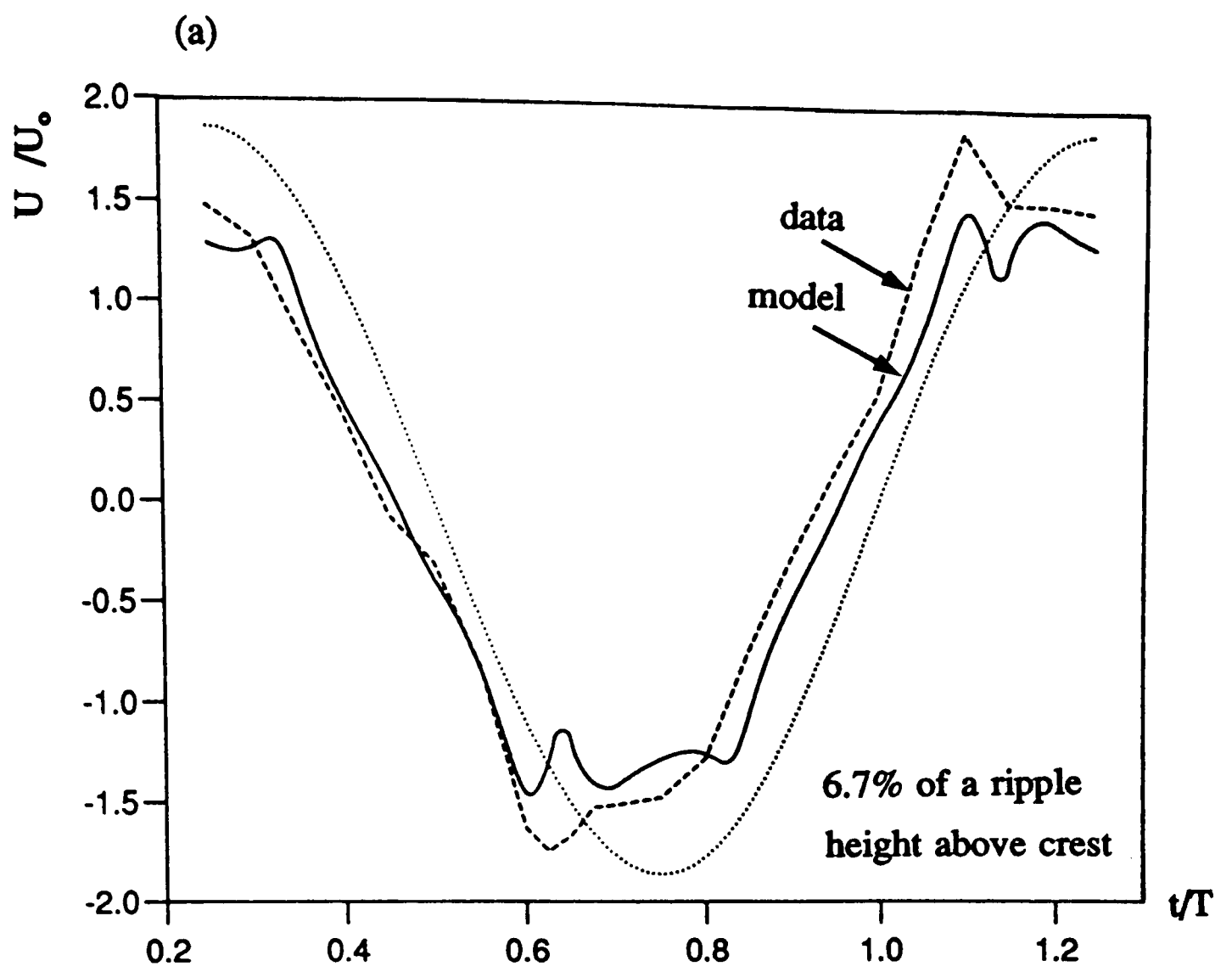


Figure 3.32 (a,b)

CHAPTER 4

THE BOUNDARY LAYER MODEL

4.1 Introduction

In the context of this study, the ‘boundary layer’ is the *oscillatory bottom boundary layer*. This layer (hereafter referred to as the boundary layer), forms immediately adjacent to the ripple profile. Figure (4.1(a)) illustrates the position of this boundary layer as it forms over the ripple during the wave cycle.

The notion of a boundary layer suggests that its flow characteristics differ from those of the main flow. These differences are primarily caused by the effect of the bed. The proximity of the bed retards the near-bed flow relative to the (bed-independent) flow above, causing velocity shear and, hence, stresses within the layer. It is these stresses, acting at the bed, that entrain sediment.

Within the boundary layer, the flow is both viscous and rotational, so the tenets of potential flow do not apply. This renders our hydrodynamical model useless for describing the boundary layer (see figure (4.1(b))). A whole new theoretical flow description is required, in order to derive the (time-varying) bed shear stresses vital to model sediment entrainment.

A mathematical description of the boundary layer is called a *boundary layer model*. The rationale of this chapter is to discuss the background to, and development of, a boundary layer model for the present study. This (boundary layer) model is driven by the hydrodynamical model, as illustrated in figure (4.1(b)). It is the boundary layer model that will provide the sediment entrainment regime required in Chapter 5.

4.1.1 Classification of the boundary layer flow regime

The structure of the boundary layer varies according to the flow regime within. Jonsson’s ‘delineation of regimes’ (see Chapter 2) is again applicable, though the equivalent roughness k_s is based on the grain size rather than the ripple height. A common assumption, which is adopted here, is to set $k_s = 2.5D_{50}$, where D_{50} is the median grain diameter. Flow in the boundary layer over ripples is considered ‘rough turbulent’. However, for the parts of the cycle when the oscillatory flow is relatively weak, the boundary layer may remain laminar.

4.1.2 The structure of the boundary layer

For low RE, the structure of the boundary layer over a smooth, flat plate is well known (see Lamb (1932)). It falls into the ‘laminar’ regime and is mathematically fairly simple to describe. For a rough flat plate, where the near bed flow is ‘rough turbulent’, the analysis requires assumptions about the structure of the turbulence in the boundary layer. The work of Jonsson and Carlsen (1976) provides useful experimental and theoretical information for both cases. Figure (4.2) is an adapted diagram from this paper. It shows instantaneous profiles of horizontal velocity over a rough, flat plate through half a cycle. In both sets of plots, the profiles for $\sigma t = 270^\circ, 315^\circ$ and 360° are instructive. They show a characteristic ‘rightwards’ bulge that occurs increasingly far up in the flow with successive phase instants. This bulge is called the ‘overshooting region’; its movement upwards within the flow is indicative of the growth of the boundary layer in time. The overshooting region is a characteristic feature of (oscillatory) wave boundary layers, although it is less pronounced in the ‘rough turbulent’ regime (c.f. ripples), where mixing is more vigorous (Jonsson (1980)).

The presence of the overshooting region complicates possible definitions of the boundary layer thickness. Jonsson and Carlsen (1976) defined an instantaneous boundary layer thickness ‘ δ_1 ’ (which is ‘ δ ’ in Jonsson (1980)) as the first height at which the velocity reaches its outer, free stream value at the phase of maximum outer velocity. Figure (4.3) (adapted from Jonsson (1980)) illustrates this definition. However, it is important to note that, at this height, the shear stress is still significant. For this reason, Jonsson stated that 2δ may be a more realistic measure of the boundary layer thickness because the shear stress is virtually extinct there. Jonsson (1980) found that, in general, δ_1 was typically 2-4% of a_o . If one ignores the overshooting region, the so-called ‘99% rule’ can be applied, whereby the boundary layer thickness is the height at which the velocity is 0.99 of the outer value.

The thickness of the boundary layer varies in time, so researchers often talk of a representative value. Ikeda *et al* (1991)) demonstrated experimentally that the boundary layer thickness varies around a mean value of $\sqrt{\nu T}$, whilst DuToit and Sleath (1981) suggest that it is of the order of 0.01λ .

For laminar flow, the bed shear stress varies sinusoidally, leading the outer flow by 45° (eg Lamb (1932)). This phase lead decreases in the rough turbulent regime. For example, Jonsson and Carlsen (1976) find the phase lead to be 25-30°. The phase lead in the stress (over the outer flow) comes about because of the relative importance of the inertial and frictional terms in the equation of motion. In the near bed region, the frictional terms dominate over the inertial terms, whilst the converse is true in the outer flow. Simply stated, frictional effects have a much quicker response time than inertial effects, so the (frictional based) bed shear stress precedes events in the outer flow. This explanation also sheds some light on why the phase lead in the rough turbulent regime is reduced - frictional effects have an increasing effect on the outer flow.

It is generally accepted that the velocity profile within the (rough turbulent) boundary layer is logarithmic;

$$U_{bl} = \frac{U_*}{\kappa} \log \frac{Y}{Y_o} \quad \text{where} \quad U_* = \sqrt{\frac{\tau_b}{\rho}} \quad 4.1 \quad (a, b)$$

where U_{bl} is the horizontal velocity in the boundary layer, U_* the friction velocity, κ is Von Karman's constant (≈ 0.40), Y is the distance from the bed, and Y_o the roughness length. For rough beds, the common practice is to replace Y_o by $k/30$.

4.1.3 Theoretical descriptions of the boundary layer

Theoretical studies of the boundary layer suffer from the fact that the problem is not 'closed' - there are more variables than unique pieces of information. Turbulence modellers have, therefore, had to make physical assumptions in order to generate the extra information required to 'close' the problem. DuToit and Sleath (1981) and Davies (1986) provide resumes of some of the different methodologies applied.

As an example of this closure, Kajiura (1968) used an eddy viscosity approach to relate the shear stress (τ) to the velocity shear

$$\tau = \rho \epsilon \frac{\partial U_{bl}}{\partial Y} \quad 4.2$$

where ϵ is the (time invariant) eddy viscosity. Kajiura subdivided the boundary layer into three regions: one very near the bed, a second up to the top of the overlap layer, and a third above this. Kajiura achieved closure by relating ϵ to U_* (and hence to the bed shear stress τ_b). A similar (though simpler) approach was adopted by Myrhaug (1982). Smith (1977) used the eddy viscosity approach in his study of boundary layers. He defined a boundary layer thickness based on a similarity argument with the laminar case:

$$\delta_w = \frac{U_{* (\max)}}{\sigma} \quad 4.3$$

This boundary layer thickness is illustrated in Figure (4.4). Smith makes the proviso that the logarithmic portion of the boundary layer is significantly smaller than δ_w .

Fredsoe (1984) considered deep, uniform, horizontal flow over a rough, flat plate - conditions that allow the linearisation of the equation of motion. Fredsoe then eliminated the pressure gradient by assuming that it remains constant over the boundary layer (i.e. no vertical velocity). This results in the so-called Von Karman's momentum integral:

$$\frac{\tau}{\rho} = \int \frac{\partial}{\partial t} (U_b - U_{bl}) dY \quad 4.4$$

(see §4.2), where U_b is the velocity at the edge of the boundary layer (the outer velocity). Fredsoe then integrates over the whole boundary layer with the assumption of a log profile in the layer. The conditions for defining the boundary layer thickness are, firstly, continuity of velocity and, secondly, zero shear stress at the edge of the boundary layer. This second condition means that the predicted boundary layer is quite thick (c.f. Jonsson (1980)).

The Fredsoe formulation requires that a new boundary layer grows from the instant of each outer flow reversal. This kills the predicted phase lead of the bed shear stress over the outer flow velocity at times of flow reversal. At each flow reversal, the boundary layer thickness is reset to zero.

4.1.4 The boundary layer over ripples

All the above literature has either measured or modelled the boundary layer over a flat bottom with no free surface. This simplifies the situation considerably - experimentalists can ignore vertical components of velocity, whilst modellers can drop the non-linear, advective terms from the basic equation of motion. These simplifications cannot be applied when studying steep ripples because both vertical velocities and horizontal velocity shear are inherent with the ripple profile. Smith and Maclean (1977) studied variations in bed shear stress over (much larger) dune profiles in a river, but the flow here was unidirectional. Theoretical studies are more numerous (eg Asp Hansen *et al* (1991)). Asp Hansen *et al* (q.v. Chapter 5) have split the ripple profile into a series of flat ledges, then used their hydrodynamical model to provide a time-varying outer velocity at one particular ledge near the ripple crest. This outer velocity is then fed into Fredsoe's 1984 model, in order to obtain a local time-varying bed shear stress at each ledge. [Macpherson (1984) did not calculate bed shear stresses, but related the instantaneous rate of sediment entrainment to a power of the local velocity.]

4.2 Formulation of the boundary layer model

4.2.1 Adaptations to the original Fredsoe (1984) formulation

The boundary layer model chosen to accompany the hydrodynamic model is the (wave only) formulation of Fredsoe (1984) as used by Asp Hansen *et al* (1991). The choice was motivated by the desire for a relatively simple but robust algorithm, that could cope with the different local flow regimes over the ripple profile. Fredsoe's model gives a flow description of boundary layer development over a rough, flat surface that is subject to an ambient, wave-induced sinusoidal motion that acts down

to the edge of the boundary layer. Certain initial adaptations will be required in order to apply Fredsoe's model to the flow over ripples:

- (i) the ripple profile needs to be split into a series of flat ledges, each with its own unsteady boundary layer microclimate.
- (ii) the 'horizontal' velocity acting at the edge of the boundary layer should be the modulus of the resultant velocity, R_b , incorporating both horizontal and vertical components, given by the hydrodynamical model, at the local bed level.

Fredsoe's model allows the linearisation of the Navier Stokes equation, because the velocity is assumed to be horizontally uniform. However, this is not true of the flow over ripples. Non-uniformity is accounted for, to some extent, by using a large number of ledges in each ripple wavelength. The following formulation of Fredsoe's model closely follows the 1984 paper, but does not assume that the 'edge of boundary layer' velocity (U_b) is sinusoidal.

4.2.2 The development of the present boundary layer model

The flow within the boundary layer is assumed to conform to the linearized Navier Stokes equation

$$\frac{\partial U_{bl}}{\partial t} = \frac{-1}{\rho} \frac{\partial P}{\partial x} + \frac{\partial}{\partial Y} \left(\frac{\tau}{\rho} \right) \quad 4.5$$

where U_{bl} is the horizontal velocity in the boundary layer, Y is the distance from the bed, τ is the stress acting at height Y , and the other notation is as defined earlier. Figure (4.5) aims to clarify the notation used. To eliminate the pressure gradient term, the conditions at the edge of the boundary layer are applied i.e. $U_{bl} = U_b$, $\tau = 0$ and the pressure is the same, so that

$$\frac{\partial U_b}{\partial t} = \frac{-1}{\rho} \frac{\partial P}{\partial x} \quad 4.6$$

Substituting equation (4.6) into equation (4.5) and integrating w.r.t. Y gives

$$\frac{\tau_b}{\rho} = \int \frac{\partial}{\partial t} (U_b - U_{bl}) dY \quad 4.7$$

where the integral is taken over the thickness of the boundary layer, and τ_b is the stress at the bed. The term $(U_b - U_{bl})$ is called the defect velocity, and equation (4.7) is the Von-Karman momentum integral. From here on, the goal of the analysis is to turn equation (4.7) into a differential equation with one unknown, to which end Fredsoe assumed that U_{bl} can be represented as a logarithmic velocity profile

$$U_{bl} = \frac{U_*}{\kappa} \log \frac{30Y}{k_s} \quad 4.8$$

where the notional ' Y_0 ' value is $k_s/30$. The limits of the integral are found by taking the bottom of the boundary layer as $k_s/30$, thus giving the top as $\delta + k_s/30$, where δ is the boundary layer thickness.

Continuity of velocity at the edge of the boundary layer states that $U_{bl} = U_b$ at $Y = \delta + k_s/30$. This leads to

$$\delta = \frac{k_s}{30} (e^j - 1) \quad \text{where} \quad j = \frac{\kappa U_b}{U_*} \quad 4.9 \quad (a, b)$$

and equation (4.7) now becomes

$$U_*^2 = \int_{\frac{k_s}{30}}^{\frac{k_s}{30} e^j} \frac{\partial}{\partial t} \left[U_b - \frac{U_*}{\kappa} \log \frac{30Y}{k_s} \right] dY \quad 4.10$$

where equation (4.1b) has been used to eliminate τ_b/ρ . Equation (4.10) may be solved (subject to the assumption that U_b is not a function of Y) to yield

$$U_*^2 = \frac{k_s}{30} (e^j - 1) \frac{dU_b}{dt} - \frac{1}{\kappa} \frac{k_s}{30} \frac{dU_*}{dt} [e^j (j-1) + 1] \quad 4.11$$

Finally, U_* and its derivative may be expressed in terms of j , which gives, after some manipulation

$$\frac{dj}{dt} = \frac{30\kappa^2}{k_s} \frac{U_b}{e^j(j-1)+1} - \frac{1}{U_b} \frac{dU_b}{dt} \left[\frac{j(e^j-j-1)}{e^j(j-1)+1} \right] \quad 4.12$$

Equation (4.12) is the equation to be solved for j , from which come U_* , τ_b/ρ and δ . The initial condition $\delta = 0$ at $t = 0$ implies that $j = 0$ at $t = 0$. Unfortunately, $j = 0$ is a singular point of equation (4.12). To get around this problem, Fredsoe used Taylor series expansions in j to obtain a small parameter version of equation (4.12). The same approach has been adopted here, in which terms up to order (j^2) have been retained. This 'small parameter' equation is

$$\frac{dj}{dt} = \frac{A}{j^2} - Bj \quad \text{where } A = \frac{60\kappa^2 U_b}{k_s}, \quad B = \frac{1}{U_b} \frac{dU_b}{dt} \quad 4.13$$

which has the solution

$$j = \left(\frac{A}{B} \right)^{\frac{1}{3}} [1 - e^{-3Bt}]^{\frac{1}{3}} \quad 4.14$$

where the initial condition is $j = 0$ at $t = 0$.

Physically, equations (4.12) and (4.14) represent (via the parameter j) the development of the boundary layer with time. The problem of the initial condition being a singularity is due to the fact that, in reality, the boundary layer thickness does not immediately become zero at flow reversal.

4.3 Implementation of the boundary layer model

4.3.1 The outer velocity for the boundary layer model

Equations (4.12) and (4.14) are non-dimensionalised with respect to the lengthscale k_s and timescale σ , to become

$$\frac{dj}{dt''} = \frac{30\kappa^2 U_b''}{e^j(j-1)+1} - \frac{1}{U_b''} \frac{dU_b''}{dt''} \left[\frac{j(e^j-j-1)}{e^j(j-1)+1} \right] \quad 4.15$$

and, for the small parameter solution

$$j = \left(\frac{C}{D} \right)^{\frac{1}{3}} [1 - e^{-3Dt''}]^{\frac{1}{3}} \quad \text{where } C = 60\kappa^2 U_b'' \quad , \quad D = \frac{1}{U_b''} \frac{dU_b''}{dt''} \quad 4.16$$

The symbol " indicates non-dimensionalisation w.r.t. k_s and σ .

The outer velocity time series $U_b(t)$ is replaced by $R_b(t)$ in an attempt to include the effect of vertical velocity in the solution. $R_b(t)$ is the *modulus* of the resultant velocity, chosen for reasons of computational convenience (Fredsoe's model never operates for negative velocities). This time series of $R_b(t)$ comes from the hydrodynamical model where the dimensional length scale is the ripple wavenumber λ . $R_b(t)$ is therefore found by first redimensionalising the hydrodynamic velocity values, then non-dimensionalising with respect to k_s and σ ;

$$R_b \text{ (boundary layer model)} = \frac{\lambda}{2\pi k_s} R_b \text{ (hydrodynamical model)}$$

4.3.2 Flow reversals in the time series of $R_b(t)$

The boundary layer model at each ledge operates with the velocity time series $R_b(t)$, calculated over one cycle. To meet the constraints of the boundary layer model, this time series must start at a flow reversal. Figure (4.6) is a schematic diagram, illustrating the process of reworking the time series of $R_b(t)$ so that it starts at a flow reversal. At successive flow reversals in $R_b(t)$, the solution is re-initialised with both U_s and δ reset to zero.

4.3.3 The boundary layer model at the ripple crest

The sand concentration studies discussed in Chapter 5 are based on the entrainment of sediment from the crest region. For this reason, a simplified version of

the boundary layer model, operating at the crest level alone, was established to obtain the local entrainment regime. This version does not require any consideration of ledges as it operates at the (notionally) flat crest.

At the outset, the hydrodynamical model is used to obtain $R_b(t)$ at the crest level. This time series is ordered so that it starts at a flow reversal. Why does the time series for R_b not start at a flow reversal if it has been obtained at the crest ? To answer this point, it is necessary to remember that the time regime of the hydrodynamical model is fixed by the time of flow reversal 12.5% of a ripple height above the crest, and not at the crest itself. In reality, the phase difference in the reversals is only one or two timesteps.

The re-ordered time series of R_b is fed into the boundary layer model and solved for the 500 time steps that comprise a full cycle. Equation (4.16) is applied for the first time step. From then on, a fourth order Runge-Kutta scheme is used to solve equation (4.15). As the second flow reversal is approached, the solution is re-initialised to zero and the process starts again.

The primary outputs from this method are time series of τ_b/ρ (from U_*) and δ . These are both computed from the time of flow reversal, so have to be manipulated back to the original time frame governed by the hydrodynamical model. This provides series of τ_b/ρ and δ that identically match the time frame of the hydrodynamical model.

4.3.4 The boundary layer model over the entire ripple profile

When considering ripple morphology, as in Chapter 6, boundary layer calculations are required over the whole ripple profile. This is computationally more involved and has led to the development of a second, more generalised application of the boundary layer model.

The ripple profile is split into 40 equal ledges in the physical plane, ledge 1 being at the lefthand trough, ledge 21 at the crest, and ledge 40 just short of the righthand trough. Figure (4.7) illustrates the disposition of these ledges. The central position of each ledge is mapped backwards into the ζ plane, and the hydrodynamical model is used to generate two associated time series of velocity: the horizontal velocity, $U_b(t)$,

and $R_b(t)$. The role of $U_b(t)$ is to retain the local flow direction - it plays no direct part in the operation of the boundary layer model. Ledge by ledge, the outer flow velocity field is calculated and fed into the boundary layer model for solution in the manner described earlier. In this way, 40 time series of bed shear stress and boundary layer thickness are obtained, which give a boundary layer description over the ripple at each time step. These time series are in the time frame of the hydrodynamical model.

4.4 Results

The principal aim of the results in this chapter is to demonstrate whether or not the present boundary layer model predicts sensible values for the relevant parameters. The physical implications of the boundary layer model are discussed later, in the context of sediment entrainment and ripple stability (Chapters 5 and 6).

4.4.1 Replicating the results of Fredsoe (1984)

An obvious first stage in analysing the suitability of the present boundary layer model, was to see if it could replicate Fredsoe's model results under the same conditions. This was done by generating two sinusoidal velocity time series for R_b , with velocity amplitudes reflecting the two values of a_o/k_s ($a_o/k_s = 10, 100$) as follows:

$$\frac{a_o}{k_s} = 10 \quad \rightarrow \quad \frac{U_o}{\sigma k_s} = 10 \quad \rightarrow \quad U_o'' = 10$$

Figures (4.8a-c) show that the present model reproduces Fredsoe's model results well. Of specific note is the phase lead of $U_b(\max)$ over the maximum outer velocity. This is 20° for $a_o/k_s=10$ and 15° for $a_o/k_s=100$. Both Fredsoe's results and the boundary layer model predict that, at maximum outer flow, the ratio δ/a_o is 0.07 and 0.04 for the two settings $a_o/k_s = 10$ and 100 respectively.

4.4.2 The boundary layer model at the ripple crest

Results are presented for the case $d/\lambda = 1.62$, $h/\lambda = 0.16$, $\lambda = 0.063$ m, $T = 2.0$ s and $h = 0.01$ m, corresponding to Test 1 of the experiments of Villaret (1992, 1993) for waves only. More details of these experiments are provided in Chapter 5.

Figure (4.9c) shows the variation in j for a full cycle. The sharp cutoffs, coinciding with local flow reversal, clearly demonstrate the effects of re-initialising the solution. Also, slight depressions in the profile at $t/T = 0.10, 0.30$ and $0.60, 0.80$ can be traced back to the passage of ejected vortices over the crest (see Figure (5.13)).

The boundary thickness plot, figure (4.9d), shows the boundary layer growing in time until its thickness is reset to zero at flow reversal.

Figure (4.9b) shows how the magnitude of $(\tau_b/\rho)''$ varies during a cycle. The main local maxima at $t/T = 0.10, 0.30$ and $t/T = 0.60, 0.80$ correspond to the passage of ejected vortices and the associated velocity enhancement. Their relative size depends on the boundary layer thickness, the thinner layer at $t/T = 0.10, 0.60$ causing increased shear within it.

4.4.3 The boundary layer model over the entire ripple profile

The results for this subsection were obtained using the same run parameters as in §4.4.2.

Figure (4.10) shows the magnitude of $(\tau_b/\rho)''$ for ledges 17 and 25. These two ledges are on opposite sides of the ripple (ledge 21 being the crest). The results demonstrate that the boundary layer model yields similar solutions, delayed by half a cycle, for equivalent ledges over the ripple profile. Both ledges are affected by the formation of growing vortices, which cause the dominant spikes at $t/T = 0.20$ and 0.70 respectively.

Figure (4.11) shows the variation in $(\tau_b/\rho)''$ through a cycle for three of the ledges on the left side of the ripple, ledge 15 being nearest the crest. The time series for the ledge 5 trace shows a local maximum at $t/T = 0.20$ which is associated with the oscillatory flow. Thereafter, the time series passes through a zero to the equivalent minimum at $t/T = 0.70$. By $t/T = 0.90$, the fifth ledge has come under the influence of

the growing vortex, causing the local (positive) peak in the bed shear stress. The time series for ledge 10 follows a similar pattern. However, the growing vortex has a greater effect and the associated peak persists further into the next cycle. For ledge 15, the newly formed growing vortex causes the local maximum at $t/T = 0.0$. The maximum in the oscillatory flow causes the next maximum (at $t/T = 0.25$). Flow reversal then ensues, changing the sign of $(\tau_b/\rho)''$, but the growing vortex quickly reverses the flow and a dominant (positive) peak is produced. The duration of negative bed shear stress decreases progressively for ledges which are successively closer to the ripple crest.

A useful output from the boundary layer model is the variation of instantaneous bed shear stress over the profile. Figure (4.12) illustrates this variation for the time instants $t/T = 0.10$ – 0.40 . For $t/T = 0.10$, positive and negative peaks on either side of the crest correspond to the presence of the ejected and growing vortices respectively. By $t/T = 0.20$, the oscillatory flow is the main contributor to the positive peak on the left of the crest. Meanwhile, the growing vortex provides the much larger negative peak over the lee slope. The effect of the growing vortex subsequently diminishes and, by $t/T = 0.40$, the variation in $(\tau_b/\rho)''$ is relatively weak.

4.5 Discussion

The aim of this chapter has been to provide the background for, and development of, a boundary layer model. This model will operate in conjunction with the hydrodynamical model to simulate the entrainment and suspension of sediment.

At this stage, it is only possible to say a limited amount about the *effectiveness* of the model. This will become apparent when it is applied in the relevant chapters. However, the following encouraging points can be made. First, the ability of the boundary layer model to reproduce Fredsoe's results for purely sinusoidal flow, demonstrates the accuracy of the present implementation. Second, the graphical output from the boundary layer model is generally consistent with the evolving vortex field in the outer flow, suggesting that the model results are qualitatively sensible.

One of the quantitative features that can be discussed at this stage is the boundary layer thickness. The Fredsoe comparisons (figures (4.8a-c)) give δ at maximum outer

flow (i.e. δ_1) as 4 and 7% of a_o respectively. As expected, these percentages are quite high (c.f. Jonsson (1980), §4.1.3). When the boundary layer model is run for the data of Villaret (1992, 1993) (figures (4.9)-(4.12)), the relevant parameters can actually be dimensionalised. These give $\delta_1 = 0.004$ m, $a_o = 0.05$ m, $\sqrt{\nu T} = 0.0014$ m and $U_{*_{(max)}} = 0.02$ m/s. The following ratios can be found:

$$\delta_1/a_o = 8\% \quad (c.f. \text{Jonsson (1980) with 2-4\%}),$$

$$\delta_1/\lambda = 6\% \quad (c.f. \text{Dutoit and Sleath (1981) with 1\%}),$$

$$\delta_1/h = 38\% \quad (c.f. \text{present hydro model with 12.5\%}),$$

$$\delta_1/\sqrt{\nu T} = 2.7 \quad (c.f. \text{Sato et al (1991)})$$

$$U_{*_{(max)}}/\sigma = 0.006 \text{ m i.e. } 60\% \text{ of a ripple height } (c.f. \text{Smith (1977)})$$

The picture emerging from these ratios is that, for the Fredsoe case of sinusoidal outer flow, the instantaneous boundary layer thickness (δ_1) is relatively large. It seems likely, therefore, that the application of the present boundary layer model to flow over ripples will also result in relatively thick boundary layers. Interestingly, if we now apply the proviso of Smith (1977) for the actual width of the log layer (10% of his boundary layer thickness at peak flow), the thickness becomes 6% of a ripple height which is more in keeping with the model choice for the boundary layer thickness.

In Chapter 3, reference was made to the large values for the boundary layer thickness. Initially, it was desired to have feedback between the hydrodynamical model and the boundary layer model. The hydrodynamical model (fed by vorticity generated within the boundary layer and quantified by Prandtl's rule) would have driven the boundary layer model. This, in turn, would have given the boundary layer thickness necessary to apply Prandtl's rule and so on. The 'feedback' scenario was discarded when it became apparent that the predicted boundary layer thickness was a significant proportion of the ripple height. The release of vorticity at such heights disrupted the (hitherto promising) evolution of the vortex field.

For the case of sinusoidal outer, free stream flow (the Fredsoe case), it is straightforward to pick out the phase lead of peak bed shear stress over the peak in the

outer velocity. Figure (4.8b) shows (via U_*) that this lead is 20° and 15° for $a_o/k_s = 10$, 100 respectively. These values are inconsistent with Jonsson's assertion that the phase lead is lower for a rougher substrate. For the case of flow over ripples, the phase lead is far harder to assess. In figure (4.9b), the global maxima at $t/T = 0.10$ and 0.60 are 54° ahead of the maximum velocity of the *far bed, oscillatory flow*. However, the phase lead of these global maxima over the peak in the local, outer, free stream velocity at the crest is unclear. It remains uncertain when these velocity maxima occur.

4.6 Conclusions

The boundary layer model presented in this chapter is an adaptation of a theory developed for flat beds. In applying these models to the case of a sloping bed, essential physics has been lost. Specifically, no account is taken of the resulting non-linear, advective terms. Despite these omissions, the model recreates most of the important features associated with boundary layers and is thought to provide a good 'first approximation' for the bed shear stresses used later to predict sediment entrainment.

A sequence of sketches and figures (from literature) concerning the oscillatory bottom boundary layer.

Figure 4.1 (a,b) Two diagrams illustrating (a) the thin boundary layer that forms adjacent to the ripple profile, and (b) how this layer is not present in the hydrodynamical model. The text explains how the hydrodynamical model provides the driving, outer velocity for the boundary layer model.

Figure 4.2 A sequence of velocity profiles within the boundary layer over a rough, flat bed, taken at different instants during a wave cycle. 0° corresponds to $t/T = 0$, 180° to $t/T = 0.5$, and so on. Copied and adapted from Jonsson and Carlsen (1976).

Figure 4.3 The definition sketch for Jonsson's ' δ_i ' definition of the boundary layer thickness. Copied and adapted from Jonsson (1980).

Figure 4.4 A sequence of velocity profiles within the boundary layer over a rough, flat bed, taken at different instants during a wave cycle. The time regime is as for figure (4.2). Copied and adapted from Smith (1977).

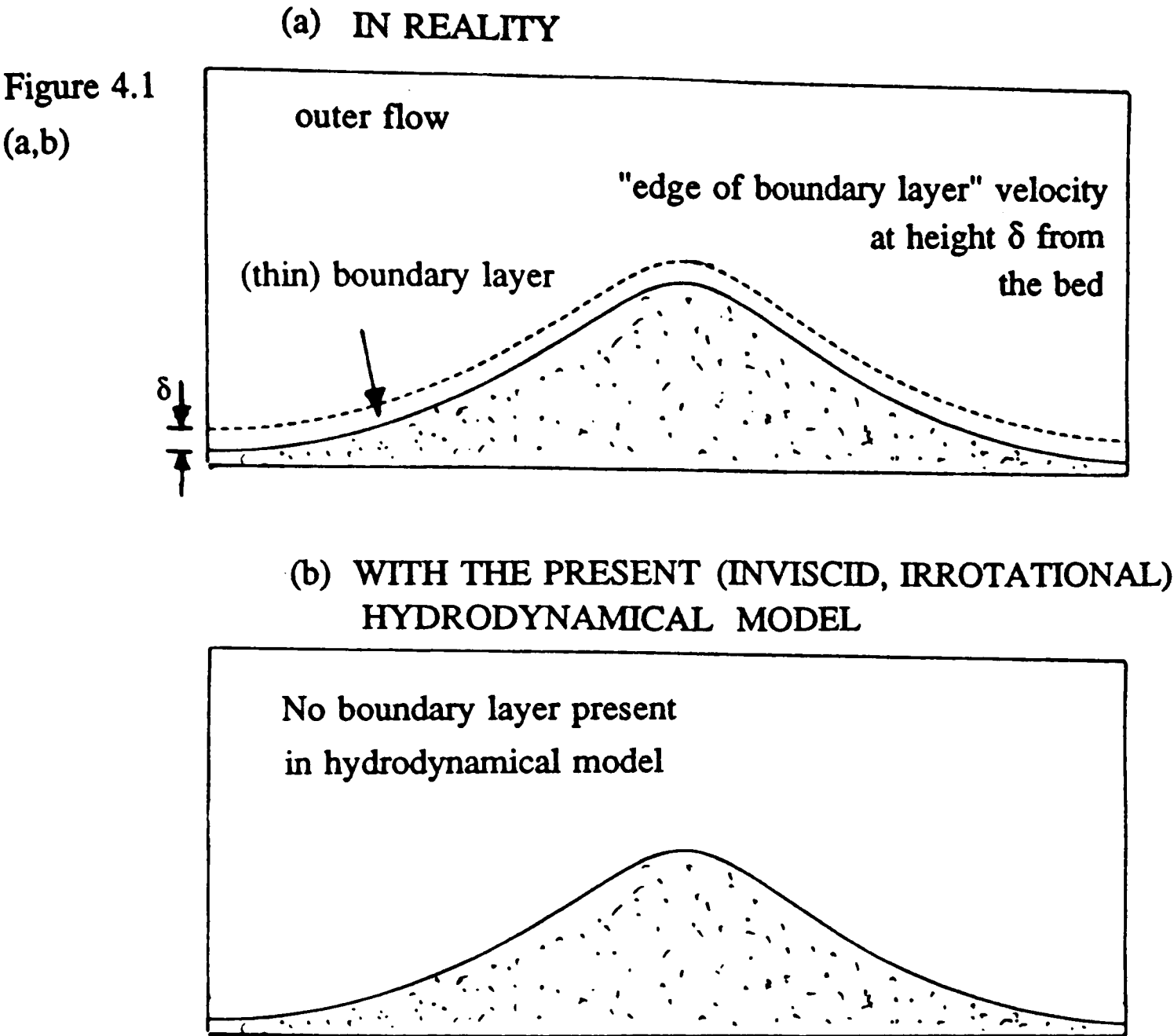


Figure 4.3

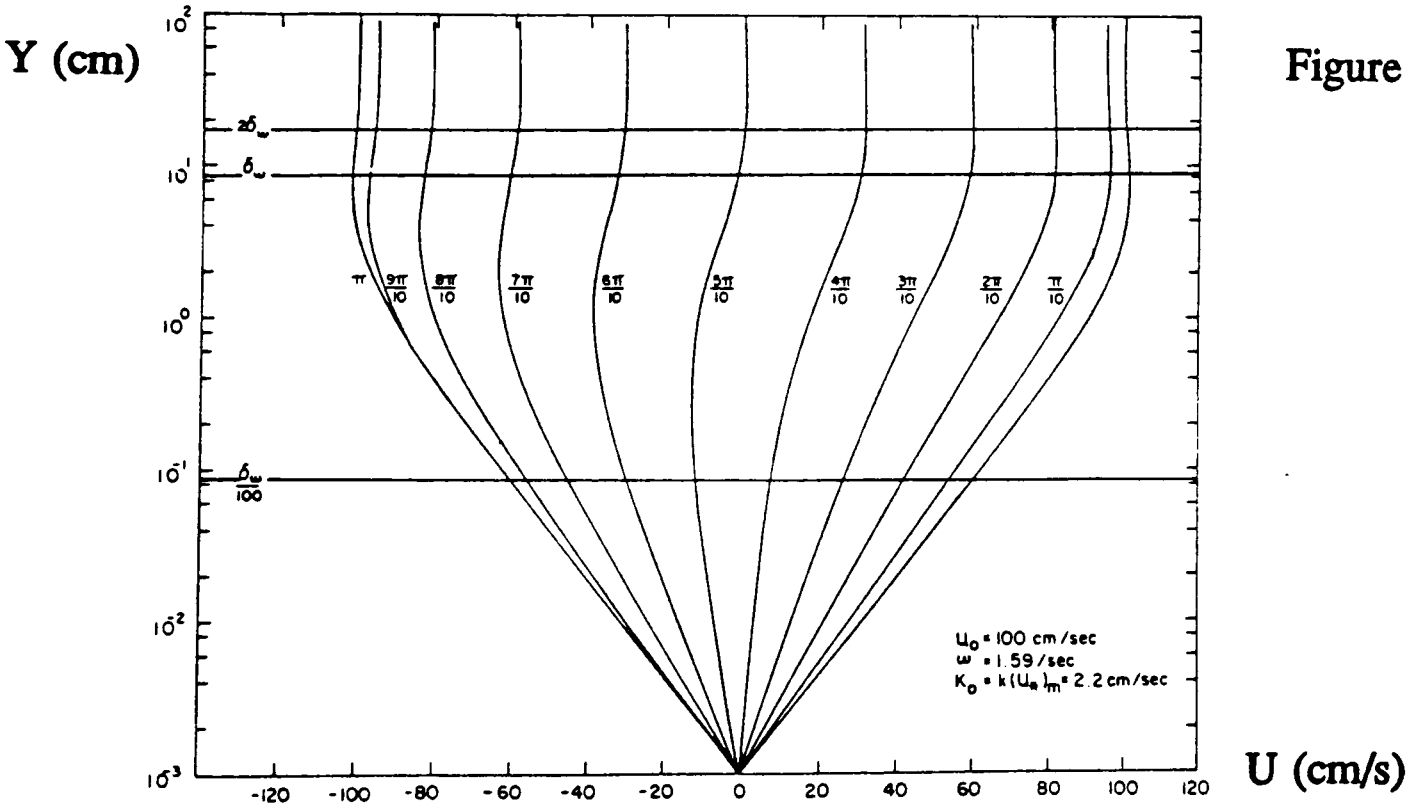
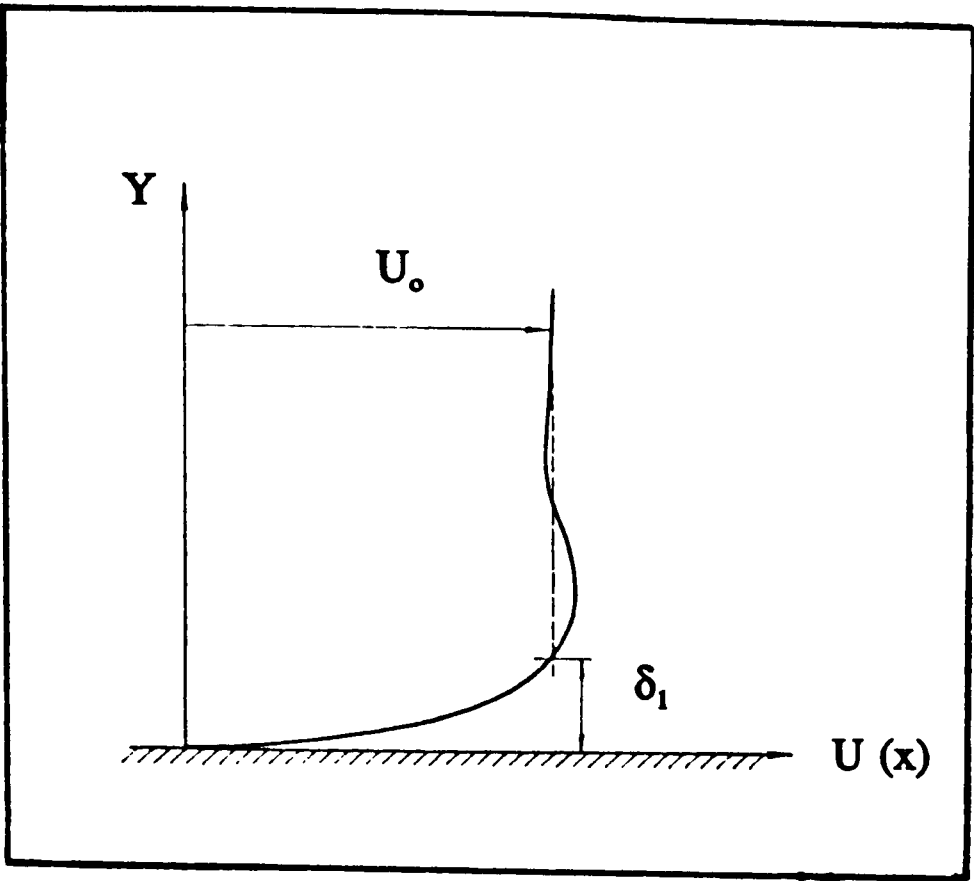


Figure 4.4

Sketches that illustrate features from the development and operation of the boundary layer model.

Figure 4.5 A sketch illustrating some of the definitions used in the development of the boundary layer model.

Figure 4.6 A sketch depicting the process whereby the 'driving' velocity time-series ($U_b(t)$) is re-ordered so that it starts at a flow reversal.

Figure 4.7 A sketch illustrating the disposition of the 40 ledges over the ripple profile, with ledge 21 at the crest.

Figure 4.5

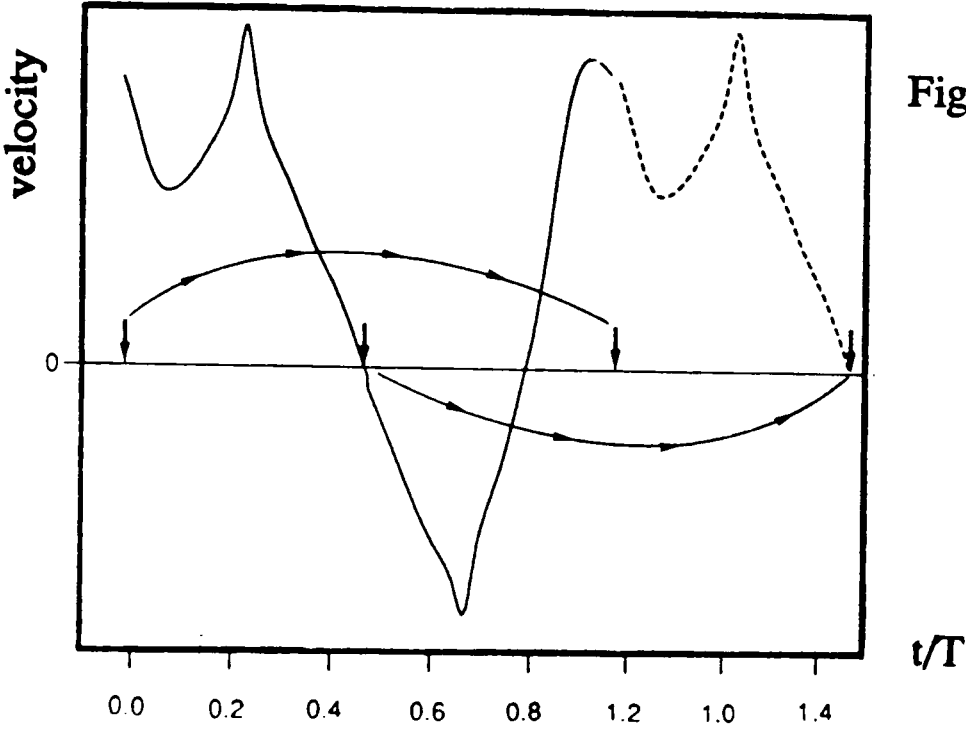
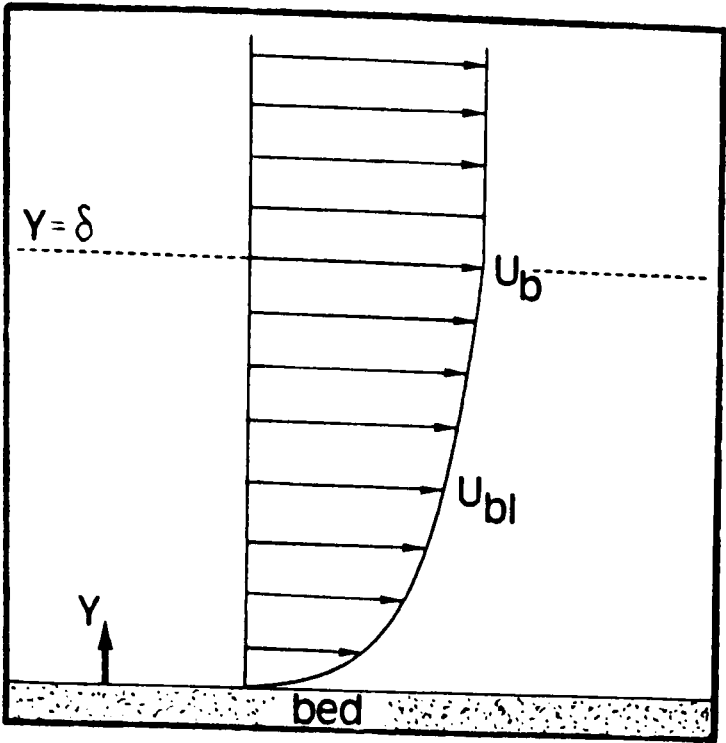


Figure 4.6

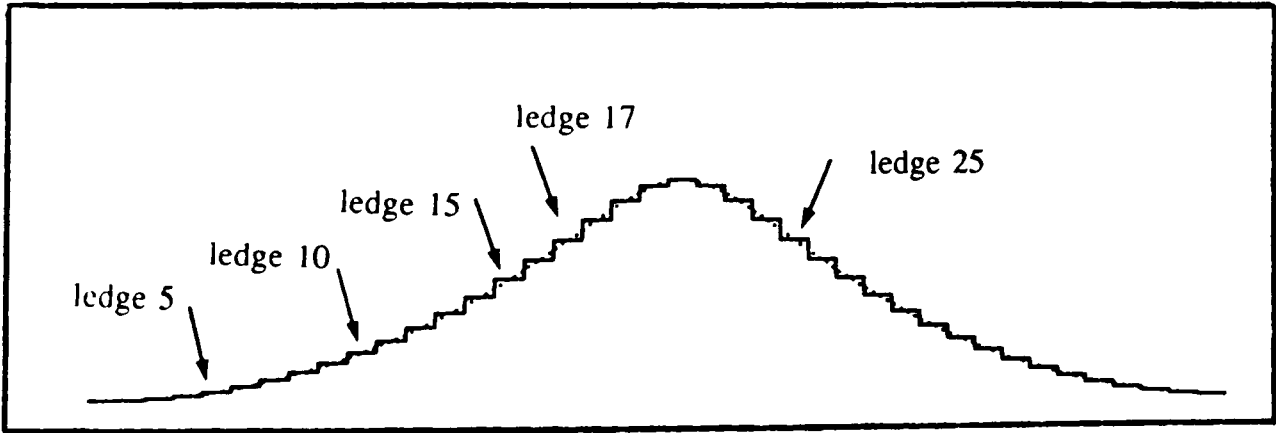


Figure 4.7

Some results aiming to show that the present adaptation of the Fredsoe (1984) model can recreate his original results.

Figure 4.8 (a)-(c) Comparison of (a) the parameter j' , (b) the (normalised) friction velocity U_* , and (c) the (normalised) boundary layer thickness, δ , with the results of Fredsoe (1984). ($a_o/k_s = 10, 100$.)

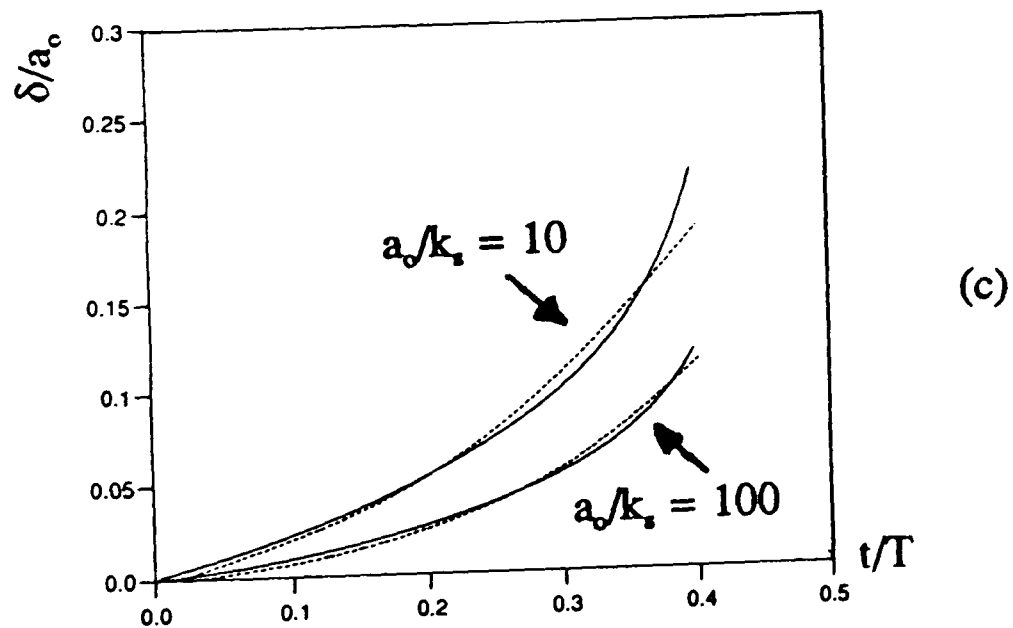
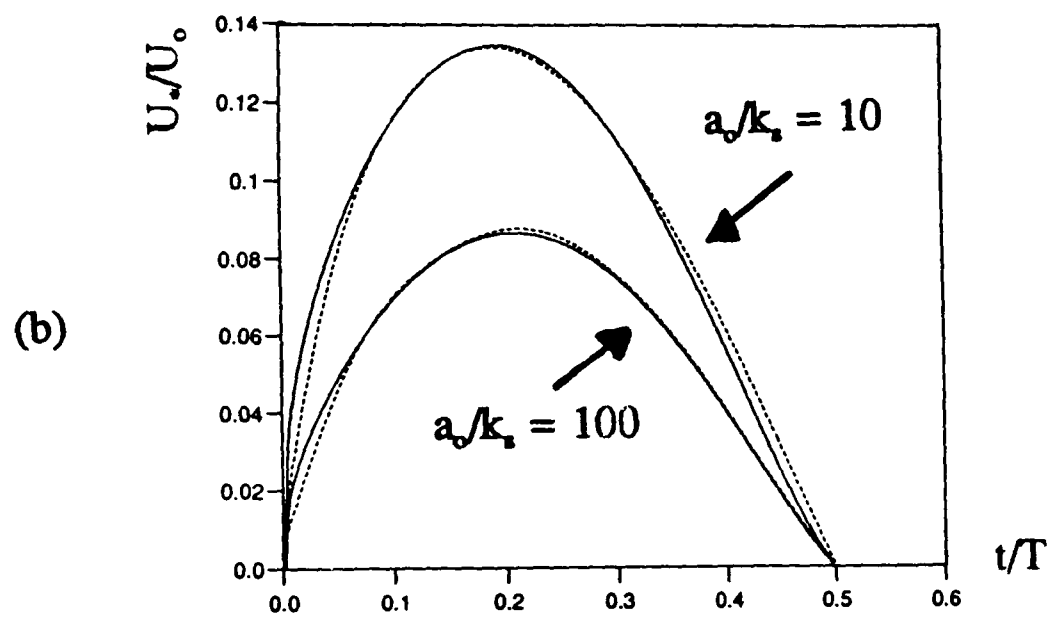
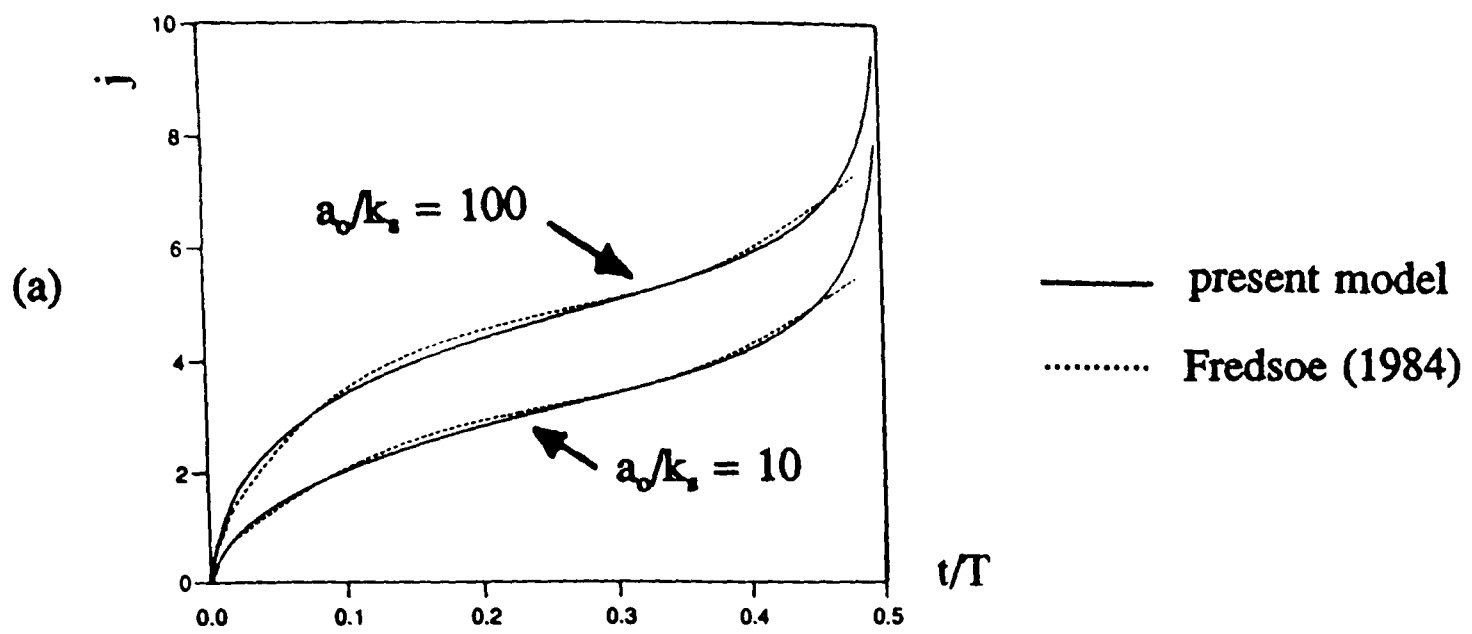


Figure 4.8 (a)-(c)

Results from the boundary layer model, when run with the settings $d_o/\lambda = 1.62$, $h/\lambda = 0.16$.

Figure 4.9 (a)-(d) A series of stacked diagrams, showing the variation of (a) the velocity time series, $R_b'(t)$, (b) the (non-dimensional) kinematic bed shear stress, $(\tau_b/\rho)''$, (c) the parameter j' , and (d) the (normalised) boundary layer thickness, δ/a_o , through a complete cycle. ($d_o/\lambda = 1.62$, $h/\lambda = 0.16$.)

Figure 4.10 The variation of (non-dimensional) kinematic bed shear stress, $(\tau_b/\rho)''$, through a complete cycle, at ledges 17 and 25. These two ledges are symmetrically placed with respect to the crest. Note the symmetrical nature of the two traces. ($d_o/\lambda = 1.62$, $h/\lambda = 0.16$.)

Figure 4.11 Variation of (non-dimensional) kinematic bed shear stress, $(\tau_b/\rho)''$, at ledges 5, 10 and 15, through a complete cycle. ($d_o/\lambda = 1.62$, $h/\lambda = 0.16$.)

Figure 4.12 Variation of (non-dimensional) kinematic bed shear stress, $(\tau_b/\rho)''$, over the ripple profile at $t/T = 0.1, 0.2, 0.3, 0.4$. ($d_o/\lambda = 1.62$, $h/\lambda = 0.16$.)

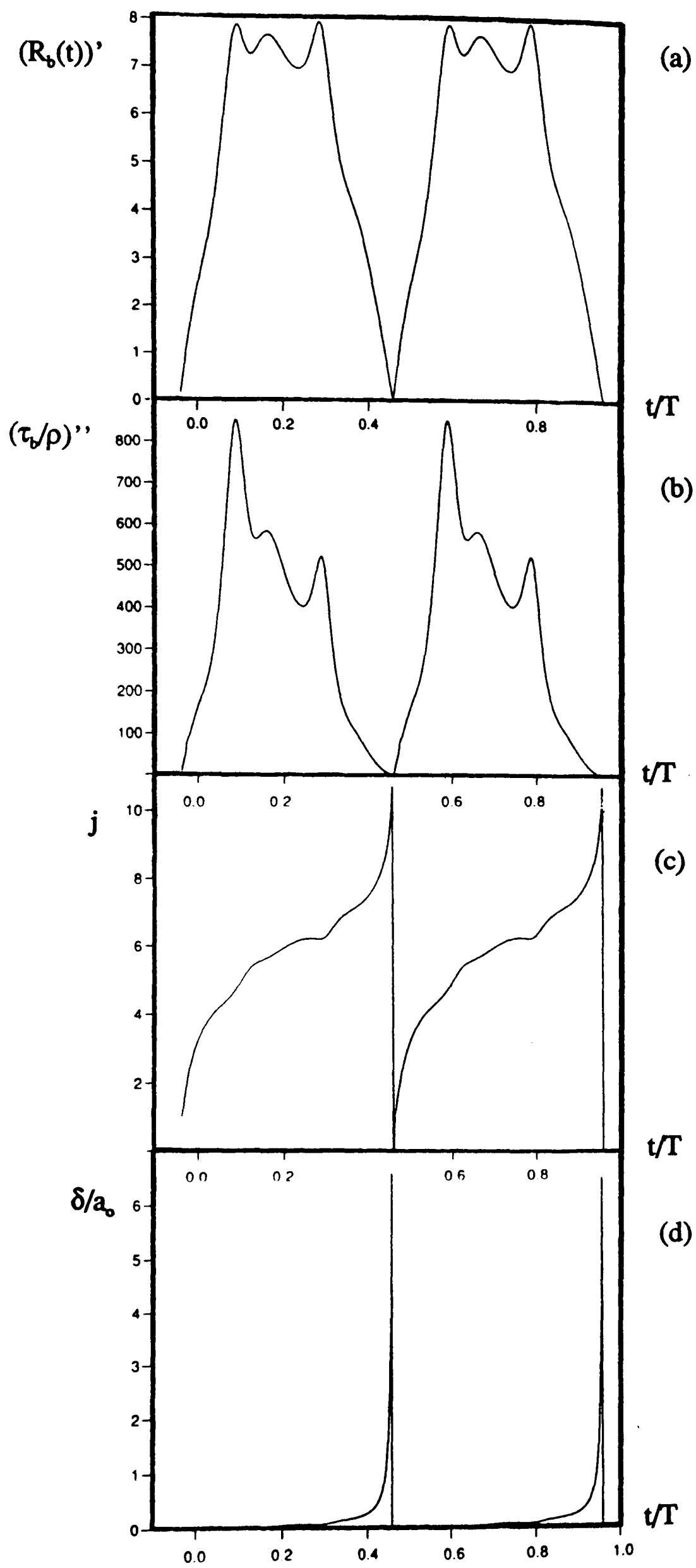


Figure 4.9 (a)-(d)

Figure 4.10

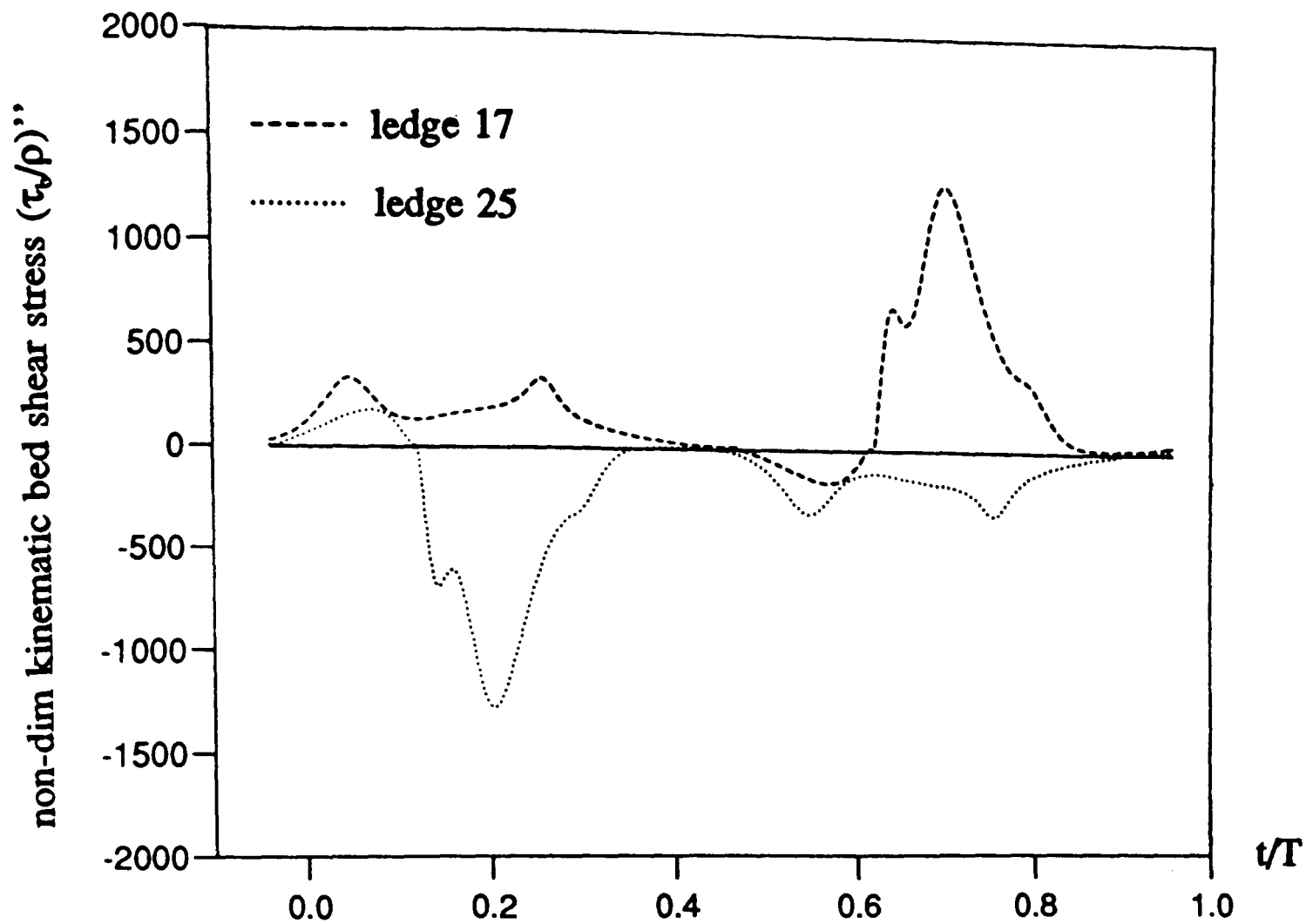


Figure 4.11

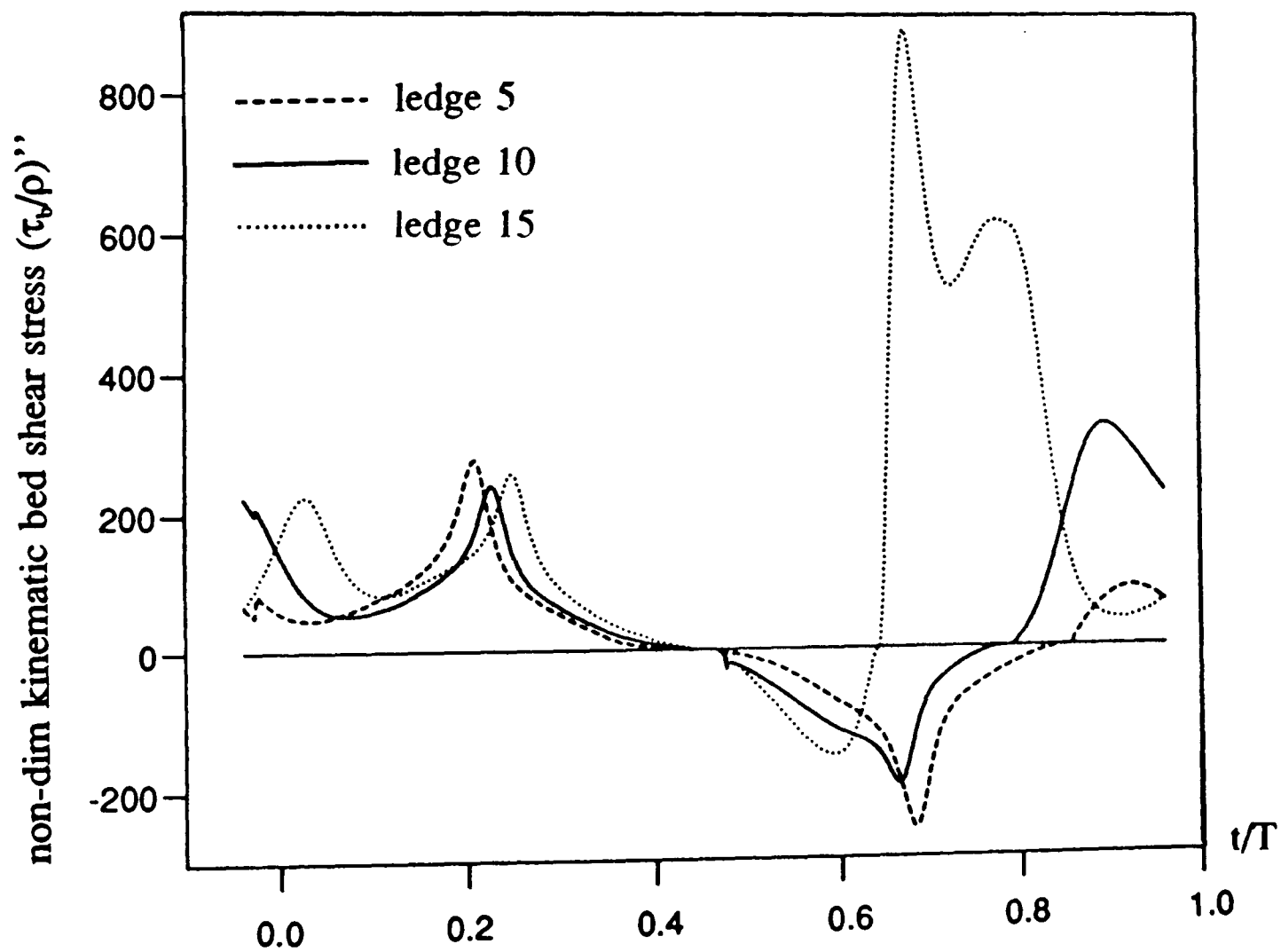
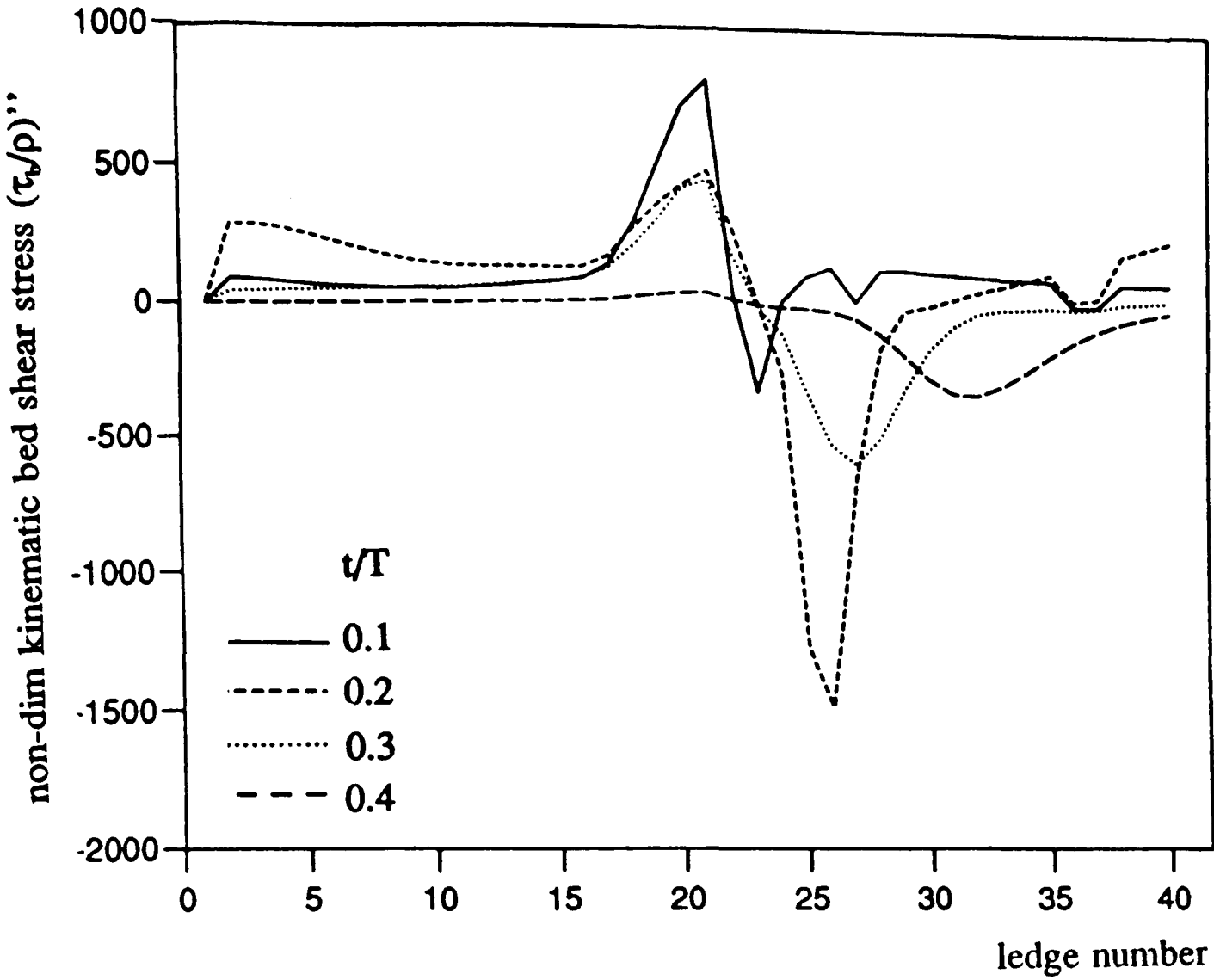


Figure 4.12



CHAPTER 5

STUDIES OF THE ENTRAINMENT AND SUSPENSION OF SEDIMENT

5.1 Introduction

The process of vortex shedding over ripples is a potent mechanism for the entrainment and suspension of sand from the bed. Once in suspension, this sand can play a key role in larger scale processes such as beach stability and off-shore bar formation. An understanding of the manner in which sand is entrained, its subsequent fate, and some 'feel' for the volumes of sediment involved, are important first steps in studying these larger scale problems. This chapter reviews relevant literature concerned with the suspension of sand over ripples, then outlines the computational algorithms used in the present study to simulate this process. The results from this *suspension simulation* are then compared with laboratory measurements of suspended sand concentrations over ripples. We (M.E.B and A.G.D) are most grateful to Dr. Catherine Villaret in this respect; her laboratory measurements of sediment concentrations were made specifically for the present study and form the backbone of the data comparisons.

A new notation has been applied in this chapter, which relates to the distance from the bed. In Chapter 4, the distance from an arbitrary point on the bed was defined as 'Y'. In this chapter, 'Y' specifically represents the distance above the ripple crest. The new 'distance from an arbitrary point on the bed' co-ordinate is Z.

5.1.1 Laboratory studies of suspended sediment over ripples

5.1.1 (a) *The manner in which sediment is entrained over ripples*

Bagnold (1946) and Sleath (1982a) have described the manner in which sediment is entrained over ripples. The following is a resume of Sleath's observations.

The opposing directions of motion of the flow up the stoss face and the (increasingly strong) flow up the lee slope caused by the growing vortex, deform the crest region into a cliff edge that overhangs the lee slope. As well as enhancing flow separation and vorticity generation, this cliff acts as a 'runway' for entrained sediment. Sand is carried as bedload up the stoss face of the ripple to be hurled off the cliff edge. Most passes over the growing vortex to land on the bed, but a small proportion falls into the growing vortex core itself and becomes trapped. [Nielsen (1984a) has studied

this trapping process theoretically, finding that sediment can become trapped within a vortex core as long as the induced velocity in the core is sufficient to overcome the fall velocity of the sediment.] Sediment is also entrained from the lee slope, where the increasing strength of the growing vortex entrains sediment from underneath it. Bagnold (1946) likens this to a spinning wheel touching the lee slope. According to Sleath, the interaction between the growing vortex and the vortex ejected from the neighbouring ripple enhances this process. On flow reversal, the newly ejected vortex carries its (trapped) sediment load with it as it travels over both the parent and neighbouring crest. This sediment becomes successively released from the ejected vortex as it loses strength, and settles to the bed.

5.1.1 (b) *The instantaneous suspended sediment regime*

The sediment entrainment and suspension regime described above produces quite complicated instantaneous suspended sediment concentration profiles. Experimentalists who have studied the time-varying concentration in oscillatory flow (eg. Nakato *et al* (1977), Sleath (1982a), Bosman (1982), Villaret (1992, 1993)) have used equipment such as optical probes, to produce time series of the concentration at particular locations. Their findings are broadly similar and summarised as follows. Time series of concentration obtained at the crest for a full cycle, exhibit four main peaks: two near flow reversal (associated with the passage of newly ejected vortices over the parent crest), and two smaller peaks near the time of maximum oscillatory flow (associated with the passage of ejected vortices from the neighbouring crest). Figure (5.1) , from Sleath (1984), illustrates this '4 peak' structure. A similar structure is also observed for concentrations at the trough, though there is a phase shift in the peaks reflecting the later passage of the vortices.

The phase of this '4 peak' structure is strongly linked to the phase of vortex passage, although Nakato *et al* (1977) find that it closely follows the phase of the vertical velocity. The number of peaks is linked to the passage of ejected vortices over successive ripples. At higher values of d/λ , vortices will pass more crests, thus causing more than 4 peaks. The magnitude of the concentrations depends both on the flow

regime and on the constituent sediment with its associated threshold of motion and fall velocity.

5.1.1 (c) *The time-averaged vertical concentration profile, $\overline{C}(Y)$*

Much attention has been given in coastal engineering literature to the time averaged vertical concentration, $\overline{C}(Y)$, where, in this chapter, Y is the distance above the ripple crest. The form for $\overline{C}(Y)$ which has been proposed by Nielsen (1979, 1984a) is

$$\overline{C}(Y) = C_o e^{-\frac{Y}{l_r}} \quad 5.1$$

where the lengthscale l_r is of the order of 1.4 ripple heights and Y is measured from the crest level. Figure (5.2) (from Nielsen (1984a)) illustrates some experimental data that justifies this choice for l_r . The datapoints for $l_r/h < 1.4$, $U/w_s < 10$ represent flow conditions where the fall velocity of the sediment (w_s) is high enough to prevent sediment trapping within the vortex cores and so inhibiting the suspension process. There is general agreement that equation (5.1) describes the form of $\overline{C}(Y)$ well, both in the laboratory (e.g. Villaret and Latteux (1992)) and in the field (e.g. Nielsen (1984b)). The value of C_o over ripples can be calculated using a formula proposed by Nielsen (1986):

$$C_o = 0.005\theta_r^3 \quad \text{where} \quad \theta_r = \frac{\theta}{\left(1 - \frac{\pi h}{\lambda}\right)^2} \quad 5.2 \quad (a, b)$$

where θ is the non-dimensional Shields parameter and θ_r is the value of this parameter following adaptation to account for flow enhancement over the ripple crest.

5.1.1 (d) *The net flux of sediment*

In a purely sinusoidal, first order wave regime, the net flux of sediment over each ripple should be zero - the transports in each half cycle being equal and opposite. In practice, however, the presence of non-sinusoidal waves, ambient currents etc., ensures

that the two half cycles are unequal. Consequently, a net flux of sediment occurs. Bijker *et al* (1976) studied this effect in the laboratory. They found that a stronger shoreward half cycle resulted in a net seaward transport of sediment, and vice-versa. Figure (5.3) illustrates why this is so, showing that the stronger shoreward vortex entrains more sediment, which is then carried seawards on ejection.

5.1.2 Field studies of the suspended sediment over ripples

There have been many studies of the suspended sediment regime over ripples. Recent studies have been aided by from improvements in measuring techniques (specifically acoustical and optical probes) and, for this reason, most emphasis is placed on modern work. Research in this area includes that of Hanes and Huntley (1986), Hanes *et al* (1988), Drake and Cacchione (1989) and Vincent and Green (1990). Four key questions are addressed in these field studies; what is the reference concentration C_o , what is the form of $\overline{C}(Y)$, how high does the suspended sediment travel into the water column, and what are the suspended sediment fluxes? We treat these in turn.

5.1.2 (a) *The reference concentration, C_o*

Experimentalists in the field have followed the lead of Smith and Maclean (1977), who studied the suspension of sediment over sand waves in steady flow. Smith and Maclean introduced the concept of linking the reference concentration C_o (taken at height $Z = Z_o$, where Z_o is the roughness lengthscale) to both the excess shear stress and the amount of sediment available for suspension. This linkage required a constant of proportionality, γ_o , which is called the resuspension coefficient. The expression for C_o proposed by Smith and Maclean (1977) is

$$C_o(Z=Z_o) = C_{bed} \frac{\gamma_o \left(\frac{\tau_b - \tau_c}{\tau_c} \right)}{1 + \gamma_o \left(\frac{\tau_b - \tau_c}{\tau_c} \right)} \quad 5.3$$

where C_{bed} is the concentration of sediment within the bed (≈ 0.65) and τ_b , τ_c are the (skin frictional) bed shear stress and threshold of motion respectively. The value of γ_o has been found to vary from $O(10^{-3})$ (Smith and Maclean (1977)) to $O(10^{-4})$ (Vincent and Green (1990)).

5.1.2 (b) *The form of $\overline{C}(Y)$*

Nielsen (1984b) found that the exponential decay form for the time-mean vertical concentration profile, $\overline{C}(Y)$, was applicable in the field as well as the laboratory. Glenn and Grant (1987) have derived a power-law form of $\overline{C}(Y)$ that is applicable to the wave-current case. Different versions of $\overline{C}(Y)$ are derived, depending (a) on whether the suspended sediment has damped out turbulence sufficiently to stratify the flow, and (b) on whether the height of interest (Y) is above or below the wave boundary layer.

5.1.2 (c) *The height of suspended sediment above the rippled bed*

Vincent and Green (1990) found that, in the field, suspended sediment can reach significant heights above the rippled bed. At their study site, sand was intermittently suspended to 30 cm above the bed, which was attributable to vortex shedding. Other researchers (eg. Williams J. (pers comm.)) have found suspended sediment this far above rippled beds in the field. There is some debate as to why it rises this high; one proposed mechanism is the superposition of long waves on the wave regime, which are 'seen' by the bed as currents.

5.1.2 (d) *Suspended sediment fluxes*

In the field, there is often a non-zero flux of sediment because of the presence of asymmetries in the near-bed flow (higher order waves, currents etc). There are two methods of calculating this time-mean flux. First, one can multiply a time-mean velocity profile with $\overline{C}(Y)$, the time-mean concentration profile. Second, one can form the product of instantaneous velocity and instantaneous concentration through the water column for a cycle, then time average the result. The first is the *product of the means*, the second the *mean of the products*. Vincent and Green (1990) found that the two

routes to the sediment flux gave different answers. They attribute this difference to the (highly significant) time instants when both the concentration and velocity are high - the product of means approach stifles this feature.

5.1.3 Theoretical studies of entrainment and suspension over ripples

5.1.3 (a) *Sediment entrainment*

Sediment moves as bedload over the ripple profile, ultimately to be entrained at the ripple crest. So-called 'bedload formulae' provide estimates of the bedload transport rate per unit width of flow, Q_b . One such formula of Meyer-Peter and Muller (1948) (source Dyer (1986)), relates Q_b to a power of the excess bed shear stress as follows:

$$\phi_b = 8 (\theta - \theta_c)^{\frac{3}{2}} = \frac{Q_b}{\sqrt{\gamma g D_{50}^3}} \quad 5.4 \quad (a, b)$$

where ϕ_b is the non-dimensional form of Q_b , and $(\theta - \theta_c)$ the non-dimensional excess bed shear stress. This formula was developed using data from flat beds of sediment. The term $(\theta - \theta_c)$, when raised to the power $3/2$, is proportional to U_*^3 and hence to the cube of the near-bed velocity. This cubing of the velocity has the effect of increasing the significance of velocity maxima and minima, relative to the more quiescent parts of the flow.

A first approximation to entrainment of sediment over ripples is to entrain sediment on the basis of the local flow microclimate at the crest, where a 'flat-bed' bedload formula should be applicable. Macpherson (1984) introduced sediment particles some distance above the ripple crest. His entrainment rule related the number of 'unit particles' released to a power of the velocity at the crest. The resulting concentration profiles provided qualitative information, but could not be converted to actual concentrations. Asp Hansen *et al* (1991) used the Fredsoe (1984) boundary layer model and the Meyer-Peter Muller bedload formula to predict sediment entrainment. Their entrainment calculations and 'sediment release' were performed part way down the stoss face. The reasoning behind this was that the largest shear stress would occur there.

Nielsen (1992) introduced the concept of so-called 'pick-up' functions, in order to ascertain sediment fluxes in the vertical. Simply stated, Nielsen's fluxes take the form

$$Q(Z, t) = p(t) \cdot F(Z) \quad 5.5$$

where $Q(Z, t)$ is the flux of sediment in the vertical, $p(t)$ the pick-up function and $F(Z, t)$ the distribution function of sediment in the vertical. The dimensions of $p(t)$ are those of sediment flux. The form of $p(t)$ reflects the entrainment of sediment from the bed in time, so shares many features with bedload formulae.

5.1.3 (b) *Movement of suspended sediment - convection versus diffusion*

Once sediment is introduced into the flow, it is necessary to have a means of moving it around. There has been much more theoretical study of suspended sediment movement over ripples, utilising one of two approaches; a Lagrangian, deterministic approach replicating convection, where sediment is moved at the local flow speed, or a diffusive approach using a coefficient of sediment diffusivity ϵ_s :

$$\frac{\partial}{\partial z} \left[\epsilon_s \frac{\partial C}{\partial z} + w_s C \right] = \frac{\partial C}{\partial t} \quad 5.6$$

The first term in equation (5.6) represents the turbulent diffusion of sediment in the vertical, which aids suspension. The second term represents the settling out of sediment. It is the difference between these two terms that dictates the time rate of change of concentration at height Z . The whole ethos of equation (5.6) is statistical, requiring a randomised distribution of sediment. Homma and Horikawa (1962) have studied the usage of equation (5.6), choosing different formulations for the sediment diffusivity. If the time-mean concentration $\overline{C}(Y)$ is used, and ϵ_s is assumed constant with height, then equation (5.6) becomes

$$\epsilon \frac{\partial \bar{C}}{\partial Y} + w_s \bar{C} = 0 \quad 5.7$$

On integration, this gives an exponential decay form for $\bar{C}(Z)$ that is analogous to equation (5.1).

In a theoretical study on the trapping of sediment within vortex cores, Nielsen (1984a) argued that convection is the dominant process in the suspension of sediment above ripples. Nielsen noted that the instantaneous concentrations (i.e the 'four peak' structure) clearly mimic the motion of ejected vortices. As well as this, the 'four peak' structure occurs for a wide range of grain sizes. This would not be the case if diffusion was the dominant mechanism. If it was, differences in fall velocity would have a marked affect on the suspension regime. The eddy diffusivity approach (via equation (5.6)) does not lend itself to the case of vortex shedding, because the suspended sediment field is far from random. Nielsen (1988) tried out three different methods of treating suspended sediment over ripples. Of the three, he found that the worst was the method based on eddy diffusivity, whilst the best was a simplistic 'grab and dump' model that crudely replicated sediment laden vortices. Recently, Nielsen (1992) linked the relative importance of convection and diffusion to grain size, stating that diffusion becomes progressively more important as the grain size decreases.

The most appropriate models of sediment suspension over ripples (Macpherson (1984), Asp Hansen *et al* (1991), c.f Chapter 3) have used a Lagrangian tracking scheme for the suspended sediment because of its purely convective nature. Figure (5.4) shows some of the results of Asp Hansen *et al*, reproduced from Fredsoe and Deigaard (1992). It shows vorticity reaching far up into the flow, carrying swirls of suspended sediment with it. Asp Hansen *et al* found generally good agreement between their computed profiles of $\bar{C}(Y)$ and experimental data. This is a direct consequence of the way their model allows sediment to migrate far from the bed.

5.2 The experimental data of C. Villaret (1992, 1993)

A series of experiments on wave and current flows above rippled beds have been carried out in a large wave flume (79 x 1.5 x 1.5m) at the Laboratoire National d'Hydraulique (E.D.F). Details of the experimental set-up and of the results obtained have been presented by Villaret and Latteux (1992). The two experiments reported here (Villaret (1992, 1993)) were carried out using the same set-up.

Both experiments were carried out with regular, progressive waves (reflection coefficient < 0.1) above a bed of fine sand ($D_{50} = 90 \mu\text{m}$, $w_s = 0.7 \text{ cm/s}$). After equilibrium ripples had formed, measurements of the time-varying velocity and sediment concentrations were made over the crest and the trough positions. The velocities were measured using an ultrasonic velocimeter, while the concentration measurements were obtained with an optical turbidity probe (OPCON). In Test 1, the ripples were long crested, while in the more vigorous conditions of Test 2, the ripples displayed a less regular pattern. The experimental parameter settings and measured ripple dimensions were as follows:

TEST 1

$T = 2.0 \text{ s}$, $\lambda = 6.3 \text{ cm}$, $h = 1.0 \text{ cm}$, $U_o = 16.0 \text{ cm/s}$, $d = 45.0 \text{ cm}$, $H = 9.0 \text{ cm}$,
with derived parameters: $d_o/\lambda = 1.62$, $h/\lambda = 0.16$, $RE = 8150$ and $M = 17.6$.

TEST 2

$T = 2.0 \text{ s}$, $\lambda = 6.3 \text{ cm}$, $h = 0.7 \text{ cm}$, $U_o = 26.0 \text{ cm/s}$, $d = 60.0 \text{ cm}$, $H = 19 \text{ cm}$,
with derived parameters: $d_o/\lambda = 2.63$, $h/\lambda = 0.11$, $RE = 21500$ and $M = 46.4$.

In Test 1, the measured residual velocities were small, while in Test 2, there was a near bed drift in the wave direction of 1-2 cm/s. In the following comparisons, the waves have been assumed to be purely sinusoidal, and drift velocities have been ignored. Figure (5.5) shows where the ripples formed in Test 1 and 2 fit in on the ripple occurrence graphs of Nielsen (1979).

Figures (5.7a,b) illustrate some of the concentration data obtained over the crest and trough in both tests. (Figure (5.6) indicates the position of these and the Test 2 measuring positions.) The data points were obtained over one of the ripples, each point being an ensemble average taken over 50 wave cycles. For Test 1, the form of figure (5.7a) clearly shows the '4 peak' structure referred to in §5.1.1(b), and the phase lag of the trough measurements relative to the crest. Passage of the ejected vortex over the parent crest is noted to occur about 20° after flow reversal. Figure (5.7b) shows some equivalent data from Test 2. The '4 peak' structure is still evident, but in this case the ejected vortex passes over the parent crest 20° prior to flow reversal.

5.3 The suspended sediment simulation

5.3.1 Introduction

The present simulation of the suspended sediment regime requires the usage of both the hydrodynamical and boundary layer models. The hydrodynamical model is used to develop a velocity time series at the crest. This is the driving velocity for the boundary layer model, which, when run, gives the rate of sediment entrained at the crest at each time step. The sediment thus entrained is tracked within the hydrodynamical model, using a Lagrangian tracking scheme with the sediment fall velocity included. Ultimately, this (tracked) suspended sediment falls to the bed.

5.3.2 Simulating the entrainment of sediment

In this chapter, the entrainment of sediment is based solely on conditions at the ripple crest. A time series of velocity at the crest level is obtained using the hydrodynamical model. This is the time series $R_b(t)$, the driving velocity for the boundary layer model. It is fed into the boundary layer model to produce a companion time series of kinematic bed shear stress $(\tau_b(t)/\rho)$ for the crest position. The non-dimensional form of the Meyer-Peter-Muller bedload formula (equation (5.4a,b)) is employed to establish the (non-dimensional) rate of sediment entrainment from the crest. The threshold value of Shields parameter (θ_c) has been obtained using figure (5.8), which is an adapted form of the Shields curve (Sleath (1984)). Komar and Miller

(1973) and Madsen and Grant (1975) also provide similar information on the threshold value of the Shields parameter. The question of the use of a threshold of motion is discussed in more detail in §5.4.1.

The above procedure gives rise to a time series of ‘entrainment values’, $\phi_b(t)$, which is read into the hydrodynamical model program as it runs. At timesteps when the threshold of sediment motion is exceeded, $\phi_b > 0$, and entrainment occurs, while $\phi_b = 0$ indicates no sediment entrainment. For those time steps when threshold is exceeded, a *computational particle* is released at the vorticity calculation/release point (z_T), bearing the associated ϕ_b value with it.

5.3.3 Simulating the suspension of sediment

Particles released into the flow are tracked in a lagrangian manner, moving at the local flow velocity, but with an added fall component w_s , which is obtained either from the experimental account or from figure (5.9) (from Dyer (1986)). The lagrangian tracking scheme applied is

$$Zsand_{new} = Zsand_{old} + (U_z, V_z - w_s) \cdot \delta t \quad 5.8$$

where $Zsand_{old}$, $Zsand_{new}$ are the old and new positions of each sand ‘particle’ in the z plane after a time step δt , and U_z , $V_z - w_s$ are the respective velocity components.

Ultimately, each particle hits the bed. When this happens, its position is recorded along with the associated ϕ_b value, and then it is removed from the simulation. Steady state conditions are usually reached after 4 cycles of sand entrainment, at which time the number of particles in suspension is approximately constant from cycle to cycle (figure 5.12).

5.3.4 Obtaining instantaneous concentrations

To obtain instantaneous concentrations, the method of Macpherson (1984) is used. A ‘box’ of side $\lambda/10$ (half the size used by Macpherson) is formed, with the point of interest as its centre. The model is run until the suspension regime is in a steady state, then at each time step, particles within the box have their ϕ_b values summed. The

resulting time series gives cumulative values of ϕ_b at each time step. These are converted to actual concentrations in the manner outlined in Appendix 2. Figure (5.10) illustrates particles in suspension, some of which have entered the measuring box. The resulting raw time series of concentration are very noisy, so a 21 point moving average is applied.

5.3.5 The vertical concentration profile $\overline{C}(Y)$

Figure (5.11) illustrates the grid used to obtain the time-averaged vertical concentration profile $\overline{C}(Y)$. The measuring grid provides spatial averaging as well, because the strips span the whole ripple profile. This grid is used fully in the knowledge that $\overline{C}(Y)$ is not normally spatially averaged. Efforts to produce profiles for $\overline{C}(Y)$ without these (wide) strips failed, because the results showed too much scatter and did not provide a clear, unequivocal picture of the nature of $\overline{C}(Y)$. At each time step, all the particles in suspension are asked which part of the grid they are in, and the cumulative ϕ_b value for each strip updated. Conversion to actual concentrations follows the same method as §5.3.4.

5.4 Results

5.4.1 The choice of the value of τ_c

In §5.3.2, it was stated that the value of τ_c (and hence θ_c) was obtained using figure (5.8). The sand used in the two tests of C. Villaret had a median diameter (D_{50}) of 90 microns, which corresponds to a threshold of motion $\tau_c = 0.15 \text{ N/m}^2$. Computationally, this value was found to be much too high; little or no sediment was entrained at the crest. Physically, this could be due to the difficulties in defining thresholds of motion in unsteady flows. Given these uncertainties, it was decided to treat τ_c as a free parameter. The value of τ_c ultimately chosen, in all cases, was one third of the estimate from figure (5.8) (e.g. 0.05 N/m^2 for Tests 1 and 2).

5.4.2 Results for Test 1 ($d_s/\lambda = 1.62$, $h/\lambda = 0.16$)

Figure (5.13) illustrates the motion of growing and ejected vortices during the

first half cycle of the converged solution. While the growing vortex forms over the lee slope, the ejected vortex passes over both the parent and neighbouring crests, hitting the bed shortly afterwards. Vortex centres remain fairly close to the bed, not venturing more than a ripple height above the crests. The phase instants associated with the passage of the ejected vortex are important for interpreting subsequent figures. This vortex passes the parent crest at $t/T = 0.10$, the first trough at $t/T = 0.20$, the neighbouring crest at $t/T = 0.30$ and, finally, the second trough at $t/T = 0.45$.

Figure (5.14) shows the associated motion of sediment particles in Test 1, with the vortex centres marked by stars. One of the measurement boxes for the instantaneous concentration profiles is shown over the middle crest.

When studying figure (5.14), three quite striking features are apparent. Firstly, the particles faithfully follow the motion of the vortices. Secondly, the particles do not diffuse within a vortex, but rather form a ring around the vortex centre. Thirdly, the particles remain relatively close to the bed.

At $t/T = 0.05$, the particle-laden ejected vortex travels towards the parent crest. The ejected vortex itself passes over at $t/T = 0.10$; meanwhile particles entrained in the crest region pass over the top of the growing vortex. During the interval $t/T = 0.15$, 0.20 , 0.25 , the ejected vortex carries particles across the trough, while entrained particles from the crest are simply thrown over the top of the growing vortex to land behind. The time instant $t/T = 0.25$ shows this latter group of particles travelling very close to the bed. At $t/T = 0.30$, the ejected vortex meets the neighbouring growing vortex, which forces particles upwards. By this time, the growing vortex is capturing particles entrained at the crest. Subsequent time instants illustrate the increasing dominance of the growing vortex. Particles travelling around this vortex appear to be checked by the flow at the near-crest stagnation point. The few remaining particles still being carried by the ejected vortex travel over the growing vortex and descend towards the bed. By $t/T = 0.50$, the flow at the crest has reversed and the recently growing vortex is free to move away with its particle load. The whole process then repeats itself in the second half cycle.

Figures (5.15a-d) show time series of concentration obtained at four positions over the ripple profile: 0.5 and 1.0 cm above the crest, and 1.5 and 2.0 cm above the trough. These are the measuring positions of Test 1, illustrated in figure (5.6). In figure (5.14), the box used to obtain the 'crest 1.0 cm' time series is shown. Casual inspection of the time series shows that the results from the two half cycles are not symmetric. This point is discussed in §5.4.4, the subsection concerning the sensitivity of the present simulation.

Figures (5.15a,b) have very similar features. They both show two major pairs of peaks at $t/T = 0.10, 0.60$, which correspond to the passage of the ejected vortex over the parent crest. The double spikes are due to the front and back of the vortex passing through, a feature clearly evident in figure (5.14). The lesser pairs of peaks at $t/T = 0.30, 0.80$ are formed by the passage of the ejected vortex over the neighbouring crest. There is a 60% reduction in the concentrations from the lower to the upper measuring position.

Figure (5.15d) shows very clear concentration peaks at $t/T = 0.20, 0.70$ due to the passage of an ejected vortex over the first trough. However, the peaks clustered around $t/T = 0.40, 0.90$ are from two agencies: the passage of an ejected vortex, and the swirl of particles around the growing vortex. The spikes at $t/T = 0.375, 0.875$ correspond to the former, and those at $t/T = 0.45, 0.95$ to the latter. Figure (5.15c) shows similar features to figure (5.15d), except that this higher measuring position does not record particles travelling around the growing vortex. A comparison of the concentrations between figures (5.15c) and (5.15d) is awkward. If we compare the spikes at $t/T = 0.20$, there is a 20% increase in concentration at the upper position. The other three main spikes suggest a reduction of about 50% from the lower to the upper positions. The peaks in the trough time series lag those at the crest by approximately 35° of phase.

Figure (5.16) shows the fate of individual particles released at three phase instants in the first half cycle. The particle released at $t/T = 0.10$ passes over to the next ripple to be swept around by its growing vortex. The reversing flow brings it back to the parent ripple, where it is again spun around a growing vortex (this vortex being on the

left side of the ripple). Finally, the particle travels rightwards, hitting the bed at the next crest. The timespan of this motion is about 1.5 cycles. The particle released at $t/T = 0.20$ simply travels over the growing vortex to land behind it. The particle released at $t/T = 0.30$ is captured by the growing vortex, which throws it in the opposite direction. This particle is then forced to the bed by the rotation of the new growing vortex formed at the start of the second half cycle.

5.4.3 Results for Test 2 ($d/\lambda = 2.63$, $h/\lambda = 0.11$)

The flow regime in Test 2 is much more vigorous than Test 1, and represents flow conditions outside those commonly studied by ripple researchers.

The 'vortex motion' plot (figure (5.17)) shares many features with the $d/\lambda = 2.5$ run discussed in §3.3.5, namely early ejection of the growing vortex and the passage of the ejected vortex over numerous ripple crests. The ejected vortex passes the parent crest at $t/T = 0.05$, then successive crests at $t/T = 0.20, 0.30$ with intermediate trough passages at $t/T = 0.15, 0.25$ and 0.40 .

Figure (5.18) shows a far more complicated particle behaviour pattern than for Test 1. As a consequence of this, each plotted time instant is discussed separately;

$t/T = 0.05$

A whirl of particles surrounds the ejected vortex as it passes over the parent crest, while particles entrained at the crest pass over the growing vortex. The large (near-bed) cluster of particles over the stoss face of each ripple has been marooned there by the recently killed ejected vortex from the previous cycle. This cluster will be referred to as the *relic cluster*.

$t/T = 0.10$

The ejected vortex travels towards the first trough. Particles that have been entrained at the crest travel under the ejected vortex, remaining in the trough region. The relic cluster is forced towards the neighbouring crest.

$t/T = 0.15$

The relic cluster is now over the neighbouring crest. Particles entrained at the crest are still passing over the growing vortex.

$t/T = 0.20$

The ejected vortex passes over the neighbouring crest. The relic cluster becomes increasingly intermingled with the sand carried by the ejected vortex. Entrained sediment passes over the growing vortex and travels near the bed towards the neighbouring crest.

$t/T = 0.25$

The ejected vortex (with the captured relic cluster) is now over the second trough. The development of the growing vortex forces entrained particles higher from the bed.

$t/T = 0.30$

The combination of the ejected vortex and the relic cluster produces a large accumulation of particles above the second crest. Entrained particles travel over the growing vortex towards the neighbouring crest.

$t/T = 0.35$

The combination of the ejected vortex and relic cluster pass over the growing vortex, which is forming two ripples to the right of the parent ripple. By now, the ejected vortex has weakened in strength and is losing its identity within the flow. However, the growing vortex is strong enough to capture particles.

$t/T = 0.40$

The growing vortex now dominates over the weakened ejected vortex, forcing its load towards the bed.

$t/T = 0.45$

The growing vortex now captures all the entrained particles, while the combined ejected vortex and relic cluster approach the bed.

$t/T = 0.50$

The growing vortex and its load are ejected. Meanwhile, the killing of the weak ejected vortex leaves the combined load isolated over the lee slope. This cluster is the relic cluster for the next half cycle, during which the entire process repeats itself.

Figures (5.19a,b) show time series of concentration for the crest and the trough respectively. The major peaks are labelled alphabetically, with dashes representing

equivalent peaks in the second half cycle. In figure (5.19a):

A,A' at $t/T = 0.0, 0.50$

Formed by the passage of the front of the ejected vortex over the parent crest.

B,B' at $t/T = 0.075, 0.575$

Formed by the back of the ejected vortex passing over the parent crest.

C,C' at $t/T = 0.15, 0.65$

Formed from the combination of the front of the ejected vortex and the relic cluster passing over the neighbouring crest.

D,D' at $t/T = 0.30, 0.80$

Formed by the ejected vortex and the relic cluster passing the third crest.

In figure (5.19b):

E,E' at $t/T \approx 0.10, 0.60$

Formed by the combined effect of the front of the ejected vortex and the relic cluster passing the first trough.

F,F' at $t/T = 0.20, 0.70$

Formed by a combination of the relic cluster and the front of an ejected vortex over the second trough.

G,G' at $t/T = 0.40, 0.90$

Formed by three agencies over the third trough - the combination of the ejected vortex and the relic cluster, along with the front edge of the growing vortex.

Figure (5.20) is similar in format to figure (5.16), though the release times chosen are different. The reason for this is that the previous three choices ($t/T = 0.10, 0.20, 0.30$) gave uninformative trails. A particle released at $t/T = 0.15$ travels over the growing vortex to land in the trough region. For release at $t/T = 0.25$, the growing vortex is strong enough to influence the motion of the released particle, causing it to loop backwards towards the crest. A particle released at $t/T = 0.35$ stays in suspension far longer. The rotation of the growing vortex forces it backwards (leftwards). Flow reversal at $t/T = 0.50$ further aids the leftwards motion of the particle, allowing it to travel two ripple crests to the left. As the particle reaches the second ripple crest to the

left, it is spun backwards (rightwards) around the growing vortex. A further flow reversal now occurs; the flow is now rightwards again, carrying the particle with it. Finally, the particle settles out onto the bed in the crest region of the ripple that is immediately to the left of the parent ripple. The timescale for the motion of this particle is about 1.5 cycles.

5.4.4 Sensitivity tests

Figures (5.21a,b) and (5.22a,b) show how variations in τ/ρ , w_s , v and the release height of the particles above the crest affect one of the concentration profiles (the 'crest 1.0 cm' profile for Test 1). The variation of all four parameters has a significant effect on the magnitudes of the peaks, but relatively little effect on their phases. Changes in τ/ρ affect the magnitudes simply by increasing or decreasing the ϕ_b values. However, it is not immediately clear why variations in the other three parameters have such a profound effect on the magnitudes. Figure (5.24) shows the effect of varying w_s on the trajectories of particles released at $t/T = 0.35$. Clearly, the effect of changing w_s on the trajectories is minimal. This is also the case for variations in the release height and v as well. The fundamental cause of the sensitivity of the magnitudes is the choice of box size. Figure (5.23) shows that the magnitudes of the concentration profiles are significantly affected by the choice of box size. Only three test cases are shown in figure (5.23); a more detailed study showed that the results only became insensitive to the dimensions of the box when it was unacceptably large compared with the ripple dimensions.

Why is the model so sensitive to the box size ? Figure (5.25) contains two graphs that overlay each other. The complete graph shows the time series $\phi_b(t)$ for Test 1, which is, essentially, the rate of introduction of sediment at the crest. The doctored graph shows the scale from the plot of the cumulative ϕ_b values that forms the basis for the instantaneous concentration for the 'crest 1cm' case (c.f.figure (5.15a)). Inspection of these two figures shows that the cumulative ϕ_b values are similar in magnitude to the ϕ_b values of individual particles. This implies that the concentration values can be significantly affected by the inclusion (or otherwise) of a few stray

particles. Variation in w_x , for example, causes subtle changes in particle trajectories. As a consequence of this, one or two extra particles will be included or excluded from the measuring box. Each individual particle contributes a significant proportion of the magnitude. Therefore, a small change in w_x has incurred a large change in the magnitude of concentration measured by the box.

This argument is further supported by the instantaneous concentration profiles (figures (5.15), (5.19)). In these figures, the results from the two half cycles are not the same. Small differences in the predicted flow regime over the two half cycles have caused large differences in the magnitude of the concentration profiles.

5.4.5 Comparisons with the data of Villaret (1992, 1993)

Figures (5.26 a-d) and (5.27a,b) show comparisons between the experimental data and model results for the time series of concentration for Tests 1 and 2 respectively. In these figures, only the fluctuating components of concentration are compared, i.e. the mean concentration has been removed in order to isolate the time-varying components. The tables at the foot of these figures record the values of mean concentration that have been removed.

Figures (5.26a,b) are the comparisons for the two crest time series of concentration for Test 1. The phases of the four concentration peaks agree well with the data, although there is a tendency for the model peaks in the second half cycle to be delayed relative to the data. This is indicative of asymmetry in the data itself, possibly due to the experimental conditions. However, there is a mismatch in both the magnitude of the peaks, and, more seriously, in the mean concentrations (see inset table). The model peaks are consistently larger than the peaks in the data. A comparison of the mean concentrations shows the model underpredicting by an order of magnitude for the 'crest 1.0 cm' case, and by about 50% for the 'crest 0.5 cm' case. Similar features can be observed in figures (5.26c,d) for the trough. Again, the phase agreement is generally good, with the first half cycle better than the second. The magnitudes of the peaks show improvements over the crest cases, but again, the mean concentrations are an order of magnitude too low.

Figure (5.27a) is a comparison of instantaneous concentrations over the crest for Test 2, with the mean component removed as before. It shows rather poor agreement in both the general features of the comparison and in the phases of the 'events'. If the centres of the peaks A,A' and B,B' are taken as the actual passage time of the ejected vortex over the parent crest, then the model lags the data by nearly 30° of phase. For the time of passage of the ejected vortex over the neighbouring crest (peak C,C'), the phase agreement is improved. The model leads the data by about 20° of phase in the first half cycle, and agrees almost exactly in the second. Interestingly, the mean concentrations are slightly more encouraging than for the Test 1 cases - 3.96 g/l as opposed to 11.15 g/l from the data. The model is underestimating the mean concentration by 64%

The major feature of the Test 2 comparisons is the over-dominant peaks (C,C' and D,D') in the model results. The peaks C,C' do appear in the data, but at a much reduced size, while the peaks D,D' are not in the data at all. The reason for the structure and presence of these large peaks is due to the relic cluster in the model, which is augmented with the ejected vortex as it travels, significantly increasing its sediment load. This feature is further exascibated by the very low fall velocity, which allows the relic cluster to remain in the flow. The presence of the relic cluster is an artefact of the hydrodynamical model whereby the ejected vortex comes too close to the bed (at $t/T \approx 0.45$ in figure (5.17)) and is killed. This does not happen in reality, as evidenced in the data.

Figure (5.27b) is the equivalent trough comparison. In this case, the agreement in the phases of key events is rather better, though a comparison of the gross features is still poor. The primary peaks E,E' (associated with the passage of the ejected vortex over the first trough) show excellent phase agreement. However, the peaks F,F' (associated with passage of the ejected vortex over the second trough) show the model leading the data by about 20° of phase. The problem of the relic cluster accounts for the large, unwarranted peaks (G,G') in the results. A comparison of the mean concentrations (5.93 g/l for the model versus 10.22 g/l for the data) shows a model underestimate of 42%.

Figure (5.28) shows the time- and horizontally averaged normalised concentration profiles, $\overline{C}(Y)$, for Tests 1 and 2. They are plotted alongside the exponential profile of $\overline{C}(Y)$ proposed by Nielsen (1979, 1984a) (see §5.1.1 (c)). The use of spatial averaging to obtain $\overline{C}(Y)$ has provided informative results. The two test cases are treated in turn:

TEST 1

The model profile of $\overline{C}(Y)$ shows a kink near the crest itself, followed by a sharp decrease. At about half a ripple height above the crest, $\overline{C}(Y)$ is only 30% of its peak value, and it decreases to zero about 1.3 ripple heights above the crest. A visual comparison with the Nielsen profile shows the model values of $\overline{C}(Y)$ overestimated near the crest itself, then dying away more rapidly with height. Some care is required in order to make a fair comparison between the model prediction for the reference concentration, C_o , with the value obtained from equation (5.2a). This is because the model profile has been obtained using the thin strips illustrated in figure (5.11), which do not allow for calculation at the crest level itself. For this reason, the model value of concentration in the bottom strip has been scaled up by a factor (1/0.95), in order to obtain C_o itself. When this scaling is performed, C_o is 2.28 g/l (model), as opposed to 2.29 g/l from Nielsen's formula (equation (5.2a)).

TEST 2

There is much better agreement between the two profiles compared with the plot for Test 1, though the model profile shows considerable variability with height. The value of C_o from Nielsen's formula (equation (5.2a)) is 4.96 g/l as opposed to 8.80 g/l from the model.

5.4.6 Comparisons with other data

Figures (5.31a-c) show three comparisons of instantaneous concentration between the model and some of the data of Nakato *et al* (1977), Sleath (1982a) and Bosman (1982), respectively. (The source for the Bosman data was Van Rijn (1991).) The parameter settings for these runs were:

Nakato <i>et al</i>	$d/\lambda = 1.61, h/\lambda = 0.14, D_{50} = 140$ microns.
Sleath	$d/\lambda = 1.45, h/\lambda = 0.15, D_{50} = 410$ microns.
Bosman	$d/\lambda = 1.74, h/\lambda = 0.18, D_{50} = 200$ microns.

Figure (5.29) illustrates the respective positions at which the comparisons were made, whilst figure (5.30) is a table recording the time-mean concentrations. The Sleath comparison differs from the other two because it has been obtained over the ripple slope. This means that the time series of concentration does not exhibit the familiar, symmetric features of the crest and trough comparisons. The three critical bed shear stresses used in the model were $\tau_c = 0.05 \text{ N/m}^2$ (Nakato *et al*), 0.07 N/m^2 (Sleath) and 0.06 N/m^2 (Bosman).

There is generally quite good agreement between the model predictions and the data in predicting the phases of 'events'. In figure (5.31a), the Nakato comparison, the (split) peaks centred around $t/T = 0.15, 0.65$ (associated with the passage of a sediment-laden ejected vortex over the trough) lead the equivalent peaks in the data by about $15\text{--}20^\circ$. The other two peaks ($t/T = 0.40, 0.90$) show very good phase agreement. A comparison of the means shows the model underestimating by an order of magnitude. In figure (5.31b), (the Sleath comparison), the model peak at $t/T = 0.15$ is delayed by about 15° of phase, with the (model) mean again an order of magnitude too low. The Bosman comparison (figure (5.31c)) shows excellent agreement when predicting the passage time of the ejected vortex over the parent crest ($t/T \approx 0.10, 0.60$). The secondary peaks ($t/T \approx 0.30, 0.70$) represent passage of the ejected vortex over the neighbouring ripple. In the data, these peaks are not symmetric between the two half cycles. For this reason, the phase of the peak at $t/T \approx 0.30$ is predicted well, while the phase of the later peak is poorly predicted. Yet again, the means are underestimated by an order of magnitude.

5.5 Discussion

5.5.1 The prediction of the quantity of suspended sediment

There is considerable doubt as to the ability of the present suspension simulation (a combination of the hydrodynamical and boundary layer models) to predict the correct

quantity of sediment in the flow. This is evidenced in all the instantaneous concentration time series; the model means of sediment concentration are far lower than those obtained by experiment. In an attempt to explain this, some of the results are compared. For this purpose, the data comparisons are placed in two groups that are outlined below.

GROUP A....*Test 1, Nakato et al, Sleath, Bosman*

This group exhibits similar characteristics: an order of magnitude disagreement in the mean concentration, but encouraging phase agreement. The Test 1 comparison shows excellent agreement for the reference concentration C_o , but the profile of $\overline{C}(Y)$ decays far too rapidly with height.

GROUP B....*Test 2*

The Test 2 comparison stands alone, exhibiting (slightly better) percentage disagreement in the concentration means, but poorer phase agreement. In Test 2, the agreement in C_o is still reasonable, while the profile of $\overline{C}(Y)$ adheres much more closely to the exponential profile of Nielsen.

Taking these results together, a possible explanation for the low means concentrations is as follows. In figure (5.28), the area under the curves gives some measure of the quantity of sediment that is present in the flow. Clearly, the area under the two model curves suggests that the model is underpredicting the quantity of sediment present in the flow. This underprediction is a percentage error, as is the disagreement in C_o values for Test 2 (the Test 1 agreement in C_o values is excellent). With these features in mind, it is contended that the model entrainment regime (the boundary layer model and the Meyer-Peter Muller bedload formula) is partly responsible for the generally poor mean concentration predictions, but not solely so. The order of magnitude disagreements in some of the means cannot be attributable to shortcomings in the entrainment regime alone. There must be other mechanisms as well.

For the sake of completeness, some computational tests were performed using the 'Test 1, crest 1.0 cm' case, to see if varying parameters associated with the entrainment regime significantly increased the means. It was found that doubling and trebling the constant ('8') in the Meyer-Peter Muller bedload formula approximately doubled and trebled the means. Similarly, having no threshold of motion, ($\tau_c = 0$), increased the mean from 0.48 g/l to 0.80 g/l. In other words, the predictions of the means could have been improved by making these changes. However, there seemed scant justification for doing this, and these parameters remained unchanged.

It is suggested that the primary culprit for the disagreement in the concentration means is the flow regime, which is failing to distribute the particles sufficiently in the flow. A basic feature missing in the present simulation of the suspended sediment regime is diffusion of the sediment particles. A diffusive, random walk element (eg. Chorin (1973), Asp Hansen *et al* (1991)) would tend to spread out the particles more evenly, and provide a mechanism to lift sediment higher up from the bed. The use of (conglomerated) sediment particles to represent numerous sand grains further aggravates the problem. In Test 2, the vigorous nature of the flow regime in some way compensates for the lack of diffusivity in the simulation, providing better agreement in mean concentrations and the form of $\bar{C}(Y)$. The more quiescent flow regimes in GROUP A lack this compensating factor.

The above points dwell heavily on shortcomings in the present simulation. There could also be experimental factors that have a bearing here. There is the ever-present possibility that the measuring instrument affected the bed. Also, the presence of three-dimensionality in the ripples may enhance the volume of sediment entrained. We know, for example, that the ripples in Test 2 showed three-dimensionality. To address these points, we note that *all* the means from GROUP A were low; it seems unlikely that experimental factors would affect all these datasets in this way.

In conclusion, the model is receiving a reasonably realistic volume of entrained sediment, but fails to distribute this sediment properly. A highly energetic flow regime (as in Test 2, with $M = 46.4$ and $RE = 21500$) helps to counteract this failure.

5.5.2 The simulation of the movement of suspended sediment

In a horizontal sense, the model simulates the movement of suspended sediment with some success, evidenced in the good phase agreement between peaks in most of the time series of concentration. This confirms, by implication, that the hydrodynamical model is predicting vortex passage times well. In particular, the phase of the peaks associated with the passage of an ejected vortex over the parent crest are accurately modelled. The suspended sediment particles tend to move in sympathy with the vortices (see figures (5.13), (5.17)), circling the vortex centres but not entering the vortex cores. Trapping of sediment within the vortex core (as discussed by Nielsen (1984a)) has not been found to occur in any of the simulations, possibly because of the very small vortex core areas in the hydrodynamical model.

The simulation of the movement of suspended sediment in the vertical is less satisfactory, as discussed in §5.4.5. The present simulation lacks a mechanism to lift sediment away from the bed. Numerous possible candidates present themselves to aid this lifting process: diffusion, improved account of old, weakened vortices, some form of turbulent 'bursting' from the bed and the presence of small currents in addition to the wave-induced oscillatory flow. The presence of entrained sediment far from the bed has been noted by many researchers (eg Vincent and Green (1990)). More study is required to elucidate the key mechanisms involved.

5.5.3 The measuring box

The sensitivity of model predictions of instantaneous concentrations to the box size suggests that this method of obtaining concentrations could be improved upon. The guiding choice for the dimensions of the box was smallness, so that it realistically mimicked the measuring volume of the instrumentation. In the Test 1 comparisons (figures (5.26a-d)), the box appears to be too small; too few particles are recorded at each time step, making the magnitude of the instantaneous concentrations highly sensitive to the input parameters. In the Test 2 comparisons (figures (5.27a,b)), the box would appear to be too large; extraneous particles are recorded, accounting for the erroneous concentration peaks at $t/T = 0.30, 0.80$ and $0.40, 0.90$. This suggests

shortcomings in the 'measuring box' technique. One possible improvement is to do away with the conglomerated particles and track individual grains. This would have the effect of dispersing sediment more evenly and perhaps provide a fairer basis for comparison with the data. Unfortunately, tracking (possibly) thousands of grains would be a huge computational exercise. Further computational development is required here.

5.6 Conclusions

In this chapter, both the boundary layer and hydrodynamical models have been used to predict the entrainment and subsequent motion of suspended sediment. A 'measuring box' technique has been used to obtain suspended sediment concentrations, which have been compared with data. The study has met with mixed success. Its main strengths include (a) the (generally) good phase agreement between the model predictions of instantaneous concentrations and the data, and (b) the reasonable agreement between the model values of C_o (the reference concentration) and those of Nielsen (1986). The former bodes well for the hydrodynamical model in predicting vortex passage times over ripples. Weaknesses of the model include (a) its inability to lift suspended sediment further from the bed, and (b) shortcomings in both the measuring box technique and the representation of sediment as conglomerate particles.

There is enough encouraging agreement between the model results and the data to suggest that the present simulation is along the right lines and is worth further development. The model simulations presented here should be considered as a first approximation to the (deterministic) modelling of the suspended sediment regime over ripples. Possible further developments include the addition of diffusion, and an improved method of obtaining concentrations.

A sequence of sketches and figures (from the literature) that support the literature review.

Figure 5.1 A schematic diagram illustrating the '4 peak' structure observed in time series of instantaneous concentration over the ripple crest. The peaks reflect the passage of sediment laden vortices. Copied and adapted from Sleath (1984).

Figure 5.2 A scatter graph (copied and adapted from Nielsen (1984a)), showing how the ratio l/h settles to the (fairly constant) value of 1.4 beyond $U_o/w_s = 10$. This value of U_o/w_s is taken by Nielsen to represent the onset of 'effective' vortex formation and shedding over ripples.

Figure 5.3 A schematic diagram that supplements the findings of Bijker *et al* (1976) concerning the net flux of sediment when the oscillatory flow is assymetric.

Figure 5.4 Some of the results from the discrete vortex model of Asp Hansen *et al* (1991). The two left diagrams are snapshots of the vorticity field at the times of zero and maximum oscillatory flow, with the two right diagrams showing the corresponding sediment field. Copied and adapted from Asp Hansen *et al* (1991). (Parameter settings not known).

Figure 5.1

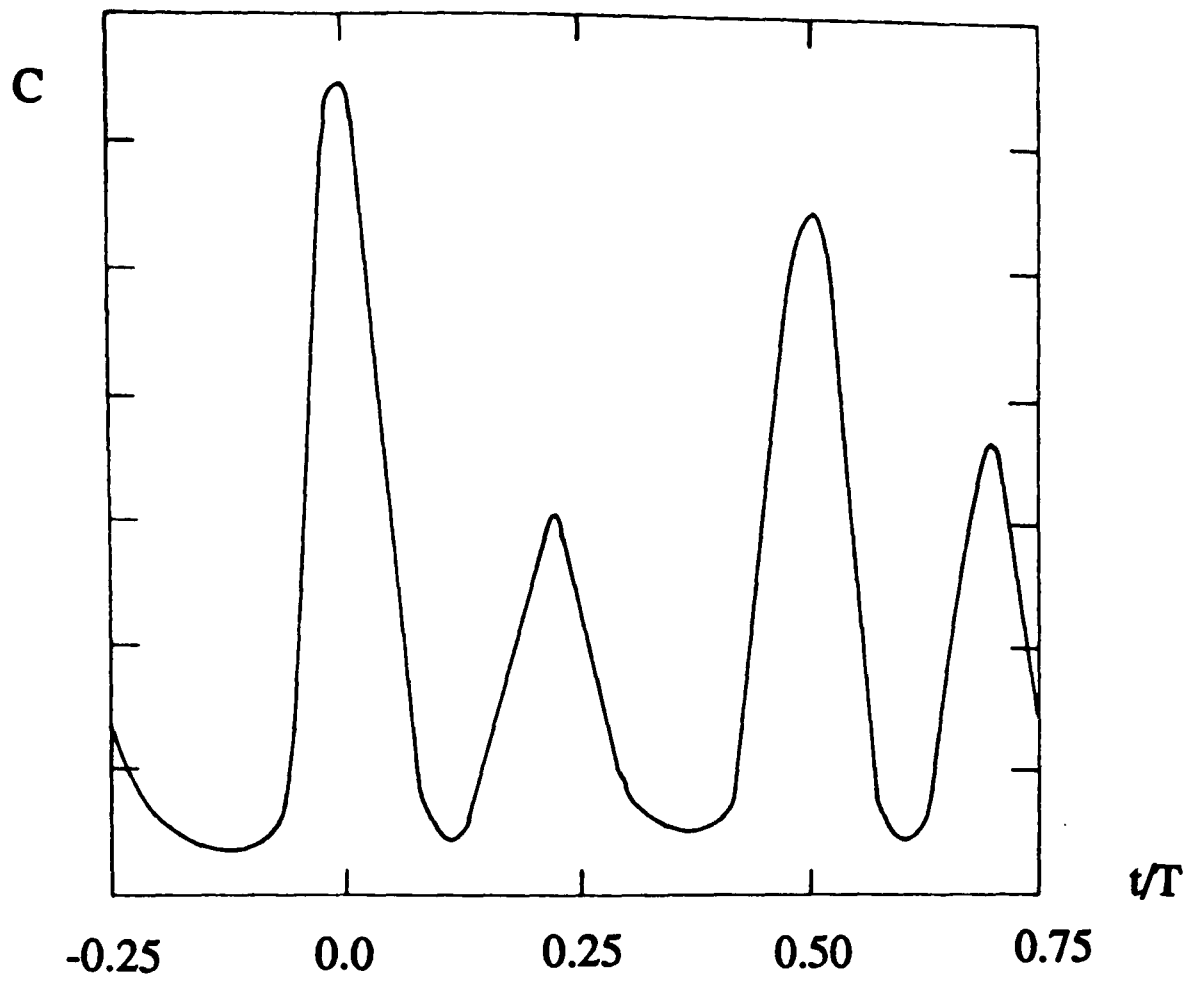


Figure 5.2

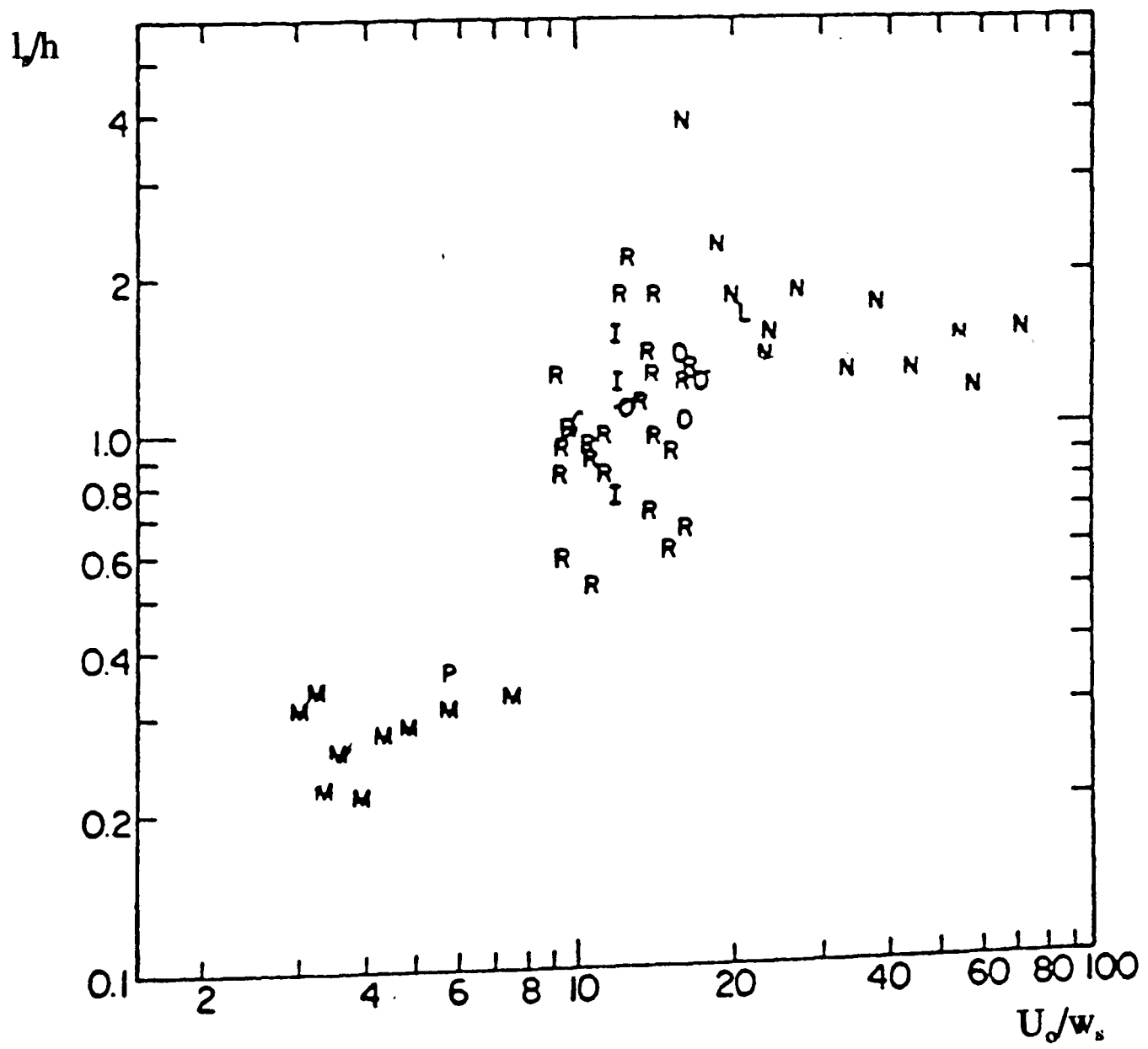


Figure 5.3

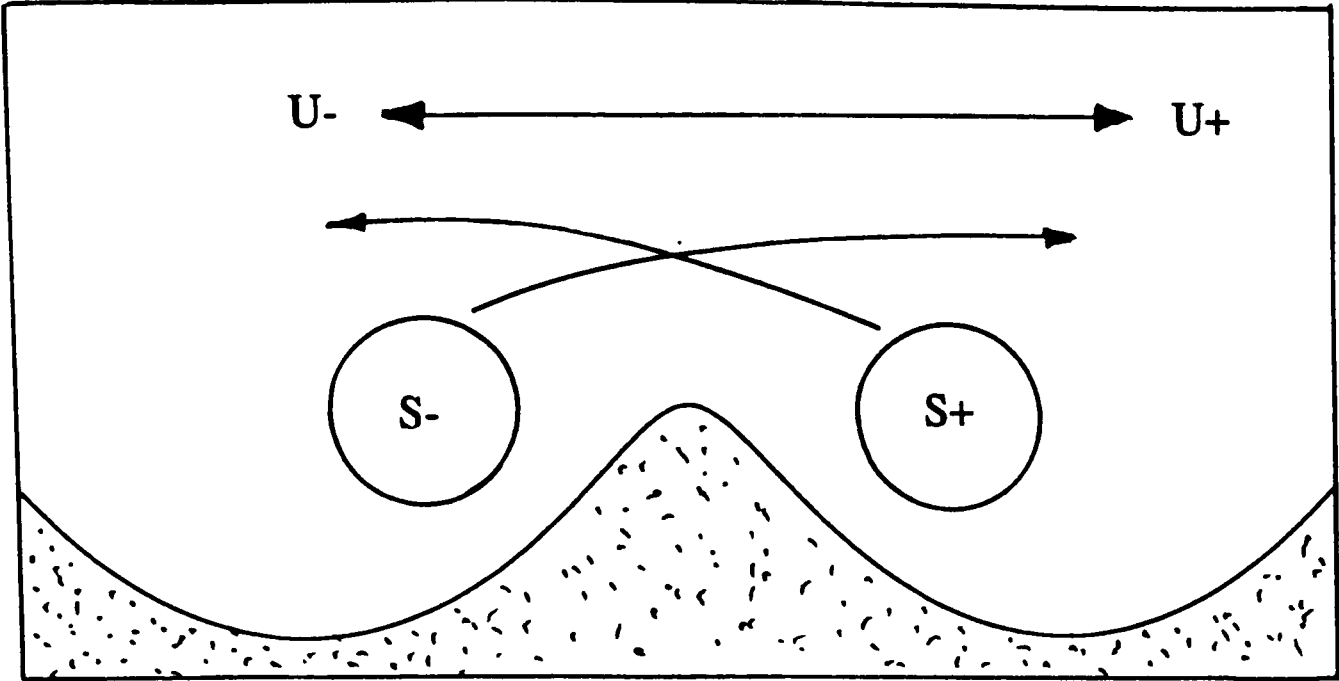
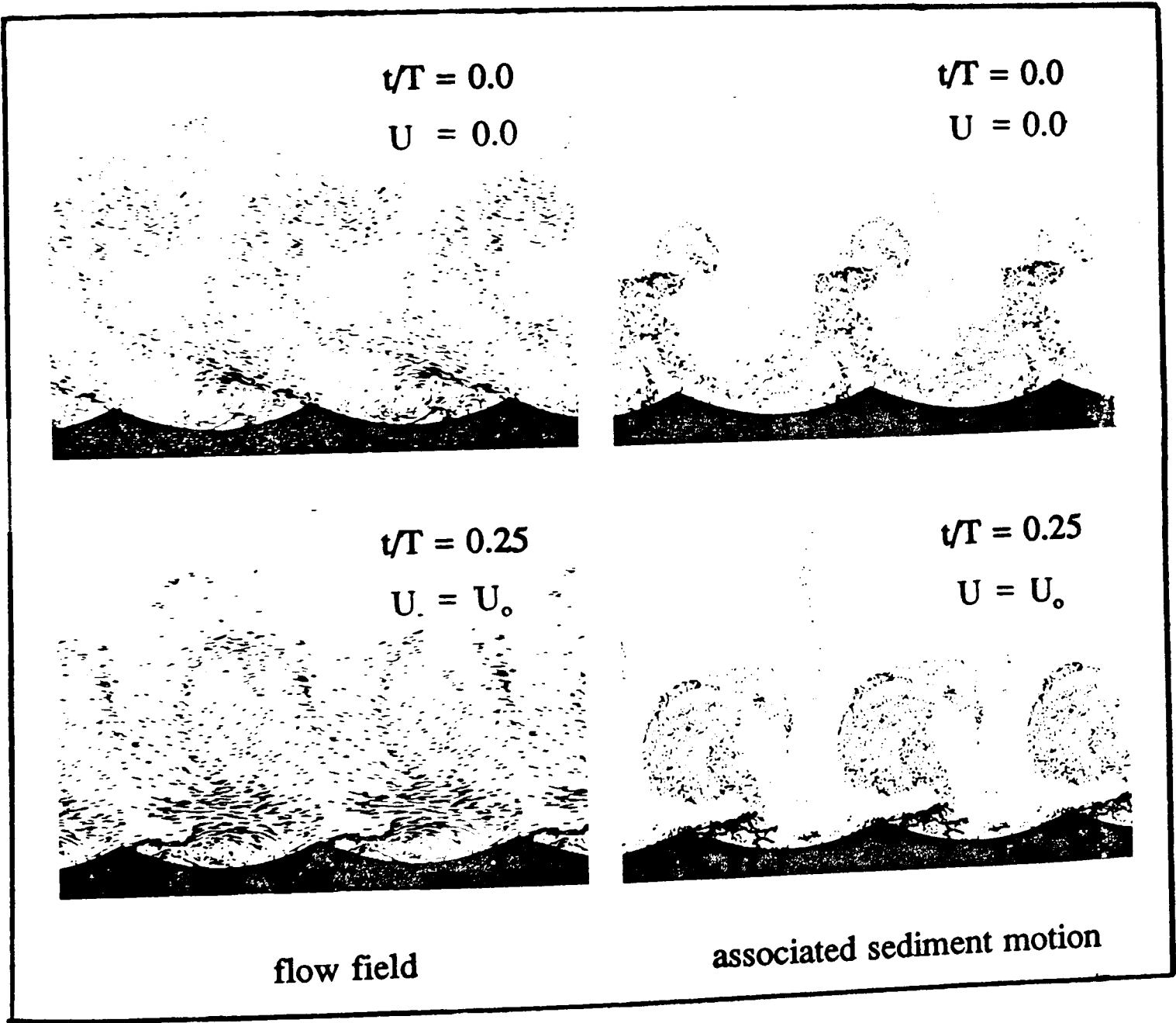


Figure 5.4



Some diagrams relating to the experimental work of Villaret (1992, 1993), which formed the basis of the Test 1 and Test 2 comparisons.

Figure 5.5 Where the ripples produced in Tests 1 and 2 fit on the curves of Nielsen (1979).

Figure 5.6 The position of the 'OPCON' probes in the two tests, where the sand concentration data was obtained.

Figure 5.7 (a,b) Some of the 'raw' data from Test 1, obtained 1 cm above the crest and 2 cm above the trough. The lower portion of the figure shows how the oscillatory flow varied during the 2 second long timeperiod. Vertical lines highlight the times of flow reversals.

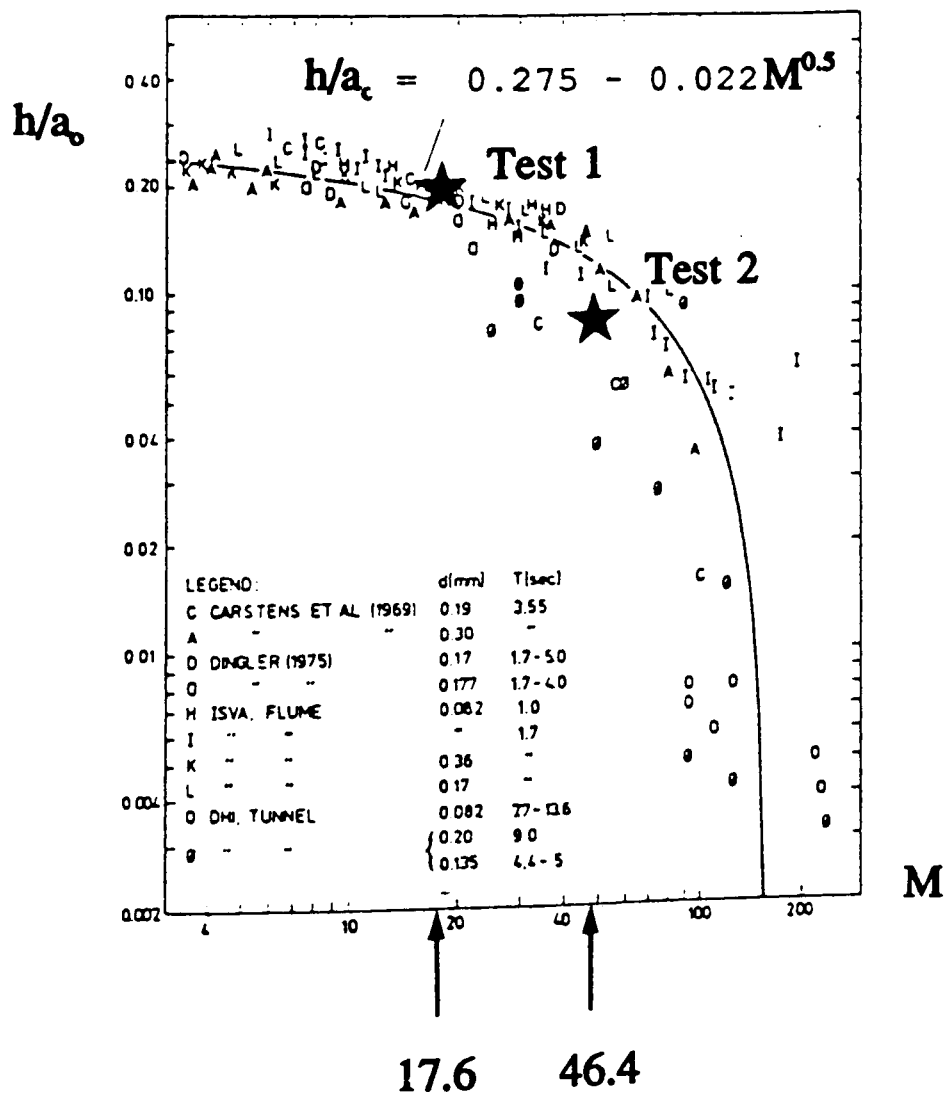
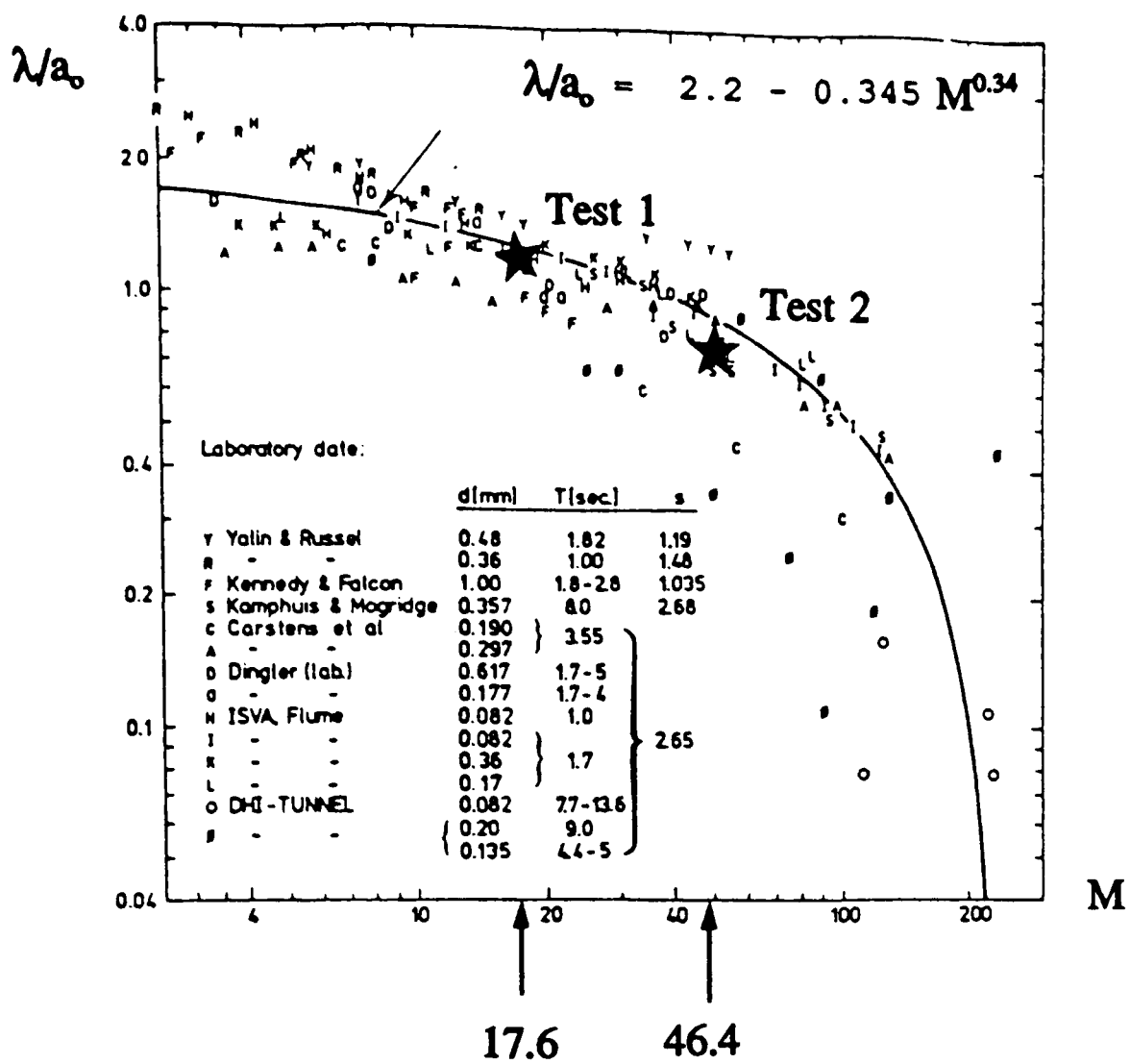


Figure 5.5

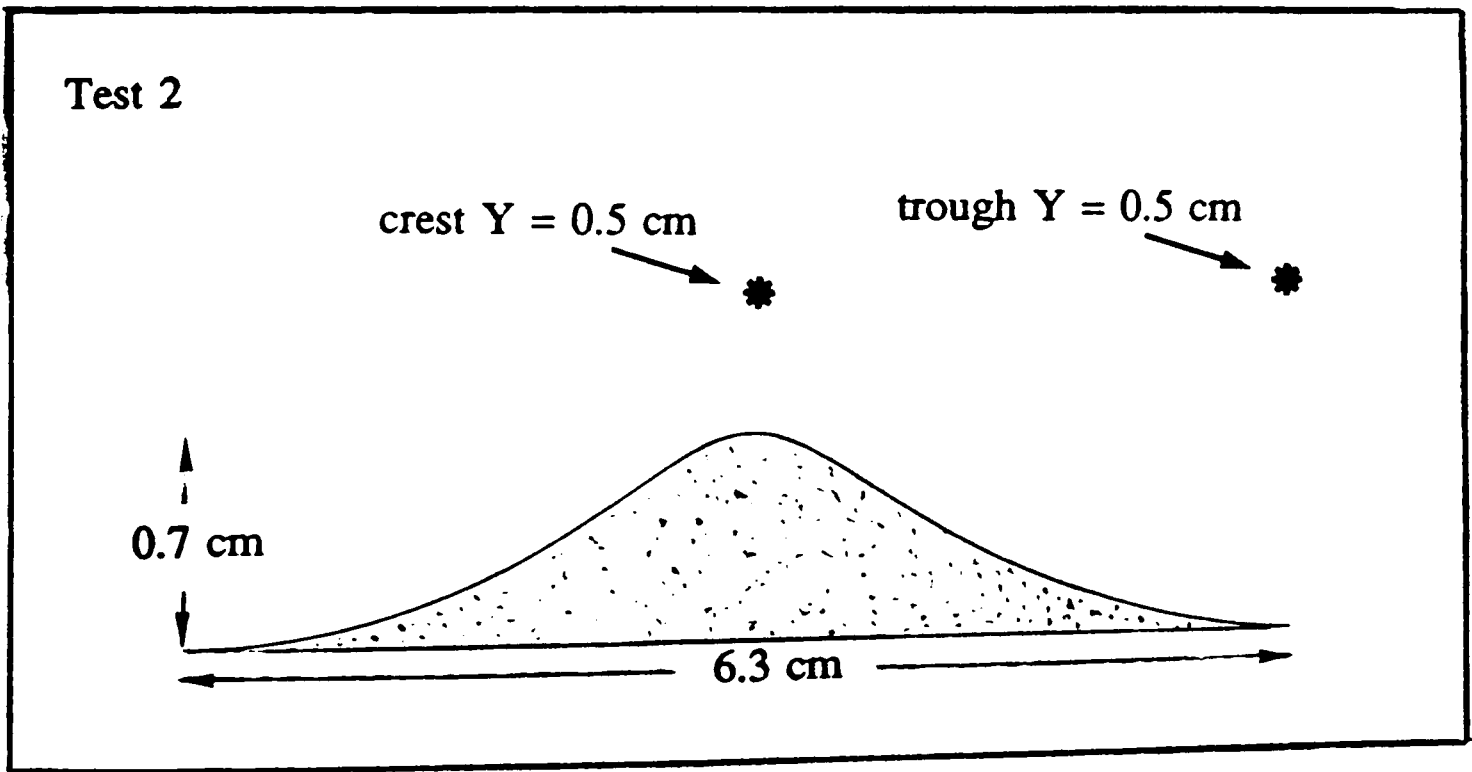
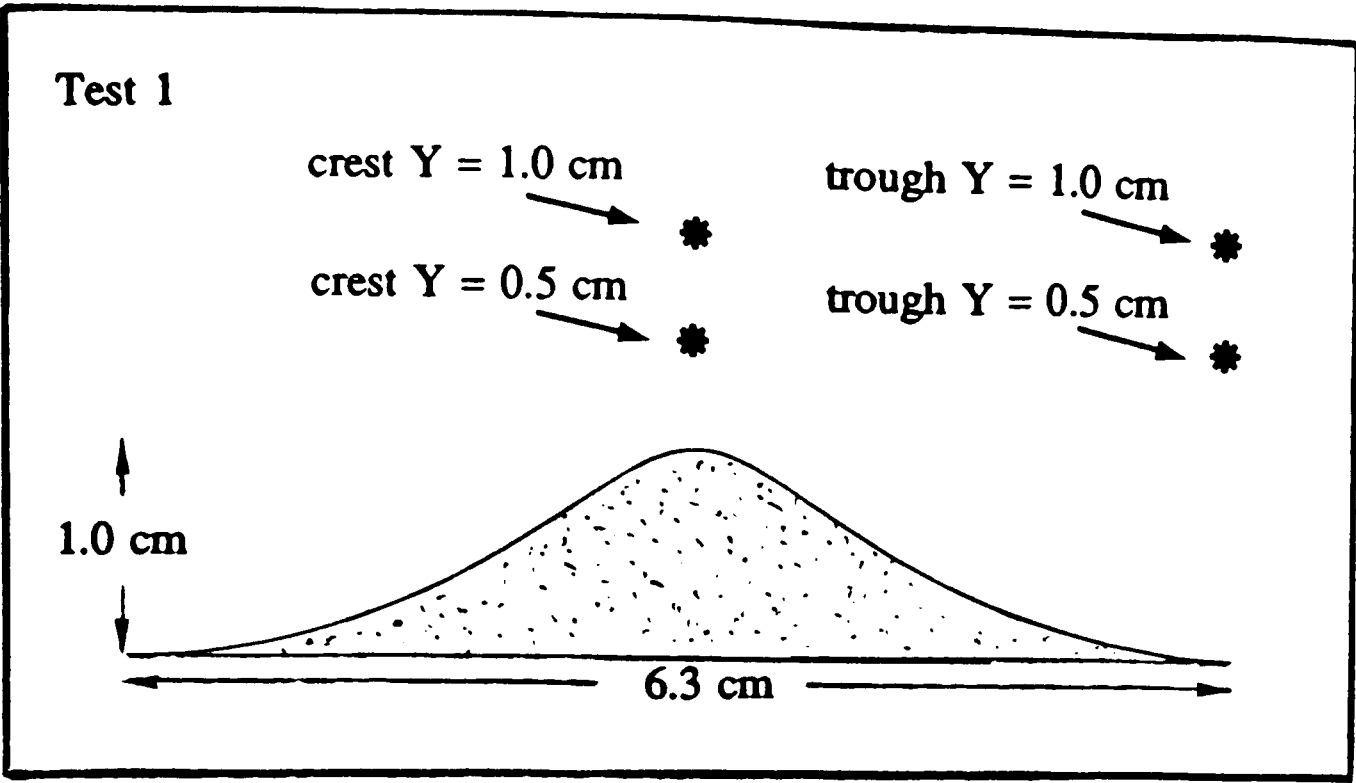


Figure 5.6

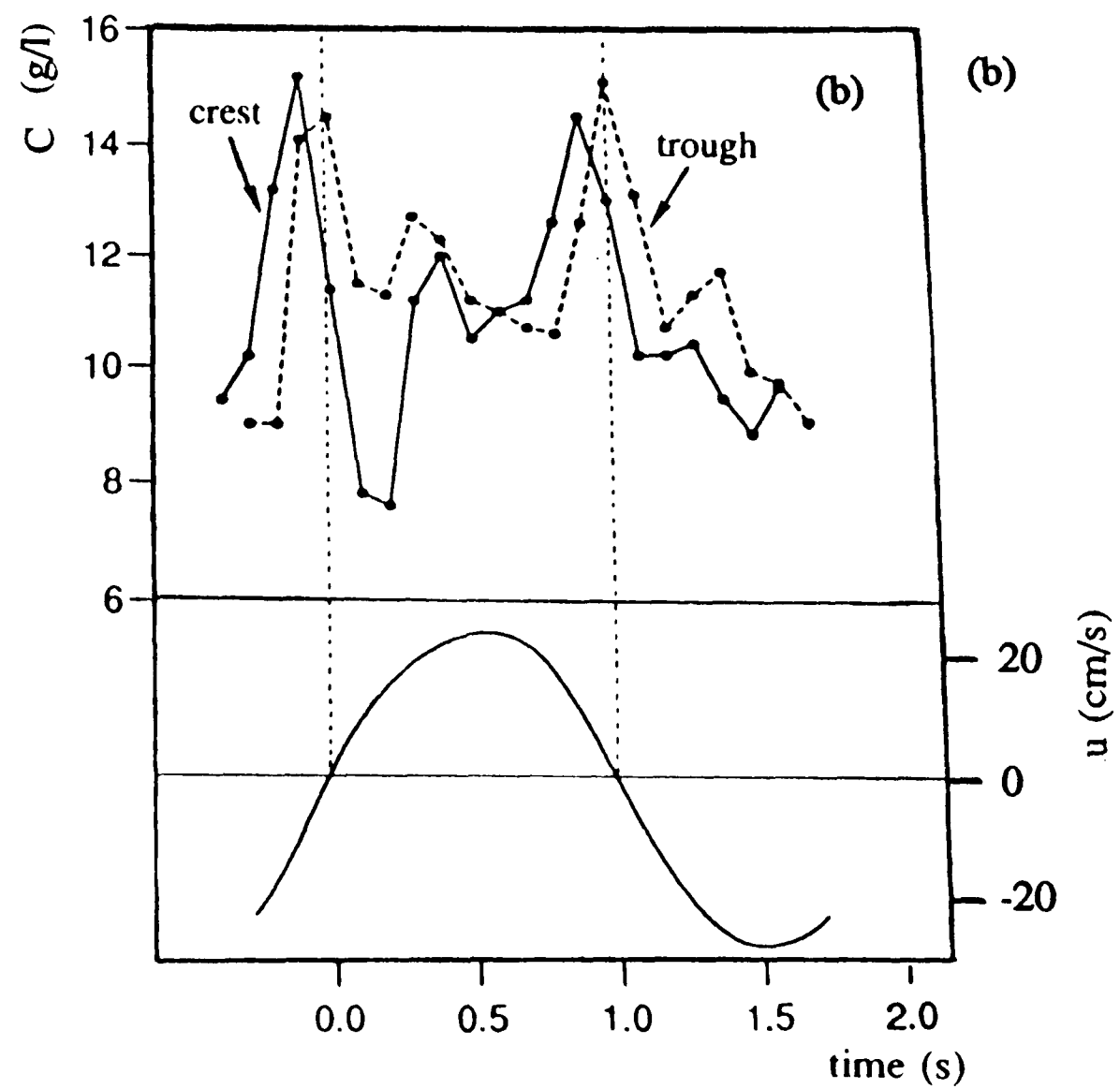
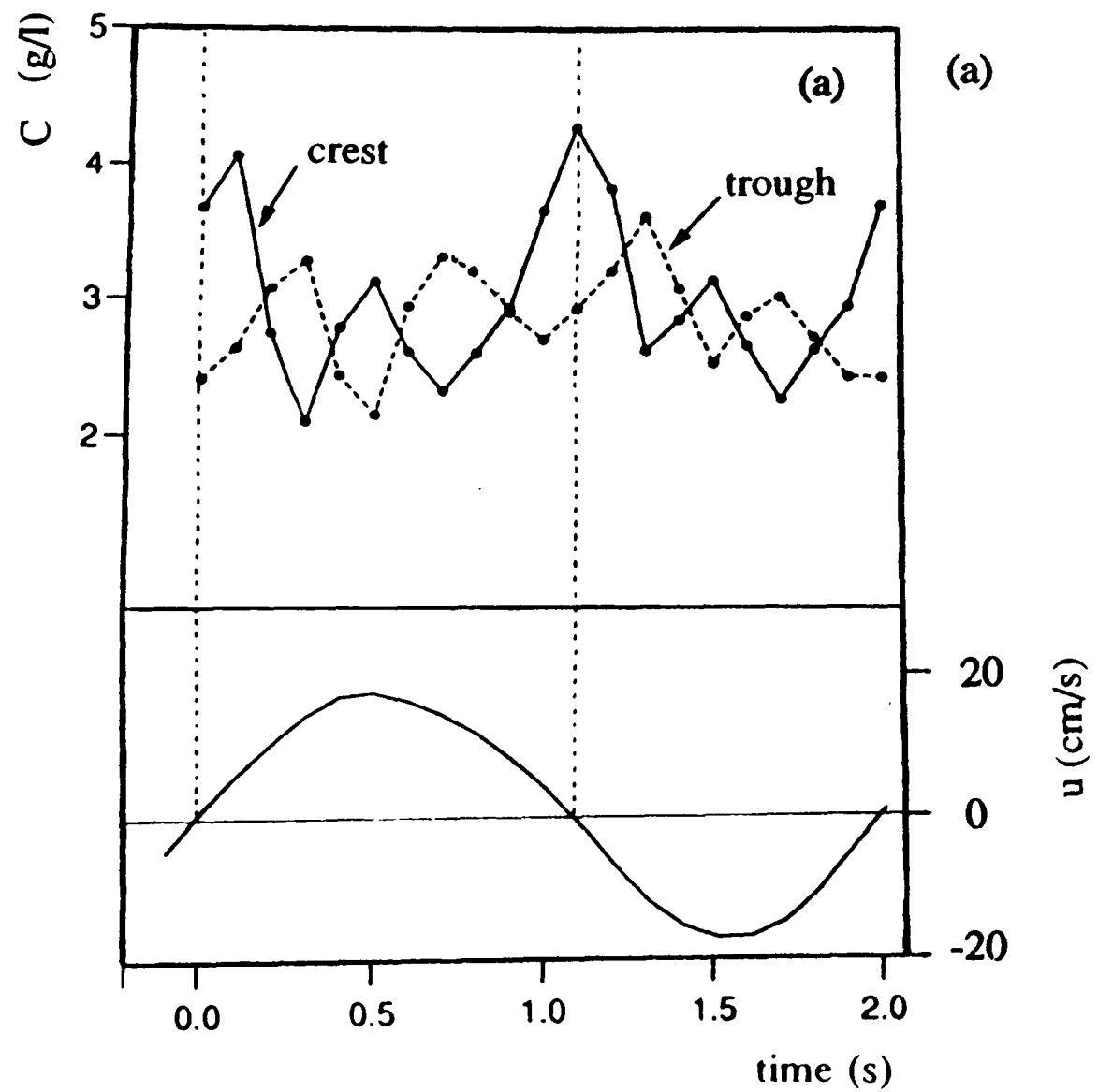


Figure 5.7 (a,b)

Some sketches (a) clarifying the methods whereby concentration predictions are made in the simulation and (b) computational aspects of the simulation.

Figure 5.8 The adapted form of Shield's curve that was used in the thesis to ascertain the critical bed shear stress (τ_c). Copied and adapted from Sleath (1984).

Figure 5.9 A graph of settling velocity (w_s) for different median grain sizes (D_{50}). This graph was used to determine w_s in data comparisons when w_s was not supplied. Copied and adapted from Dyer (1986).

Figure 5.10 A sketch illustrating the position, z_T , at which sand particles are released, and the box method for obtaining instantaneous concentration profiles.

Figure 5.11 A sketch illustrating the grid used to obtain the spatial- and cycle-averaged concentration profiles ($\overline{C}(Y)$).

Figure 5.12 Convergence of the sand suspension regime, illustrated by how the number of particles in the flow at $t/T = 0.40$ varies per cycle.

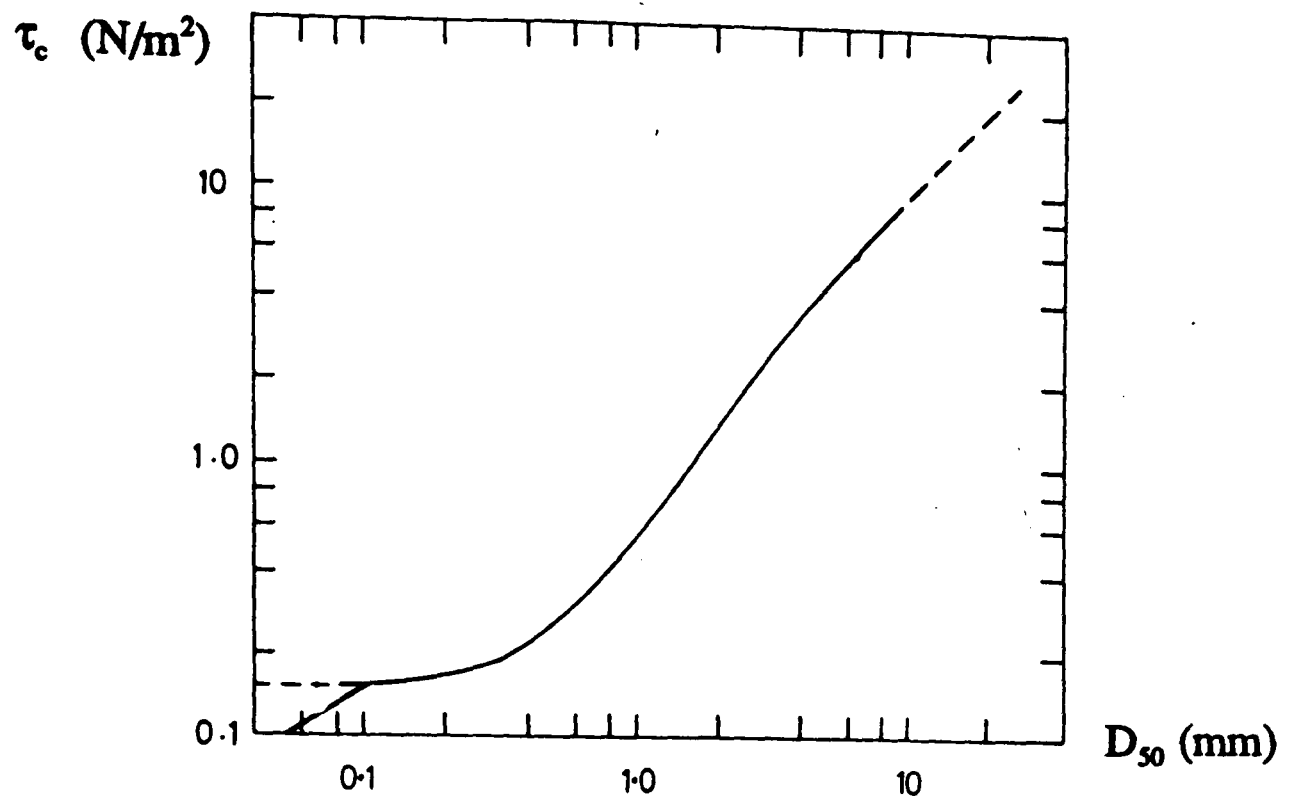
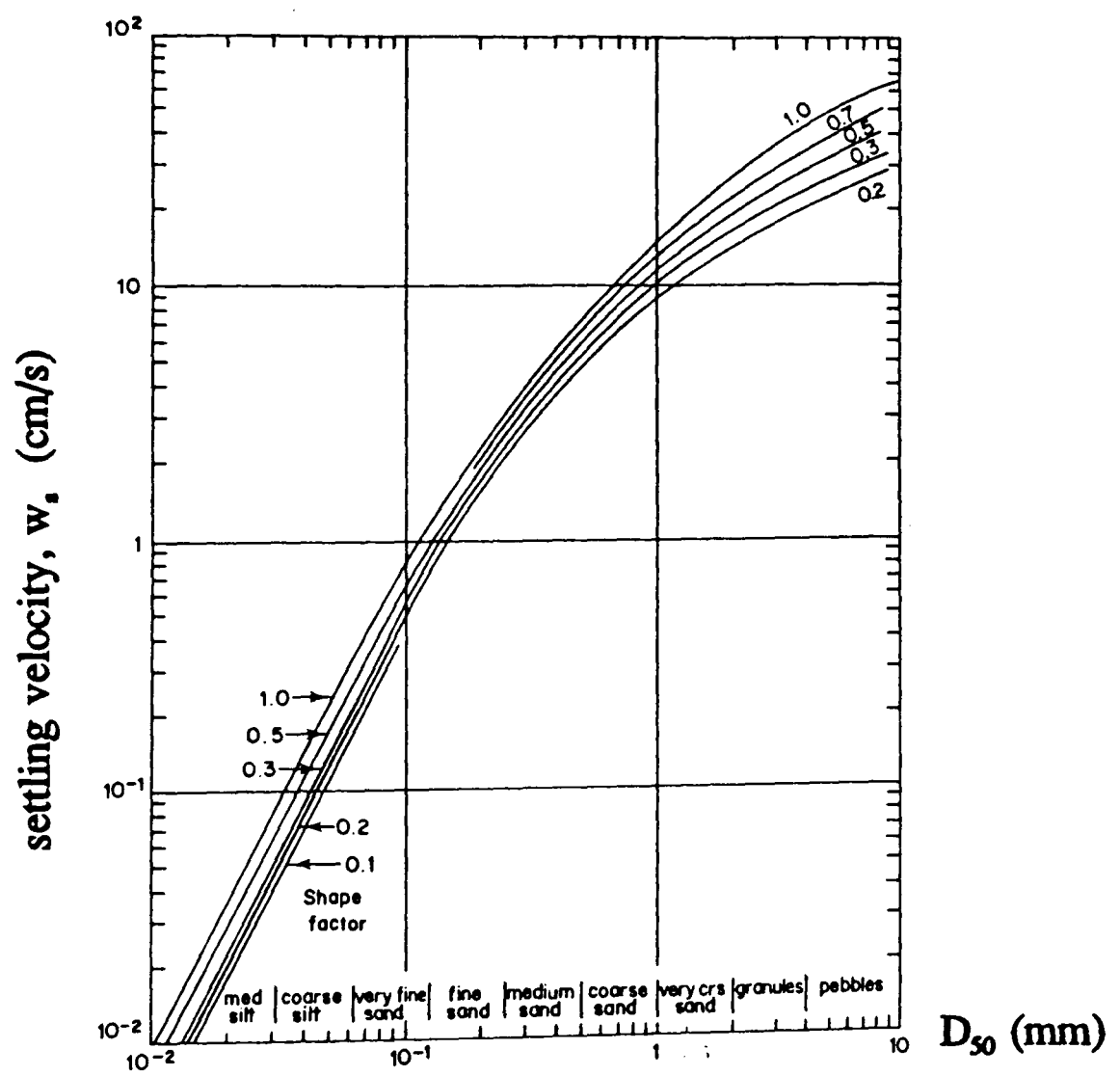


Figure 5.8

Figure 5.9



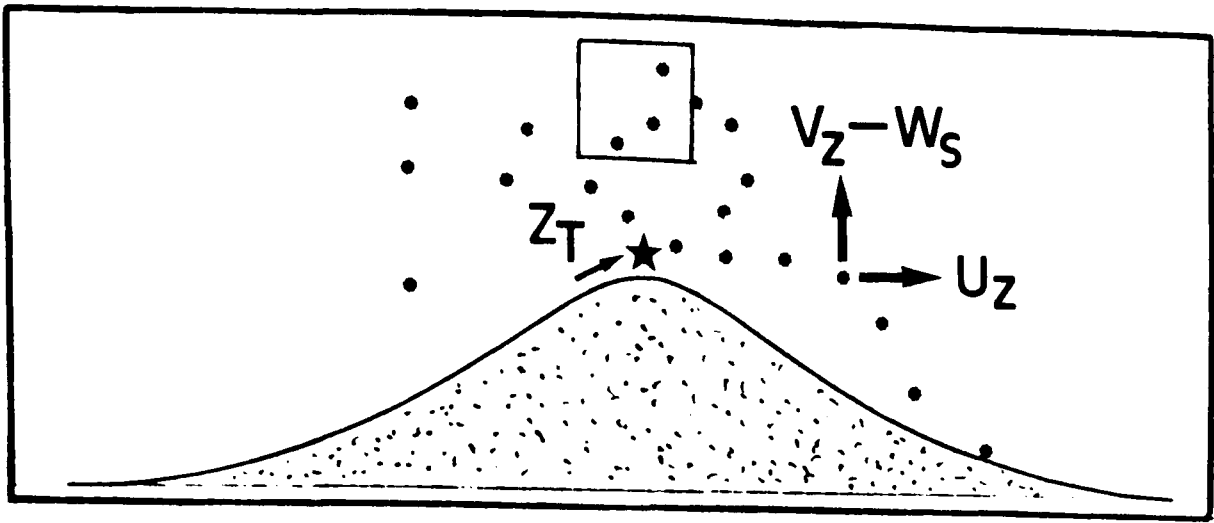


Figure 5.10

Figure 5.11

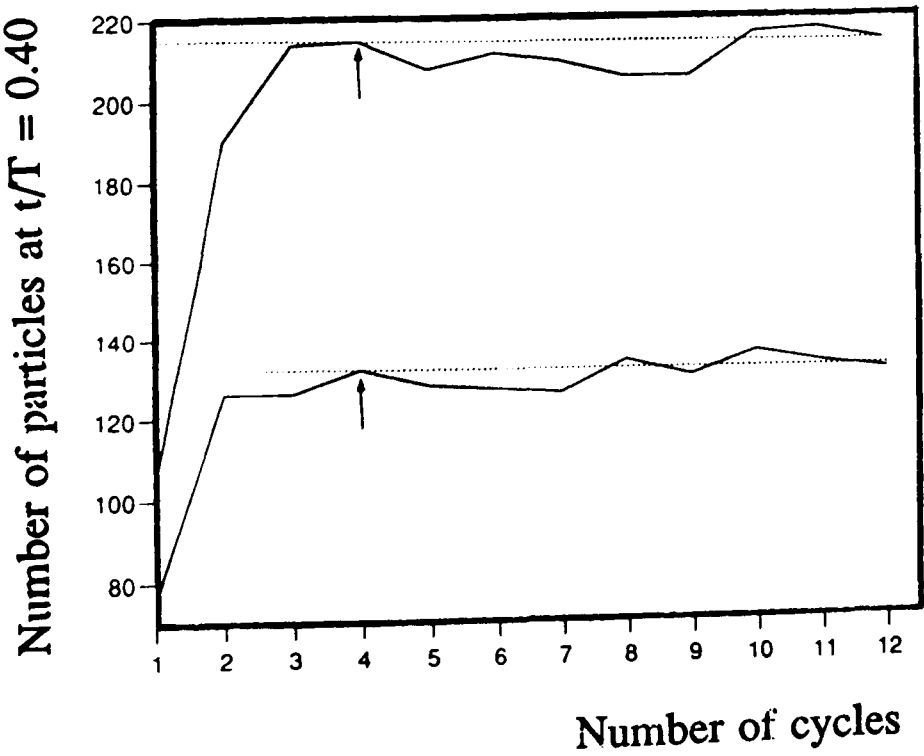
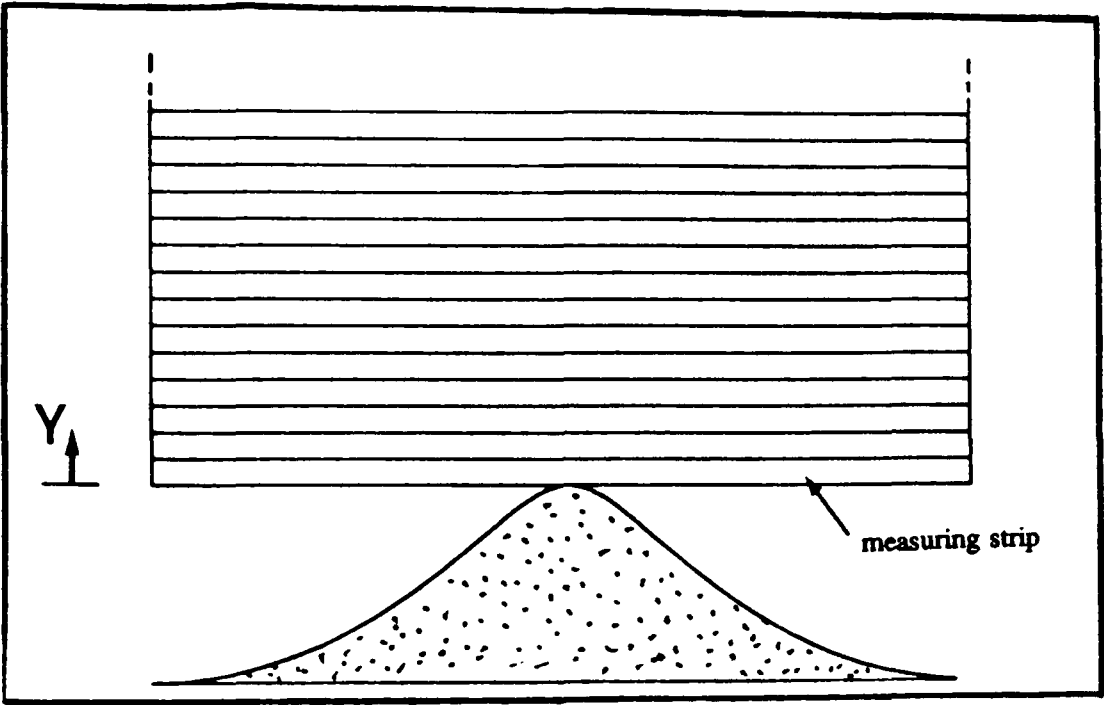


Figure 5.12

Results for the Test 1 settings of $d_o/\lambda = 1.62$, $h/\lambda = 0.16$.

Figure 5.13 Vortex positions for Test 1 in the first half cycle. (G = growing vortex, E = ejected vortex.)

Figure 5.14 The movement of sand particles in the first half cycle for Test 1. The box marks the 'crest 1.0 cm' measuring box, whilst stars represent vortex centres.

Figure 5.15 (a)-(d) Test 1: model predictions of the inst. concentration at four positions over the ripple profile; (a) crest $Y = 1.0$ cm, (b) crest $Y = 0.5$ cm, (c) trough $Y = 1.0$ cm and (d) trough $Y = 0.5$ cm.

Figure 5.16 Particle trails at specific phase instants for Test 1.

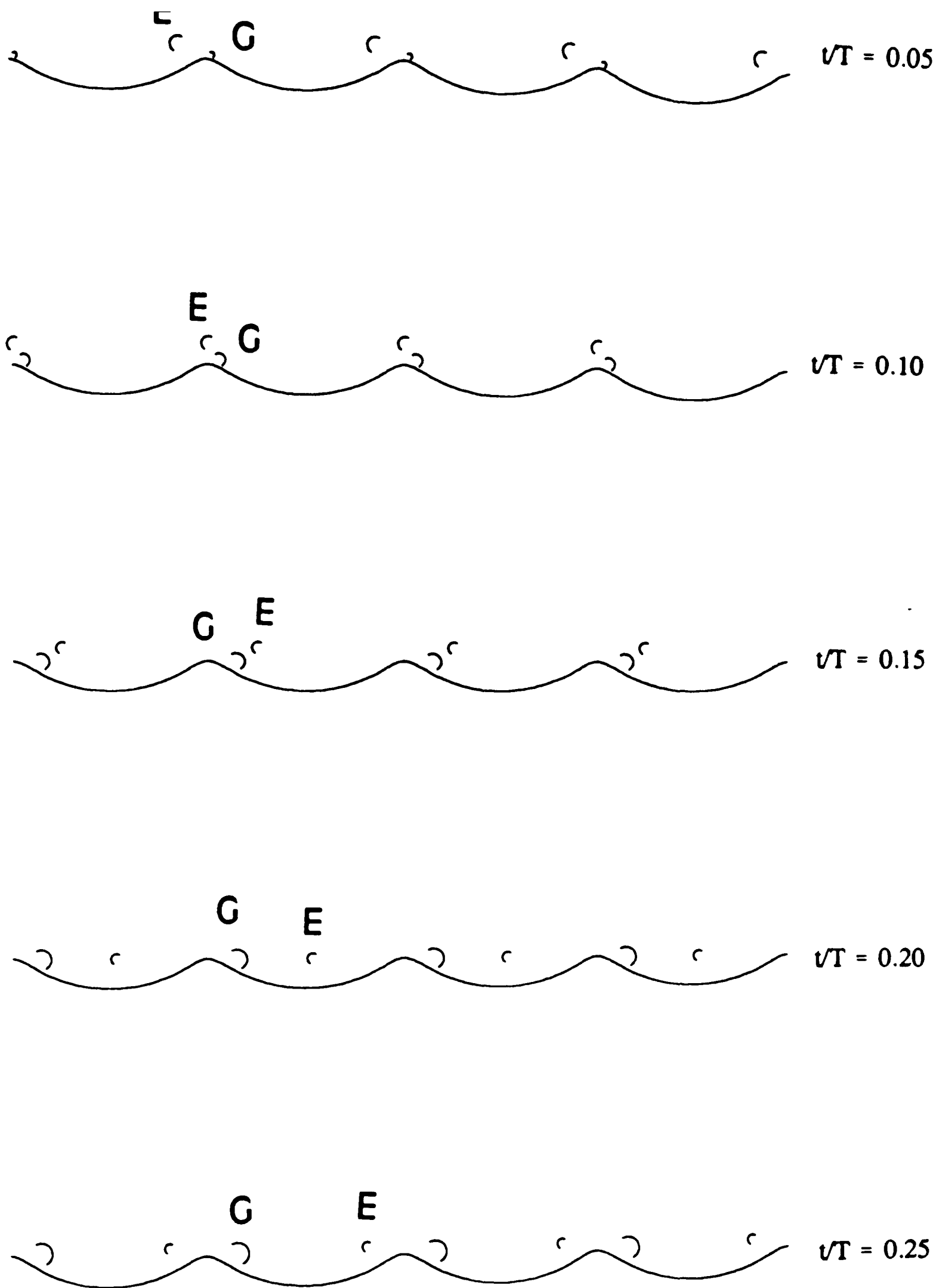


Figure 5.13

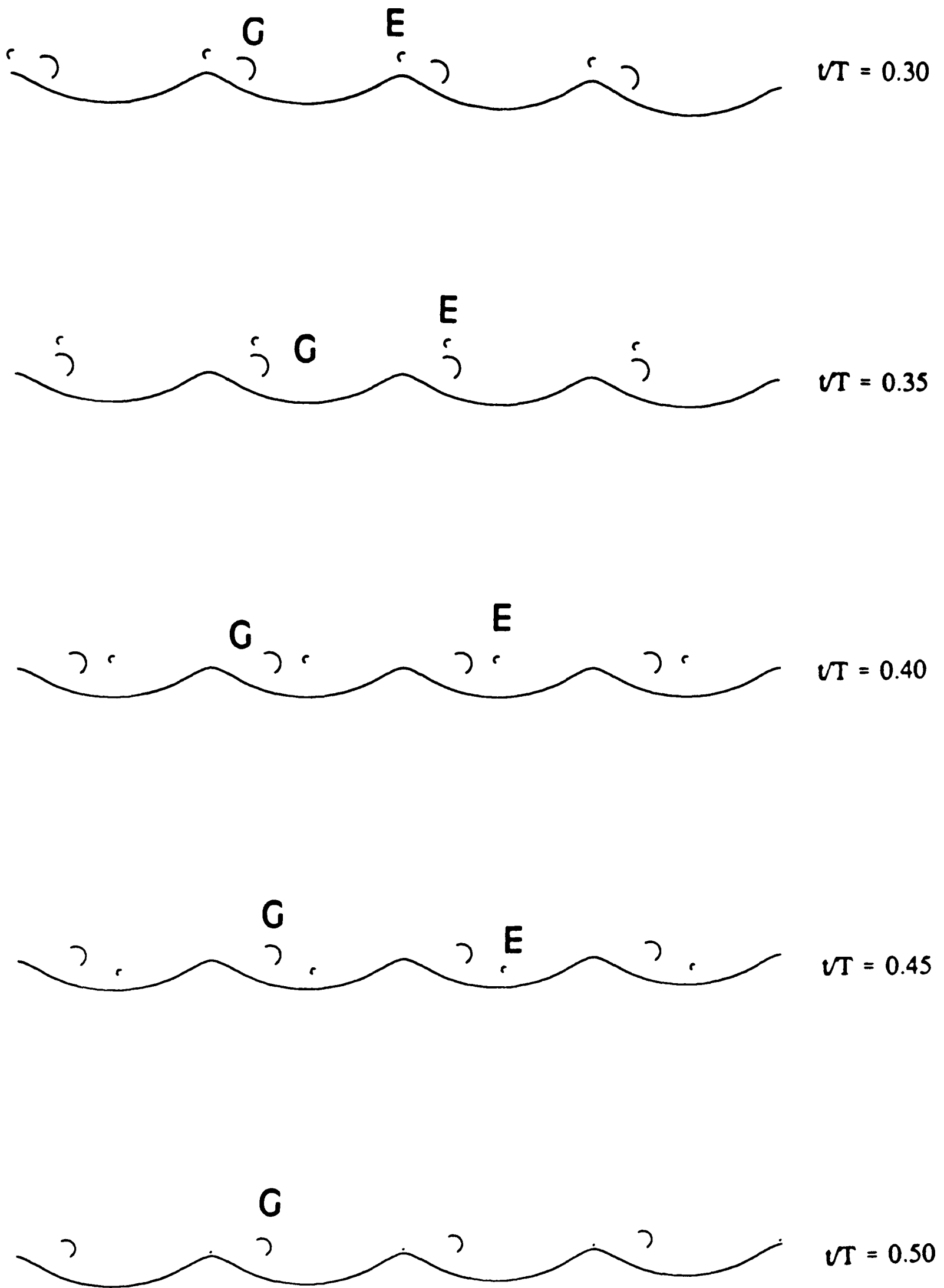


Figure 5.13



Figure 5.14



Figure 5.14

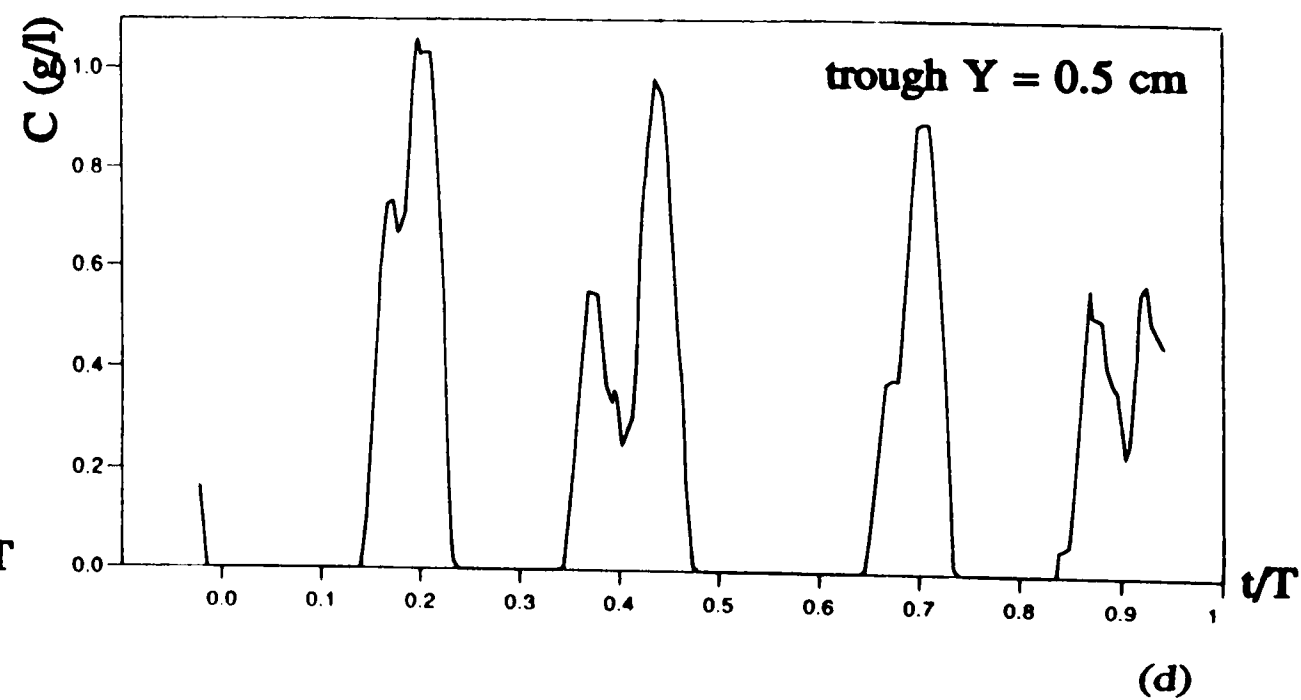
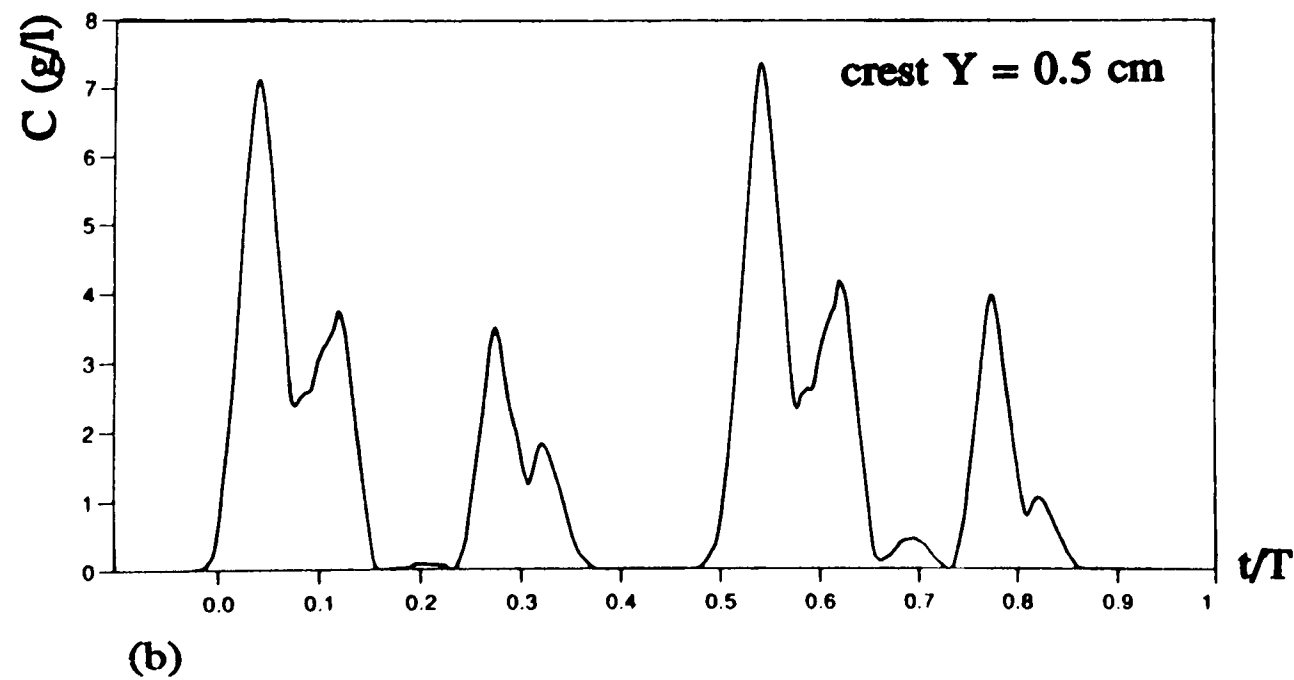
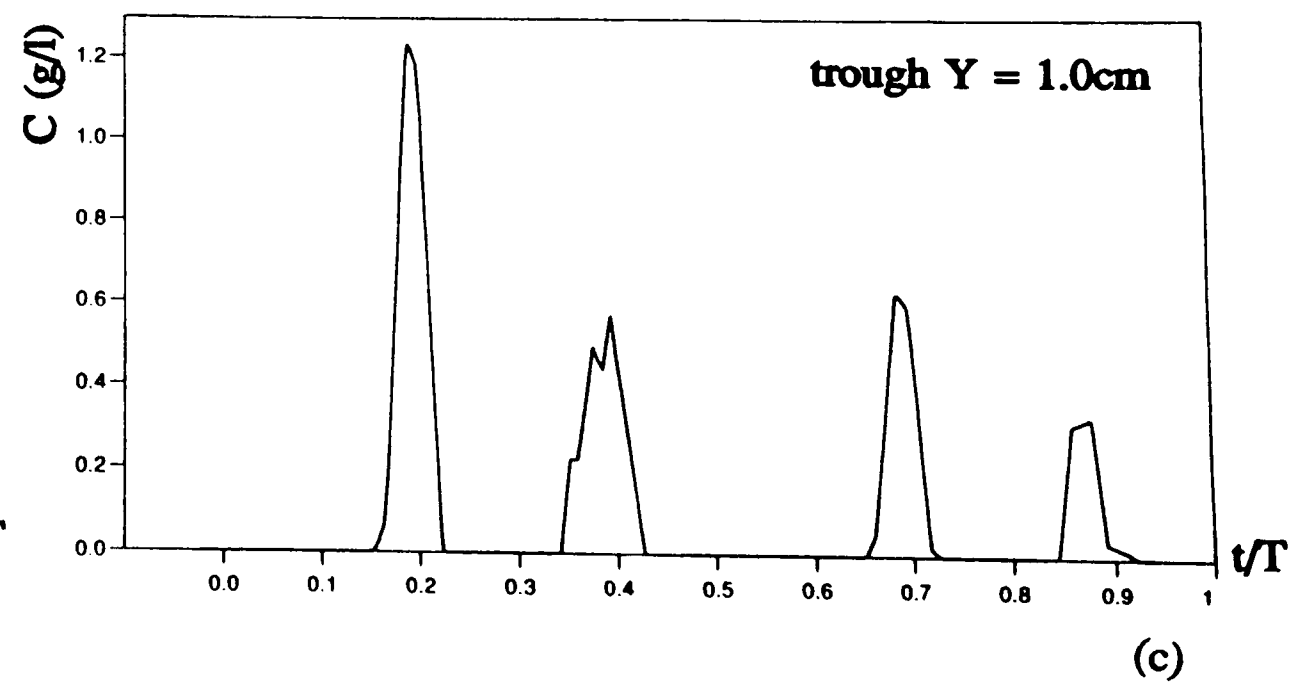
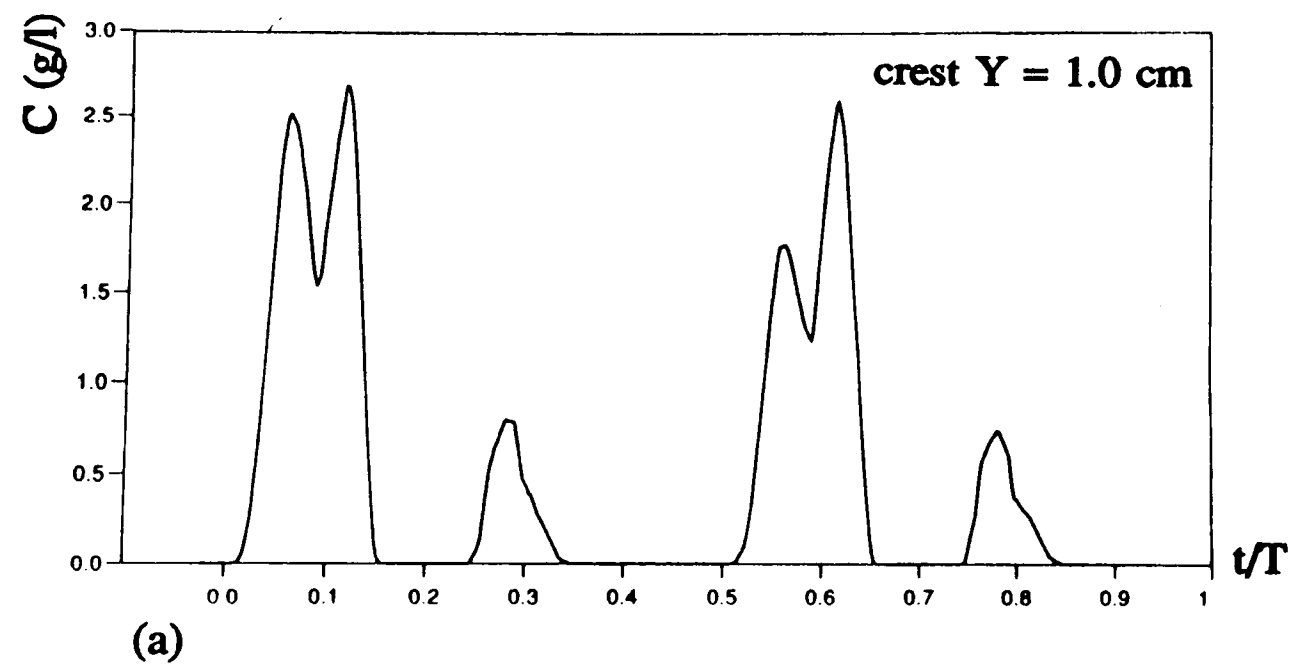


Figure 5.15 (a)-(d)

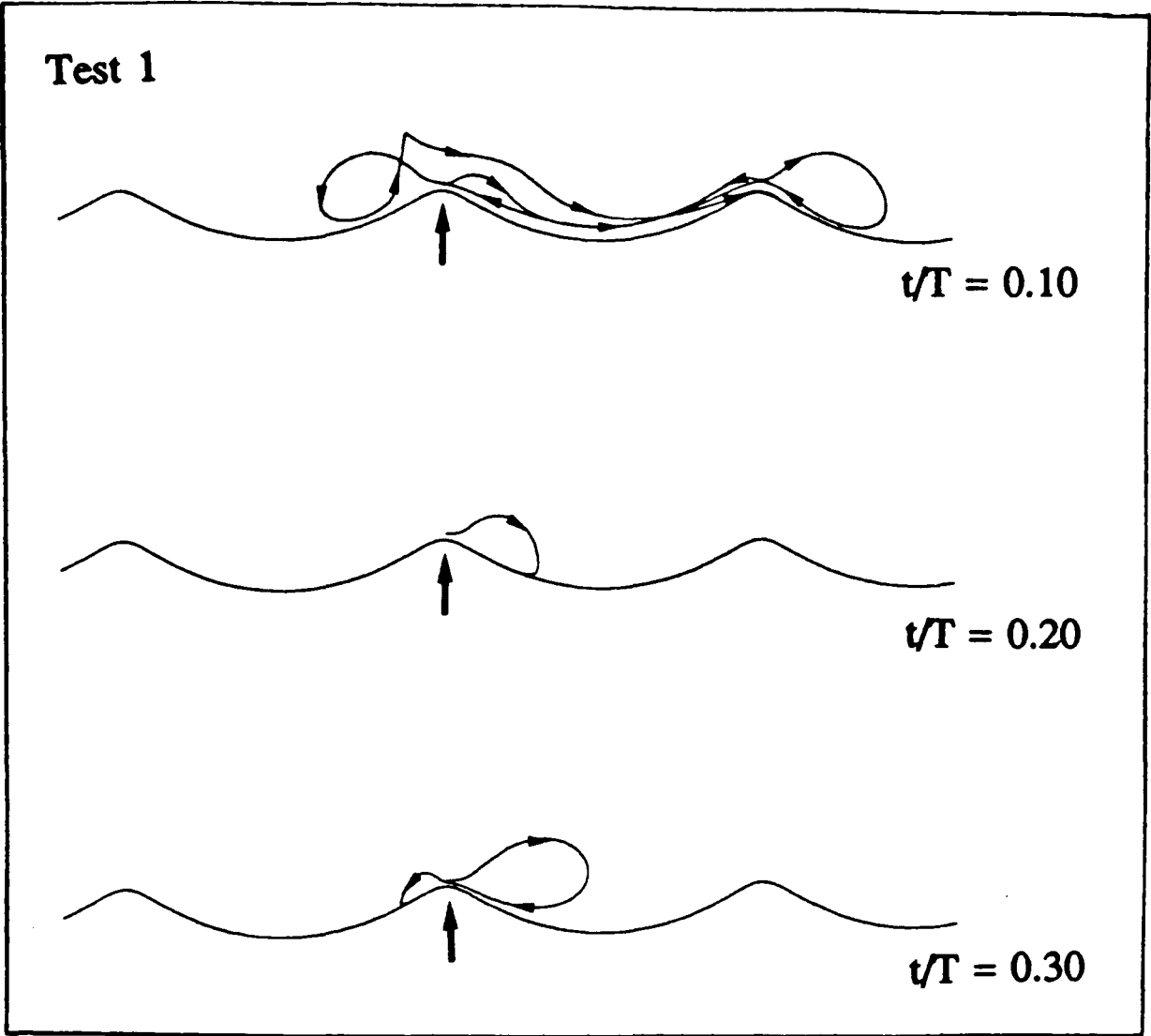


Figure 5.16

Results for the Test 2 settings of $d_o/\lambda = 2.63$, $h/\lambda = 0.11$.

Figure 5.17 Vortex positions for Test 2 in the first half cycle. (G = growing vortex, E = ejected vortex.)

Figure 5.18 The movement of sand particles in the first half cycle for Test 2. The box marks the 'crest 0.5 cm' measuring box, whilst stars represent vortex centres.

Figure 5.19 (a,b) Test 2: model predictions of the inst. concentration at (a) crest, $Y = 0.5$ cm, and (b) trough, $Y = 0.5$ cm.

Figure 5.20 Particle trails at specific phase instants for Test 2.

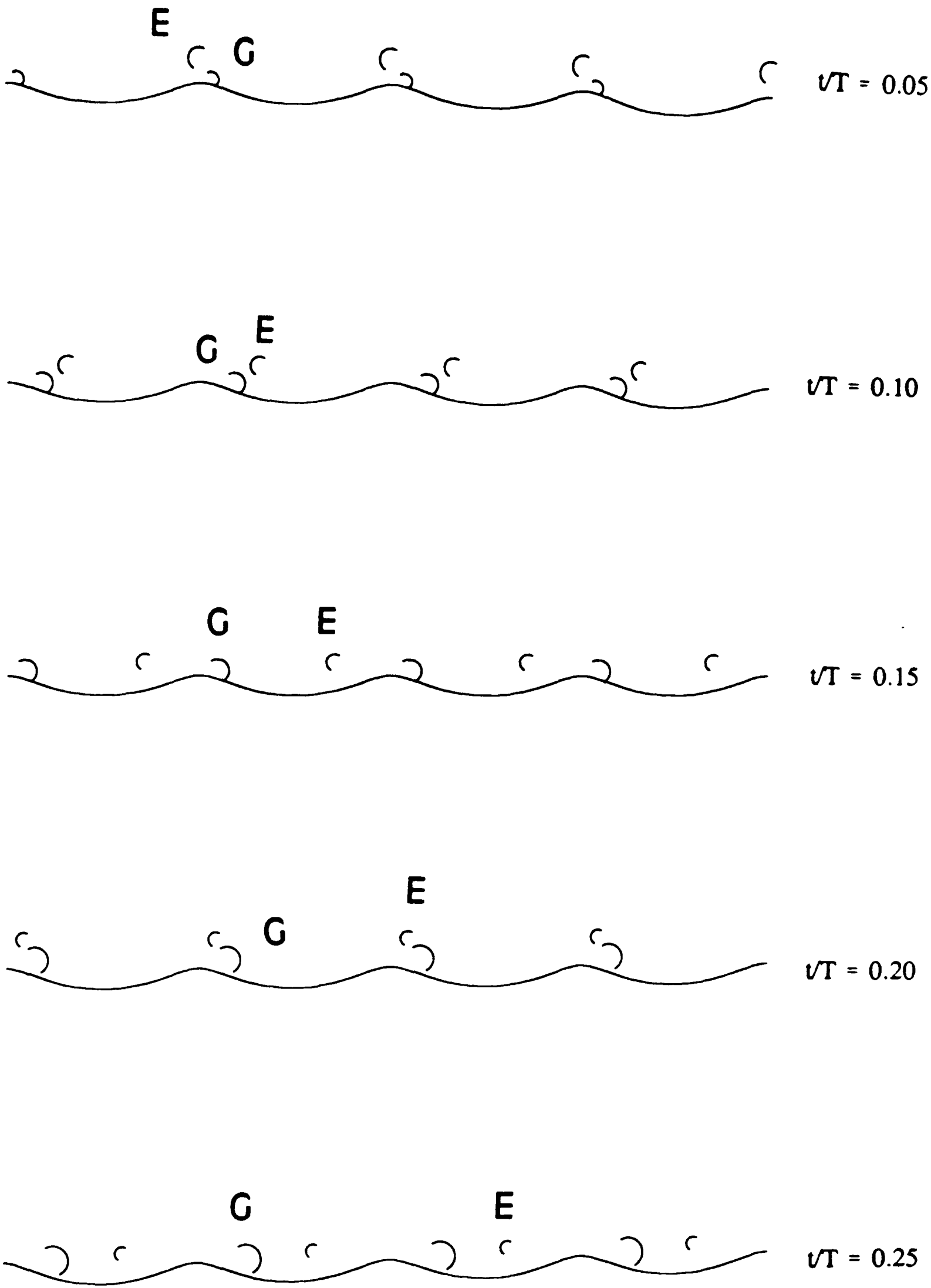


Figure 5.17

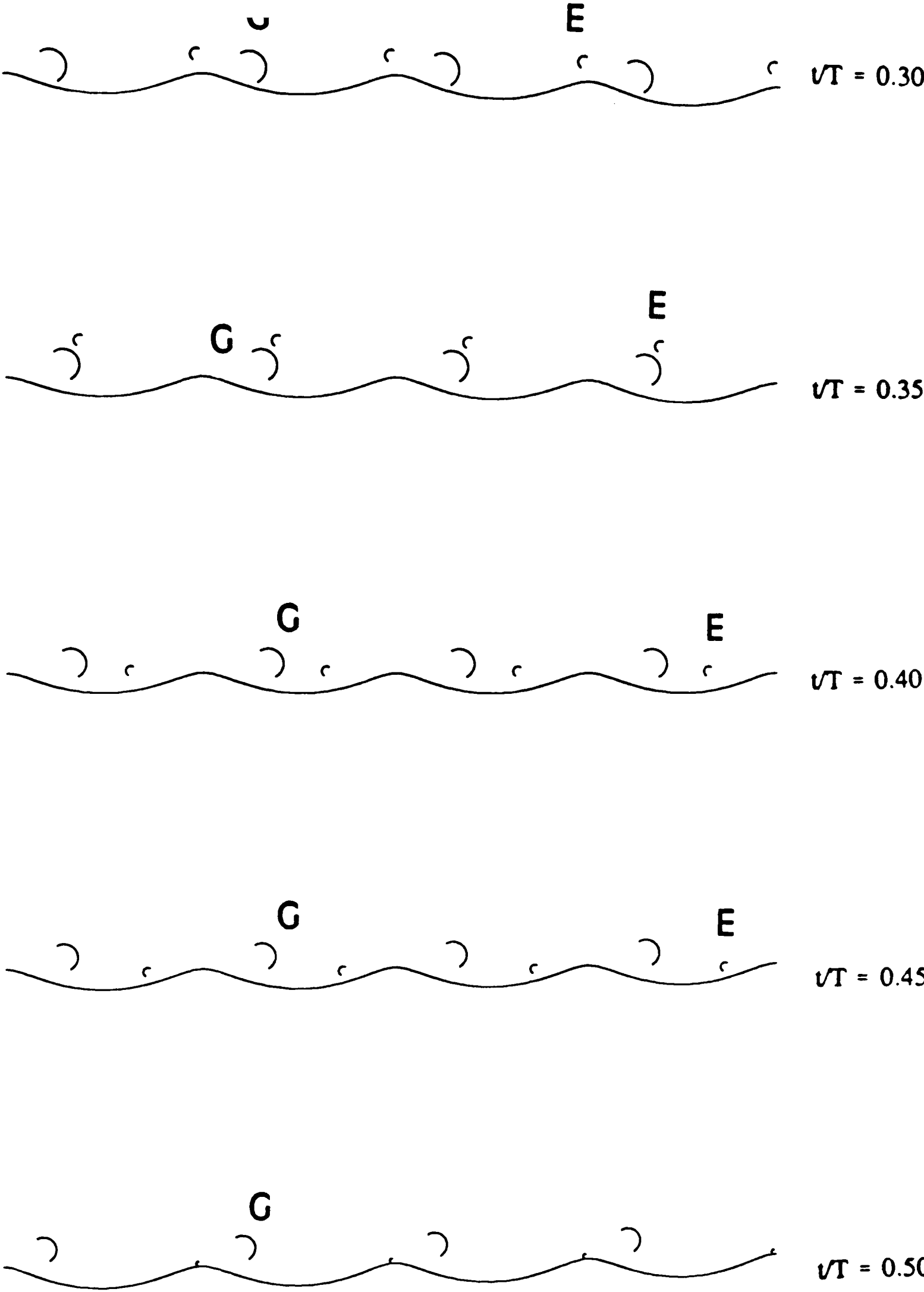


Figure 5.17

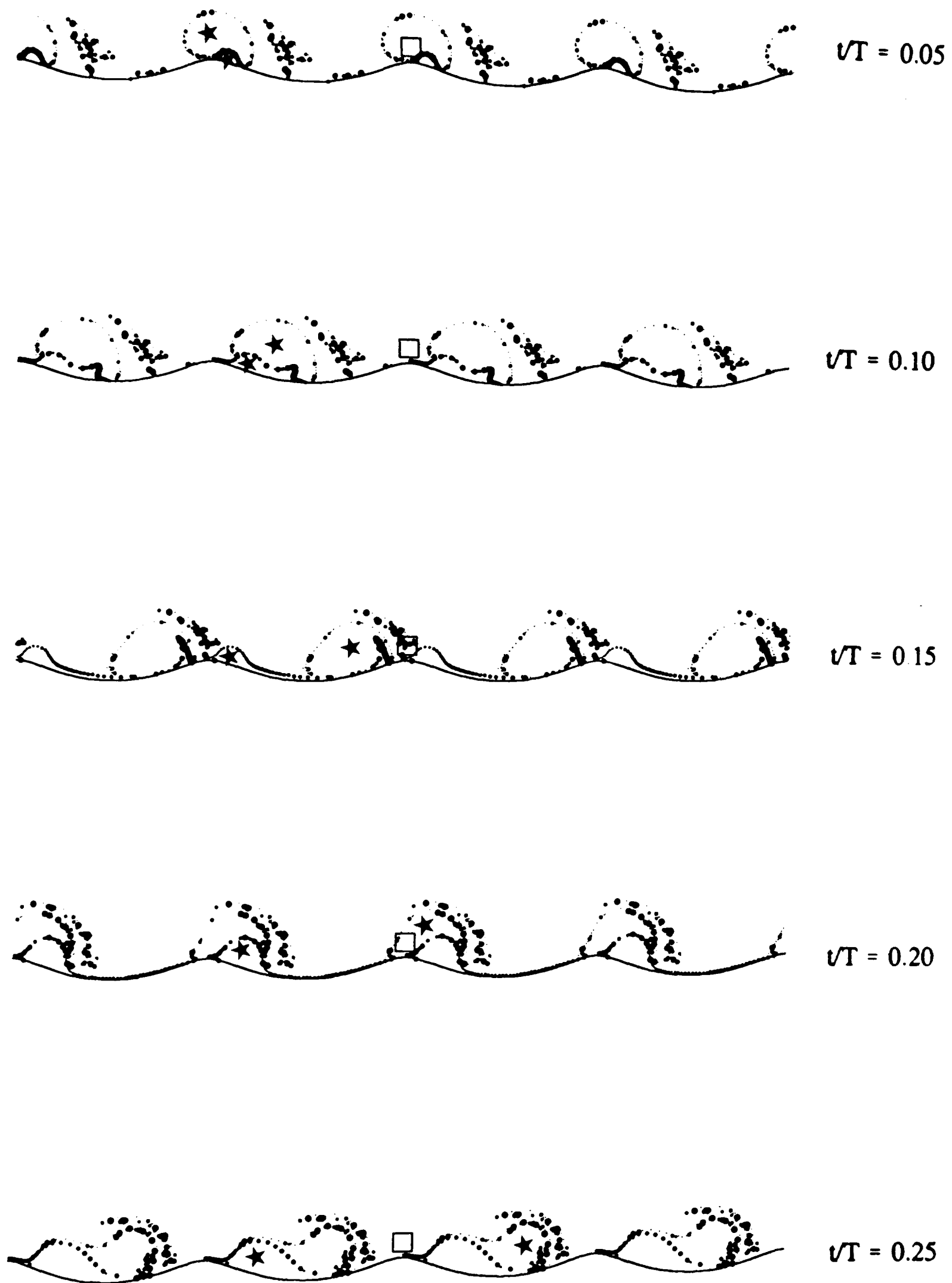


Figure 5.18

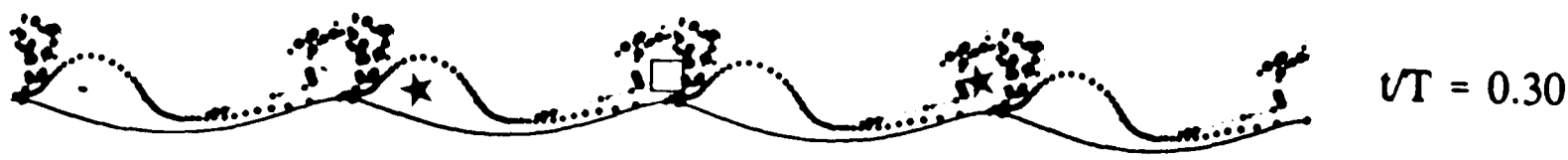


Figure 5.18

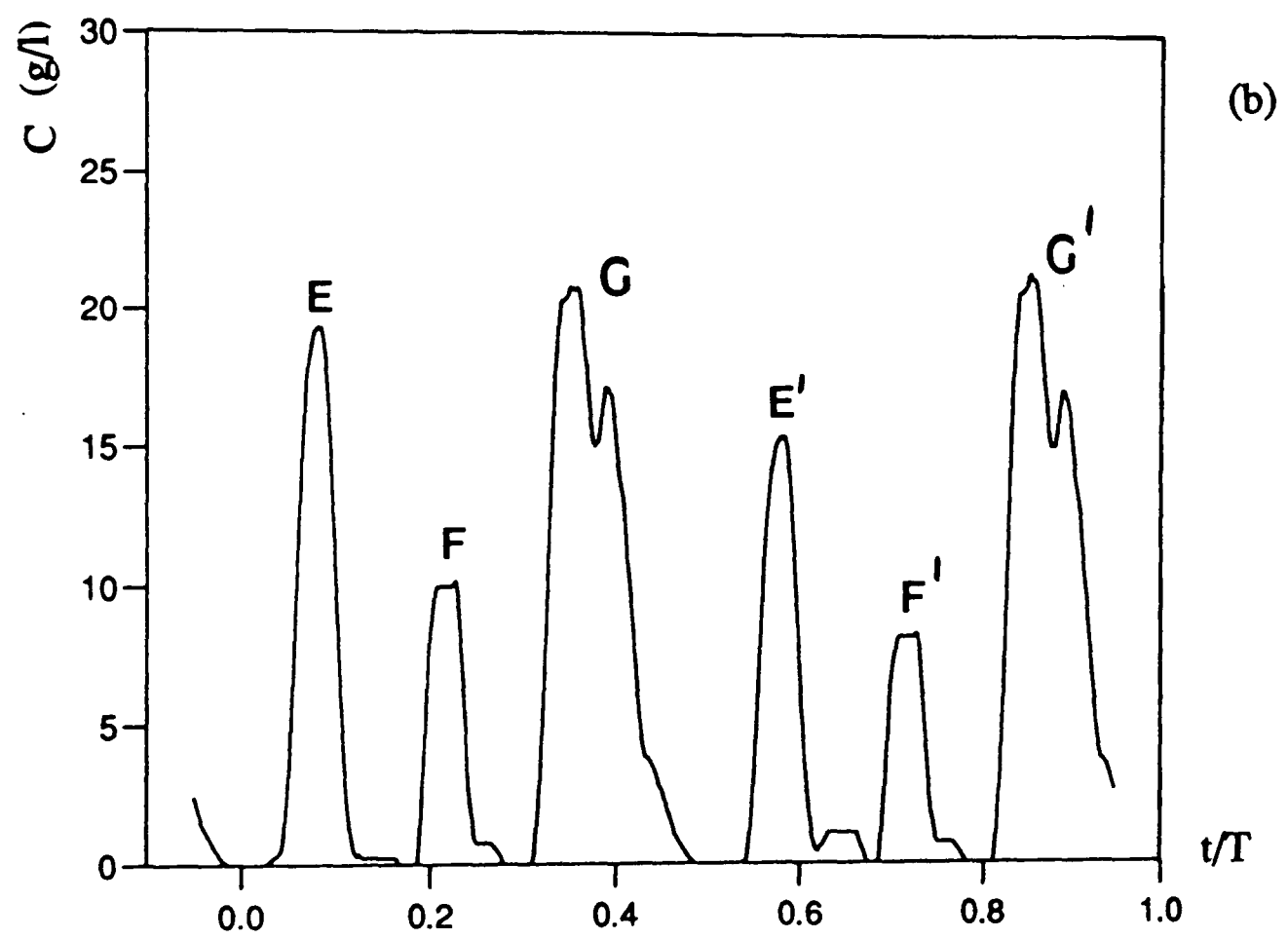
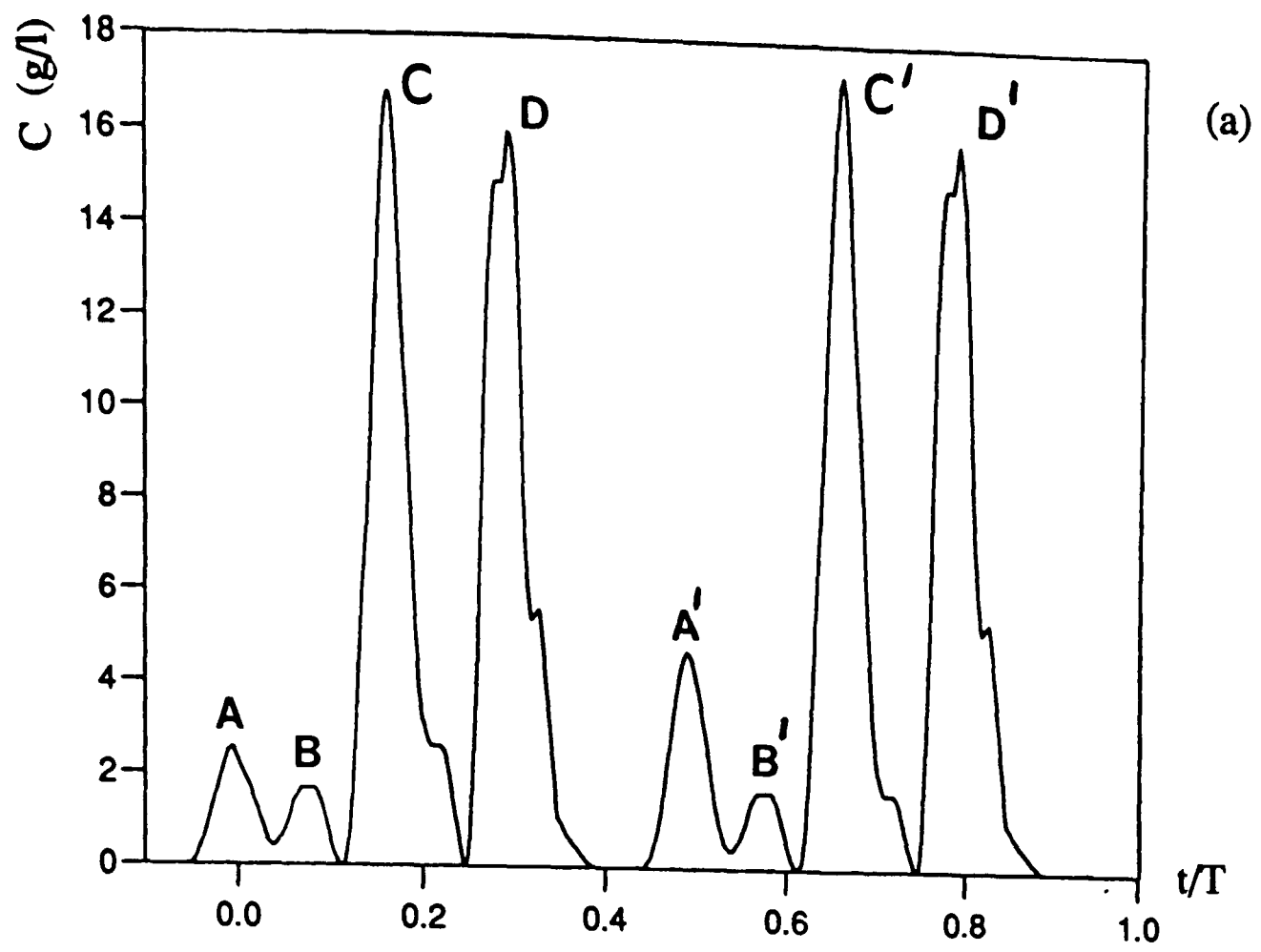


Figure 5.19 (a,b)

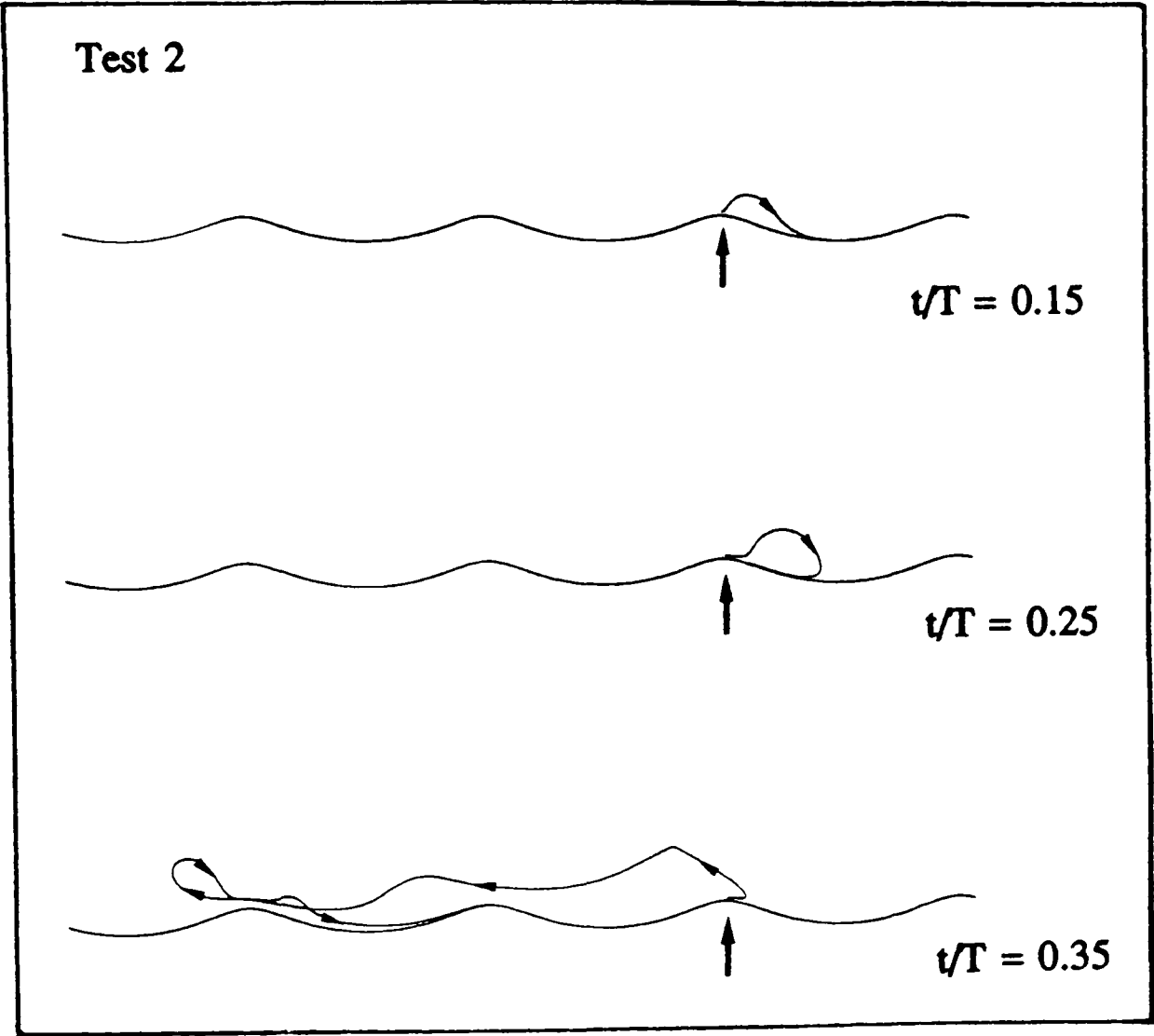


Figure 5.20

Results of some sensitivity tests on four of the parameters concerned with the simulation - the critical bed shear stress, τ_c , the height at which particles are released, z_T , the fall velocity of the sediment, w_s and the kinematic viscosity, ν . These sensitivity tests are then followed by a consideration of the effects of the box size on the results for instantaneous concentrations. All these test were carried out with the Test 1 settings, using the 'crest 1 cm' box.

Figure 5.21 (a,b) Sensitivity of the 'Test 1, crest 1.0 cm' inst. concentration to changes in (a) the critical bed shear stress τ_c , and (b) the point at which particles are released.

Figure 5.22 (a,b) Sensitivity of the 'Test 1, crest 1.0 cm' inst. concentration to changes in (c) the fall velocity w_s and (d) the kinematic viscosity ν .

Figure 5.23 Sensitivity of the inst. concentration to box size. (Test 1, crest 1.0 cm).

Figure 5.24 Sensitivity of the trail of a particle released at $t/T = 0.30$ to two values of fall velocity - $w_s = 0.6$ and 0.8 cm/s.

Figure 5.25 Cumulative ϕ_b values and ϕ_b time series for particle release. (Test 1 etc).

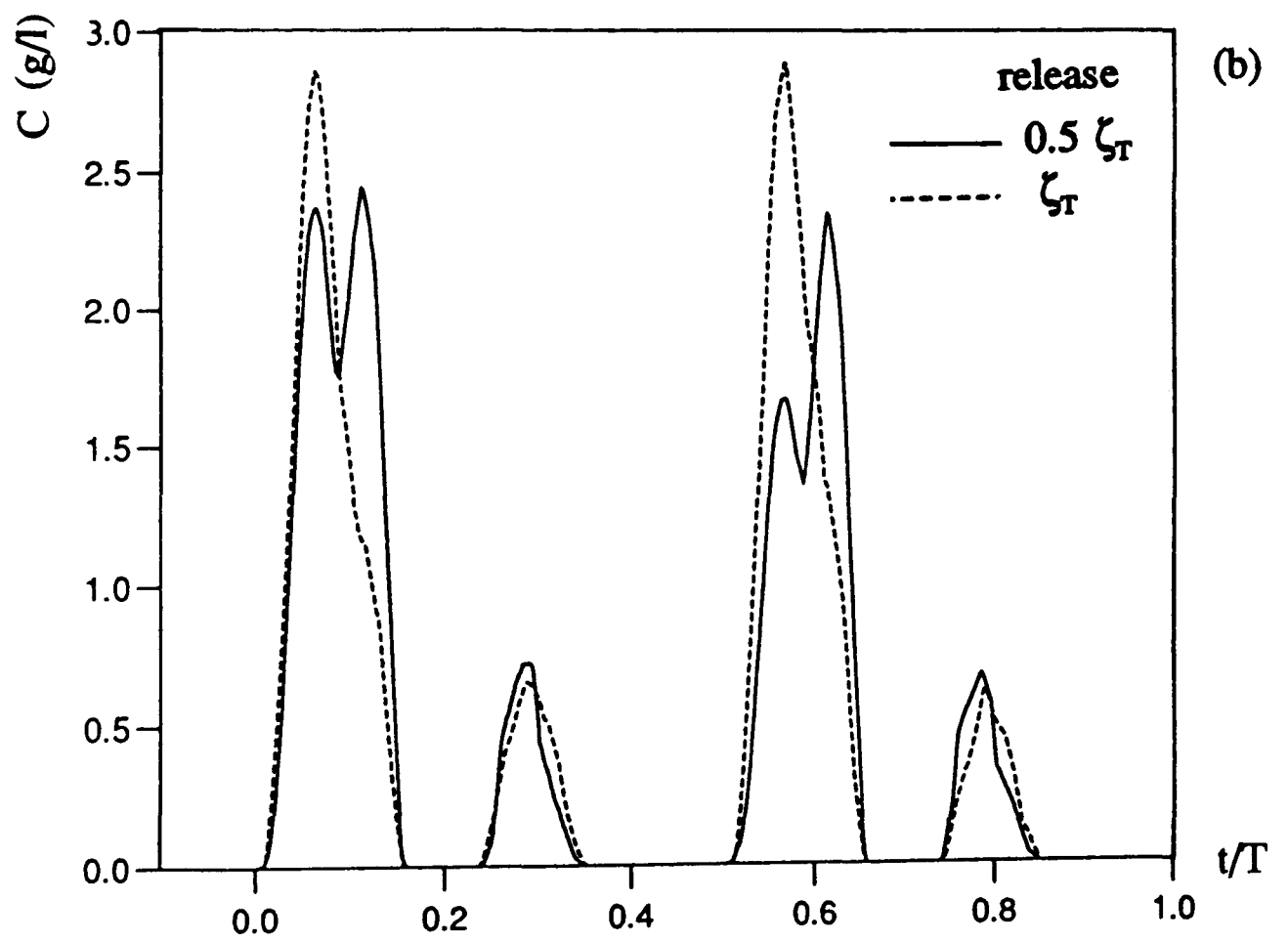
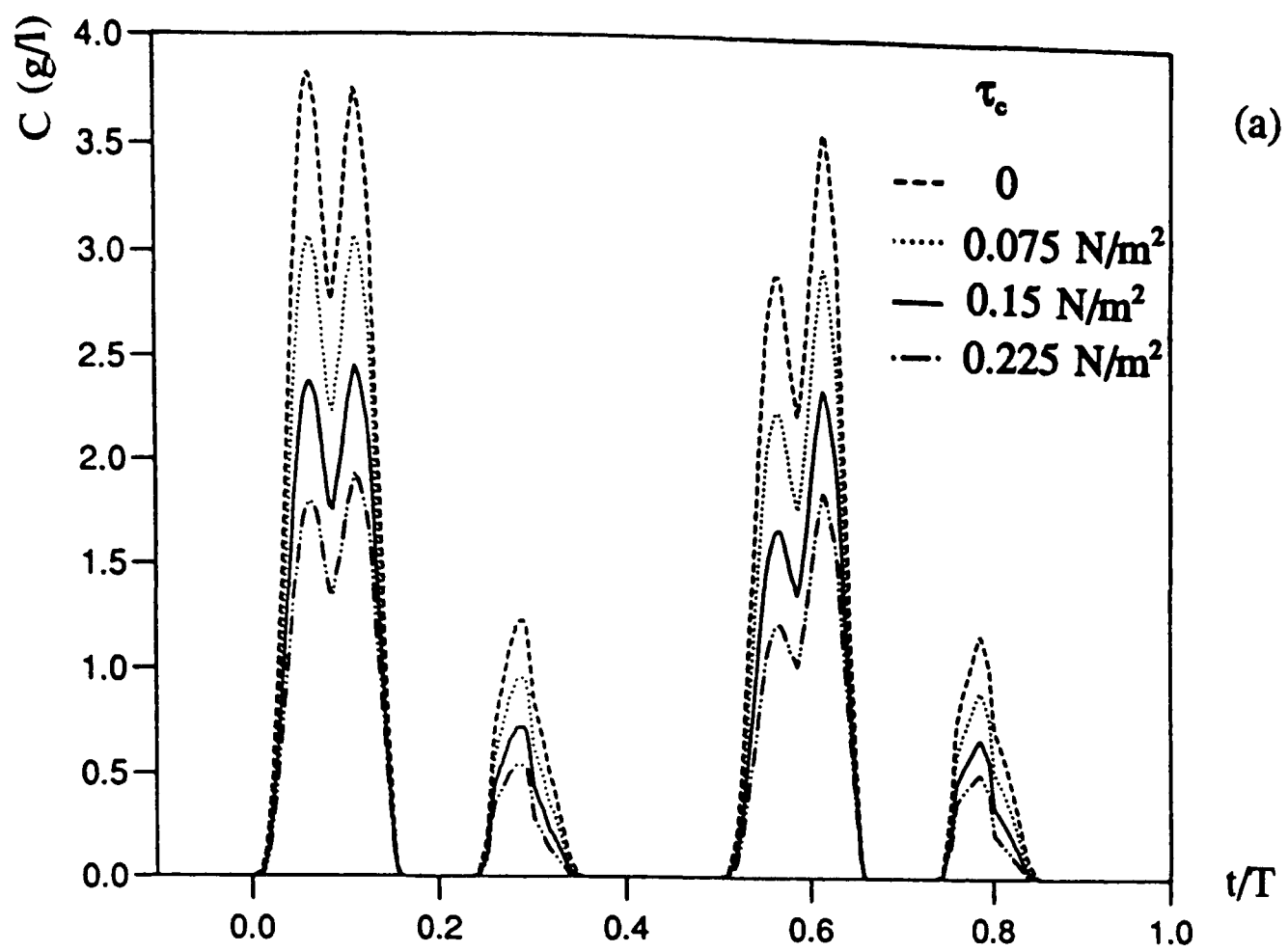


Figure 5.21 (a,b)

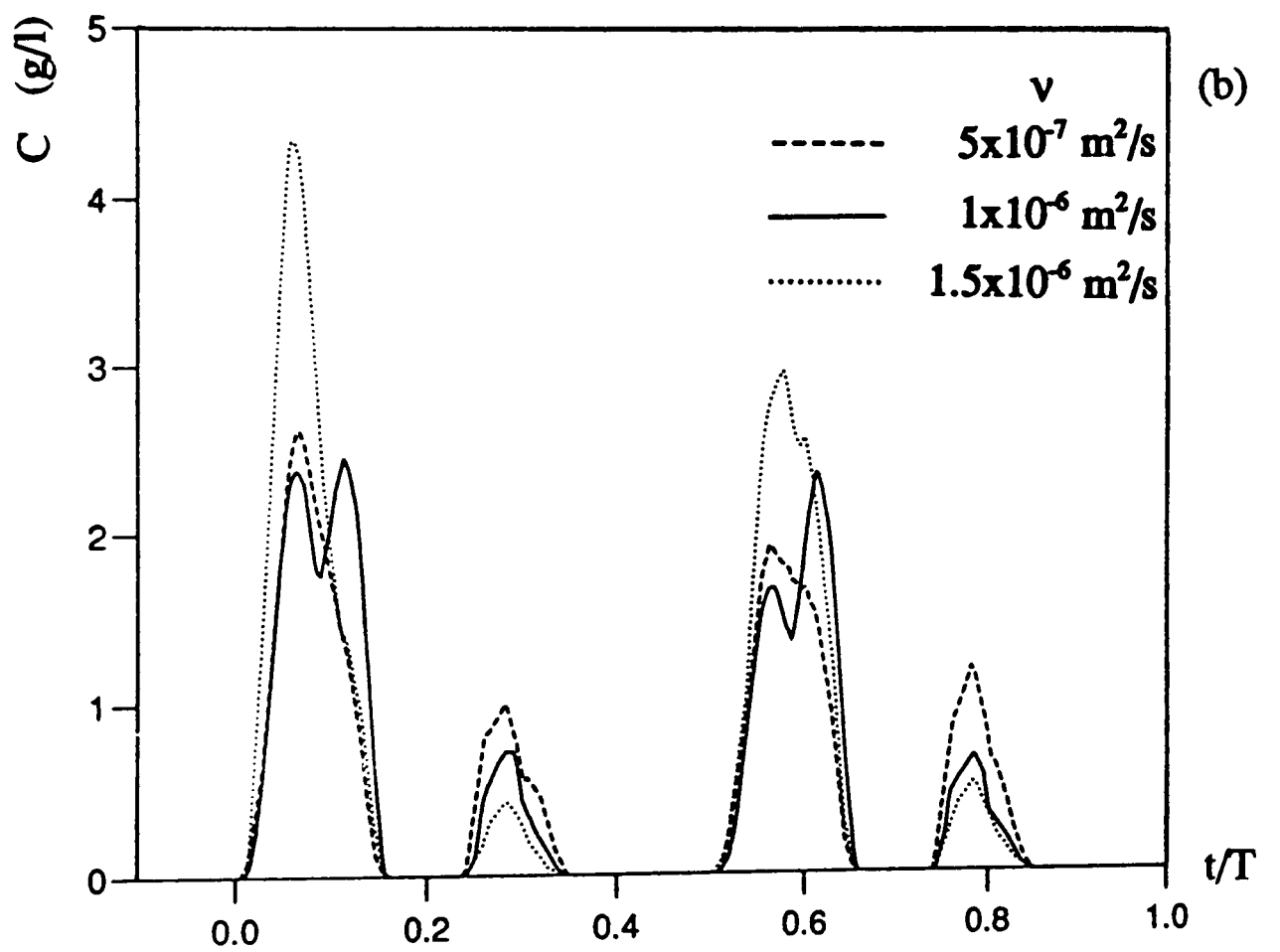
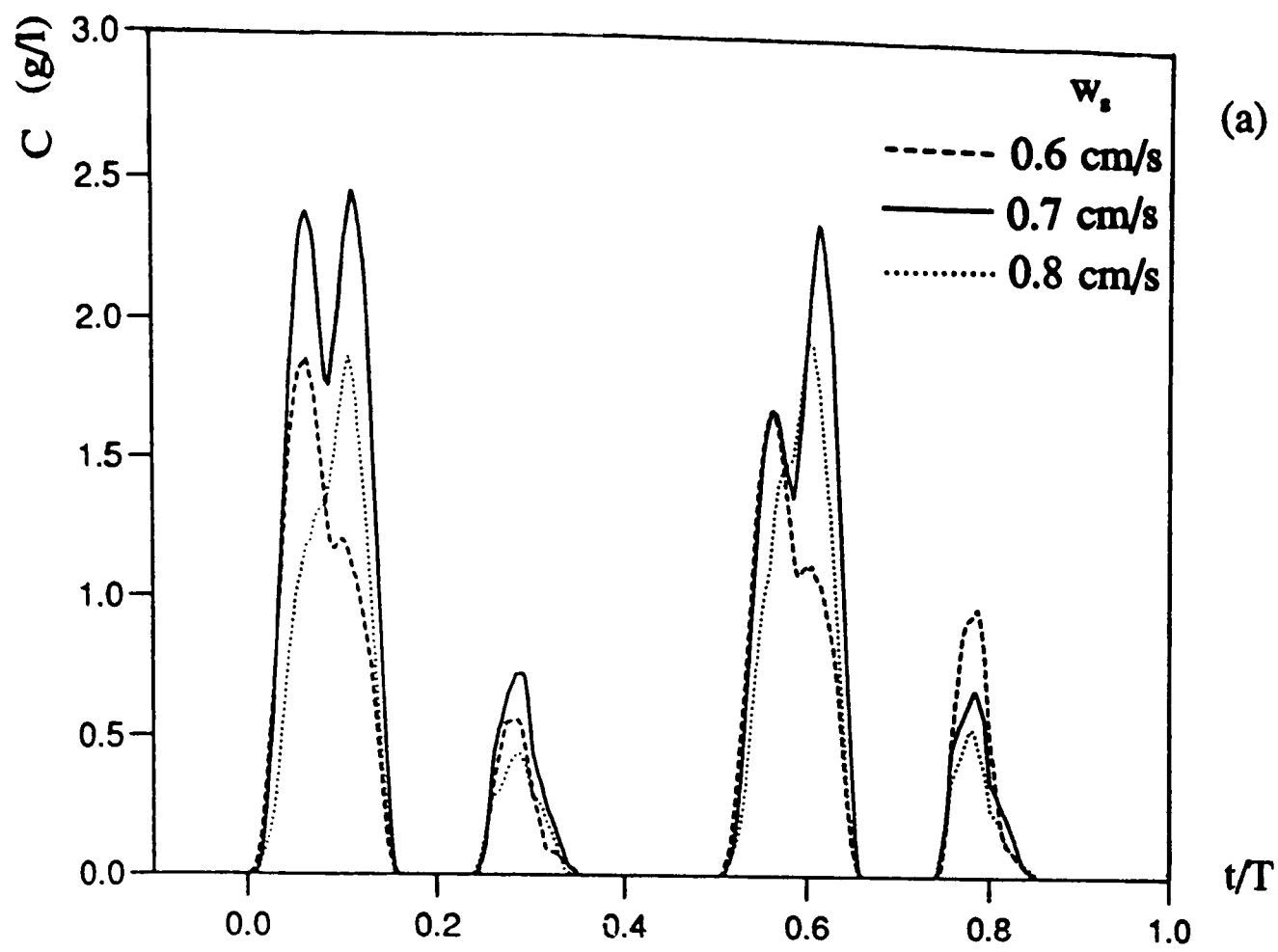


Figure 5.22 (a,b)

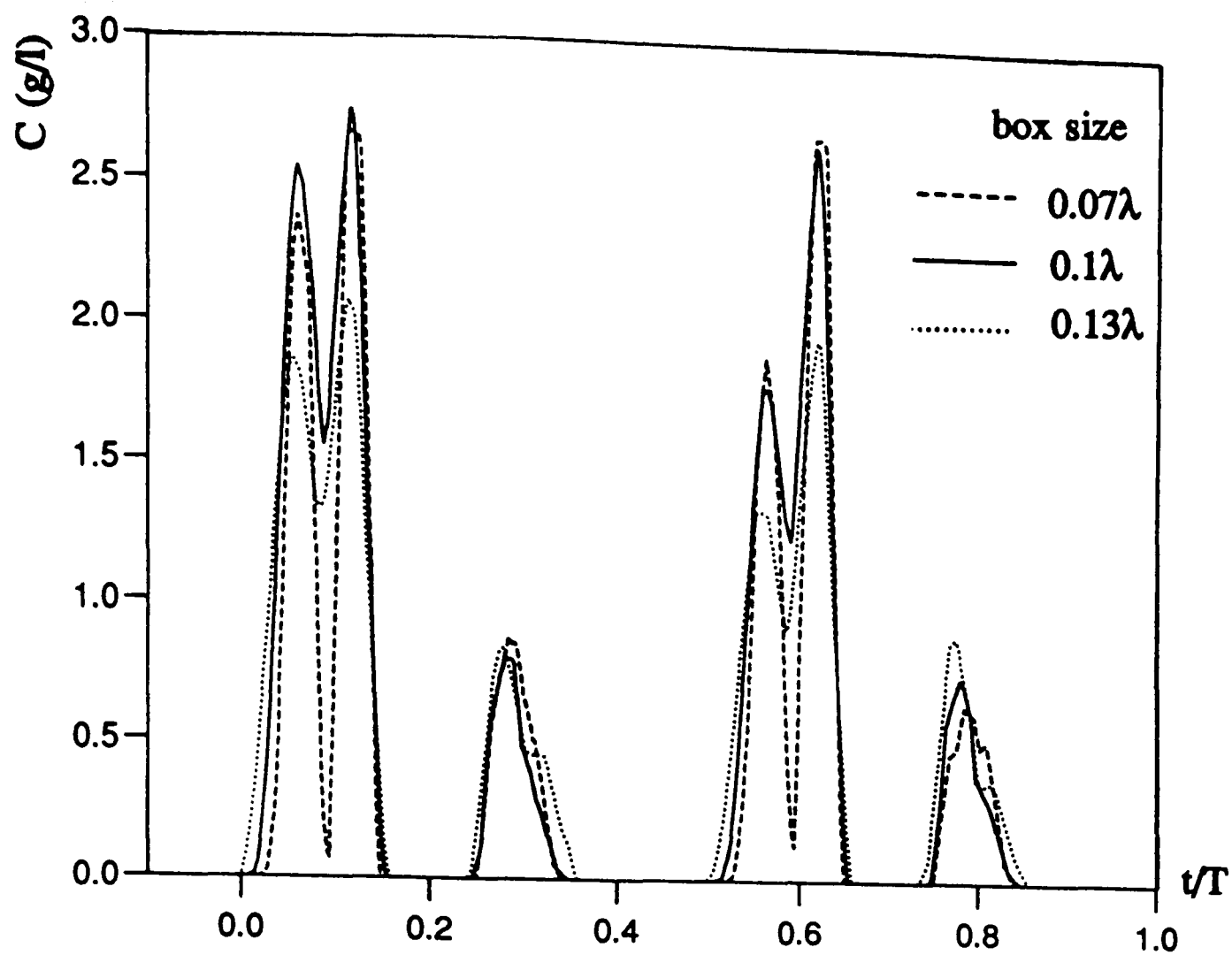


Figure 5.24

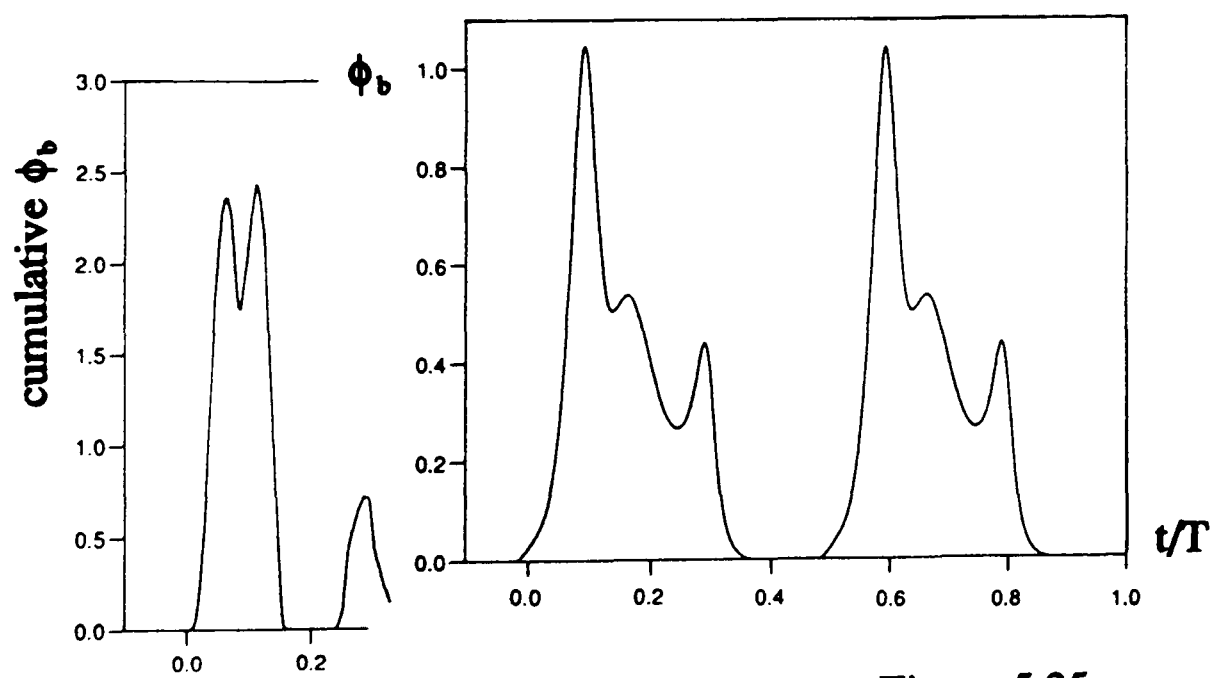
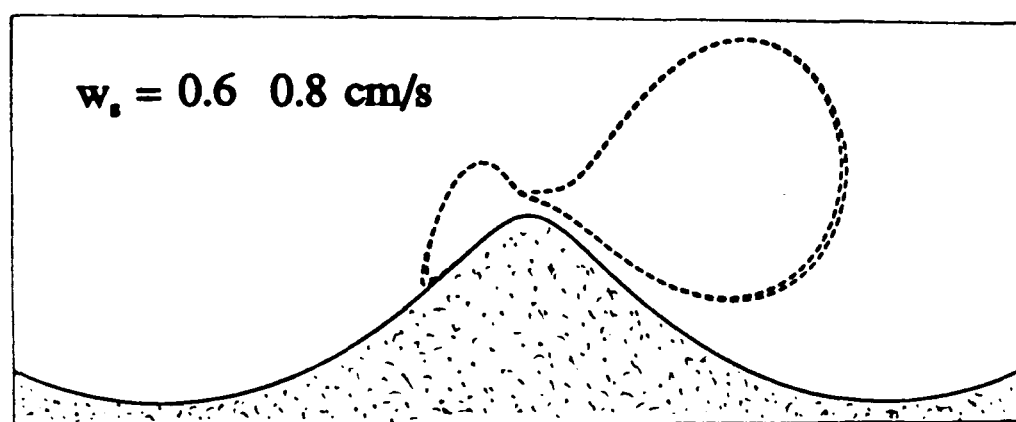


Figure 5.25

Results of the data comparisons.

Figure 5.26 (a)-(d) Comparisons of inst. concentration for Test 1 at four positions over the ripple profile (see figure (5.15 (a,b))). The table records the time-mean concentrations.

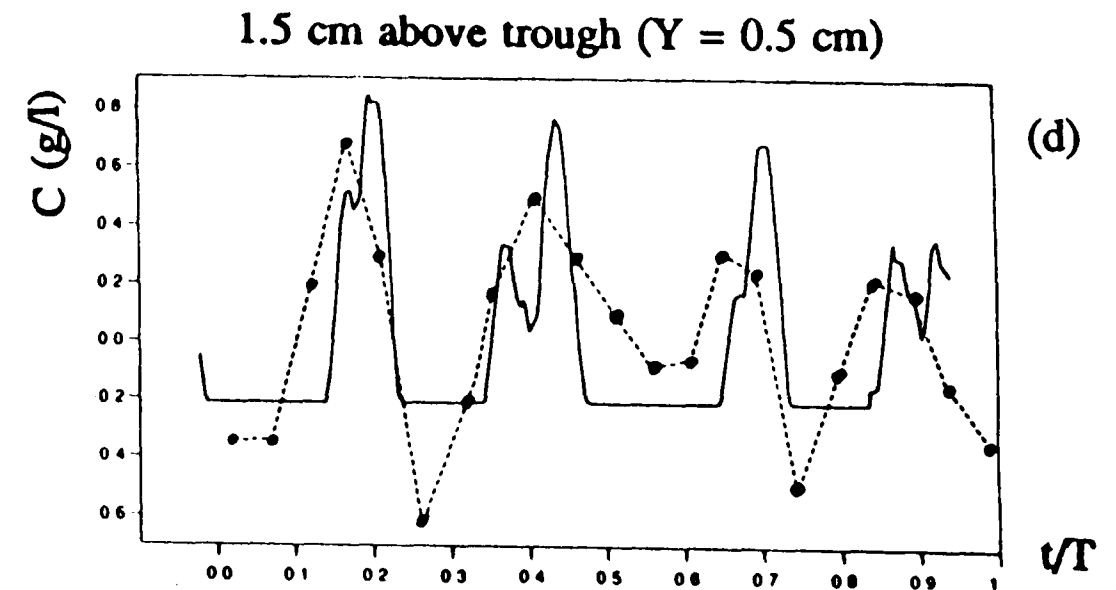
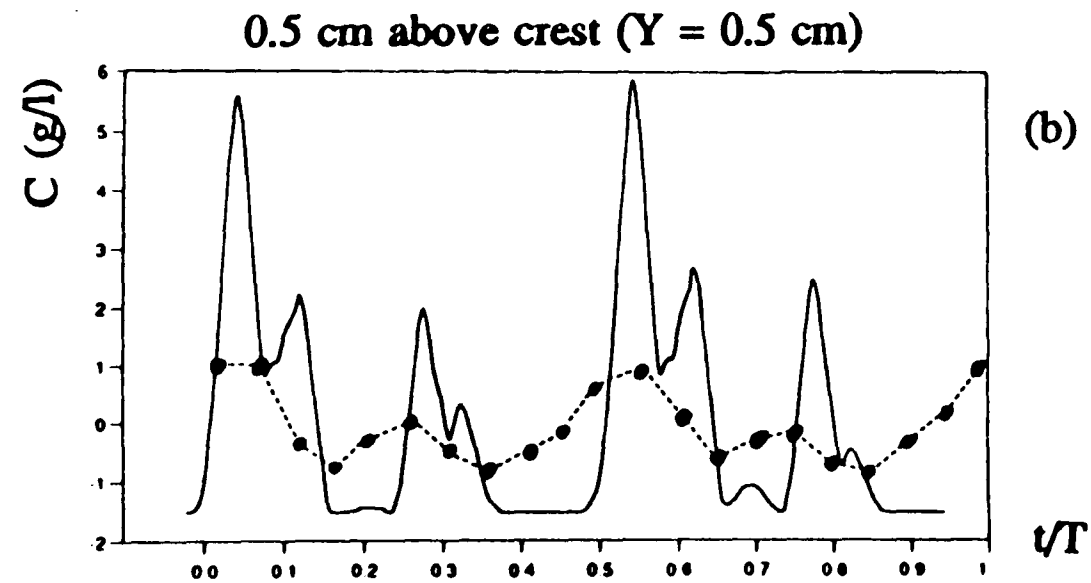
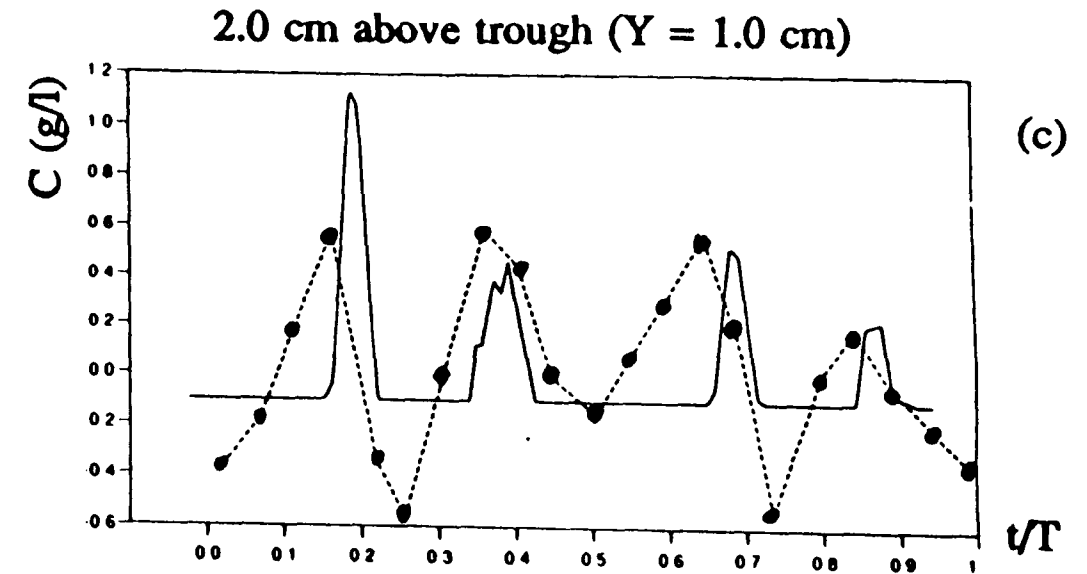
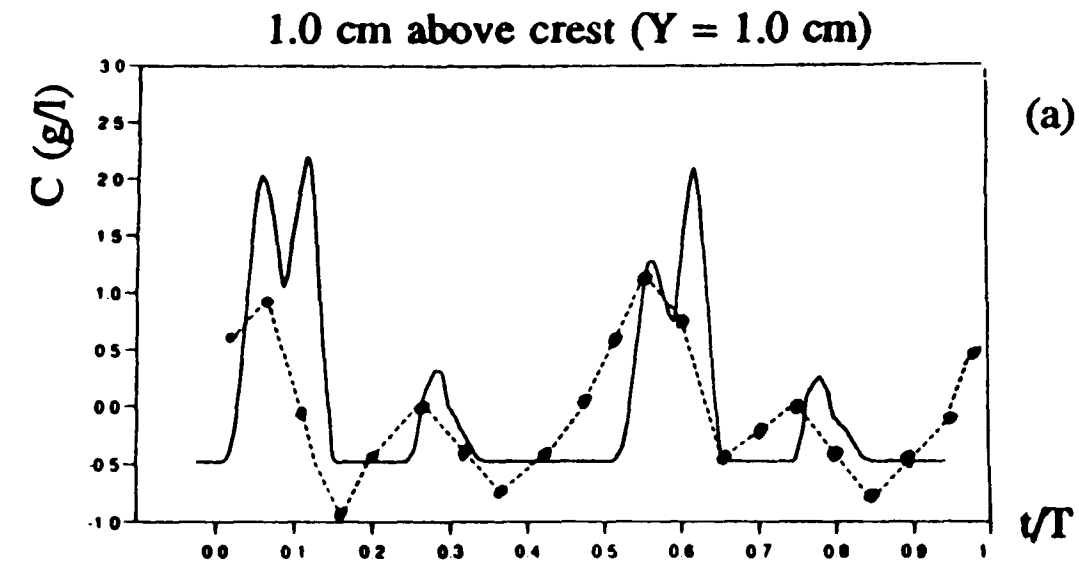
Figure 5.27 (a,b) Comparison of inst. concentration for Test 2 at two positions over the ripple profile. The table records the time-mean concentrations.

Figure 5.28 The vertical concentration profile, $\overline{C}(Y)$, for Tests 1 and 2, plotted alongside the exponential decay law of Nielsen (equation (5.1)). The table below records the values of reference concentration C_o obtained both from the model and equation (5.2)

Figure 5.29 The position over the ripple at which the measurements of (a) Nakato *et al* (1977), (b) Sleath (1982a) and (c) Bosman (1982) were obtained.

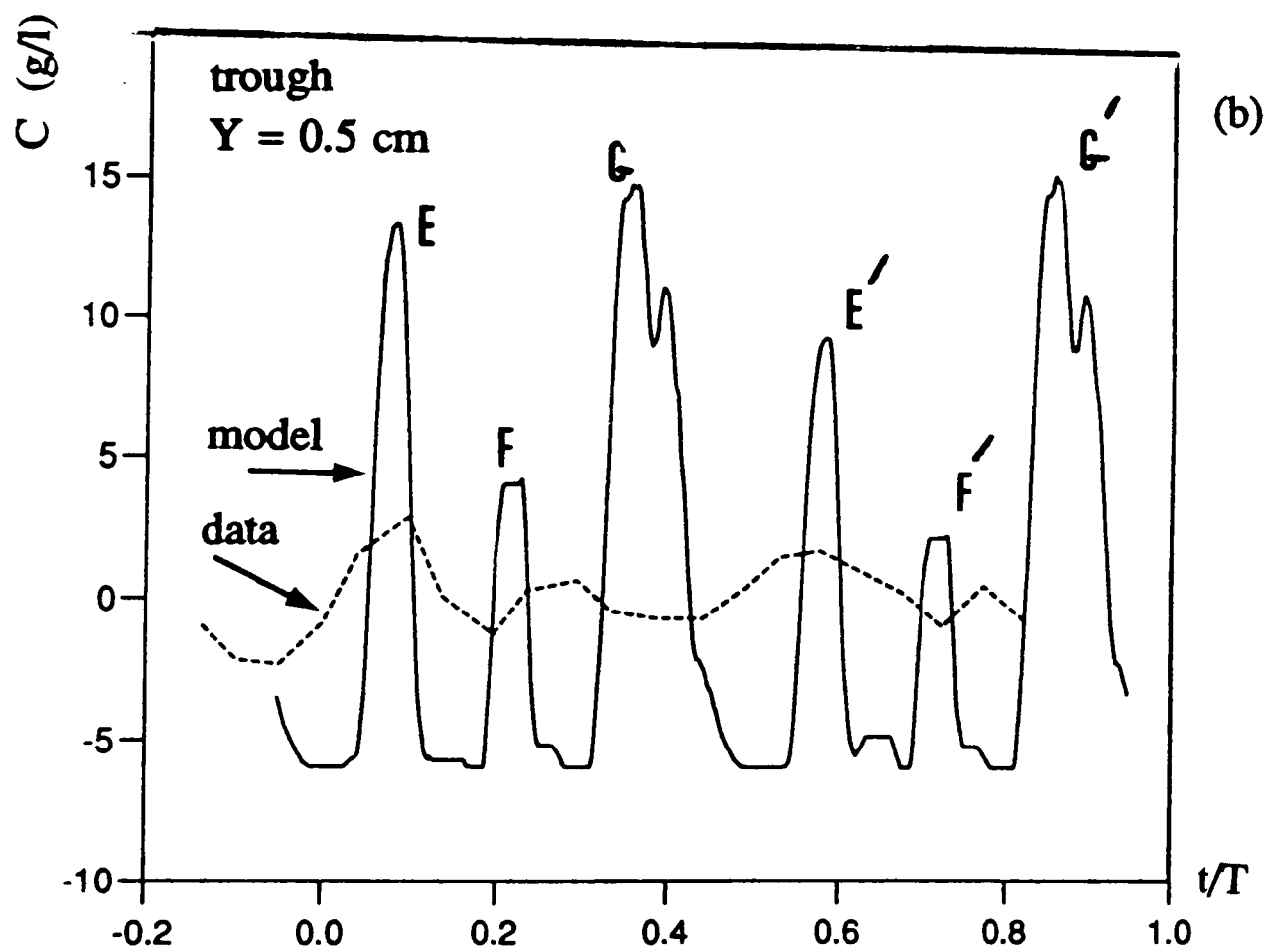
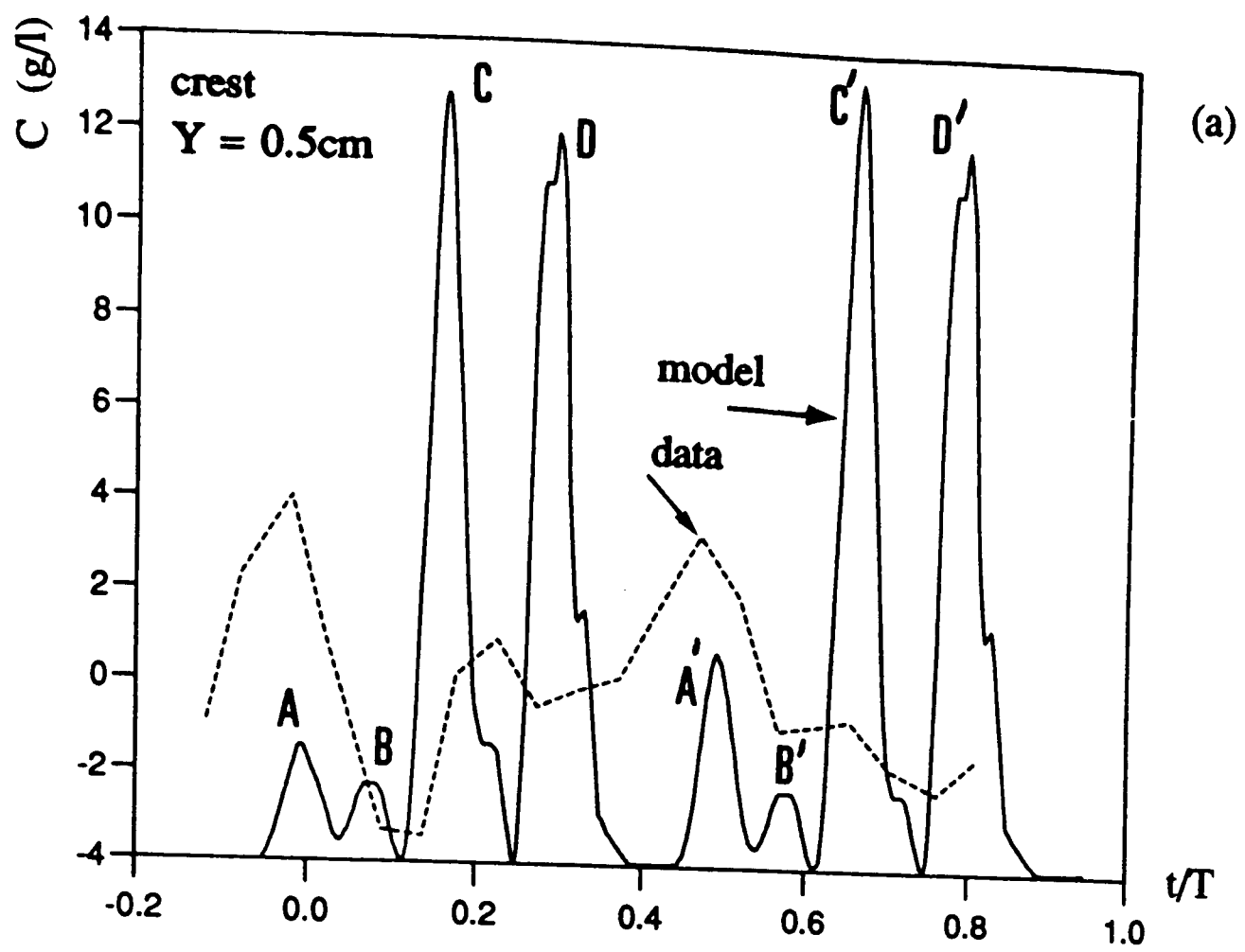
Figure 5.30 The time-mean concentrations for the three above studies.

Figure 5.31 Comparisons of inst. concentrations with the measurements of (a) Nakato *et al* (1977), (b) Sleath (1982a) and (c) Bosman (1982).



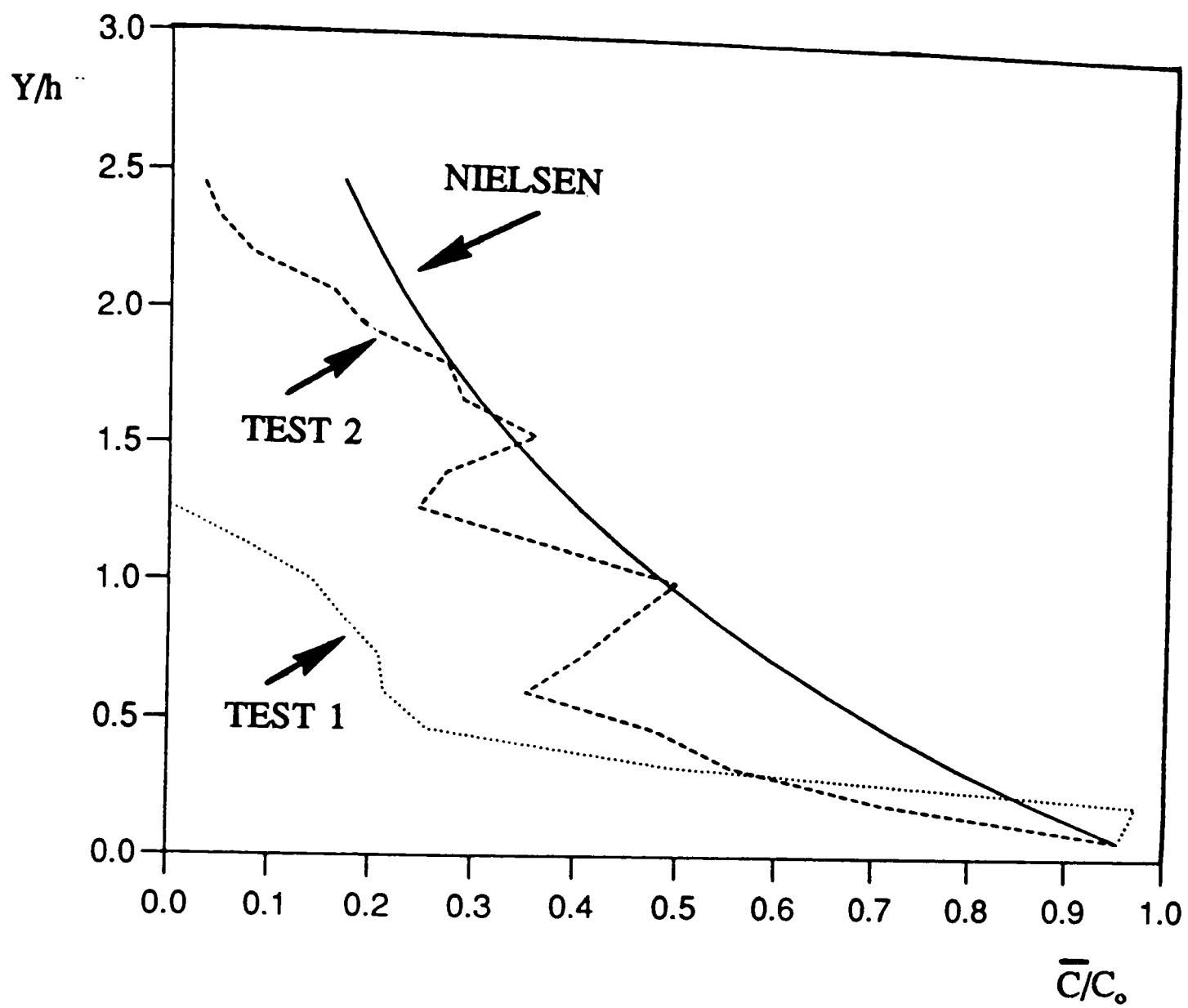
Mean conc. (g/l)	crest $Y = 1.0$ cm	crest $Y = 0.5$ cm	trough $Y = 1.0$ cm	trough $Y = 0.5$ cm
Lab. data	3.09	3.37	3.21	3.60
Present model	0.48	1.52	0.10	0.22

Figure 5.26 (a)-(d)



Mean concentration (g/l)	crest Y = 0.5 cm	trough Y = 0.5 cm
Laboratory data	3.96	10.22
Present model	11.15	5.93

Figure 5.27 (a,b)



	Model C_o (g/l)	Nielsen C_o (g/l)
Test 1	2.28	2.29
Test 2	8.80	4.96

Figure 5.28

Figure 5.29

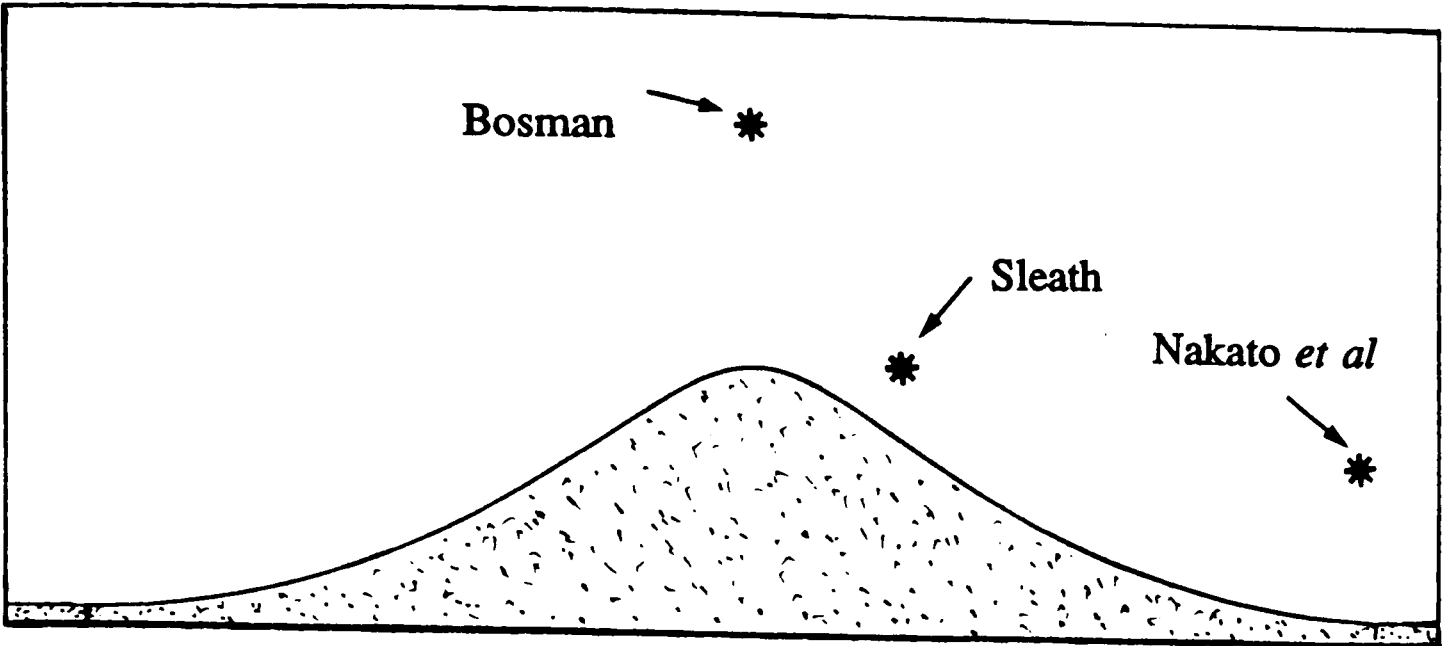


Figure 5.30

Mean concentration	Nakato et al (1977)	Sleath (1982a)	Bosman (1982)
Lab. data	14326 ppm	2.68 kg/m ³	13.57 kg/m ³
Present model	1208 ppm	0.24 kg/m ³	2.27 kg/m ³

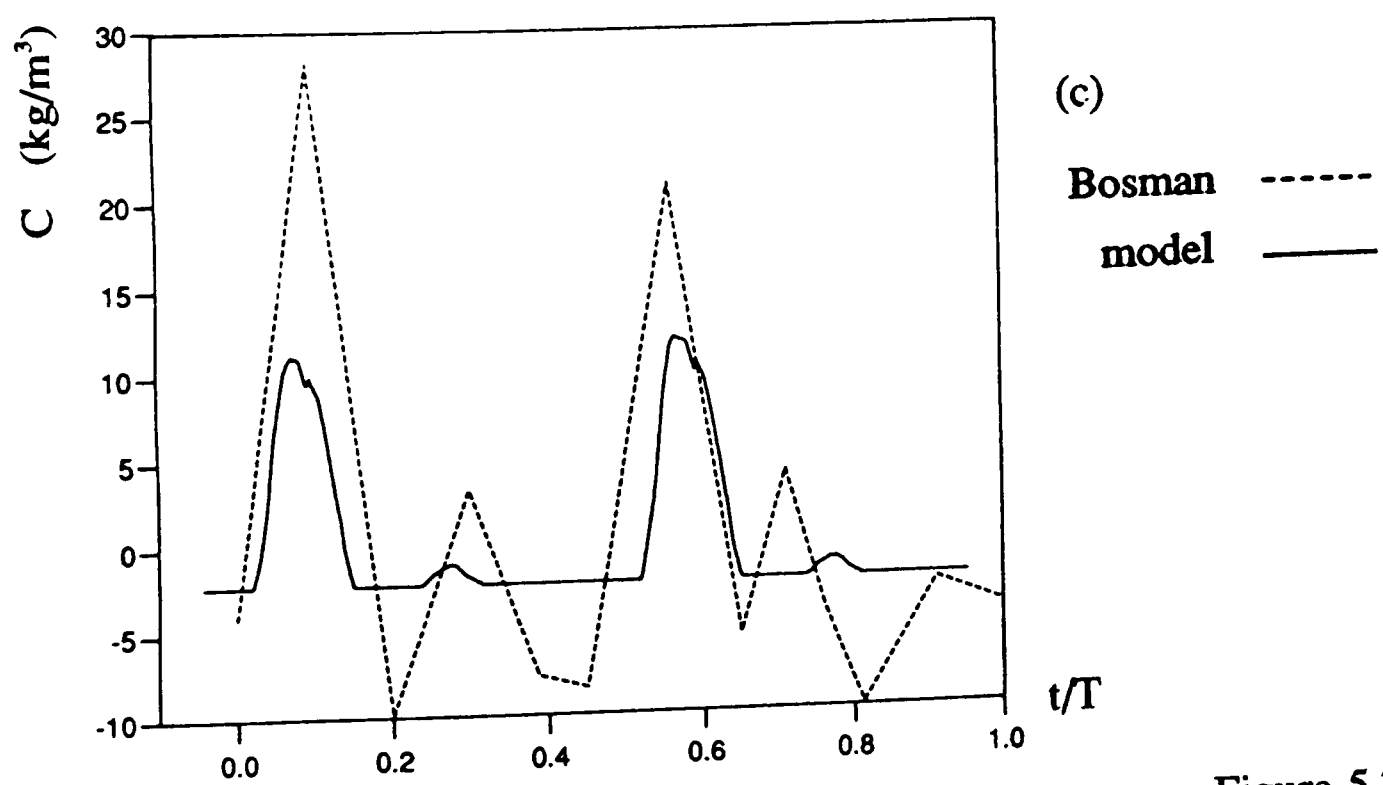
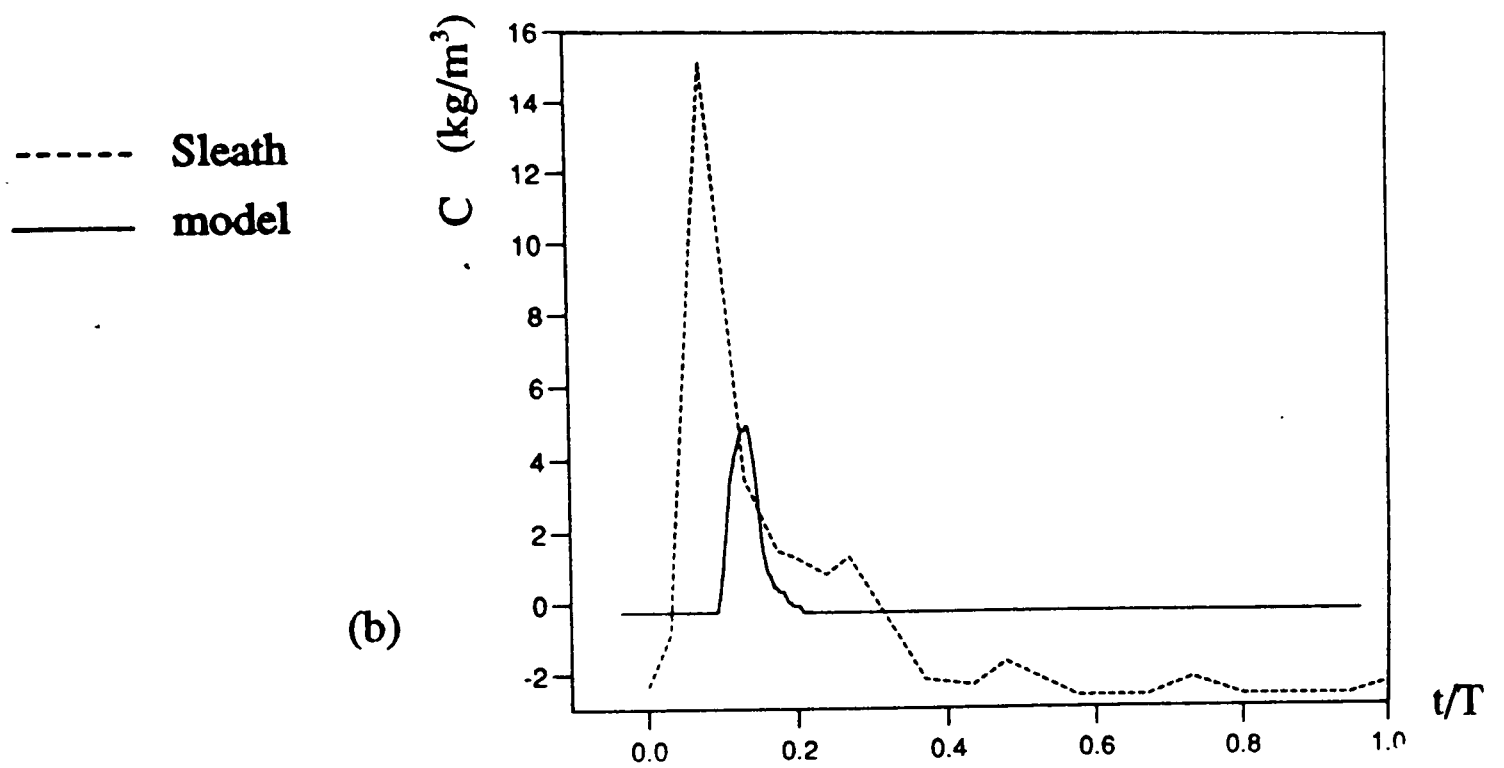
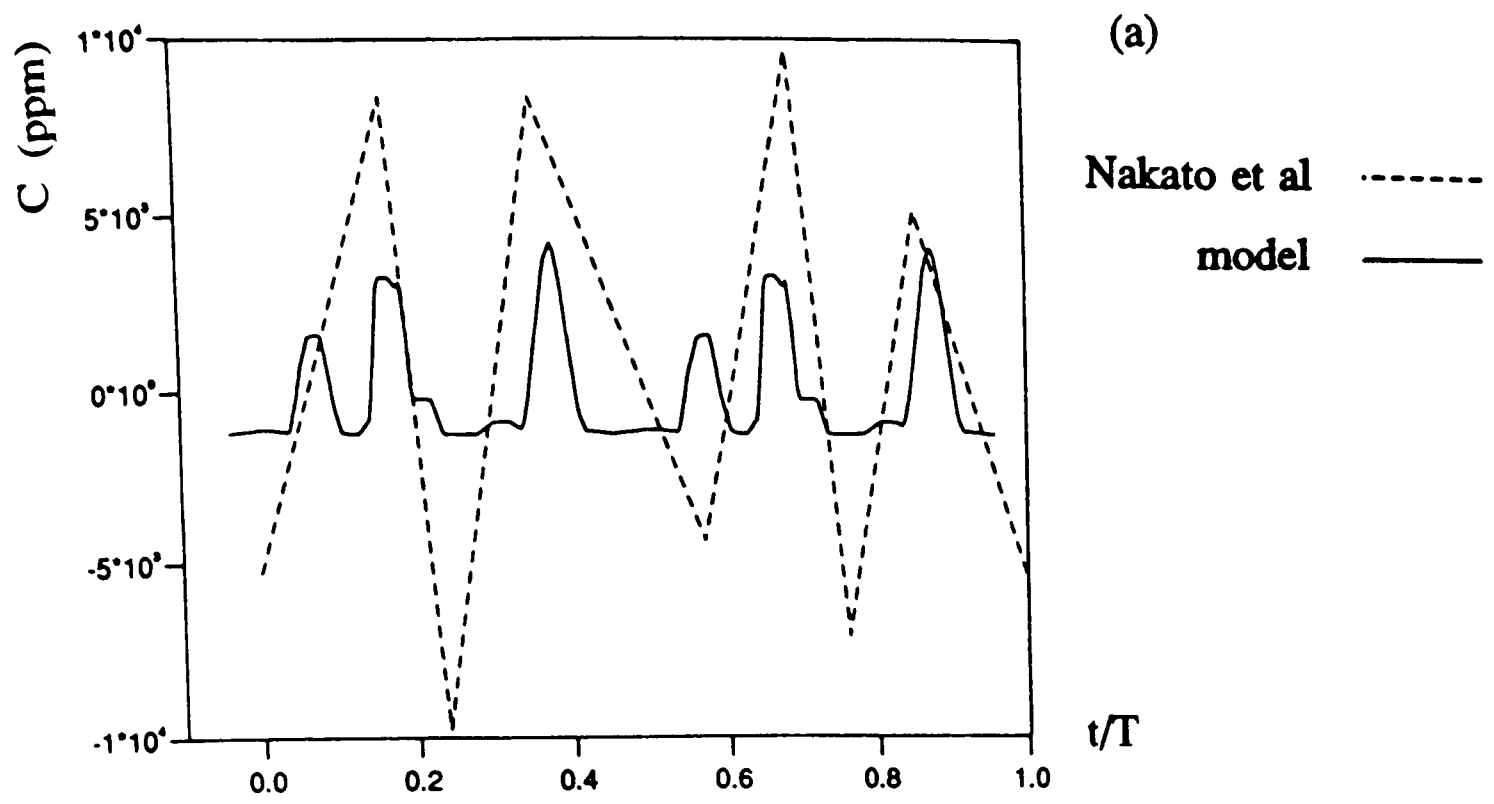


Figure 5.31 (a)-(c)

CHAPTER 6

RIPPLE STABILITY :

**THE MOVEMENT OF SEDIMENT AS BEDLOAD
OVER THE ENTIRE RIPPLE PROFILE**

6.1 Introduction

A novel and challenging test of the present work is to see if the present suite of models (hydrodynamical, boundary layer and suspension) can make meaningful predictions about both sediment movement over ripples and temporal changes in ripple morphology. These could then be combined in order to predict ripple stability. In computational terms, the models would be used to assess where accretion and depletion of sediment has occurred over the ripple profile. Net accretion of sediment in the crest region relative to the trough would be indicative of ripple stability, whilst the converse would suggest a flattening off of the ripples.

The process of moving sediment over ripples requires some consideration of slope effects, specifically the inclusion of slope effects in (flat bed) bedload formulae. Whitehouse (1991) undertook an experimental study of slope effects on bedload transport in unidirectional flow, then compared the data with a (slope-corrected) bedload transport formula due to Hardisty (1983). He found that the slope-corrected bedload equation significantly underestimated the actual effect of the slope. Fredsoe (1974) used a slope-modified critical bed shear stress in his study of dune formation in unidirectional flow.

The rationale of this chapter is that it is an exploratory exercise, aimed at seeing if the computational methodology outlined below is a viable (theoretical) way for predicting ripple stability. This work is at a formative stage.

6.2 Computational methodology

In order to pursue the above objectives, the ripple profile has been split into 40 ledges, and the boundary layer model applied as described in §4.3.4. This process provides a time varying description of τ_b/ρ through the wave cycle at each ledge. The concept of assessing bedform stability via the accretion and depletion of sediment on ledges has recently been used by O'Hare (1992) in a theoretical model of the evolution of sand bars.

Sediment is moved as bedload over the ripple profile using a slope-corrected form of the Meyer-Peter Muller bedload formula, as quoted in Fredsoe and Deigaard (1992):

$$\phi_b = 8 \left[\theta - \left(1 - \frac{1}{\tan \phi} \frac{dy}{dx} \right) \theta_c \right]^{\frac{3}{2}} \quad 6.1$$

$$\phi_b = \frac{Q_b}{\sqrt{\gamma g D_{50}^3}} \quad 6.2$$

where ϕ is the angle of static repose and the remaining symbols are as defined in §5.1.3 (a), equation (5.4 (a,b)). The role of the slope term (in round brackets) is to increase or decrease the critical (threshold) bed shear stress as dictated by the local flow direction and bed gradient (dy/dx).

Equation (6.2) gives Q_b , the volumetric transport rate (per unit width) of sediment moving from each ledge at each time step, while the local flow (U_b) dictates the direction of this movement. At a particular ledge, therefore, sediment is both dispatched and received. We call these quantities $Q_{b(off)}$ and $Q_{b(on)}$ respectively. If the amount of sediment raining on the ledge from the suspended load is denoted as $Q_{b(fall)}$, then the summation

$$Q_{b(net)} = Q_{b(on)} + Q_{b(fall)} - Q_{b(off)}$$

gives a measure of the rate of change of sediment at a particular ledge. This is shown schematically in figure (6.2), while figure (6.1) illustrates the disposition of the ledges.

Initially, $Q_{b(off)}$ is calculated at each of the 40 ledges using equation (6.2). $Q_{b(on)}$ follows directly from these values, the local flow direction dictating which direction the sediment is moved. Spatial periodicity is imposed by the linking of ledge 1 to ledge 40. At the crest itself (ledge 21), $Q_{b(off)}$ is assumed to be entrained into suspension, which affects the values of $Q_{b(on)}$ for ledges 20 and 22. The fall component, $Q_{b(fall)}$, is obtained from the suspended sediment simulation (Chapter 5).

6.3 Results

Results are presented for the Test 1 settings (with $d/\lambda = 1.62$, $h/\lambda = 0.16$). These first assess the ability of the present method to move sediment over the ripple profile. After this, cumulative ' Q_b ' totals on each of the ledges are presented, in order to identify where net accretion and denudation occur. Finally, the implications of these morphological changes are assessed with regard to ripple stability.

6.3.1 Results with no threshold of sediment motion ($\tau_c/\rho = 0$)

6.3.1 (a) *The movement of sediment over the ripple profile*

A constant (and unwelcome) feature of all the results is the erroneous value of $Q_{b(off)}$ and $Q_{b(on)}$ at ledge 1. This is a consequence of the problem noted in Chapter 4, regarding the velocity discontinuity caused by the early destruction of the ejected vortex.

Figure (6.3) relates to the bed shear stress plot (figure (4.11)) in Chapter 4 and has the same general features. Here, though, the vertical axis is a scalar quantity, $Q_{b(on)}$ - the magnitude of the volumetric sediment transport rate per unit width onto each ledge. The discontinuities in bedload transport just before oscillatory flow reversal (at $t/T = 0$), the local maxima at about the time of maximum oscillatory flow ($t/T \approx 0.25$) and the large, dominant maximum in the second half cycle due to the growing vortex, are all features noted in connection with figure (4.11). In the present context, these maxima represent phase instants when the movement of sediment onto the ledges is relatively high. For ledge 15, the vortex-induced maximum at $t/T = 0.80$ is more than twice the magnitude of the oscillatory flow induced peak at $t/T = 0.25$. The peak at $t/T = 0.80$ is slightly later than the equivalent maximum in figure (4.11) because $Q_{b(on)}$ is governed by the bed shear stress regime at the neighbouring ledges, not ledge 15 itself.

Figure (6.4) shows the variation in $Q_{b(on)}$ over the ripple profile at four phase instants during the first half cycle. Again, the traces share many similar features with the companion graph in Chapter 4 (figure (4.12)). If one disregards the variability in the trough region (ledges 1,2,39,40) (see above), then the left side of the ripple shows increasing amounts of sediment being moved as the crest (ledge 21) is approached. The

trace for $t/T = 0.10$ is enhanced by the rotational effects of the ejected vortex as it passes the crest. On the right of the ripple, over which the growing vortex is forming, the traces are less ordered or continuous. This is the first indication of a failing in the boundary layer model for moving sediment over the profile. Sediment is not able to pass through the stagnation/separation points formed by the growing vortex's separation region. As an example of this, the trace for $t/T = 0.30$ shows no sediment moving onto ledges 22 or 31 - the positions of the stagnation/separation points. The vortex-induced transport over ledge 25 (at $t/T = 0.20$) is an order of magnitude larger than any of the spikes caused by the oscillatory flow. Thus the crest is being starved of a relatively large quantity of sediment.

Figure (6.5) shows the cumulative values of $Q_{b(on)}$ and $Q_{b(off)}$ over the ripple profile during the first half cycle. The curves match each other well, with $Q_{b(on)}$ leading $Q_{b(off)}$ by one ledge as expected. This suggests that the model is moving sediment properly up the stoss face. The difference in magnitude at the crest itself (ledge 21) is due to the loss of the $Q_{b(off)}$ component there. This loss deprives either ledge 20 or ledge 22 of sediment. On the right (lee) slope of the ripple, the model moves sediment from the right trough in an orderly fashion until the crest region is reached. Here, the growing vortex (with its associated stagnation/separation points) disrupts the exchange of sediment from ledge to ledge.

6.3.1 (b) *Net accumulation and deposition over the ripple profile*

Having analysed the way in which sediment moves over the ripple profile, attention now turns to the net accumulation and deposition of sediment. Figure (6.6) shows the cumulative total for $Q_{b(fall)}$ over the profile for one cycle. For purposes of analysis, the profile has been split into a 'crest region' (ledges 12-30) and a 'trough region' (ledges 1-11, 31-40). With this division, $3.5 \times 10^{-4} \text{ m}^2/\text{s}$ lands in the crest region and $3.18 \times 10^{-4} \text{ m}^2/\text{s}$ settles in the trough region, suggesting net deposition of falling sediment in the crest region. A basic, numerical check of this data shows that the total value for $Q_{b(fall)}$ over the whole ripple profile exceeds the total amount of sediment released at the crest by $7.25 \times 10^{-6} \text{ m}^2/\text{s}$ or by 1%. These values should ideally be equal,

and the (small) discrepancy is attributable to cycle by cycle fluctuations in the hydrodynamical model.

Figure (6.7) shows the cumulative total of $Q_{b(net)}$ over the entire ripple profile during a cycle. The hiatus at ledge 1 is due to the hydrodynamic problems discussed earlier. The intense regions of accumulation and erosion either side of the crest are caused by growing vortices forming in each half cycle, a feature discussed in §6.4. At the crest itself, there is net erosion suggesting that sediment being entrained into suspension is not being replaced. These results (excluding ledge 1) show a net erosion rate of $1.24 \times 10^{-4} \text{ m}^2/\text{s}$ in the crest region (ledges 12-30) and a net accumulation rate of $5.74 \times 10^{-5} \text{ m}^2/\text{s}$ in the trough region. The inference from this data is that the troughs would fill up at the expense of the crest, and the ripple would be unstable. The total sum of this data over the ripple profile (including ledge 1) should be zero. However, it actually gives $1.0 \times 10^{-5} \text{ m}^2/\text{s}$, an imbalance consistent with the error for $Q_{b(fall)}$ ($7.25 \times 10^{-6} \text{ m}^2/\text{s}$).

6.3.2 The inclusion of a threshold of sediment motion

The effect of the inclusion of two thresholds, $\tau_c = 0.05, 0.10 \text{ N/m}^2$, is considered. A non-zero threshold condition warrants consideration of the so-called *slope term*

$$1 - \frac{1}{\tan \phi} \frac{\partial y}{\partial x}$$

A slope term greater than 1 is indicative of an increased threshold and, hence, slope-retarded sediment movement, while a slope term less than 1 indicates slope-enhanced movement. Figure (6.8) illustrates the operation of the slope term for $t/T = 0.20$, $\tau_c = 0.05 \text{ N/m}^2$. At this time, the oscillatory flow is from left to right. Over the left (stoss) slope, the flow is uphill, so the slope term is greater than 1, reaching its maximum value at the position of maximum slope. Once the crest is passed, over ledges 21 to 23, the flow is downhill, so the slope term is less than 1. However, the growing vortex over the lee slope causes an uphill flow, so the slope term again becomes greater than 1. Finally, beyond the region of influence of the growing vortex, the flow is once more downhill and the slope term again becomes less than 1. As the trough is approached,

the gradient tends to zero, the slope term tends to 1, and the flat-bed form of the Meyer-Peter Muller bedload formula is recovered.

Figure (6.9) shows cumulative values of $Q_{b(oa)}$ during the first half cycle, for $\tau_c = 0, 0.05$ and 0.10 N/m^2 (see figure (6.5)). The imposition of a threshold reduces the magnitudes but, in general, does not affect the shape of the curves. One (pleasing) exception to this assertion is that the thresholds have damped out the hydrodynamically based errors at ledge 1.

Figure (6.10) has the same format as figure (6.7). The inclusion of the thresholds has two main affects. Firstly, erosion at the crest (ledge 21) is significantly increased, while secondly, $Q_{b(soe)}$ achieves a better balance in the trough region. For $\tau_c = 0.05 \text{ N/m}^2$, the crest region loses $2.10 \times 10^{-4} \text{ m}^2/\text{s}$, while the trough region gains $1.91 \times 10^{-4} \text{ m}^2/\text{s}$. With $\tau_c = 0.10 \text{ N/m}^2$, the crest region loses $1.68 \times 10^{-4} \text{ m}^2/\text{s}$ whilst the trough region gains $1.66 \times 10^{-4} \text{ m}^2/\text{s}$. This again suggests instability of the ripples. In both cases, the same small imbalances in the total sum of sediment considered occur, as in the non-threshold case discussed in §6.3.1(b).

6.4 Discussion

The results in §6.3 provide a clear picture of the ability of the model to move sediment over ripple profiles and, hence, predict their stability. In each half cycle, sediment on the stoss face of the ripple is being entrained and moved up the slope in a continuous stream (see figure (6.5)). However, over the lee slope, the growing vortex disrupts this process, so the crest is being starved of this contribution of sediment. This disruption is also evidenced in figure (6.5), where the value of $Q_{b(oa)}$ is reduced almost to zero at certain positions on the lee slope. The explanation for this concerns the presence of stagnation/separation points associated with the growing vortex. By their very definition, these are positions at which the local flow is stagnant. The model is predicting that sediment reaching these positions cannot pass through. Therefore, the intense erosional effects beneath the growing vortex cause local scour between the stagnation/separation points, with this sediment load accumulating at the points themselves. Figure (6.11) is a sketch illustrating this effect. Each growing vortex has

two separation/stagnation points, an upper one near the crest and a lower one on the lee slope. This lower point moves down the lee slope as the growing vortex develops, which allows its trapped load to travel. However, the upper point remains fixed near the crest, so sediment is trapped there. In reality, sediment has mass, and hence inertia, so moves up the lee slope without disruption.

The results for $Q_{b(Net)}$ (figures (6.7), (6.10)) show erosion of sediment at the crest ledge itself which is a direct consequence of sediment trapping at the stagnation points. Figure (6.10) demonstrates that with or without a threshold, sediment is removed from the crest region and accumulates in the trough region. This would ultimately cause the ripples to be wiped out, which does not agree with observations (stable ripples being formed under the same conditions in the laboratory). No firm statements are made as regards the general validity of these findings: the aim of this particular study is speculative, seeing if the present computational algorithm is a viable predictor of ripple stability.

The model predicts that the rotation of the growing vortex over the lee slope (the effect which Bagnold (1946) likens to a spinning wheel) mobilises a larger quantity of sediment than the oscillatory flow on the stoss face. This source of sediment is not reaching the crest in the model, because of the near-crest stagnation point. Therefore, the model is starving the crest of a significant supply of sediment.

6.5 Conclusions

The present suite of models have been used to move sediment over the whole ripple profile in order to make predictions about ripple stability. Although the results presented are not altogether successful, their shortcomings may be explained quite simply in terms of the inability of the model to move sediment through stagnation points. This shortcoming must be addressed before the present computational algorithm can be successfully used to predict ripple stability.

Theoretical studies of ripple stability and the movement of sediment over their profiles are in their infancy. There is much scope for further work here.

Some explanatory sketches for this chapter.

Figure 6.1 The disposition of the 40 ledges over the ripple profile.

Figure 6.2 The three component parts of Q_b at a particular ledge.

Figure 6.1

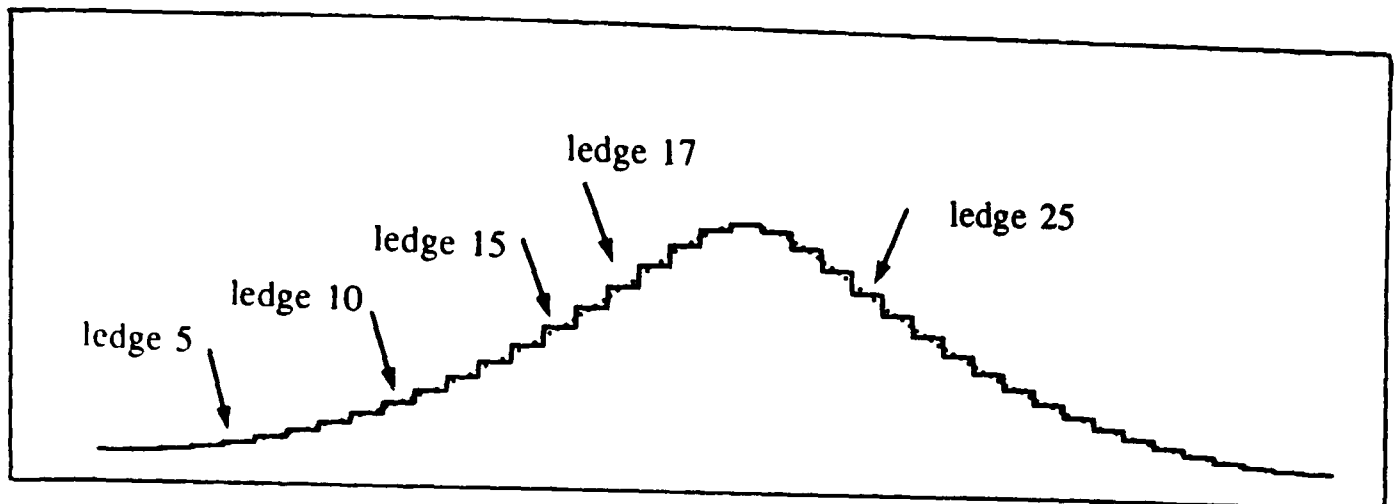
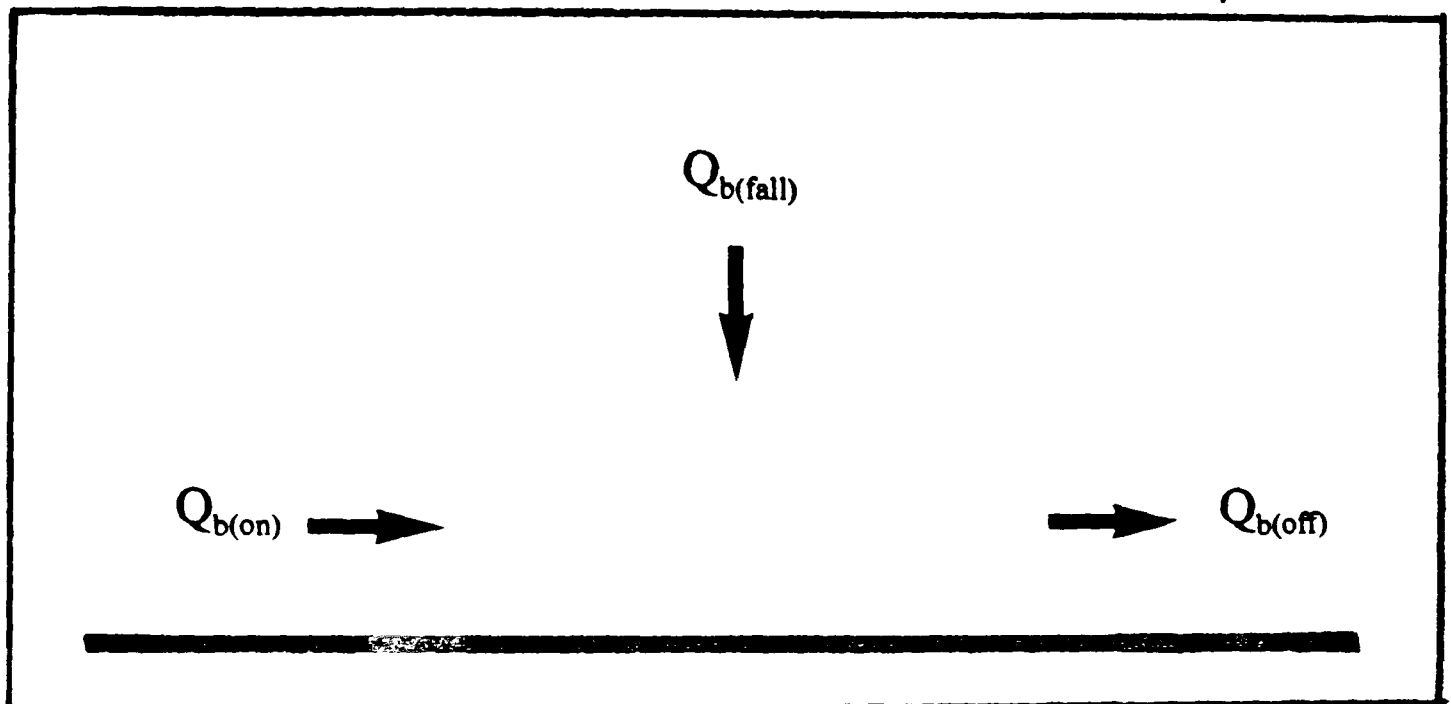


Figure 6.2



Some results for the Test 1 settings ($d_o/\lambda = 1.62$, $h/\lambda = 0.16$) without the imposition of a critical bed shear stress (threshold of motion).

Figure 6.3 The magnitude of $Q_{b(on)}$ for ledges 5, 10 and 15 through a cycle. (Test 1 conditions.)

Figure 6.4 The magnitude of $Q_{b(on)}$ at four phase instants ($t/T = 0.1, 0.2, 0.3$ and 0.4) over the ripple profile. (Test 1 conditions.)

Figure 6.5 The cumulative totals for $Q_{b(on)}$ and $Q_{b(off)}$ over the ripple profile during the first half cycle. (Test 1 conditions.)

Figure 6.6 The cumulative total of $Q_{b(fall)}$ over the ripple profile for a complete cycle. (Test 1 conditions.)

Figure 6.7 The cumulative for $Q_{b(net)}$ over the ripple profile for a complete cycle. (Test 1 conditions.)

Figure 6.3

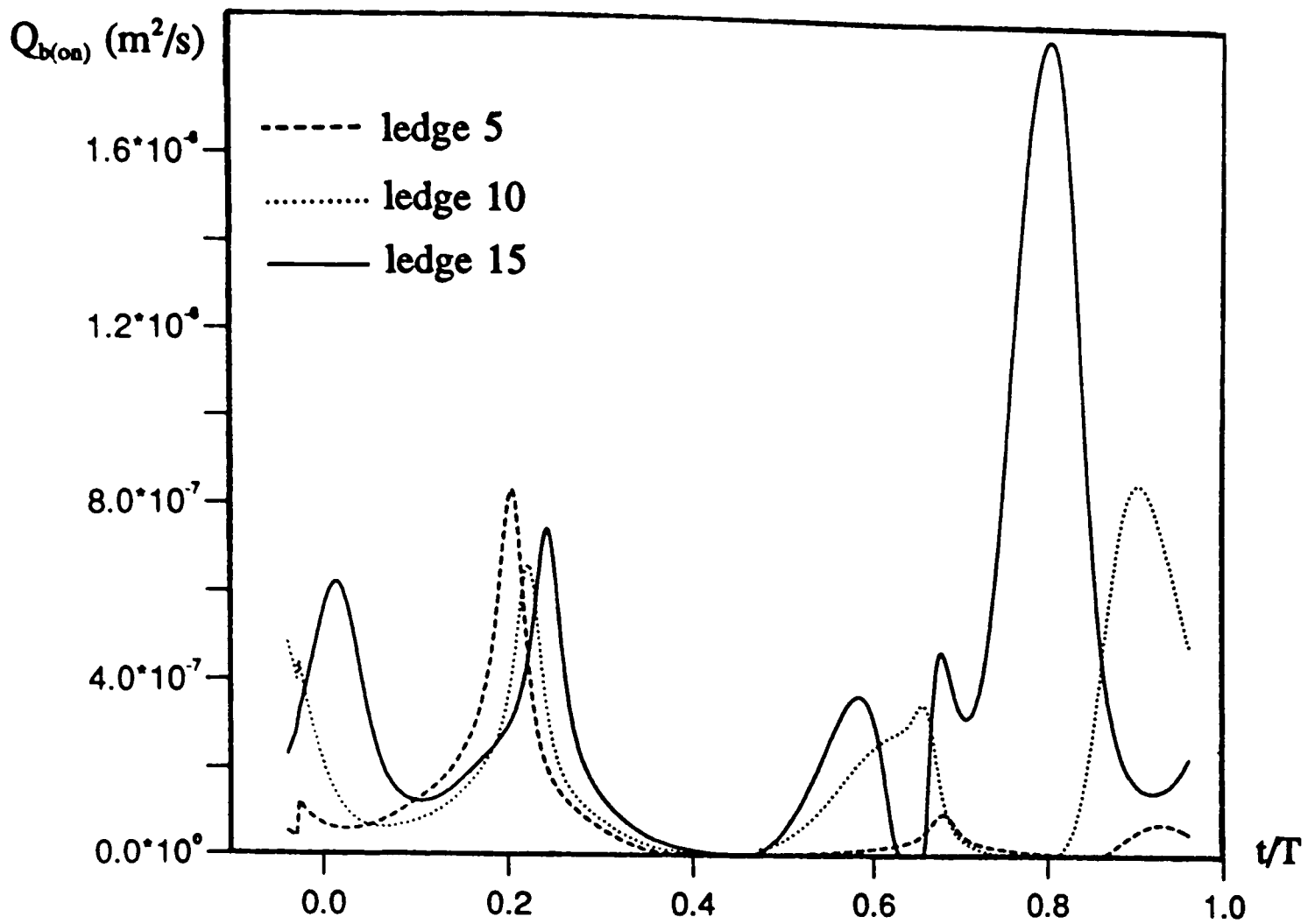
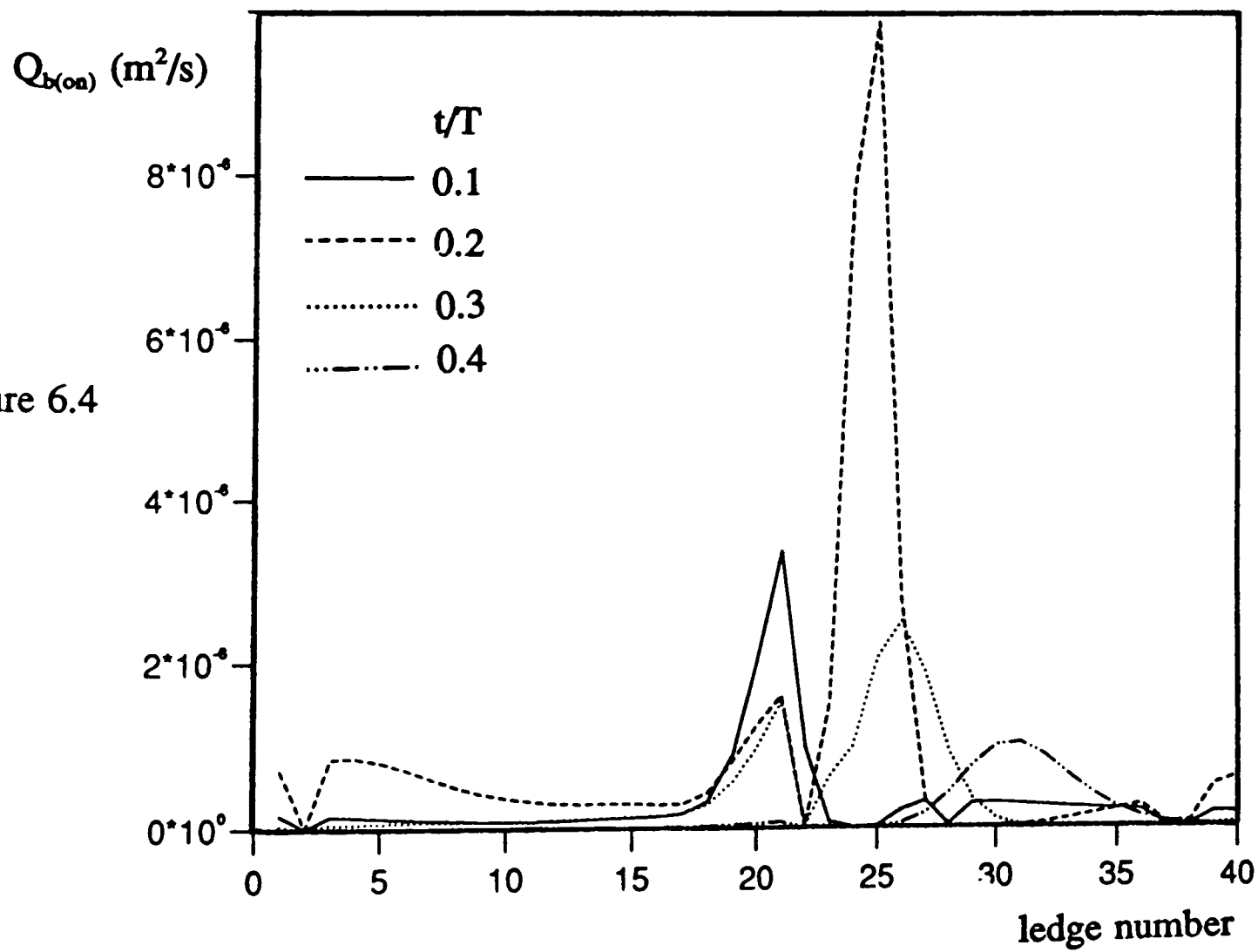


Figure 6.4



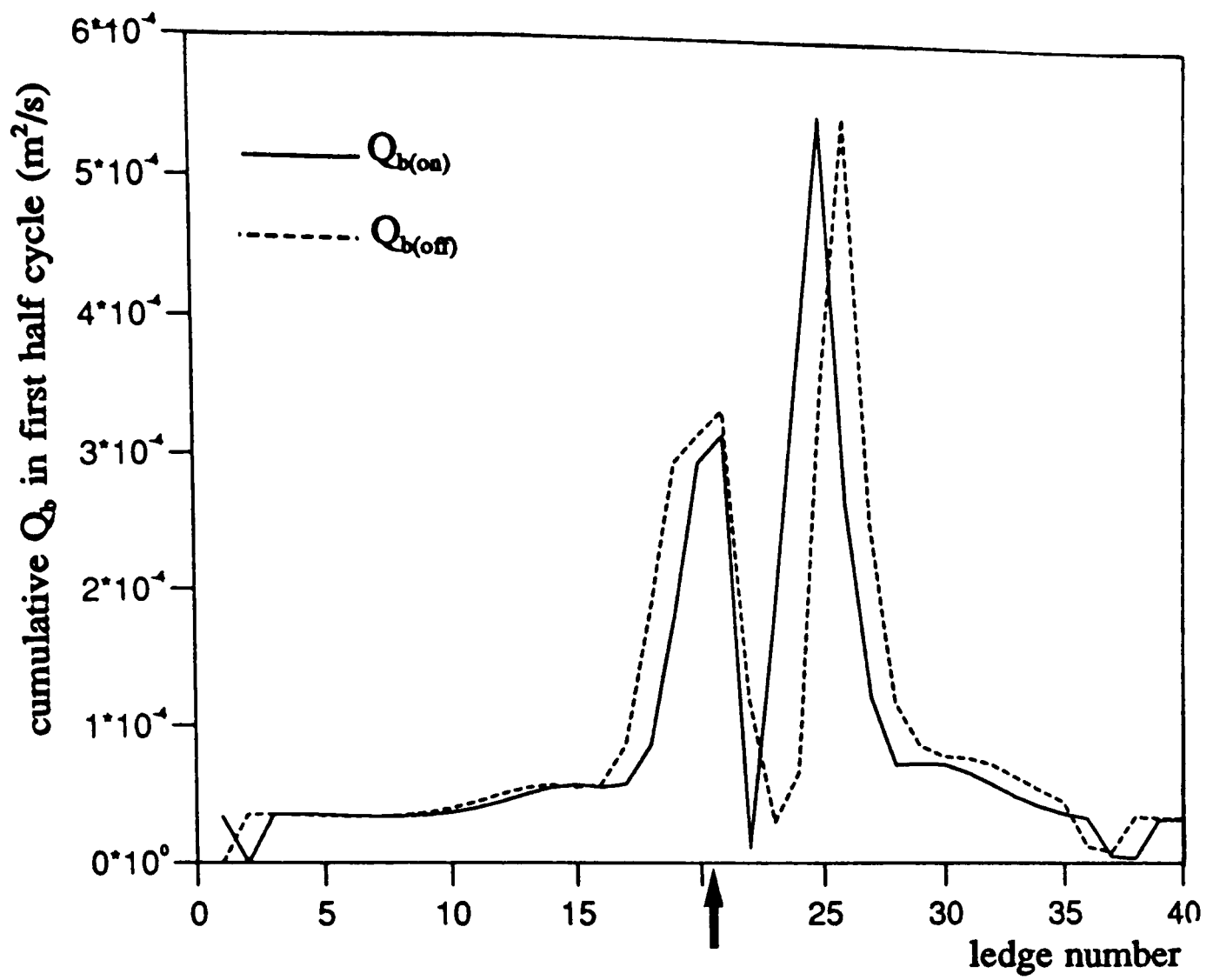


Figure 6.6

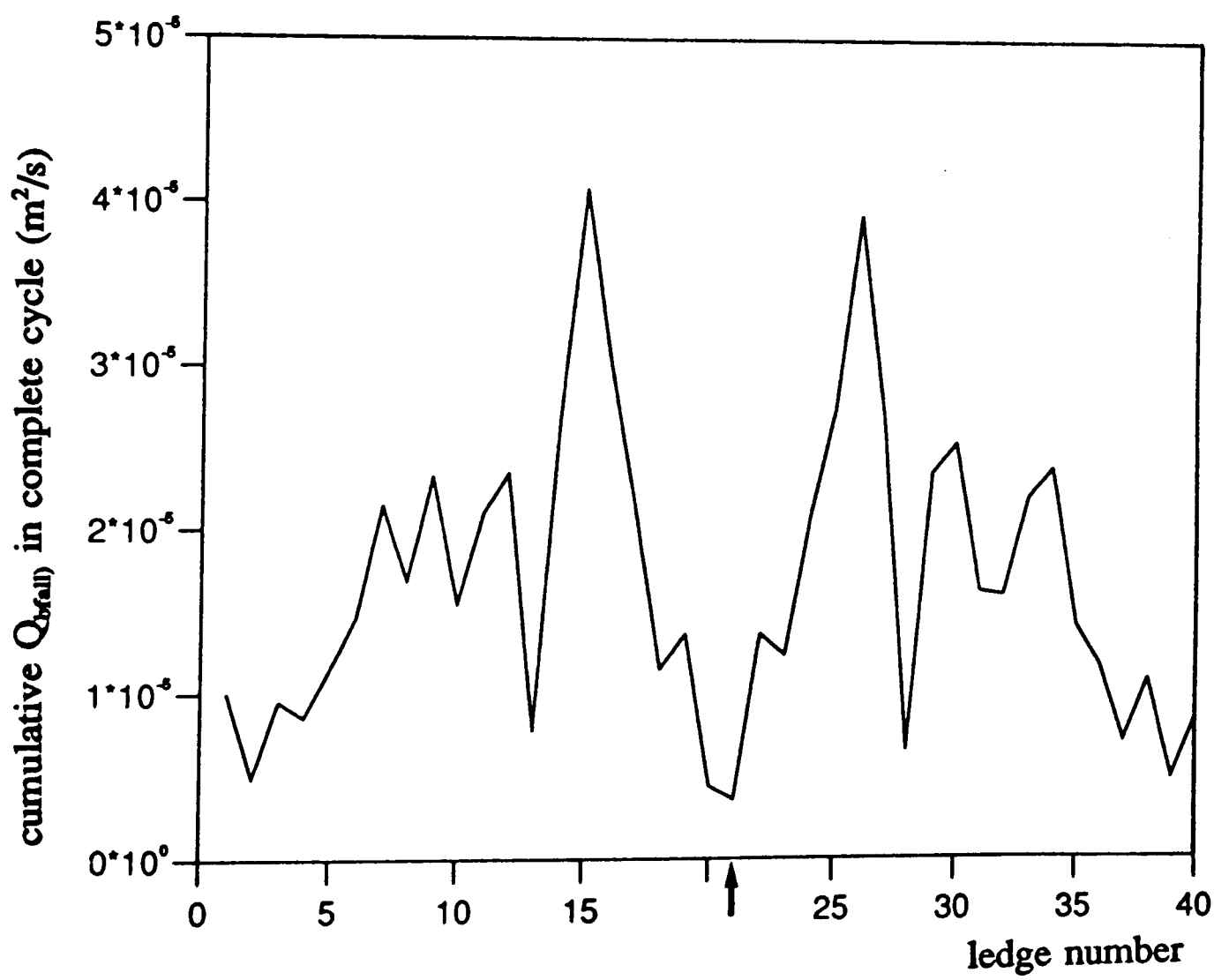
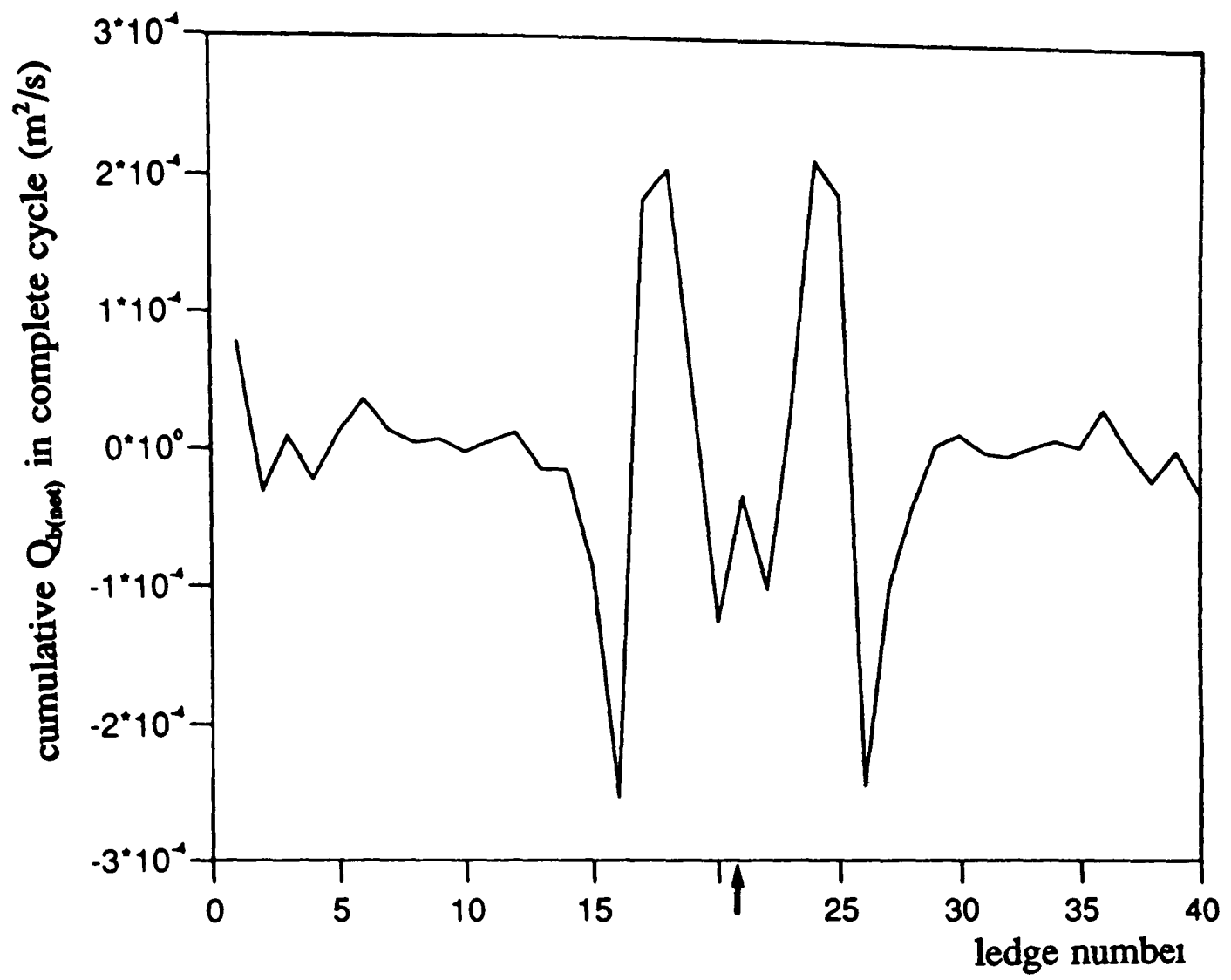


Figure 6.7



Some results for the Test 1 settings, where a threshold of sediment motion has been included.

Figure 6.8 The operation of the slope-term at the phase instant $t/T = 0.20$. (Test 1 conditions.)

Figure 6.9 The cumulative total for $Q_{b(on)}$ over the ripple profile for the first half cycle, with $\tau_c = 0, 0.05$ and 0.10 N/m^2 . (Test 1 conditions.)

Figure 6.10 The cumulative total for $Q_{b(net)}$ over the ripple profile for a complete cycle, with $\tau_c = 0, 0.05$ and 0.10 N/m^2 . (Test 1 conditions.)

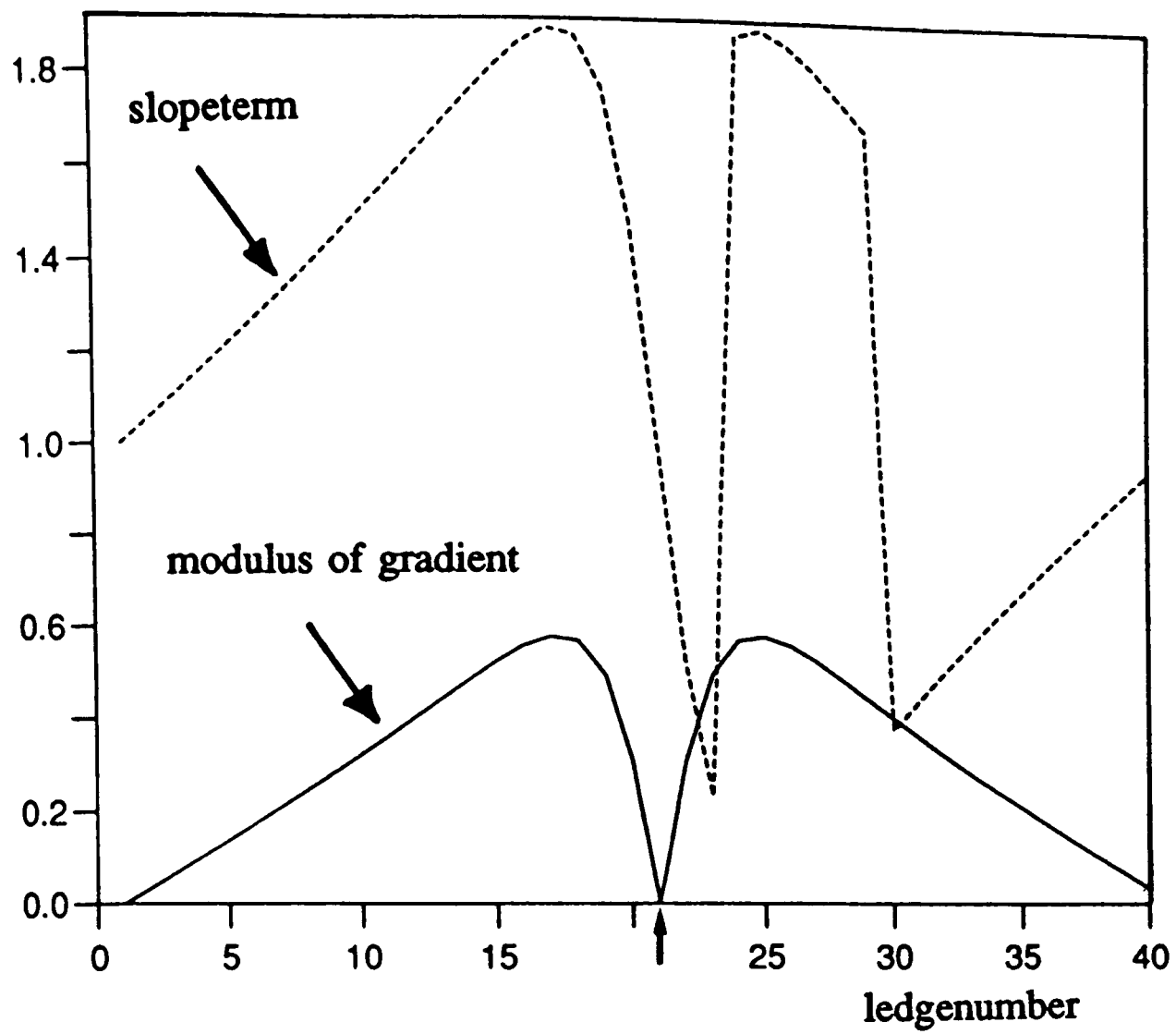
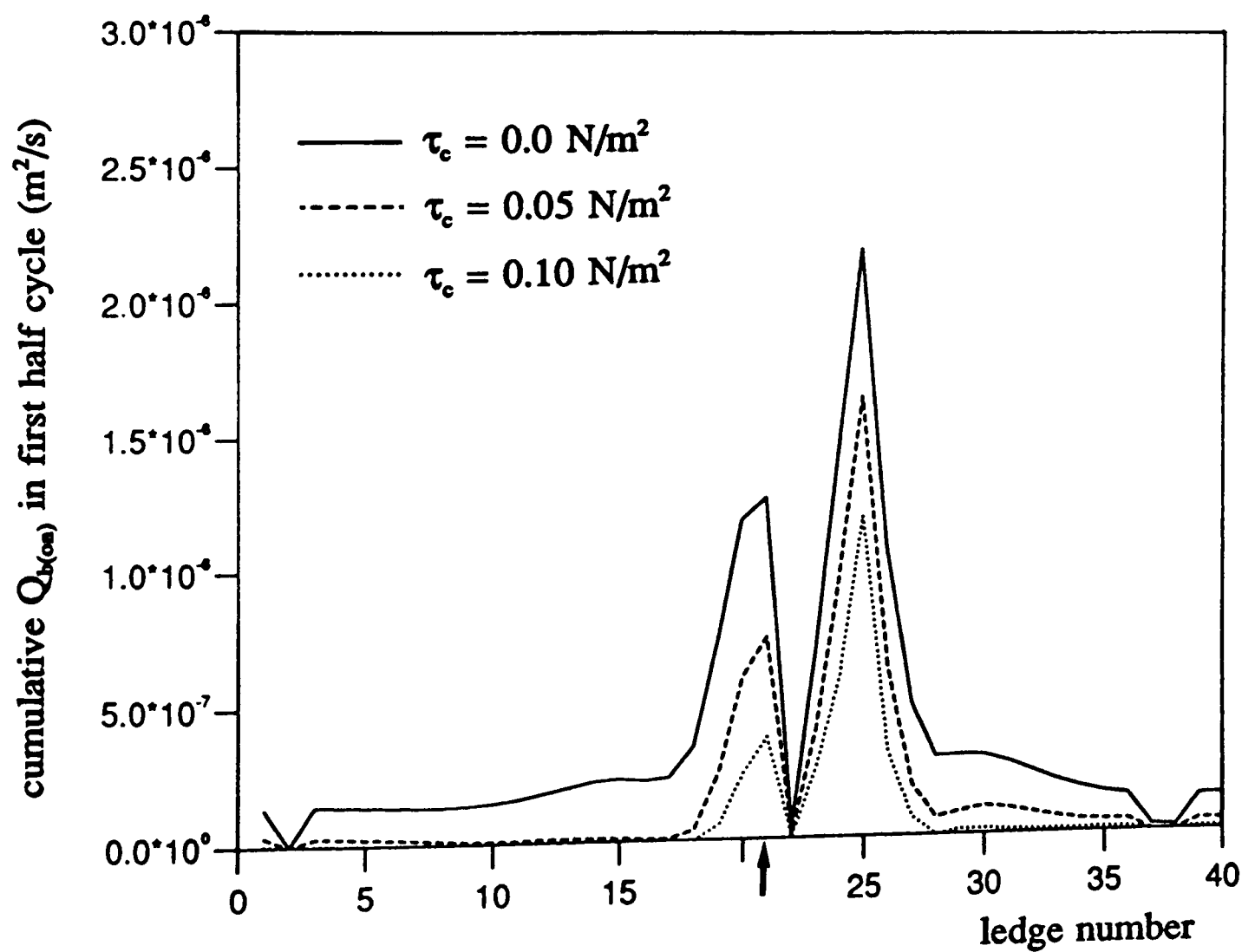


Figure 6.8

Figure 6.9



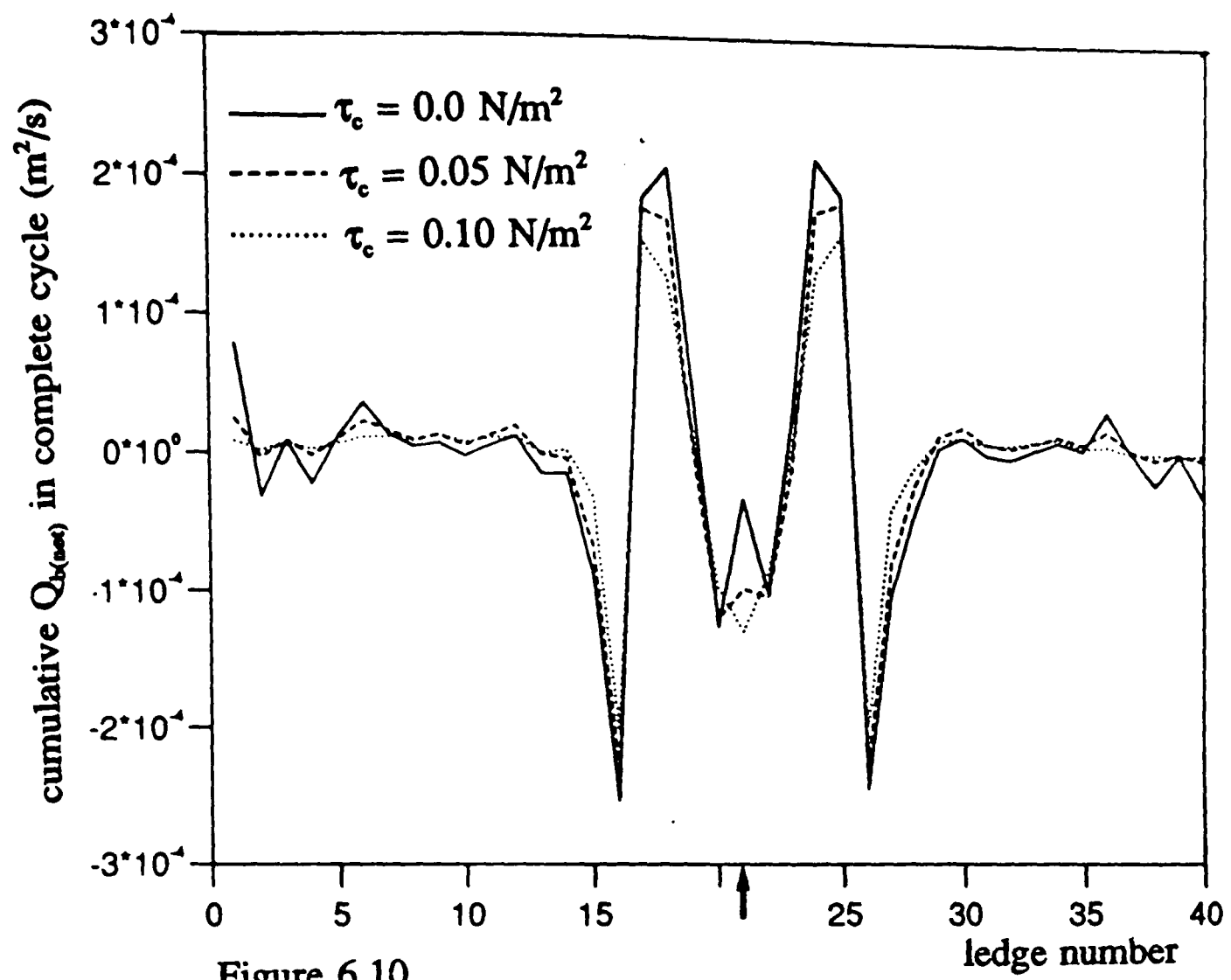
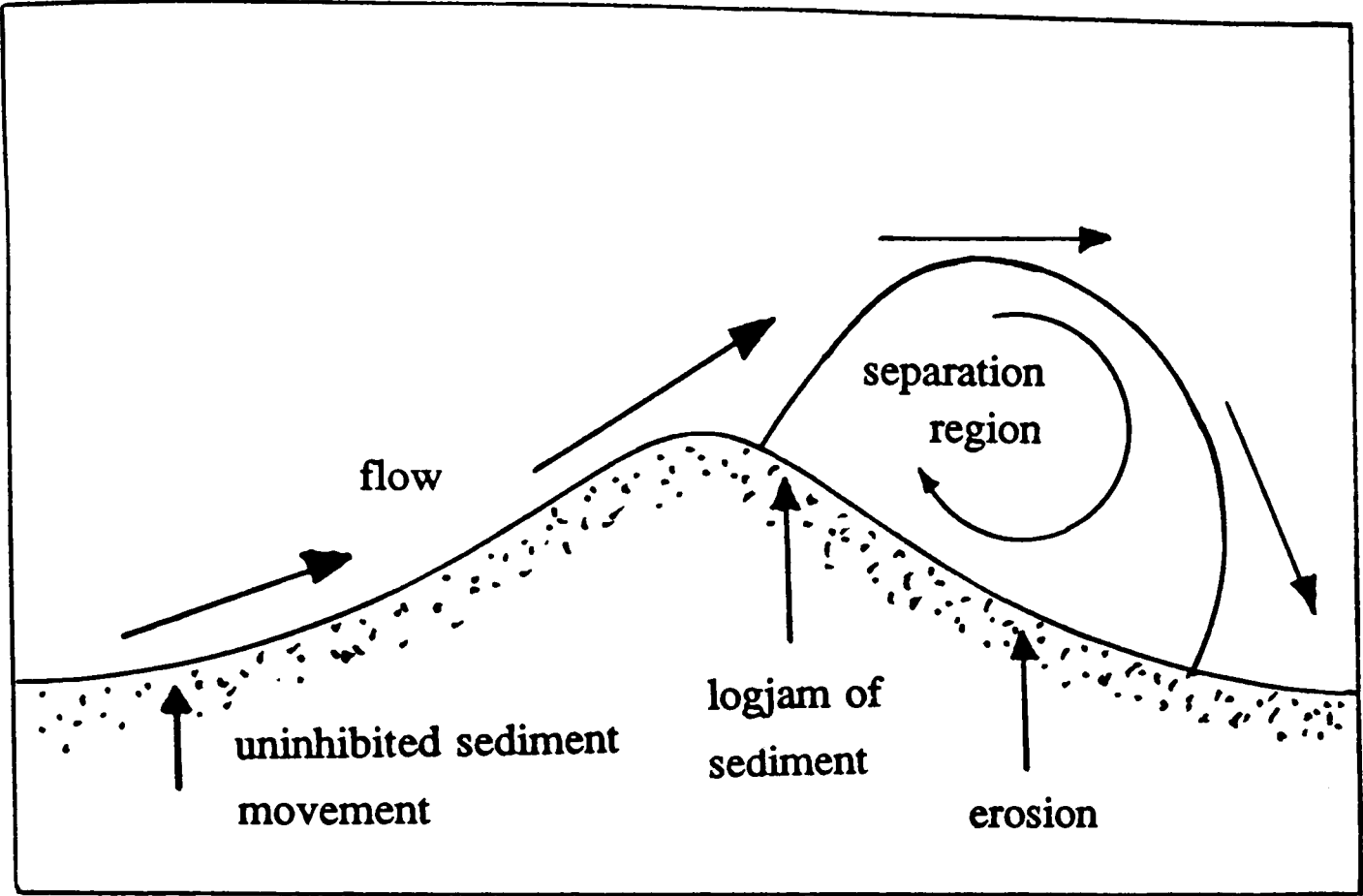


Figure 6.10

A diagram relating to the discussion; specifically, why sediment is trapped over the lee slope.

Figure 6.11 A schematic diagram illustrating how sediment becomes trapped by the stagnation points associated with the growing vortex.

Figure 6.11



CHAPTER 7

THE FORCE ON THE BED 'PER RIPPLE'

7.1 Introduction

Waves travelling towards the shore dissipate energy through bottom drag as they interact with the bed. This dissipation is significantly enhanced by the presence of ripples. Vortex formation and shedding causes pressure imbalances in the fluid surrounding each of the ripples, producing a net force on the ripple profile and hence energy dissipation. It is convenient to treat the net force and energy dissipation in a spatially averaged sense, calculating these quantities 'per ripple'.

The stress acting on the ripple through the above mechanism (τ_b) is not the same as the stress (τ_b) that is described in Chapters 4, 5 and 6. The former is based on *form drag* (acting on the ripple profile), while the latter is based on *skin friction* (associated with the interaction of the flow with the actual substrate of the ripple).

The material in this chapter follows a familiar format. First, some of the background theory relating to the (spatially averaged) force and associated energy dissipation is discussed. This is followed by the development of a computational algorithm which allows the prediction of these quantities, using the hydrodynamical model. These predictions are then compared with established data.

7.1.1 Time averaged quantities :- the energy dissipation factor

(a) *Experimental studies*

Experimental studies of the energy dissipation over ripples are numerous, e.g. Bagnold (1946), Carstens *et al* (1969), Lofquist (1980) and Sleath (1985). These researchers concentrate on the behaviour of a (non-dimensional) coefficient that arises in the derivation of the mean energy dissipation rate over the ripple per unit width (E), as opposed to E itself. However, the definition of this coefficient varies from study to study because of differing derivations for E . Sleath (1985) links various versions of this coefficient, one of which is f_* , the *energy dissipation factor* as defined by Jonsson (1980);

$$f_o = \frac{3\pi}{2\rho U_o^3} \quad 7.1$$

in the usual notation. §7.2.1 contains a derivation for $\overline{C_D}$, the preferred coefficient of Longuet-Higgins (1981), where $f_o = 2\overline{C_D}$.

The value of E has been obtained experimentally, either from the mechanical operation of the oscillating tray (Bagnold(1946), Sleath (1985)) or, in an oscillating water tunnel, from the pressure gradient force (Carstens *et al* (1969), Lofquist (1980)).

There is wide ranging agreement on the trends of the various energy dissipation coefficients with increasing d/λ and ripple steepness. The coefficient increases steadily to a maximum at around $d/\lambda = 1.5$ (though Bagnold found the maximum at about $d/\lambda = 2.0$), then diminishes as d/λ increases. Figure (7.1) illustrates a possible reason for the maxima in f_o , this being some resonant interaction between ejected vortices and ripples at certain values of d/λ . Steeper ripples produce increased values for the coefficients.

Figure (7.2) shows the results of Carstens *et al* (1969) and Lofquist (1980) in an adaptation of a diagram taken from Sleath (1982b). This figure illustrates scatter in the magnitudes of f_o , specifically in the peak values, which vary from 0.20 to 0.35. This indicates significant disagreement between researchers on the values of the dissipation coefficient. The value of f_o is of order 0.2, which is two orders of magnitude higher than values for rough, flat beds (see Longuet-Higgins (1981)).

(b) Theoretical studies

There have been rather few theoretical studies of energy dissipation over rippled beds (Sleath (1982b), Longuet-Higgins (1981), Macpherson (1984) and Blondeaux and Vittori (1991)). The theoretical approach is similar to the experimental one, except that E has to be evaluated from analytical expressions for the net force on the ripple profile.

Sleath (1982b) and Blondeaux and Vittori (1991) present the variation in f_o with d/λ , for ripples of steepness 0.17. Blondeaux and Vittori find a single peak in f_o of about 0.12 at $d/\lambda = 2.0$, with f_o decreasing monotonically thereafter. Sleath, however,

finds a more complicated trend in f_o . His results are presented in figure (7.3), taken from Sleath (1985). The curve marked " $\beta/k = 20$ " corresponds to our 'central run' settings (c.f. Chapter 3). For this curve, Sleath finds a global maximum ($f_o \approx 0.25$) at $d_o/\lambda \approx 1.0$, followed by a decrease through to a second maximum ($f_o \approx 0.20$) at $d_o/\lambda \approx 2.25$. The presence of two maxima ties in with the scenario illustrated in figure (7.1) (see §7.1.1 (a)), itself due to Sleath (pers. comm.).

Longuet-Higgins used a time-varying form of Blasius's theorem and complex integration along contours in the physical plane to establish the force on the ripple profile. This method is discussed in more detail in Appendix 1. The value of $\overline{C_D}$ is of the order of 0.1, which is in agreement with experiment. Longuet-Higgins also found a maximum in $\overline{C_D}$ at $d_o/\lambda = 1.5$, and decreasing values thereafter. The four-vortex model of Macpherson agreed with the experimental data, except that it did not show any maximum in $\overline{C_D}$; on the contrary, the values decrease from $d_o/\lambda = 1.0$.

7.1.2 Instantaneous quantities

Jonsson (1980) related the peak stress at the bed to the maximum velocity in the outer oscillatory flow (U_o) by a friction factor f_w ;

$$\tau_{o(max)} = f_w \cdot \frac{1}{2} \rho U_o^2 \quad 7.2$$

where $\tau_{o(max)}$ is the peak stress in the cycle. Figure (7.4), taken from Jonsson (1980), shows data and model predictions for f_w against the 'relative roughness' a_o/k_s . For small a_o/k_s , f_w is believed to be constant, but this belief is backed only by a few datapoints from Bagnold (1946). The value of f_w then decreases with increasing a_o/k_s . Using the assumption of a near-bed logarithmic layer (as in Chapter 4), Jonsson obtained a theoretical result for f_w as a function of a_o/k_s , which was then fitted to experimental data:-

$$\frac{1}{4\sqrt{f_w}} + \log_{10} \frac{1}{4\sqrt{f_w}} = -0.08 + \log_{10} \frac{a_o}{k_s} \quad 7.3$$

This expression is also plotted in figure (7.4).

The friction factor f_w was conceived for a notionally 'flat' bed where the water motions (based on a_o) are considerably larger than the equivalent roughness (k_s) i.e. $a_o/k_s > 1$. On a level bed, where the sediment grains are the roughness elements, this condition is easily met because k_s scales on the sediment size (see Chapters 4, 5). However, where bedforms such as ripples are the roughness elements (as opposed to the substrate itself), k_s scales on the bedforms themselves. In order to preserve the notional flatness, the water motions must consequently be much larger than the dimensions of the bedforms. Therefore applying f_w to the ripple regime (where the water motions are equivalent in size to the ripples and a_o/k_s is $O(1)$) is pushing the 'notional flat bed' proviso to the limits of plausibility. This is why there is such a paucity of data for f_w at these low values of a_o/k_s . One aim of the present study is to see if the hydrodynamical model can be used to elucidate the behaviour of f_w in this region.

Lofquist (1980) presented results for the time variation in stress acting on naturally formed ripples. Figure (7.5) shows time series of ' $f(\theta)$ ' (Lofquist's notation for the time varying stress) for different values of U_o . These show a complicated pattern, linked to both the oscillatory flow and the vortices. Lofquist notes the existence of at most two peaks in $0 < t/T < 0.25$ (caused by the oscillatory flow and the effect of vortex ejection) and one peak in $0.25 < t/T < 0.5$ (caused by the growing vortex). These curves can be linked to f_w , since $\tau_{o(max)}$ is the global maximum of $f(\theta)$ in the half cycle.

7.2 Computational algorithms for calculating $\overline{C_D}$ and f_w

Algorithms are presented whereby output from the hydrodynamical model can be used to obtain values for $\overline{C_D}$ and f_w . The former quantity is used to provide a further comparison of the hydrodynamical model with previously established data, while the latter is used to try and provide more information on the horizontal portion of Jonsson's graph (which is the regime in which the hydrodynamical model operates).

7.2.1 The algorithm for obtaining $\overline{C_D}$

The derivation of the expression for $\overline{C_D}$ closely follows that in Longuet-Higgins (1981). As a starting point, the components of force per ripple derived in Appendix 1, F_{osc} and F_{vort} , can be expressed as stresses by dividing them by the ripple wavelength λ , such that

$$\tau_{osc} = \frac{h}{2} \rho \frac{dU}{dt} , \quad \tau_{vort} = \frac{\pi \rho}{\lambda} \sum \frac{\partial}{\partial t} [(\Delta \kappa_s) \chi_s] \quad 7.4 \text{ (a, b)}$$

τ_{osc} is the stress caused by the oscillatory flow, while τ_{vort} is the stress attributable to the vortices. Time averaging of these stresses cancels out the contribution from the oscillatory flow, τ_{osc} , so it is ignored. The mean energy dissipation rate per unit area, E , is given by

$$E = \overline{U \tau_{vort}} \quad 7.5$$

where the overbar denotes time averaging. If we set $\tau_{vort} = \rho C_D U |U|$, where C_D is a time varying drag coefficient, then

$$E = \overline{U \cdot \rho C_D U |U|} = \rho \overline{C_D |U|^3} \quad 7.6$$

Re-arranging this, we obtain

$$\overline{C_D} = \frac{E}{\rho |U|^3} \quad 7.7$$

A replacement of the overbars by their integral representations gives

$$\overline{C_D} = \frac{3\pi}{4\rho U_o^3} \cdot \frac{1}{T} \cdot \int_0^T U \tau_{vort} dt \quad 7.8$$

Substituting equation (7.4b) into equation (7.8) gives

$$\overline{C_D} = \frac{3\pi^2}{4U_o^3} \cdot \frac{1}{\lambda T} \int_0^T U \sum \frac{\partial}{\partial t} [(\Delta\kappa_s)\chi_s] dt \quad 7.9$$

Equation (7.9), in its differenced form, has been used to obtain the value of $\overline{C_D}$. This calculation has been performed during the 12th cycle, following convergence of the hydrodynamical model.

7.2.2 The algorithm for obtaining f_w

The method used for finding f_w has involved the calculation of the maximum value of the stress (τ_o) acting on the profile through the cycle. The absence of time averaging means that both τ_{osc} and τ_{vort} need to be included. The total, time varying kinematic stress on the bed is given by

$$\frac{\tau_o}{\rho} = \frac{\tau_{osc}}{\rho} + \frac{\tau_{vort}}{\rho} \quad 7.10$$

Equation (7.10) has been calculated throughout the first half cycle and its maximum value, $\tau_{o(max)}/\rho$, stored. The value of f_w then comes directly from equation (7.2).

It was stated earlier that calculating f_w over a rippled bed was pushing the 'notional flat bed' condition to its limit of plausibility. This problem manifests itself in the following ambiguity, noted by Sleath (1982b, 1984). Sleath stated that, per ripple, the effect of the oscillatory flow (which provides τ_{osc}) differs, depending on whether the control volume stretches from trough to trough or from crest to crest. In the present study, the control volume stretches from trough to trough (see figure (A1.1) in Appendix 1). On a flat bed, for which f_w was conceived, this problem does not occur.

To allow comparison with the results of Jonsson (1980), the usual d/λ scale is converted to the equivalent a/k_s scale as follows:-

The equivalent roughness k_s , which here refers to the ripples themselves, is parameterised as $k_s = 4h$ (Swart (1976)). This result, along with the fact that $a_o = d/\sqrt{2}$, gives

$$\frac{a_o}{k_s} = \frac{d_o}{8h} = \frac{1}{8(h/\lambda)} \cdot \frac{d_o}{\lambda} \quad 7.11$$

7.3 Results

Results are presented for the variation of $\overline{C_D}$ and f_w with d_o/λ and a_o/k_s respectively. The program implementing the hydrodynamical model has been run with the two algorithms outlined in §7.2. Two constraints affected these computations. First, there seemed no justification in calculating $\overline{C_D}$ below $d_o/\lambda = 1.0$, because vortex formation is not present in this range. Second, the program itself dictated the upper limits of d_o/λ for which model results could be obtained. Computational instability, in the form of erratic flow reversals at the crest, crashed the program at high values of d_o/λ .

7.3.1 Results for $\overline{C_D}$

Figure (7.6) shows the variation of $\overline{C_D}$ with d_o/λ for $h/\lambda = 0.13, 0.15$ and 0.17 . The curves all show global maxima ($\overline{C_D} = 0.09, 0.105, 0.12$) at $d_o/\lambda = 2.5$. However, apart from this common feature, there are qualitative differences between the $h/\lambda = 0.13$ curve and the others. For $h/\lambda = 0.15, 0.17$, the curves increase through local maxima ($\overline{C_D} = 0.09, 0.105$) at $d_o/\lambda = 1.8$ to the global maxima already noted. Beyond $d_o/\lambda = 2.5$, both curves decrease to their end points. The curve for $h/\lambda = 0.13$ has no local maxima at $d_o/\lambda = 1.8$, but simply increases upto the global maxima at $d_o/\lambda = 2.5$. As this curve reaches its endpoint, it shows a tendency to rise again.

Figure (7.7) shows the present values of f_w for $h/\lambda = 0.17$ superimposed onto a diagram from Macpherson (1984), adapted in turn from Sleath (1982b). It shows various researchers' values for f_w . The present predictions are in reasonable quantitative agreement with these earlier results and data, though the values of f_w seem a bit low for smaller values of d_o/λ . However, two of the qualitative features are less encouraging. First, the present curve does not show the expected maximum in the region of $d_o/\lambda = 1.5$. Second, the tendency for the present curve to rise with increasing d_o/λ is at odds with the majority of the data. One exception to this is the four-vortex model of

Macpherson (1984), which also shows this tendency. In anticipation of the following discussion, it may be recalled that Macpherson also amalgamates the growing vortex.

There is the suggestion in figures (7.6), (7.7) that the model is failing to give physically sensible values for $\overline{C_D}$ beyond $d/\lambda \approx 2.0$.

7.3.2 Results for τ_o and f_w

Figure (7.8) shows a typical time series of τ_{osc}/ρ , τ_{vort}/ρ and τ_o/ρ (using the central run settings from Chapter 3) over a full cycle. It shows the maximum value of τ_o/ρ , ($\tau_{o(max)}/\rho$), occurring at $t/T = 0.1$ and 0.6 . The sharp spikes at $t/T = 0.05, 0.55$ in both the τ_o/ρ and τ_{vort}/ρ curves are coincident. They are due to deletion of the relic vortex from the hydrodynamical model.

Figure (7.9) shows the predicted variation of f_w with a/k_s , plotted alongside Jonsson's equation (7.3). [Not all the values of f_w are shown - all three curves showed erratic behaviour beyond certain values of a/k_s . These critical values of a/k_s actually correspond to one value of d/λ , $d/\lambda = 2.0$.] The constant value of f_w (for $a/k_s < 1.57$) is taken as 0.30. As discussed earlier, the aim of this exercise was to see if the present model could elucidate the nature of f_w in the horizontal portion of Jonsson's curve. In general terms, the model overestimates f_w by about 25% for $h/\lambda = 0.17$, predicts f_w well for $h/\lambda = 0.15$, and underestimates f_w by up to 15% for $h/\lambda = 0.13$. What few values of f_w there are, show a tendency for the curves to 'wish' to connect with the sloping portion of Jonsson's curves.

7.4 Discussion

The results illustrated in figures (7.6) and (7.7) show that, quantitatively, the values of f_o (from $\overline{C_D}$) are consistent with those found by other researchers. Also, increasing ripple steepness gives rise to increasing values for $\overline{C_D}$. For $h/\lambda = 0.15, 0.17$, qualitative agreement is also quite good, with the local maxima in $\overline{C_D}$ occurring at $d/\lambda = 1.8$. For higher values of d/λ , however, qualitative agreement is poor since $\overline{C_D}$ keeps increasing. The results for $h/\lambda = 0.13$ are consistently disappointing, though they do fit into the general pattern.

It is of interest to see why the curves for $\overline{C_D}$ do not follow the accepted trends for higher values of d/λ . Three possible explanations are proposed, the first concerning the relic vortex, the second concerned with the size of the separation region associated with the growing vortex, and the third to do with its motion.

In figure (7.8), the deletion of the relic vortex has a profound effect on the instantaneous shear stresses. This makes the presence of the relic vortex near the bed a prime suspect for the misbehaviour of the $\overline{C_D}$ curves. To this end, the $\overline{C_D}$ curve for ripple steepness 0.17 was recalculated without the contribution from the relic vortices. This is figure (7.10), which shows that neglecting the relic vortex does not improve matters - the curve still shows the same trends. The first possible explanation does not hold.

An analysis of the individual contributions to $\overline{C_D}$ shows that the major contributor is the growing vortex, which generally accounts for about 70% of $\overline{C_D}$. This helps to explain why changes in ripple steepness have such a profound effect on the values of $\overline{C_D}$ (i.e. increasing steepness enhances flow separation and hence the strength of the growing vortex). We look, therefore, to the growing vortex for a possible explanation as to why the model is not giving realistic results for $\overline{C_D}$ at higher values of d/λ . Physically, with increasing d/λ , shed vorticity tends to fill up more and more of the trough. Figure (7.11) is a schematic diagram illustrating these points. The affect of this 'trough filling' is to mute the pressure differences on either side of the ripple profile, hence reducing the net force and the energy dissipation coefficient. The vortex amalgamation algorithm applied to growing vortices in the present hydrodynamical model gathers up shed vorticity, restraining it over the lee slope. Figure (7.12) demonstrates that, even with a high value of d/λ , the growing vortex (with its associated separation region) remains fixed over the lee slope, and does not fill the trough with vorticity. It is suggested that the vortex amalgamation scheme inhibits the trough filling process, thus delaying the observed decrease in $\overline{C_D}$.

The third possible explanation refers back to material discussed in § 3.3.2 about different growing vortex trails either side of $d/\lambda = 2.1$. In figure (3.20), the centre of the growing vortex rises away from the bed, somewhat before its ejection. Given that

the drag coefficient depends on the height of the vortex above the bed, this tendency may well affect the values of $\overline{C_D}$. A judgement as to which of these last two explanations is correct is reserved till later in this discussion.

Figure (7.8) provides a basis for comparison between the model and the findings of Lofquist (1980). As found in Lofquist's measurements, the model predicts a positive value for τ_o/ρ at $t/T = 0.0$, and a peak in the interval $0.0 < t/T < 0.25$. However, no peak is predicted in the range $0.25 < t/T < 0.50$. The model predicts large values of τ_{vor}/ρ in the early parts of this range, but these are cancelled out by the oscillatory flow contribution τ_{osc}/ρ .

The curves for f_w have been significantly reduced because of their misbehaviour beyond $d/\lambda = 2.0$. However, if one considers, first, the numerous assumptions that have gone into the hydrodynamical model and, second, the fact that these lower values of a_o/k_s are at the limit of applicability for f_w , the values for f_w are not unreasonable. It would be unjustifiable to draw firm conclusions from this graph regarding the nature of the horizontal section of Jonsson's curve; they may continue to increase in this region, but at a slower rate.

The fact that the curves for f_w misbehave beyond $d/\lambda = 2.0$ is revealing, because this again places emphasis on the value $d/\lambda = 2.1$. It seems likely, therefore, that the third explanation above is the reason for the misbehaviour in both $\overline{C_D}$ and f_w . The motion of the growing vortex over the lee slope has an unwelcome affect on the model predictions of the force acting on the ripple profile.

7.5 Conclusions

The material presented in this chapter, combined with the analysis in Appendix 1, has allowed the present hydrodynamical model to be tested against previous results for the force and energy dissipation over ripples. The usage of the model to find f_w for low values of a_o/k_s has been an extra avenue of interest.

Results for the drag coefficient, $\overline{C_D}$, show that the model produces values for f_o ($=2\overline{C_D}$) that generally agree with existing experimental and model findings. However,

the values for the drag coefficient do not fall beyond $d/\lambda \approx 1.5$. It is suggested that the motion of the growing vortex may well be responsible for this.

The use of the model to elucidate the nature of f_w for low values of a/k_s has met with mixed success. The values obtained are reasonable, but the model could not be pushed far enough to provide a clear picture of the trends. The model suggests that f_w may actually be increasing (but at a slower rate) for low values of a/k_s , instead of remaining constant as in Jonsson's equation (equation (7.3)). This requires further study.

A sequence of sketches and figures (from the literature) concerning the force 'per ripple' on the bed.

Figure 7.1 A schematic diagram (due to Sleath (pers. comm.) that seeks to explain why f_o has maxima at certain values of d_o/λ .

Figure 7.2 A graph (from Sleath (1982b)), showing experimental data for the variation of f_o with d_o/λ .

Figure 7.3 A pair of curves from the results of Sleath (1985), showing how f_o varies with a_o/λ . Copied and adapted from Sleath (1985).

Figure 7.4 Experimental data points showing how f_w varies with the relative roughness a_o/k_s . The dashed curve is equation (7.3). Copied and adapted from Jonsson (1980).

Figure 7.5 A sequence of time series of (non-dimensional) bed shear stress for various values of λ/a_o , from the data of Lofquist (1980). Copied and adapted from Lofquist (1980).

Figure 7.1

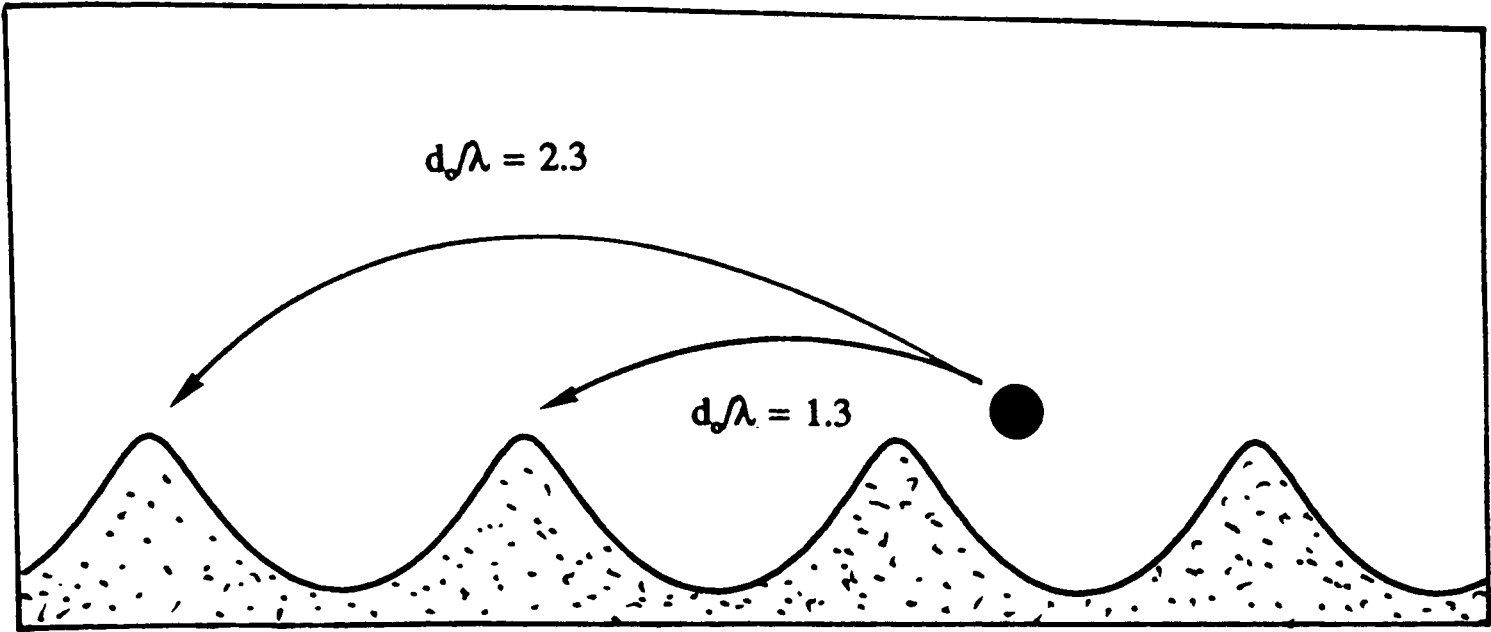


Figure 7.2

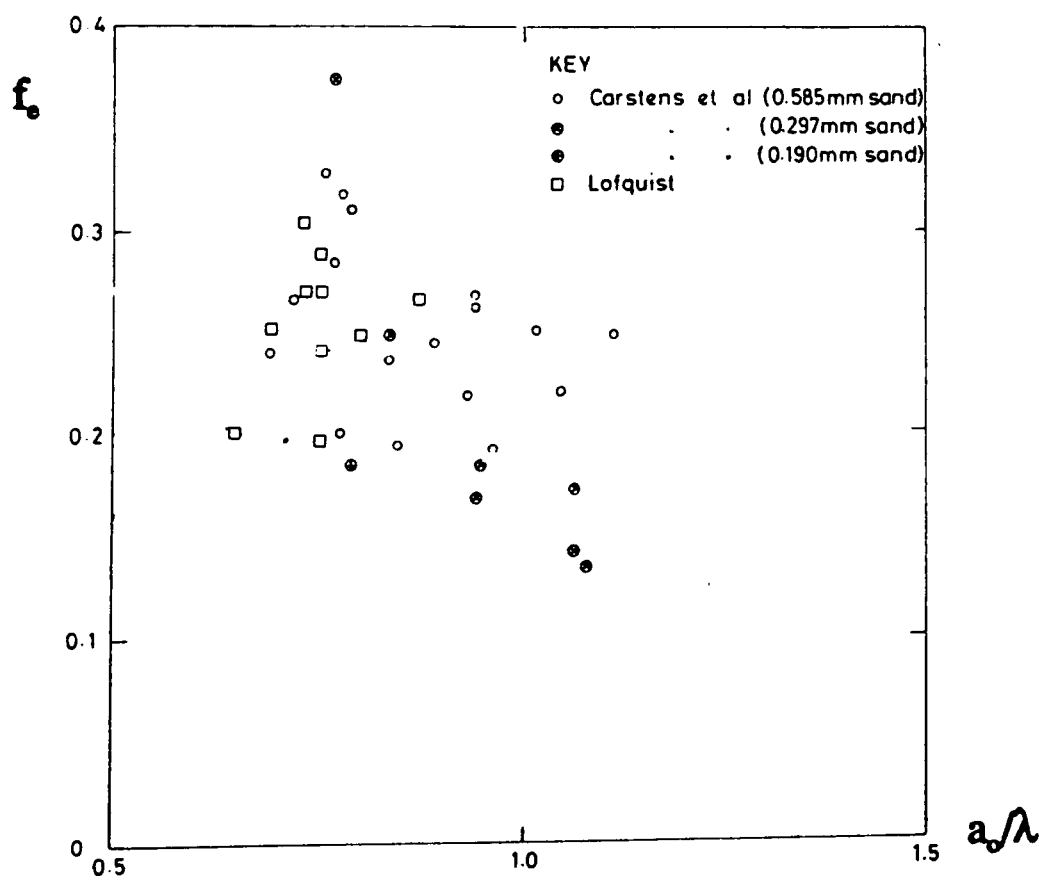
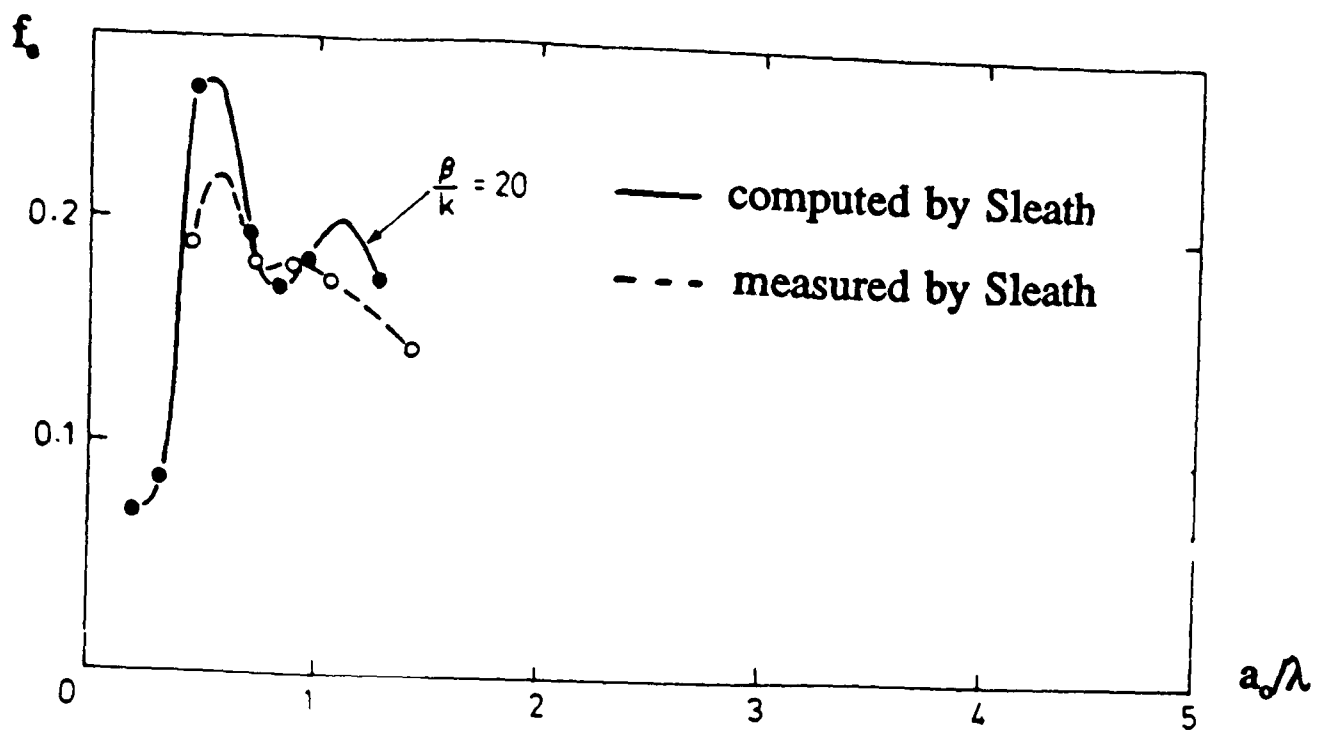
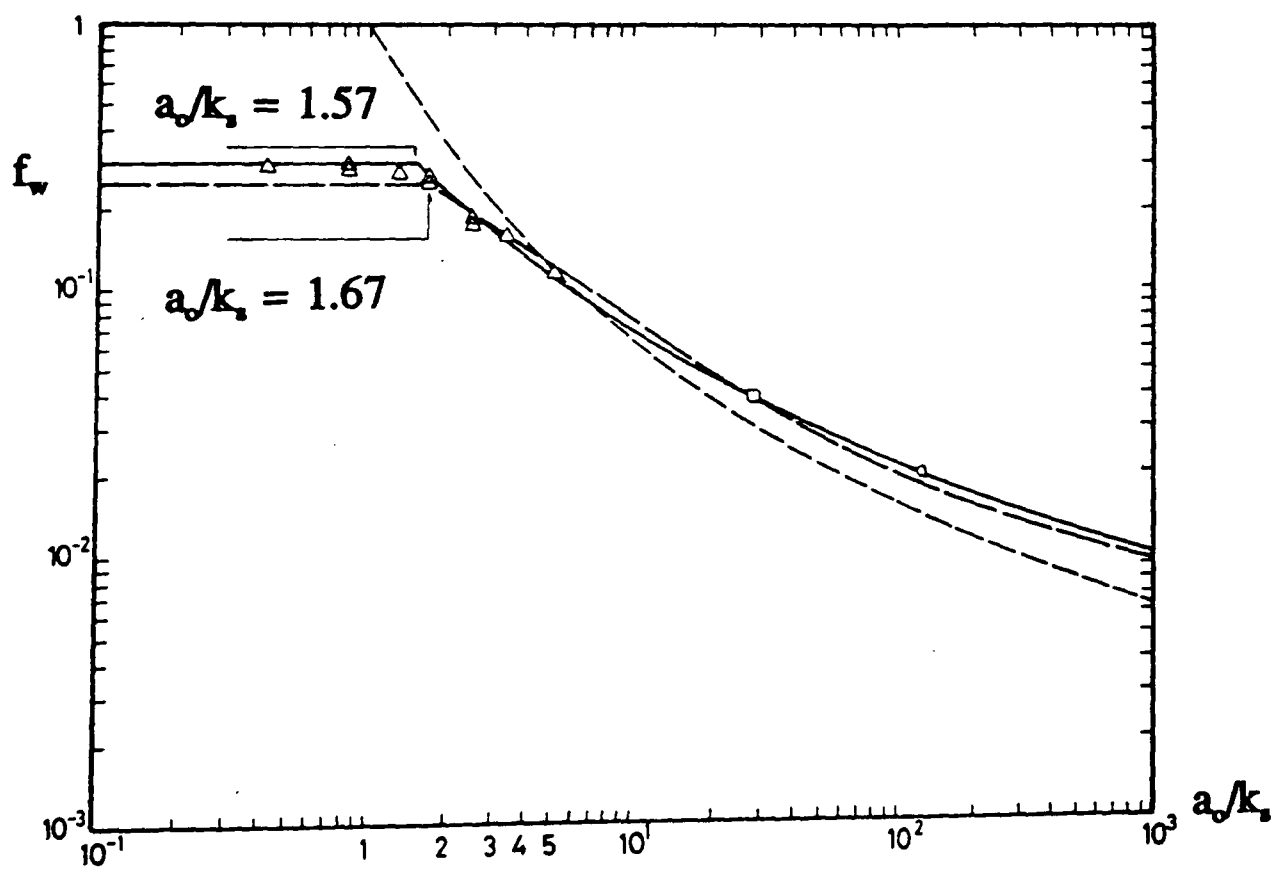


Figure 7.3



$$\text{Sleath's } \frac{\beta}{k} = \frac{1}{I} \sqrt{\frac{\sigma}{2\nu}}$$

Figure 7.4



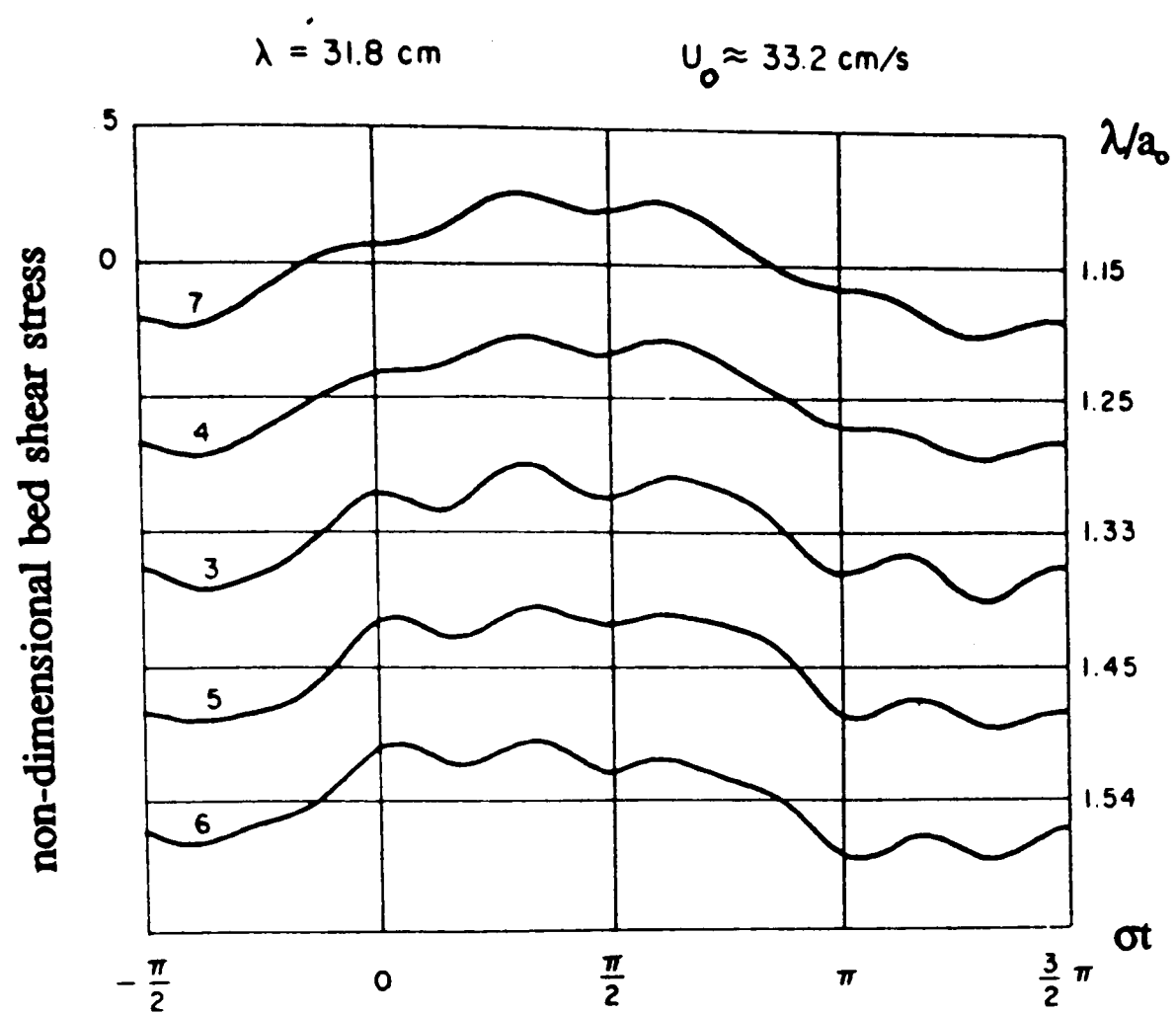


Figure 7.5

Results for both the energy dissipation coefficient, f_e , and Jonsson's friction factor, f_w .

Figure 7.6 Variation in the cycle-averaged drag coefficient $\overline{C_D}$ with d_o/λ , for three ripple steepnesses: $h/\lambda = 0.13, 0.15$ and 0.17 .

Figure 7.7 The model results for $f_e (= 2\overline{C_D})$ against d_o/λ with $h/\lambda = 0.17$, grafted onto a graph from Macpherson (1984) - originally due to Sleath (1982b).

Figure 7.8 Variation of $(\tau_{osc}/\rho)''$, $(\tau_{vort}/\rho)''$ and $(\tau_o/\rho)''$ through a complete cycle. (Central settings.)

Figure 7.9 Comparisons between Jonsson's friction factor (f_w), as calculated from the model and from equation (7.3) for three steepnesses: $h/\lambda = 0.13, 0.15$ and 0.17 .

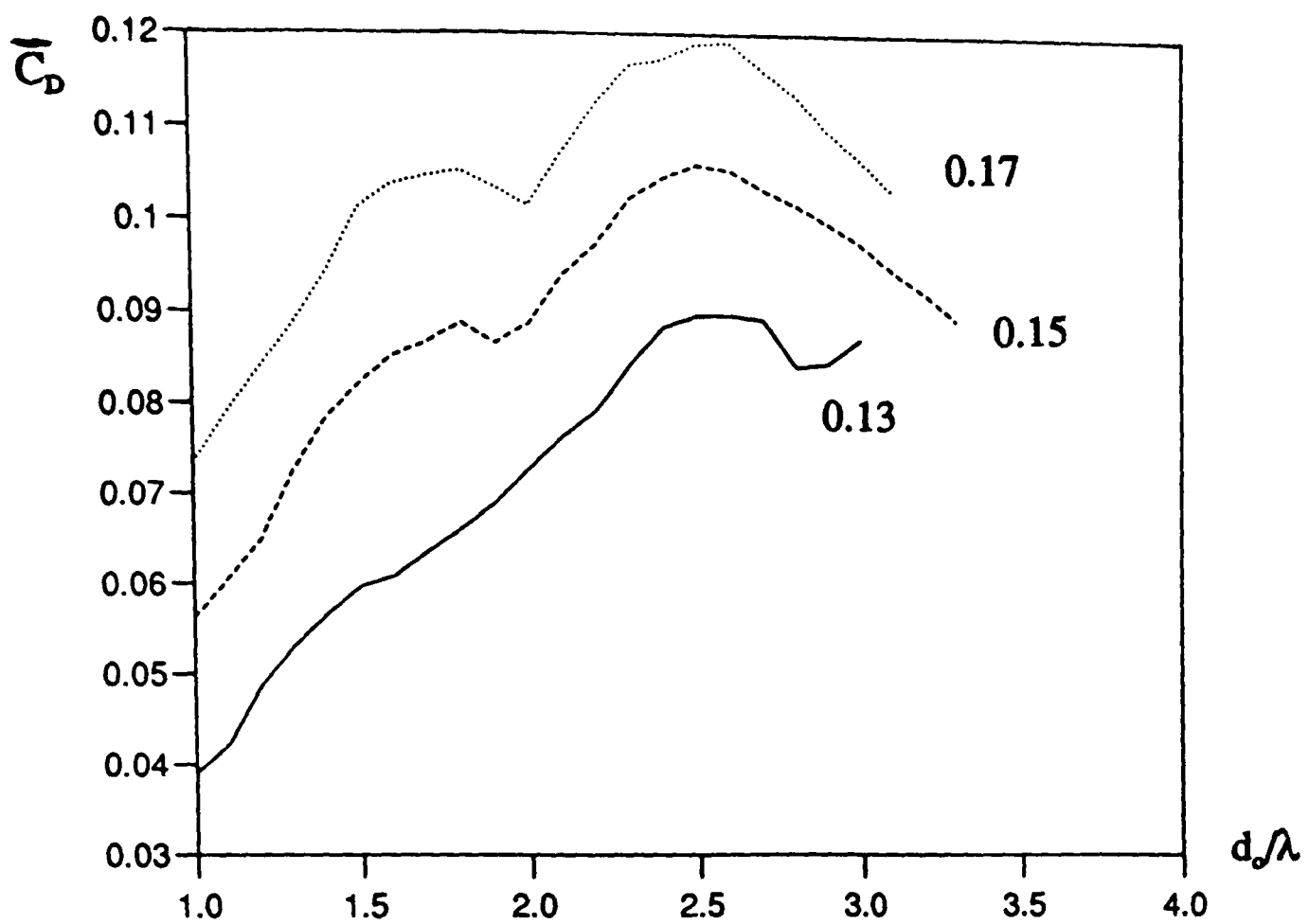


Figure 7.6

Figure 7.7

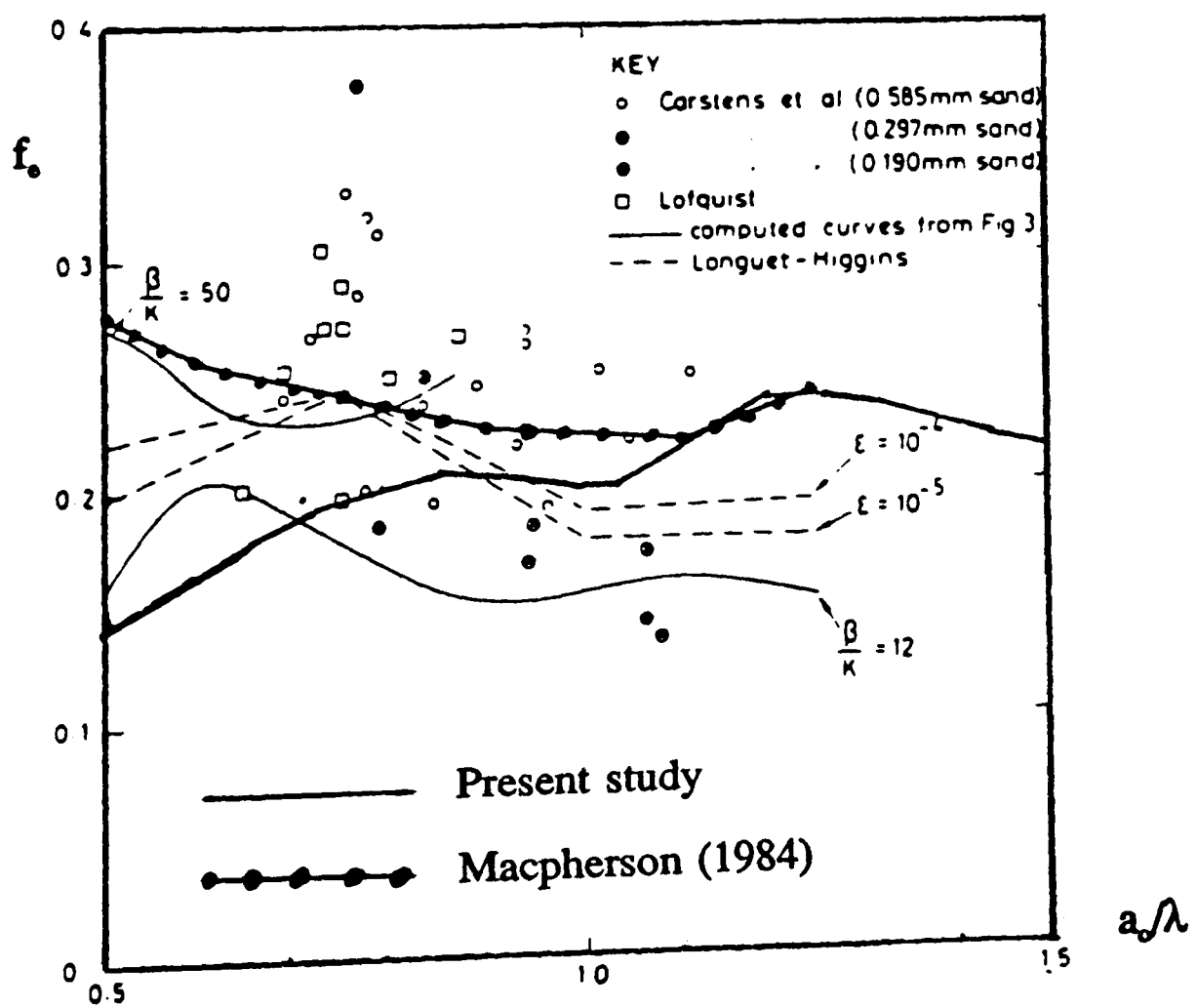


Figure 7.8

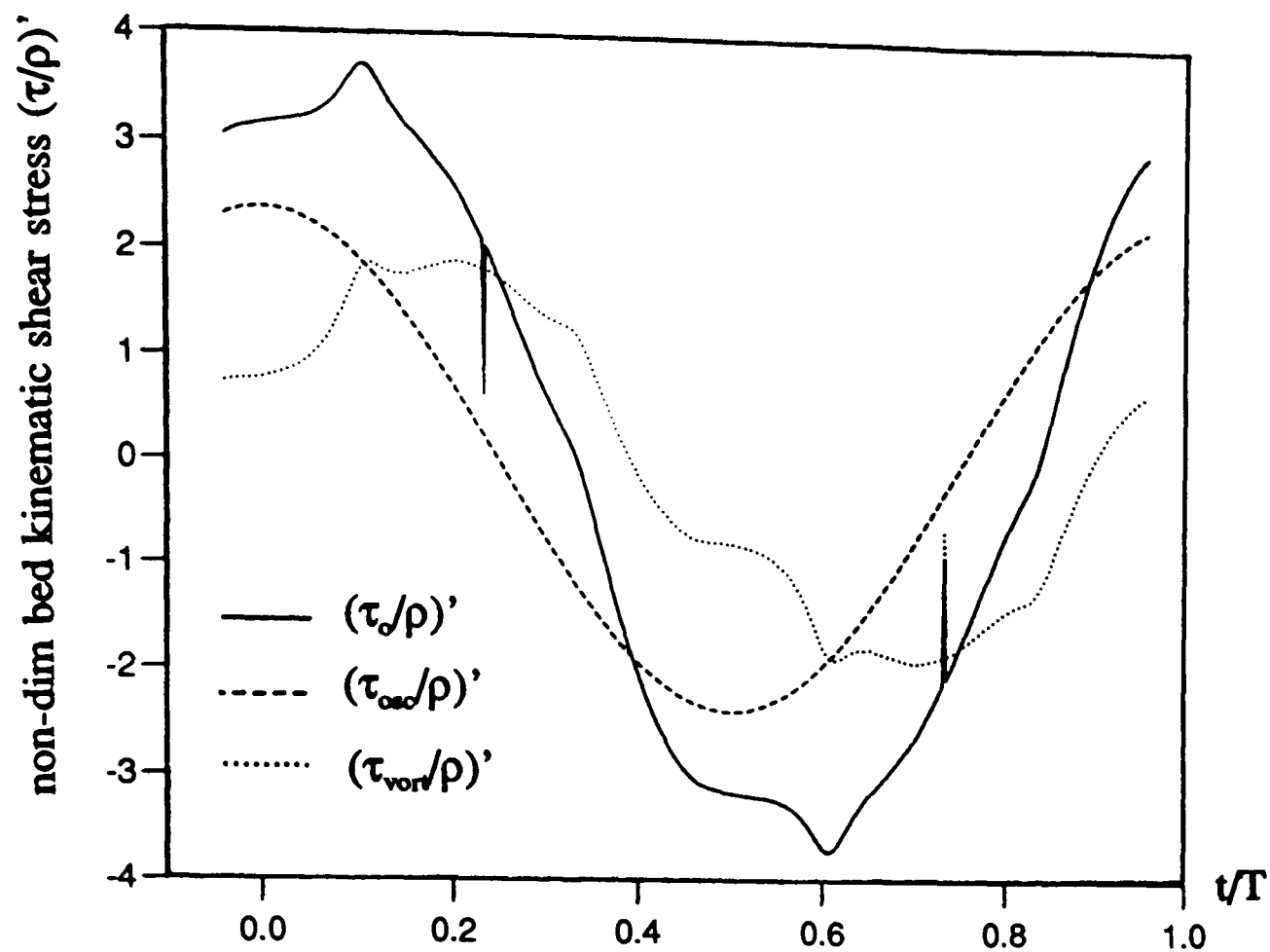
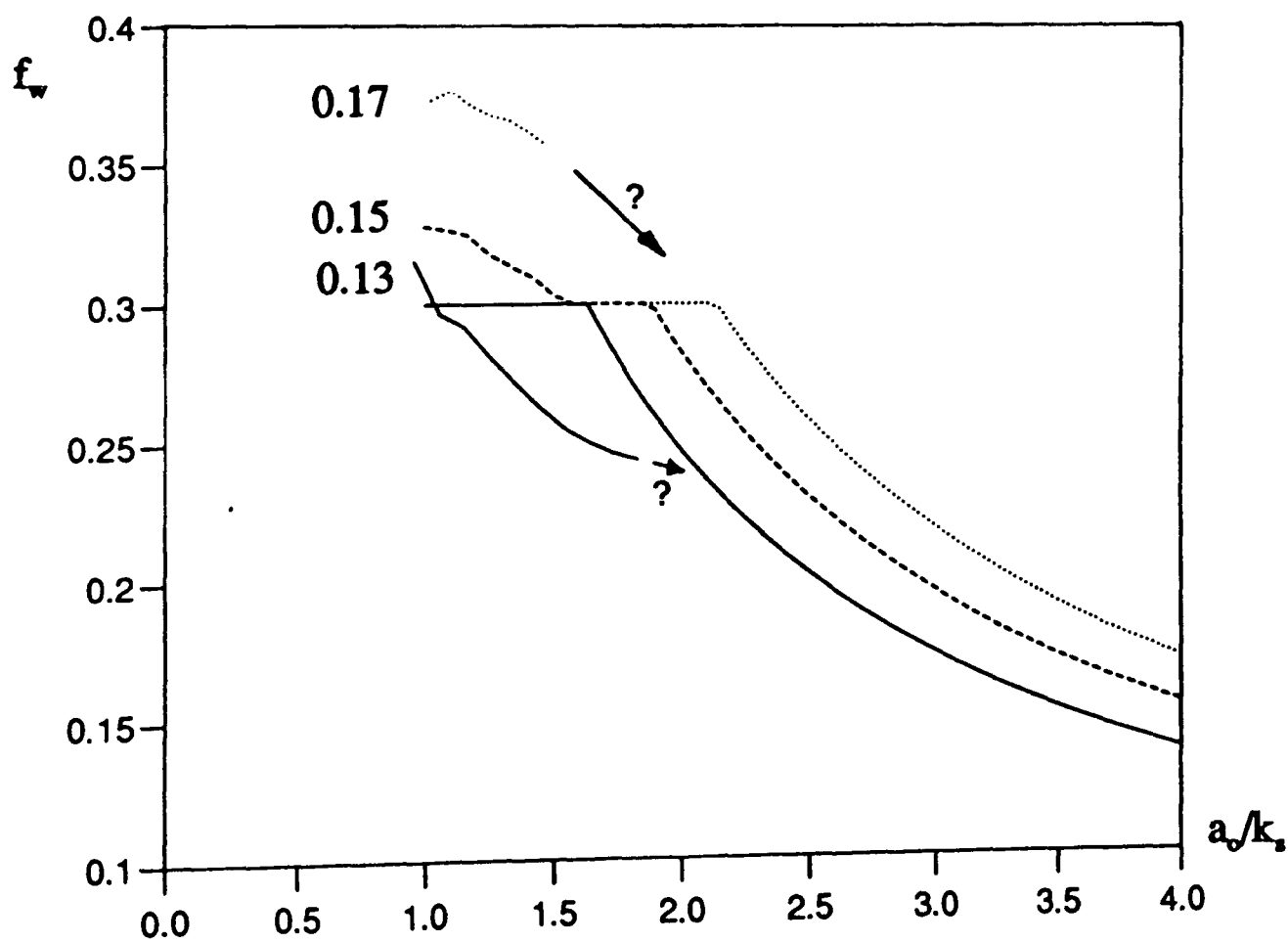


Figure 7.9



Some material that supplement the discussion

Figure 7.10 The variation of the cycle averaged drag coefficient ($\overline{C_D}$) versus d/λ , calculated for one ripple steepness ($h/\lambda = 0.17$) and without the contribution of the relic vortices.

Figure 7.11 A sketch that aims to illustrate how, with higher values of d/ρ , increasingly more of the trough region becomes filled with vorticity.

Figure 7.12 The actual size of the separation region (at $t/T = 0.30$) for $d/\lambda = 1.3, 2.5$, predicted by the hydrodynamical model. Even at $d/\lambda = 2.5$, the separation region barely encroaches on the stoss face of the neighbouring ripple.

Figure 7.10

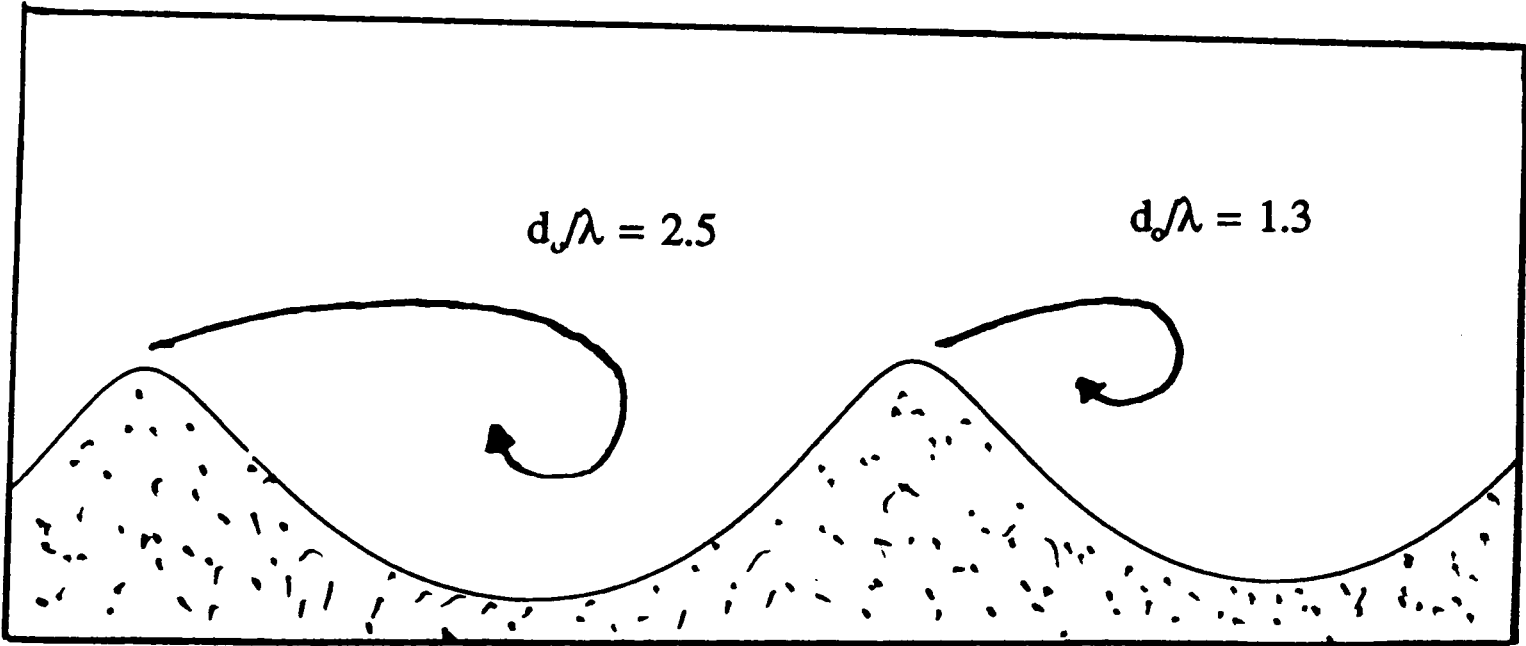
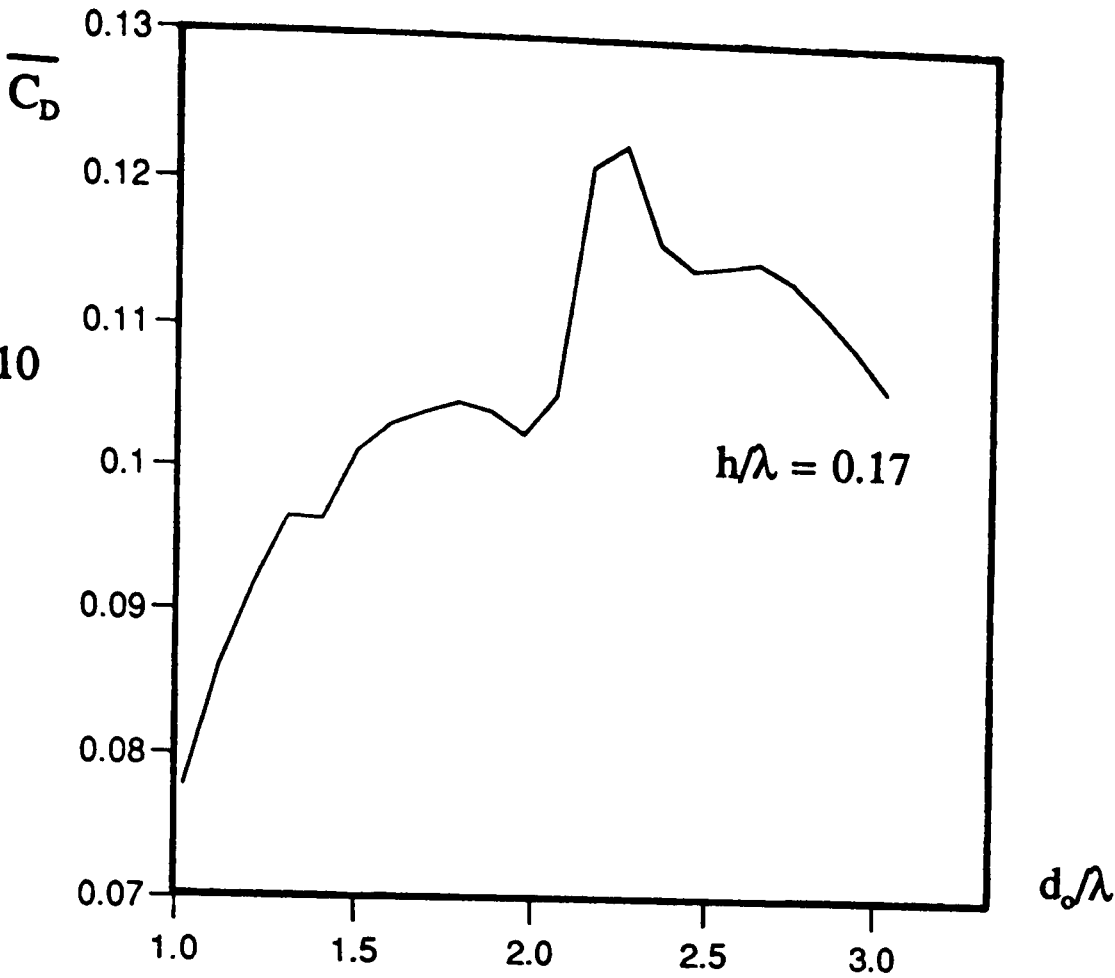
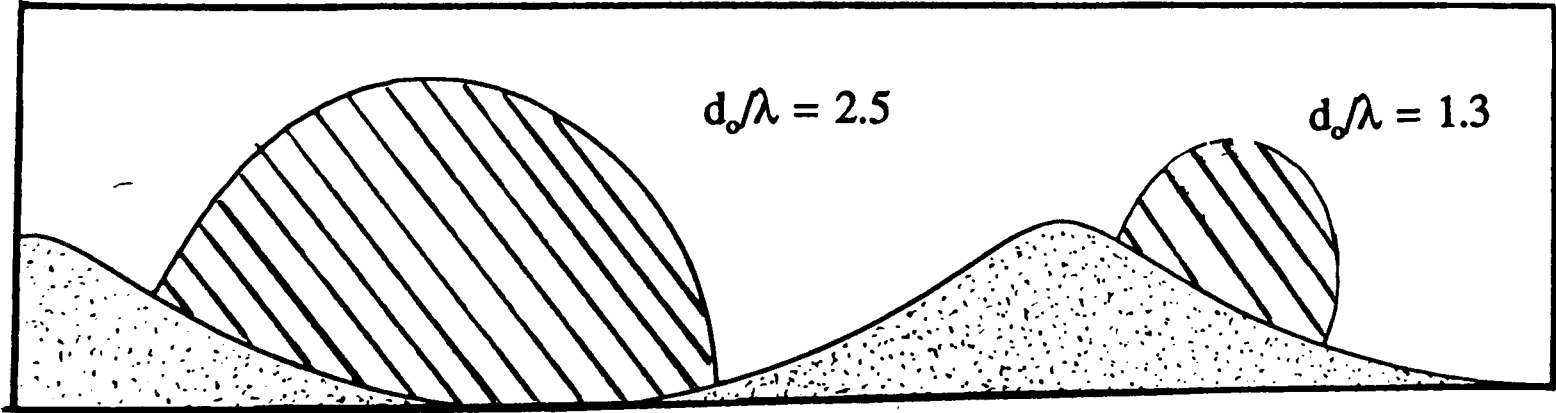


Figure 7.11

Figure 7.12



CHAPTER 8

CONCLUSION

8.1 Introduction

The two primary aims of this thesis have been (i) to gain further understanding of the vortex shedding regime over two-dimensional ripples under the action of waves, and (ii) to simulate the resulting entrainment and suspension of sediment in order to provide coastal engineers with details of sediment concentrations over beds of ripples.

A suite of theoretical models has been developed for this purpose. First, a hydrodynamical 'discrete vortex' model recreates the observed flow field over ripples. In turn, the hydrodynamical model provides the driving impetus for a boundary layer model, which describes the near-bed flow regime. Sediment is entrained at the ripple crest on the basis of bed shear stresses obtained from the boundary layer model. Once into suspension, sediment is moved within the framework of the hydrodynamical model, using Lagrangian-style 'tracking'. Two supplementary avenues of study have been undertaken:- (a) a study of the nature of the time-varying and cycle-averaged force over the ripple profile and (b) an exploratory study to see if the suite of models can be used to make predictions about ripple stability.

8.2 A brief resume of each of the chapters

As a prelude to discussing to what extent these aims have been achieved, we provide a short resume of the findings from each of the chapters.

8.2.1 The hydrodynamical model (Chapter 3)

The hydrodynamical model (Chapter 3) has proved quite successful in recreating the flow regime over ripples. The motion of vortices is generally realistic; (evolving) growing vortices form over the lee slope, and are then ejected over the parent crest towards neighbouring ripples. Derived quantities from the hydrodynamical model (vortex strengths, velocity time series etc) have given useful insights into the vortex shedding regime. In this respect, the strength signatures of individual vortices and the (in depth) study of the effect of both d/λ and ripple steepness on the motion of the (evolving) growing vortex are particularly interesting. The former show that vortices attain their maximum strength before they cease to be 'fed' new vorticity, whilst the

latter show that both parameters fundamentally affect the motion of the growing vortex. Two main doubts surround the hydrodynamical model: firstly, the prediction that vortices remain close to the bed, invariably being deleted from the model when forced to the bed in a weakened state; secondly, the change in the motion of the growing vortex associated with $d_s/\lambda > 2.1$ and steeper ripples. Neither feature significantly impares the hydrodynamical model, but their effects are noticeable in other chapters.

8.2.2 The boundary layer model (Chapter 4)

It is far more difficult to summarise findings from the boundary layer model (Chapter 4). The adapted form of Fredsoe's boundary layer model can still recreate Fredsoe's original results, which inspires some confidence in its mechanical operation. The results presented, using the Test 1 settings, are easily interpretable in terms of the prevalent flow regime, suggesting sensible behaviour of the model. It is the studies of sediment entrainment that provide the main test of the boundary layer model. A decision was taken to not try and feed the boundary layer model back into the 'vortex generation' element of the hydrodynamical model. This was because the predictions of boundary layer thickness given by the former were too large to be compatible with the latter.

8.2.3 The suspended sediment simulation (Chapter 5)

The studies of the suspended sediment regime over ripples (Chapter 5) met with mixed success. Encouraging predictions from the simulation include the replication of the 'four peak' structure of the instantaneous concentration profiles, quite good agreement in the phase of these peaks, and the comparisons between the predicted and calculated values of Nielsen's C_o . Numerous data comparisons, however, confirm that the predictions of the quantity of sediment within the flow are severely underestimated. The two culprits for this shortfall are (i) the boundary layer model with the associated Meyer-Peter Muller bedload rule, and, (ii) the inability of the hydrodynamical model to distribute sediment properly. The second point highlights the role of diffusion, which is not accounted for in the present simulation. Numerical experiment suggests that both

the manner in which suspended sediment is represented (via agglomerated particles) and the concentration profiles obtained (via measuring boxes) may be improved upon.

8.2.4 Ripple stability (Chapter 6)

The material presented in Chapter 6 is of an exploratory nature, aiming to see if the present suite of models could be used to make predictions about ripple stability. The answer to this is, unfortunately, no. However, the study of the predicted movement of sand over the ripple profile raises some very interesting questions. Specifically, how can a bedload rule move sediment through stagnation points? In the present simulation, sediment cannot pass through these points, so never reaches the crest. In reality, sediment clearly moves up the lee slope, under the growing vortex, to reach the crest, its inertia allowing it to pass through stagnation points.

8.2.5 The force on the bed 'per ripple' (Chapter 7)

In Chapter 7, results for the energy dissipation coefficient f_e show good agreement with established data up until $d_0/\lambda = 2.1$, then depart from the accepted trends beyond. Evidence suggests that this departure is due to the change in the motion of the growing vortex (see §7.4), which contributes about 70% to the value of f_e . An attempt to elucidate the nature of the friction factor f_w for the ripple regime showed that it had a tendency to increase slowly for $a_0/k_s < 1.57$. However, these findings are speculative. The values for f_w also showed misbehaviour for $d_0/\lambda > 2.1$.

8.3 General conclusions concerning the present study

If the study is taken in its entirety, then it becomes clear that the first of the two primary aims has been met, while the second has been met in part. The material relating to the flow structure over the ripples is consistently more reliable and informative. Results from the hydrodynamical model, the boundary layer model and the studies of the force on the bed 'per ripple' have given a valuable insight into the vortex shedding regime. The results from the studies of sediment entrainment and suspension show that many key features of this regime are, qualitatively, well predicted. However,

the demand for reliable numbers (concentrations etc) has not been met. There is the makings of a trustworthy simulation here, but more work is required before it can be used to provide sediment concentration predictions for other researchers. It should be noted that the second of the two primary aims is much more adventurous and pioneering than the first, perhaps illustrating the increased uncertainties of sediment transport in comparison with hydrodynamics.

8.4 Improvements to the present study

This chapter has, by its very nature, highlighted where possible improvements in the present study may be made. The most useful improvement to the hydrodynamical model would be an experimental study of vortex decay during its lifetime. This would do away with the artificially chosen decay regimes applied. If the small changes in the motion of the growing vortex seen beyond $d_0/\lambda = 2.1$ are so damaging to f_c and f_w , then what does this say about the effect of an arbitrarily chosen decay rule? Improvements to the suspended sediment studies include the account of sediment entrainment over the entire ripple profile, the effects of diffusion and the splitting up of agglomerated particles. All these options are feasible, but the first and third would require significant development. It may be that the Meyer-Peter Muller bedload formula is not the best way of assessing the volume of sediment entrained. Chapter 6 requires some mechanism to allow bedload sediment to pass through stagnation points before the present study can be used to predict ripple stability. The findings in Chapter 7 merely respond to the evolving vortex regime, so any improvements here will come directly from improvements in the hydrodynamical model.

8.5 The scope for further work

The scope for further work in this field is enormous. In reality, the driving oscillatory flow over the ripples is not symmetric, due to the presence of higher order wave forms (e.g. Stokes waves), a steady current or both. The inclusion of these effects would be a useful development, allowing the prediction of residual currents and net sediment transport. *(These developments are presently being pursued by MEB and*

AGD.) A model simulation that could faithfully predict sediment concentrations over ripples in both wave and wave-current regimes would be a powerful tool indeed. A two-dimensional simulation (as presented here) takes no account of spanwise variation in the ripple profiles. Ripples exposed at low tide often show sinuosity and a tendency to blend into each other. It would be useful to find out how much this three-dimensionality affects the sediment regime, perhaps by comparing results for straight-crested and naturally sinuous ripples. The effects of slope on bedload transport are still poorly understood, primarily because most of the bedload formulae were conceived in flat bed conditions. Finally, with regard to the ripples themselves, there is still no definitive answer as to why ripples are stable at certain parameter ranges and not at others. The author agrees with the view of Sleath (1982a) that it is a combination of hydrodynamical and sedimentological factors. The flow regime (via d_s/λ and the ripple steepness) determines how far the vortices travel on ejection and their load-bearing capability (from their strength). Favourable hydrodynamical factors for stable ripples include sediment laden vortices dumping their loads in the crest region, and the range of travel of ejected vortices being such that they can boost the rotation of growing vortices.

REFERENCES

- Asp Hansen E., Fredsoe J. & Deigaard R. (1991). Distribution of suspended sediment over wave generated ripples. *Int. symp. on the Transport of sediment and its modelling, Italy, Sept 2-5, 1991*.
- Bagnold R.A. (1946). Motion of waves in shallow water. Interaction between waves and sand bottoms. *Proc. Royal Soc. London.* A187, 1-15.
- Bijker E.W., van Hijum E. & Vellinga P. (1976). Sand Transport by waves. *Proc. 15th Int. conf. on Coastal Engng, Hawaii.* 1149-1167.
- Blondeaux P. (1990). Sand ripples under sea waves. Part 1. Ripple formation. *J. Fluid Mech.* 218, 1-17.
- Blondeaux P. & Vittori G. (1991). Vorticity dynamics in an oscillatory flow over a rippled bed. *J. Fluid Mech.*, 226, 257-289.
- Bosman J. (1982). The influence of bottom slope, water depth, breaking waves, orbital velocity and current velocity on the concentration distribution under waves and currents (in Dutch). *Delft Hydraulics, report M1875, Delft, The Netherlands*.
- Boyd R., Forbes D.L. & Heffler D.E. (1988). Time-sequence observations of wave-formed sand ripples on the ocean shoreface. *Sedimentology*, 34, 449-464.
- Carstens M.R. & Nielsen F.M. (1967). Evolution of a duned bed under oscillatory flow. *J. Geophys. Res.* 72, 3053-3059.
- Carstens M.R., Nielsen F.M. & Altinbilek H.D. (1969). Bed forms generated in the laboratory under oscillatory flow. *Tech. memo. number 28, Coastal Engng Res. Centre, Fort Belvoir, Virginia*.
- Clements R.R. (1973). An inviscid model of two dimensional vortex shedding. *J. Fluid Mech.* 57, 321-336.
- Clements R.R. & Maull D.J. (1975). The representation of sheets of vorticity by discrete vortices. *Prog. Aerospace Sci.* 16, 129-146.
- Chorin A.J. (1973). Numerical study of slightly viscous flow. *J. Fluid. Mech.* 57, 785-796.

- Davies A.G. (1984a). Observations of the stability of oscillatory flow above the seabed and of sand ripple formation. *Cont. Shelf Res.* 4, 553-580.
- Davies A.G. (1984b). Field observations of wave induced motion above the seabed and of the resulting sediment movement. Institute of Oceanographic Sciences Report Number 179. *Inst. Oceanographic Sciences Rep. No. 179.*
- Davies A.G. (1986). A model of oscillatory rough turbulent boundary layer flow. *Estuarine, Coastal and Shelf Sci.* 23, 353-374.
- Despard R.A. & Miller J.A. (1971). Separation in oscillating laminar boundary layer flows. *J. Fluid Mech.* 47, 21-31.
- Drake D.E. & Cacchione D.A. (1989). Estimates of the suspended sediment reference concentration (C_r) and resuspension coefficient (γ_r) from near-bed observations on the California shelf. *Cont. Shelf Res.* 9, 51-64.
- DuToit C.G. & Sleath J.F.A. (1981). Velocity measurements close to a rippled bed in oscillatory flow. *J. Fluid Mech.* 112, 71-96.
- Dyer K.R. (1986). *Coastal and Estuarine Sediment dynamics*. Edited by J. Wiley & sons, Chichester.
- Evans R.A. & Bloor M.I.G. (1977). The starting mechanism of wave induced flow through a sharp edged orifice. *J. Fluid Mech.* 82, 115-128.
- Fredsoe J. (1974). On the development of dunes in erodible channels. *J. Fluid Mech.* 64, 1-16.
- Fredsoe J. (1984). Turbulent boundary layers in wave-current motion. *J. Hydraulic Engng.* 110, 1103-1120.
- Fredsoe J. & Deigaard R. (1992). *Mechanics of Coastal Sediment Transport*. (Advanced series in Oc. Engng., Vol 3), World Scientific, ed. P.L.F. Liu.
- Gerrard J.H. (1967). Numerical computation of the magnitude and frequency of the lift on a circular cylinder. *Phil. Trans. Royal Soc. London.* 261, 1137-1162
- Glenn S.M. & Grant W.D. (1987). A suspended sediment stratification correction for combined wave and current flows. *J. Geophys. Res.* 92, 8244-8264.
- Hanes D.N. & Huntley D.A. (1986). Continuous suspended sand measurements in a wave dominated nearshore environment. *Cont. Shelf Res.* 6, 585-596.

- Hanes D.N., Vincent C.E., Huntley D.A. & Clarke T.A. (1988). Acoustic measurements of suspended sand concentration in the C²S² experiment at Stanhope Lane, P.E.I. *Mar. Geol.* 81, 185-196.
- Hara T. & Mei C.C. (1990). Oscillating flow over periodic ripples. *J. Fluid Mech.* 211, 183-209.
- Hardisty J. (1983). An assessment and calibration of formulations for Bagnold's bedload equation. *J. Sed. Petrology.* 53, 1007-1010.
- Homma M. & Horikawa K. (1962). Suspended sediment due to wave action. *Proc. 8th Int. Conf. on Coastal Engng., Mexico.* 168-193.
- Ikeda S., Horikawa K., Nakamura H. & Kenji N. (1991). Oscillatory boundary layer over a sand ripple model. *Coastal Engng. Japan.* 34(1), 15-29.
- Inman D.L. (1957). Wave-generated ripples in nearshore sands. *US Army Corps of Engrs, Beach Erosion Board, Technical Memorandum* 100.
- Jonsson I.G. (1966). Wave boundary layers and friction factors. *Coastal Engineering. Proc. Int. Conf. Coastal Engng., Tokyo, 1966.* Chapter 10, 127-148
- Jonsson I.G. (1980). A new approach to oscillatory rough turbulent boundary layers. *Oc. Engng.* 7, 109-152.
- Jonsson I.G. & Carlsen N.A. (1976). Experimental and theoretical investigation in an oscillatory rough turbulent boundary layer. *J. Hydraulic Res.* 14, 45-60.
- Kajiura K. (1968). A model of the bottom boundary layer in water waves. *Bulletin of the Earthquake Res. Inst., Univ. Tokyo.* 46, 75-123.
- Kennedy J.F. & Falcon M. (1965). Wave generated sediment ripples. *Report No. 86, Hydrodynamics lab., Dept. Civil. Engng. M.I.T.*
- Kiya M. & Arie M. (1977a). A contribution to an inviscid vortex shedding model for an inclined flat plane in uniform flow. *J. Fluid Mech.* 82, 223-240.
- Kiya M. & Arie M. (1977b). An inviscid numerical simulation of vortex shedding from an inclined flat plane in shear flow. *J. Fluid Mech.* 82, 241-253.
- Komar P.D. & Miller M.C. (1973). The threshold of sediment movement under oscillatory water waves. *J. Sed. Petrology.* 43, 1101-1110.

- Kundu P.K. (1990). *Fluid Mechanics*. Academic Press Incorporation.
- Lamb H. (1932). *Hydrodynamics*. 6th Edition. Cambridge University Press.
- Leonard A. (1980). Vortex methods for flow simulation. *J. Comp. Phys.* 37, 289-335.
- Lofquist K.E.B. (1978). Sand ripple growth in an oscillatory water flow tunnel. *U.S. Army Corps of Engrs., Coastal Engng. Res. Centre, Tech. paper no. 78-5*.
- Lofquist K.E.B. (1980). Measurements of oscillatory drag on sand ripples. *Proc. 17th Int. Conf. Coastal Engng., 1980., Am. Soc. Civil Engrs.* 3087-3106.
- Longuet-Higgins M.S. (1981). Oscillating flow over steep sand ripples. *J. Fluid Mech.* 107, 1-36.
- Macpherson B. (1984). Flow and sediment transport over steep sand ripples. PhD thesis at Univ. of Cambridge, U.K.
- Madsen O.S. & Grant W.S. (1975). The threshold of sediment movement under waves: a discussion. *J. Sed. Petrology.* 45, 360-361.
- Marin F. (1992). Etude experimentale de l'écoulement genere par la houle au-dessus d'un fond de rides. PhD thesis at Univ. of Le Havre, France.
- Meyer-Peter E. & Muller R. (1948). Formulae for bedload transport. *Proc. 2nd Cong. Int. Assoc. Hydraulic Res., Stockholm, Sweden*.
- Miller M.C. & Komar P.D. (1980a). Oscillation sand ripples generated by laboratory apparatus. *J. Sed. Petrology.* 50, 173-182.
- Miller M.C. & Komar P.D. (1980b). A field investigation of the relationship between oscillation ripple spacing and the near bottom water orbital motions. *J. Sed. Petrology.* 50, 183-191.
- Milne-Thomson L.M. (1968). *Theoretical Hydrodynamics*. (5th edition), London, Macmillan Press Ltd.
- Mogridge G.R. & Kamphuis J.W. (1973). Experiments on bedforms generated by wave action. *Proc. 13th Int. Conf. on Coastal Engng 1972., Am. Soc. Civil Engrs.* 1123-1142.
- Manohar M. (1955). Mechanics of bottom sediment movement due to wave action. *Beach Erosion Board Technical Memo 75*.

- Myrhaug D. (1982). On a theoretical model of rough turbulent wave boundary layers. *Oc. Engng.* 9, 547-565.
- Nakato T. Locher F.A. Glover J.R. & Kennedy J.F. (1977). Wave entrainment of sediment from rippled beds. *J. Waterways, Coastal and Oc. Div., Am. Soc. Civil Engrs.* 103(WW1), 83-99.
- Nielsen P. (1979). Some basic concepts of wave sediment transport. *Inst. of Hydrodynamical and Hydraulic Engng., Tech. Univ. of Denmark*, Series paper 20.
- Nielsen P. (1981). Dynamics and geometry of wave-generated ripples. *J. Geophys. Res.* 86, 6467-6472.
- Nielsen P. (1984a). On the motion of suspended sand particles. *J. Geophys. Res.* 89, 616-626.
- Nielsen P. (1984b). Field measurements of time-averaged suspended sediment concentrations under waves. *Coastal Engng.* 8, 51-72.
- Nielsen P. (1986). Suspended sediment concentrations under waves. *Coastal Engng.* 10, 23-31.
- Nielsen P. (1988). Three simple models of wave sediment transport. *Coastal Engng.* 12, 43-62.
- Nielsen P. (1992). *Coastal Bottom Boundary Layers and Sediment Transport*. (Advanced series in Oc. Engng., Vol 4). World Scientific, ed. P.L.F. Liu.
- O'Hare T. J. (1992). Sand bar evolution beneath partially standing waves. PhD thesis at Univ. of Wales, UK.
- Prandtl L. & Tietjans O.G. (1934). *Fundamentals of Hydro and Aeromechanics*. Dover.
- Ranasoma M. (1992). Measurements in combined oscillatory and steady flow over rippled beds. PhD thesis at Univ. of Cambridge, UK.
- Rosenhead L. (1931). Formation of vortices from a surface of discontinuity. *Proc. Royal Soc. London.* A134, 170-192.
- Sarpkaya T. (1975). An inviscid model of two dimensional vortex shedding for transient and asymptotically steady separated flow over an inclined plate. *J. Fluid Mech.* 68, 109-128.

- Sarpkaya T. (1989). Computational methods with vortices - 1988 Freeman Scholar Lecture. *J. Fluid Engng., Trans. Am. Soc. Civil Engrs.* 111, 5-52.
- Sarpkaya T. & Schoaff R.L. (1979). Inviscid model of two-dimensional vortex shedding by a circular cylinder. *Am. Inst. Aerospace and Aeronautics Journal.* 17, 1193-1200.
- Sato S., Shimosaki K. & Watanabe A. (1987). Measurements of oscillatory turbulent boundary layer flow above ripples with a laser-doppler velocimeter. *Coastal Engng. in Japan.* 30, 89-98.
- Sawamoto M. (1980). Flow field over rippled beds induced by wave action. *Proc. 3rd Int. Symp. Stochastic Hydraulics, Aug. 1980, Tokyo, Japan.*
- Sawamoto M. & Yagamuchi S. (1979). Theoretical modelling on wave entrainment of sand particles from rippled beds. *Trans. Japanese Soc. Civil Engrs.* 11, 170-171.
- Shibayama T. & Horikawa K. (1980). Laboratory study on sediment transport mechanism due to wave action. *Proc. Japanese Soc. Civil Engrs.* 296, 131-141.
- Sleath J.F.A. (1973). A numerical study of the influence of bottom roughness on mass transport by water waves. *Proceedings of the Int. Conf. on Num. Methods in Fluid Dyn., Southampton, U.K.*
- Sleath J.F.A. (1974). Velocities above a rough bed in oscillatory flow. *J. Waterways, Harbours and Coastal Engng. Div., Am. Soc. Civil Engrs.* 100(WW4). 287-304.
- Sleath J.F.A. (1976a). On rolling grain ripples. *J. Hydraulic Res.* 14(1), 69-81.
- Sleath J.F.A. (1976b). Forces on a rough bed in oscillatory flow. *J. Hydraulic Res.* 14(2), 155-164.
- Sleath J.F.A. (1982a). The suspension of sand by waves. *J. Hydraulic Res.* 20(5), 439-452.
- Sleath J.F.A. (1982b). Friction coefficients of rippled beds in oscillatory flow. *Cont. Shelf Res.* 1, 33-47.
- Sleath J.F.A. (1984). *Sea Bed Mechanics.* John Wiley and sons, New York.

- Sleath J.F.A. (1985). Energy dissipation in oscillatory flow over rippled beds. *Coastal Engng.* 9, 159-170.
- Smith J.D. (1977). Modelling of sediment transport on continental shelves. In *The Sea* Vol 6. E.D. Goldberg, I.N. McCave, J.J. O'Brien & J.H. Steele. Edited by J. Wiley and sons, New York. Pages 539-578.
- Smith J.D. & McLean S.R. (1977). Spatially averaged flow over a wavy surface. *J. Geophys. Res.* 82, 1735-1746.
- Smith P.A. & Stansby P.K. (1989). Postcritical flow around a circular cylinder by the vortex method. *J. Fluids and Structures.* 3, 275-291.
- Soulsby R.L. & Dyer K.R. (1988). Sand transport on the continental shelf. *Ann. Rev. Fluid Mech.* 20, 295-324.
- Stansby P.K. (1977). An inviscid model of vortex shedding from a circular cylinder by the vortex method. *Proc. Inst. Civil Engrs.* 63, 865-880.
- Stansby P.K. & Dixon A.G. (1983). Simulation of flow around cylinders by a lagrangian vortex scheme. *App. Oc. Res.* 5, 167-178
- Stansby P.K. & Isaacson M. (1987). Recent developments in offshore hydrodynamics. *App. Oc. Res.* 9, 118-127.
- Swart D.H. (1976). Coastal sediment transport. Computation of longshore transport. *Delft Hydraulic Lab. Report r968 rt 1.*
- Taneda S. (1977). Visual study of unsteady separated flows around bodies. *Prog. Aerospace Sci.* 17, 287-348.
- Tunstall E.B. (1973). Experimental study of vortices generated by oscillatoy flow over rippled surfaces. PhD thesis at Univ. of California, San Diego, U.S.
- Tunstall E.B. & Inman D.L. (1975). Vortex generation by oscillatory flow over rippled surfaces. *J. Geophys. Res.* 80, 3475-3484.
- Van Rijn L.C. (1992). Sediment transport in combined currents and waves. *Euromech 262 - Sand transport in Rivers, Estuaries and the Sea.* (edited by Soulsby and Bettess). 3-15

- Villaret C. & Latteux B. (1992). Entrainment and transport of fine sand by combined waves and currents: an experimental study. *Proc. Int. Conf on Coastal Engng., Venice, Italy, 1992.*
- Villaret C. (1992, 1993). Unpublished data made available for this thesis.
- Vincent C.E. & Green M.O. (1990). Field measurements of the suspended sand concentration profiles and fluxes and of the resuspension coefficient γ_0 over a rippled bed. *J. Geophys. Res.* 95, 11591-11601.
- Whitehouse R.J.S. (1991). Slope-inclusive bed load transport; experimental assessment and implications for models of bedform development. *Euromech 262 - Sand Transport in Rivers, Estuaries and the Sea.* (edited by Soulsby and Bettess).
- Williams J.C.(III). (1977). Incompressible boundary layer separation. *Ann. Rev. Fluid Mech.* 9, 113-114.

APPENDIX 1. The derivation of the components of force acting on the ripple profile

According to the requirements of the PhD, the author (MEB) acknowledges the aid of his supervisor (AGD) with this derivation.

The components of force exerted by the fluid on the ripple profile are calculated using contour integration techniques and Blasius's Theorem. Figure (A1.1) illustrates the contour of integration (C) in the z-plane used to calculate the force on one ripple wavelength. Contour C_1 corresponds to the bed; C_2 and C_4 are two sides separated by one wavelength, and C_3 is the top (which is at infinity above the bed). Cauchy's integral theorem is applied to perform the integrations. Vortex centres within C represent mathematical singularities, requiring the evaluation of residues.

The complex potential for the flow regime is

$$\Omega = -U\zeta + \sum iK_{s,u} \log \sin \frac{\pi}{\lambda} (z - z_s) + \sum iK_{s,l} \log \sin \frac{\pi}{\lambda} (z - \overline{z'_s}) \quad A1$$

where U is the oscillatory flow far from the bed, z_s, z'_s are the centres of the s vortices above and below the bed and $K_{s,u}$ and $K_{s,l}$ are their respective vortex strengths. The time-varying form of Blasius's Theorem applied is

$$F + iG = \frac{1}{2} i\rho \oint_{C_1} \overline{\left(\frac{d\Omega}{dz} \right)^2} dz - i\rho \oint_{C_1} \frac{\partial \Omega}{\partial t} dz \quad A2$$

where F and G are the horizontal (drag) and vertical (lift) components of force and ρ is the fluid density. Longuet-Higgins (1981) includes a third term (involving $\partial \Omega / \partial t$) in his expression for Blasius's Theorem. This is dropped here because the ripple profile along which we are integrating along, is, in fact, the time-invariant zero streamline.

Two terms (J_1 and J_2) are isolated from equation (A2) and solved separately;

$$J_1 = \oint_{C_1} \left(\frac{d\Omega}{dz} \right)^2 dz, \quad J_2 = \oint_{C_1} \frac{\partial \Omega}{\partial t} dz \quad \text{A3 (a, b)}$$

The evaluation of the integral J_1

Cauchy's theorem requires the summation of $\int (d\Omega/dz)^2 dz$ along the four contours. The nature of this integral is such that the contributions from the two side contours (C_2 and C_4) cancel each other out. This leaves

$$\oint_{C_1} \left(\frac{d\Omega}{dz} \right)^2 dz + \oint_{C_3} ()^2 dz = J_1 + J_{12} = 2\pi i \sum (\text{residues of } \left(\frac{d\Omega}{dt} \right)^2 \in C) \quad \text{A4}$$

where

$$\frac{d\Omega}{dz} = -U \frac{\partial \zeta}{\partial z} + \sum \frac{i\pi K_{s,u}}{\lambda} \cot \frac{\pi}{\lambda} (z - z_s) + \sum \frac{i\pi K_{s,l}}{\lambda} \cot \frac{\pi}{\lambda} (z - \overline{z'_s}) \quad \text{A5}$$

The integral J_{12} can be simplified because (a) $\partial \zeta / \partial z \rightarrow 1$ and (b) the vortex terms $\rightarrow 0$ as $\chi \rightarrow \infty$. Thus

$$J_{12} = \int_{\lambda/2}^{-\lambda/2} (-U)^2 dx = -\lambda U^2 \quad \text{A6}$$

To find the residues of $(d\Omega/dz)^2$ within C , it is first necessary to expand the $\cot(\pi/\lambda)(z - z_s)$ term in equation (A5) as follows:

$$\cot \frac{\pi}{\lambda} (z - z_s) = \frac{\lambda}{\pi} \frac{1}{z - z_s} + O(z - z_s) \quad \text{A7}$$

The required residues are obtained from the coefficient of $1/(z - z_s)$ in the expansion of $(d\Omega/dz)^2$. Substituting equation (A7) into equation (A5) gives this coefficient as

$$2 \sum i K_{s,u} \left[-U \frac{\partial \zeta}{\partial z} + \sum \frac{i \pi}{\lambda} K_{s,l} \cot \frac{\pi}{\lambda} (z - \bar{z}_s) \right] \quad A8$$

$$= 2 \sum i K_{s,u} (-u_s + i v_s) \quad A9$$

where u_s, v_s are the velocity components in the z plane. Equation (A9) has been obtained using the definition of $d\Omega/dz$. Substituting equations (A6), (A9) into (A4) gives

$$J_1 = \lambda U^2 + 4 \pi \sum K_{s,u} (u_s - i v_s) \quad A10$$

Evaluation of J_2

Differentiating equation (A1) with respect to t gives

$$\frac{\partial \Omega}{\partial t} = -\dot{U} \zeta + \sum i K_{s,u} \left(\frac{-\pi \dot{z}_s}{\lambda} \right) \cot \frac{\pi}{\lambda} (z - z_s) + \sum i K_{s,l} \left(\frac{-\pi \dot{\bar{z}}_s}{\lambda} \right) \cot \left(\frac{\pi}{\lambda} (z - \bar{z}_s) \right) \quad A11$$

where dots represent time derivatives. Here, it is assumed that the vortex strengths are time invariant. Cauchy's integral formula gives

$$\oint_{c_1} + \oint_{c_2} + \oint_{c_3} + \oint_{c_4} \frac{\partial \Omega}{\partial t} dz = 2 \pi i \sum (\text{residues of } \partial \Omega / \partial t \in C) \quad A12$$

To proceed from here, the expression for $\partial \Omega / \partial t$ (equation (A11)) may be split into two parts, reflecting the contributions from the oscillatory flow and the vortices respectively;

$$J_{21} = \oint_{c_1} \frac{\partial \Omega_{osc}}{\partial t} dz = \oint_{c_1} -\dot{U} \zeta dz \quad A13$$

and

$$J_{22} = \oint_{C_1} \frac{\partial \Omega_{vort}}{\partial t} dz = \oint_{C_1} \left[\sum iK_{s,u} \left(\frac{-\pi \dot{z}_s}{\lambda} \right) \cot \frac{\pi}{\lambda} (z - z_s) + \right. \\ \left. + \sum iK_{s,l} \left(\frac{-\pi \dot{z}_s^*}{\lambda} \right) \cot \frac{\pi}{\lambda} (z - \overline{z_s^*}) \right] dz \quad A14$$

where $J_2 = J_{21} + J_{22}$.

Evaluation of the integral J_{21}

Cauchy's integral formula gives

$$\oint_{C_1} + \oint_{C_2} + \oint_{C_3} + \oint_{C_4} \frac{\partial \Omega_{osc}}{\partial t} dz = 2\pi i \sum (\text{residues of } \partial \Omega_{osc} / \partial t \in C) \quad A15$$

On C_2, C_4 , $\zeta = \pm \lambda/2 + i\chi$, while on C_3 , $\zeta = x + iy_\infty$. Also, J_{21} has no poles within C , so the right hand side of equation (A15) is zero. Thus equation (A15) becomes

$$\int_{C_1} \frac{\partial \Omega_{osc}}{\partial t} dz + \int_{-h/2}^{y_\infty} -\dot{U} \left(\frac{\lambda}{2} + i\chi \right) \cdot i dy + \int_{\lambda/2}^{-\lambda/2} -\dot{U}(x + iy_\infty) \cdot dx + \int_{y_\infty}^{-h/2} -\dot{U} \left(-\frac{\lambda}{2} + i\chi \right) \cdot i dy = 0 \quad A16$$

giving

$$J_{21} = \oint_{C_1} \frac{\partial \Omega_{osc}}{\partial t} dz = \dot{U} \lambda i \frac{h}{2} \quad A17$$

Evaluation of the integral J_{22}

The evaluation of J_{22} is more complicated. The contributions Cauchy's theorem from the two side contours (C_2 and C_4) cancel out, so that Cauchy's integral formula reduces to

$$\oint_{C_1} + \oint_{C_3} \frac{\partial \Omega_{\text{vort}}}{\partial t} dz = 2\pi i \sum (\text{residues of } \partial \Omega_{\text{vort}} / \partial t \in C) \quad \text{A18}$$

To evaluate this integral, it is first necessary to establish the form of $\partial \Omega_{\text{vort}} / \partial t$ on C_3 . The contour C_3 is far from the bed, allowing certain (crucial) alterations to the form of $(\partial \Omega / \partial t)_{\text{vort}}$ there. Firstly, z plane co-ordinates and their time derivatives may be replaced by their equivalent ζ plane co-ordinates (i.e. $z \approx \xi + i\chi$, $\dot{z} \approx \dot{\xi} + i\dot{\chi}$). Secondly, on C_3 , $\chi \rightarrow \infty$, giving

$$\cot \frac{\pi}{\lambda} (\zeta - \zeta_s) \rightarrow -i, \quad \cot \frac{\pi}{\lambda} (\zeta - \bar{\zeta}_s) \rightarrow -i \quad \text{A19 (a, b)}$$

Thus, on C_3

$$\frac{\partial \Omega_{\text{vort}}}{\partial t} = \sum \frac{-\pi}{\lambda} i \dot{\chi}_s (\Delta K_s) \quad \text{A20}$$

where $\Delta K_s = K_{s,u} - K_{s,l}$. Integrating equation (A20) along C_3 gives

$$\oint_{C_3} \frac{\partial \Omega_{\text{vort}}}{\partial t} dz = \int_{\lambda/2}^{-\lambda/2} \sum \frac{-\pi}{\lambda} i \dot{\chi}_s \Delta K_s dx = \sum \pi i \dot{\chi}_s \Delta K_s \quad \text{A21}$$

The residue of $(\partial \Omega / \partial t)_{\text{vort}}$ within C will be the coefficient of the term in $1/(z - z_s)$. If the cotangent expansion is applied as before, then this coefficient is found to be

$$\sum i K_{s,u} \dot{z}_s = \sum i K_{s,u} (u_s + i v_s) \quad \text{A22}$$

Substituting equations (A21), (A22) into equation (A18) gives

$$J_{22} = -\sum \pi i \dot{\chi}_s \Delta K_s + \sum 2\pi K_{s,u} (u_s + i v_s) \quad \text{A23}$$

Finally, combining the results for J_{21} (from equation (A17)) and J_{22} (from equation (A23)) gives

$$J_2 = U \lambda i \frac{h}{2} - \sum \pi i \dot{\chi}_s \Delta K_s + \sum 2\pi K_{s,u} (u_s + i v_s) \quad \text{A24}$$

The substitution of equations (A4) and (A24) into Blasius's Theorem (equation (A2)) gives the force components F (drag) and G (lift). These are

$$F = \rho \dot{U} \lambda \frac{h}{2} + \pi \rho \sum \dot{\chi}_s \Delta K_s = F_{osc} + F_{vort} \quad \text{A25}$$

and

$$G = \frac{1}{2} \rho \lambda U^2 \quad \text{A26}$$

More generally, account needs to be taken of time variation in the vortex strengths, in which case the components become

$$F = \rho \dot{U} \lambda \frac{h}{2} + \pi \rho \sum \frac{\partial}{\partial t} [\Delta K_s \chi_s] \quad \text{A27}$$

and

$$G = \frac{1}{2} \rho \lambda U^2 \quad \text{A28}$$

Equation (A27) is the drag force on the ripple profile. The first term (F_{osc}) arises from the contribution of the oscillatory flow, whilst the second (F_{vort}) comes from the effect of vortices. The form of this second term conforms to the equivalent findings of Longuet-Higgins (1981), namely that the force is the time-rate of change of the product of the vortices' height from the bed and their strength.

APPENDIX 2. Obtaining a concentration profile - a worked example

It was thought useful to take the reader through the process of obtaining an instantaneous concentration profile, from the very start. We have taken the run parameters from Test 1 as our worked example. The experimental parameters received from C. Villaret in connection with Test 1 were: $T = 2$ s, $\lambda = 0.063$ m, $h = 0.01$ m, $U_o = 0.16$ m/s, $D_{50} = 9 \times 10^{-5}$ m, and $w_s = 0.007$ m/s. The flow diagram (figure (A2.1)) accompanying this appendix supplements this description.

The initial requirement for obtaining a concentration profile is to run the hydrodynamical model to produce a velocity time series at the crest level. This is used to 'drive' the boundary layer model. Some relevant flow parameters are $l = 100$ m⁻¹, $\sigma = \pi$ s⁻¹, $h/\lambda = 0.16$ and $d_o/\lambda = 1.62$. This information allows us to calculate the necessary input parameters demanded by the hydrodynamical model; $U_o' = 5.08$, $b' = 0.16\pi$ and $v' = 3.17 \times 10^{-3}$.

Running the hydrodynamical model gives us the time series of velocity at the crest. This time series is both reworked and re-non-dimensionalised in the manner described in §4.3, where the new lengthscale, $k_s = 2.5D_{50} = 2.25 \times 10^{-4}$ m. The boundary layer model requires a critical bed shear stress, τ_c . The graph of Sleath (1984) gives $\tau_c = 0.15$ N/m², but, as stated in §5.4.1, this value is found to be too high, so τ_c is taken as one third of this value i.e. $\tau_c = 0.05$ N/m². When non-dimensionalised with respect to k_s and σ , the kinematic critical bed shear stress, $(\tau_c/\rho)'' = 100$.

The boundary layer model has provided us with a time series of kinematic bed shear stress. Two things remain to be done before this series can be used to simulate sediment entrainment at the crest. First, it must be converted to a (so-called) ϕ_b time series, where ϕ_b is the non-dimensional volume transport rate per unit width of flow. This is achieved using the Meyer-Peter Muller bedload formula (equation (5.4)). Second, this ϕ_b time series needs to be reworked back to its original form, so that it runs in synchronisation with the hydrodynamical model.

We are now in a position to re-run a version of the hydrodynamical model that incorporates sediment entrainment and movement. Measuring boxes are required to obtain instantaneous concentration profiles. As an example of their operation, we look at the profile obtained 1.0 cm above the crest. With $Y = 0.01$ m, the height above the x-axis is $y = 0.015$ m. The centre of the box is thus at a height $y' = ly = 1.5$. Our box dimensions are $-0.3 < x_c < 0.3$, $1.2 < y_c < 1.8$. This defines the measuring box, which has sides approximately $\lambda/10$ long. The instantaneous concentration profiles thus obtained are (invariably) very spikey. For this reason, a 21 point moving average is used to out the results.

It is necessary to convert the cumulative values of ϕ_b recorded at each time step into actual concentrations (C. Villaret quoted sediment concentration in g/l). To do this, we first convert the cumulative ϕ_b values into equivalent Q_b values, using the definition of Q_b in equation (5.4). Q_b is a transport rate per unit width with units m^2/s . Therefore, secondly, the values of Q_b per time step are then multiplied by the (physical) time step (i.e 2 seconds divided by 500). This gives a quantity analogous to an 'area' of sediment. The ratio of this area to the actual (dimensional) area of the box gives a non-dimensional concentration of sediment within the box. Finally, this non-dimensional concentration is converted to a concentration in g/l by multiplying the ratio by 2650 g/l, this value being the density of sediment in g/l.

Figures that supplement the two appendices

Figure A1.1 The contour of integration (C) used in the derivation of the force components 'per ripple' on the bed.

Figure A2.1 A flow diagram illustrating the stages that are passed through in order to obtain an instantaneous concentration profile.

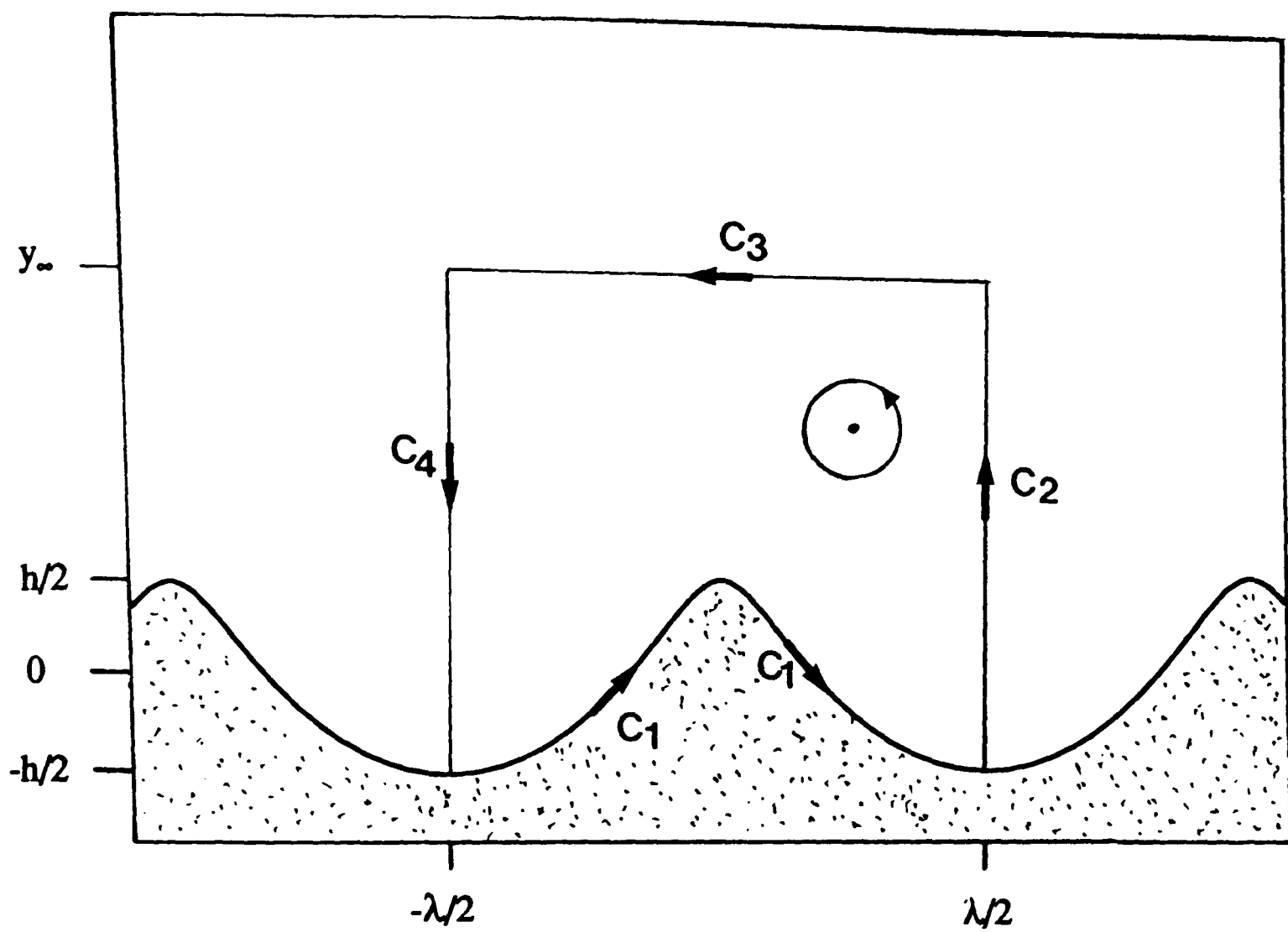


Figure A1.1

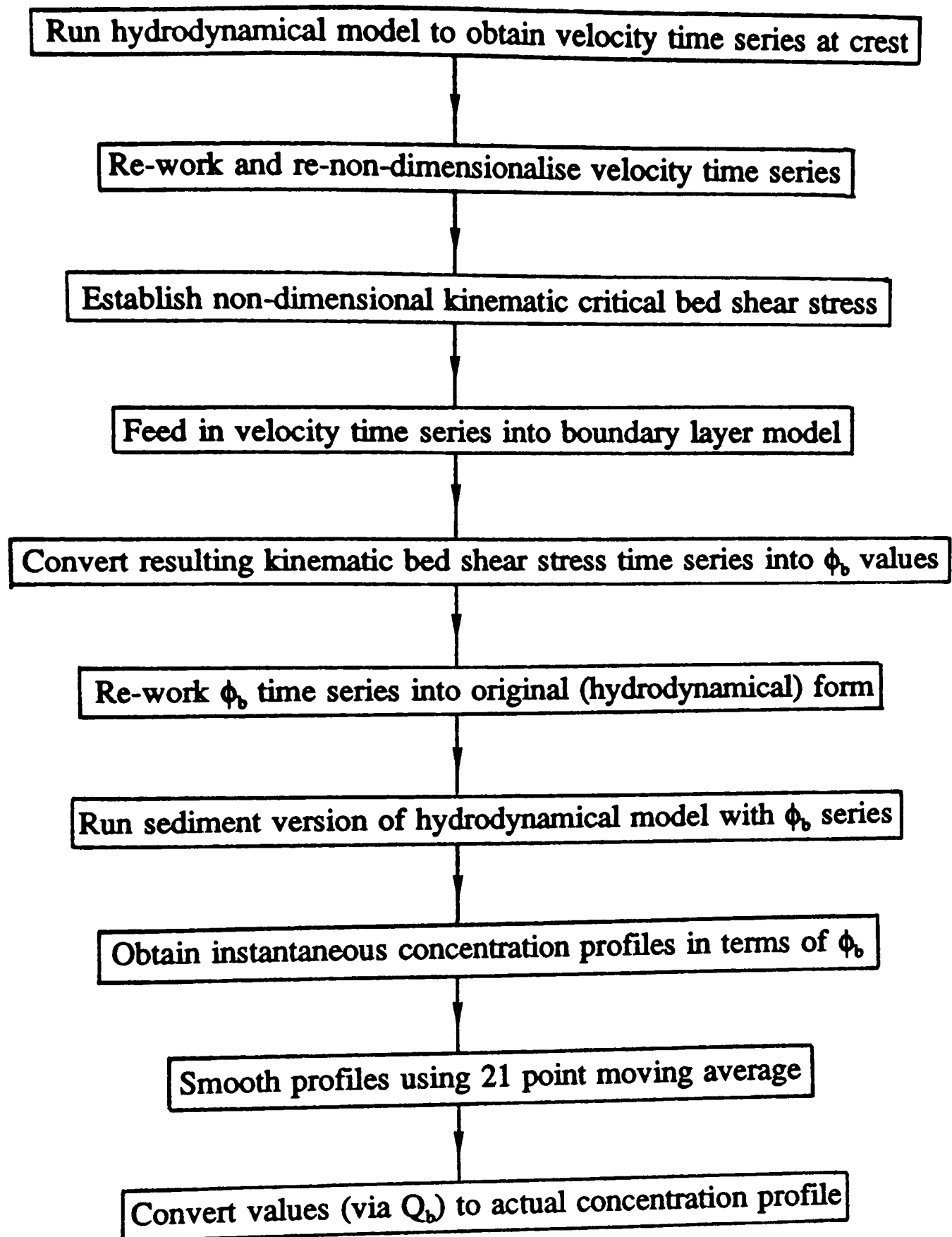


Figure A2.1